



UNIVERSITÀ
degli STUDI
di CATANIA

**UNIVERSITÀ DEGLI STUDI DI CATANIA
IN CONVENZIONE CON:**



UNIVERSITÀ DEGLI STUDI DI PALERMO
DOTTORATO DI RICERCA IN

Scienza Dei Materiali e Nanotecnologie– XXX CICLO

Simona Filice

***Nanomaterials and polymeric nanocomposites
for photocatalytic applications***

Tutor: Prof.re Giuseppe Compagnini

Co-Tutor: Dott.ssa Silvia Scalese

Coordinatore: Prof.ssa Maria Grazia Grimaldi

TESI PER IL CONSEGUIMENTO DEL TITOLO DI DOTTORE DI RICERCA

Index

INTRODUCTION AND AIM OF THE THESIS WORK	1
1.1 Introduction	1
1.1.1 The energy problem.....	1
1.1.2 The “water” problem	4
1.1.2.1 Water Contaminants	5
1.1.2.2 Methodologies for water purification	6
1.2 Photocatalysis.....	12
1.2.1 Photocatalytic process for water purification.....	13
1.2.2 Photocatalytic process for hydrogen production	15
1.2.3 Parameters affecting the photocatalytic process	18
1.3 Nanotechnology for water purification and hydrogen production	20
1.3.1 Nanomaterials for water purification	21
1.3.2 Polymeric nanocomposites for water purification.....	22
1.3.3 Nanomaterials for hydrogen production.....	25
LASER IRRADIATION OF GRAPHENE OXIDE SOLUTIONS FOR WATER PURIFICATION APPLICATIONS	27
2.1 Graphene oxide (GO)	27
2.1.1 GO functionalization and reduction	30
2.1.2 Modification of GO by laser irradiation.....	33
2.1.3 GO for water purification application	34
2.1.4 GO for photocatalytic application	36
2.2 GO and irradiated GO: study of antibacterial properties and toxicity	39
2.3 Laser irradiated GO and titania for dye removal.....	47
LASER IRRADIATION OF INORGANIC SEMICONDUCTORS FOR PHOTOCATALYTIC WATER SPLITTING	55
3.1 Pulsed Laser Irradiation in Liquid (PLIL).....	55

3.1.1 Laser irradiation of inorganic semiconductor	59
3.2 Titanium dioxide	61
3.2.1 Enhancement of TiO ₂ photocatalytic activity.....	64
3.2.2 TiO ₂ photocatalytic application.....	66
3.2.3 Visible laser irradiation of titania colloids	67
3.2.4 UV laser irradiation of titania colloids	76
3.3 Bismuth oxide and Bi-based materials	78
3.3.1 Bi ₂ O ₃ photocatalytic application	80
3.3.2 Laser irradiation of β-Bi ₂ O ₃ nanospheres in different liquid environments: reactivity and structural changes	82
POLYMERIC NANOCOMPOSITES FOR PHOTOCATALYTIC APPLICATIONS	89
4.1 Sulfonated polymers in water purification	89
4.1.1 Nafion.....	89
4.1.2 Nexar	93
4.2 Nafion hybrid nanocomposite membranes for water purification applications.....	99
4.2.1 Materials preparation and characterization	99
4.2.2 Nafion hybrid nanocomposite membranes for cationic and anionic dye removal	103
4.3 Effect of the GO sulfonation on the dye removal in water	112
4.4 Sulfonated pentablock copolymer for water purification applications	117
4.4.1 Materials preparation and characterization	117
4.4.2 s-PBC hybrid nanocomposite membranes for dye removal.....	126
4.4.3 Bi ₂ O ₃ /sPBC composite for visible photocatalytic applications.....	136
CONCLUSIONS AND FUTURE PERSPECTIVES	139
REFERENCES.....	144
Appendix A: Characterization techniques	150

Appendix B: Azo Dyes	155
Appendix C: Irradiation Lamps	158
Curriculum vitae	160
List of Publications	161

Chapter 1

INTRODUCTION AND AIM OF THE THESIS WORK

1.1 Introduction

In this chapter the fundamental concepts regarding the global issues of clean energy production and water purification are introduced, focusing on conventional methods and new approaches to these problems. Nanomaterials and nanocomposites are described as emerging, functional materials for the above mentioned purposes; in particular, the use of these materials in photocatalytic processes is in strong development and diffusion. Photocatalysis is a green and low cost process compared with the classical methodologies for water treatment and hydrogen production.

1.1.1 The energy problem

In the energy sector, the 2020 goals introduced by European policy makers were based on three main objectives: security of supply, competitive markets and sustainability. The 2020 energy goals are to have a 20% (or even 30%) reduction in CO₂ emissions compared to 1990 levels, 20% of the energy, on the basis of consumption, coming from renewables and a 20% increase in energy efficiency. A wide range of technologies and methods exist to improve energy efficiency, turn renewables into viable energy sources and reduce emissions. All EU countries have adopted national renewable energy action plans including (1) sectorial targets for electricity, heating and cooling, and transport; (2) planned policy measures; (3) the different mix of renewables technologies; and (4) the planned use of cooperation mechanisms. Among all the renewable energy sources, the most promising one is hydrogen. In the following paragraphs, all the advantages of this energy source are explained.

In the 21st century, there is a constant demand for energy to satisfy the needs of current lifestyles. At the present stage, our society still relies on non-renewable sources: fossil fuels still represent the main source of energy for the world, despite the fact that Earth absorbs 3.85×10^{24} J per year of solar energy [Takanabe (2014)]. Fossil fuels are high in energy, readily available, relatively cheap and easy to transport. However, increasing emissions of greenhouse gases such as carbon dioxide (CO₂) from the combustion of fossil fuels are among the main causes of global climate change [Solomon (2007)]. Global warming would have devastating effects on the planet by increasing in sea levels leading to loss of land and extinction of species, by affecting agriculture and causing famine. Burning fossil fuels also leads to air pollution by the release of harmful gases (i.e carbon dioxide, carbon monoxide, nitrogen oxides, sulphur dioxide) and particulates, this affects the environment and human health. As a consequence, orders of magnitude cleaner and renewable energy systems with respect to actually

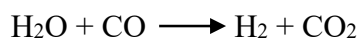
used ones are required in order to meet the growing demand for energy while significantly reducing toxic gases emissions.

There are a number of alternative energy sources including solar power, wind, biomass, biofuels, geothermal and hydrogen. The main advantages of hydrogen are its high energy capacity (enthalpy of combustion is as high as 286 kJ/mol) and environmental friendliness (the only product after burning is water i.e. no harmful gases are produced). H₂ is one of the most suitable energy carrier candidates having the best energy to mass ratio when compared to other existing fuels such as natural gas or petroleum. Furthermore, H₂ can be used directly as a fuel, or it can be transformed into higher value hydrocarbon molecules and liquid fuels for transportation using existing infrastructure. In other words, large amounts of energy can be stored for long time using this molecule. A disadvantage of hydrogen fuel is that it has a low energy to volume ratio making its storage and transportation complicate [Schlapbach (2001)]. The shifting to hydrogen-based economy is based on various fundamental and organizational factors, mainly concerning production, storage and distribution. Among these, the production has received considerable attention.

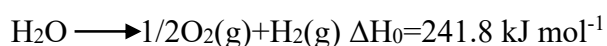
Hydrogen can be stored by pressured tanks, by condensation to liquid or even solid and by its adsorption in solids with high surface areas [Schlapbach (2001)]. Pressured tanks require additional pressure within high safety risks. Liquid hydrogen may be an alternative to them but it requires cryogenic storage. Furthermore, its liquefaction imposes a large energy loss to cool it down to since it boils around 20.268 K (−252.882 °C or −423.188 °F). The tanks must also be well insulated to prevent boil off increasing costs. Recently, a lot of studies have been focused on the use of high surface area solids to store hydrogen by its reversible adsorption on solid surfaces as carbon.

Hydrogen is the smallest and lightest element on earth. As a consequence, in order to transport large amounts of hydrogen it must be either pressurized and delivered as a compressed gas, or liquefied. Today, hydrogen is transported from the point of production to the point of use via pipeline, over the road in cryogenic liquid tanker trucks or gaseous tube trailers.

Another problem with hydrogen fuel is that even though hydrogen is the most abundant element in the universe, it is not present as itself but in other forms as water or methane. Current methods for hydrogen production concern the extraction from natural gas (48%), oil (30%), coal (18%) and electrolysis (4%). Steam reforming is the cheapest method of producing hydrogen [Twigg (1989)]: methane is heated in the presence of steam and a Ni catalyst at high temperatures (700-1100 °C). Methane is broken up forming carbon monoxide CO and hydrogen H₂. This is then followed by the water gas shift reaction, using the produced CO to generate more hydrogen and CO₂.



For what concerns energy and environmental issues, the present technique is defective and even unacceptable. First, the process is an intensive endothermic reaction and requires a temperature as high as 700-1000 °C. Secondly, the non-renewable fossil fuels are consumed and the greenhouse gas CO₂ is emitted as a byproduct in the process; one ton of produced hydrogen will also generate 9 to 12 tons of CO₂. As a consequence, an alternative method to produce hydrogen is desired. The use of water as hydrogen source is a way to save depletable fossil fuels and eliminate unwanted emissions of CO₂. External energy input, as electrical power, is required to split water into H₂ and O₂. The process is widely known as electrolysis of water.



Electrolysis uses electricity to split water into hydrogen and oxygen. Electrodes usually Pt, Ir or stainless steel are placed into water, a potential is applied between the electrodes generating the production of hydrogen at the cathode and oxygen at the anode. The water splitting process for H₂ generation is cyclic and environmentally friendly, since the raw material is abundant and cheap and the combustion of H₂ in air produces only water. Anyway, the overall potential for splitting water is equal to -1.23 V. This means that a voltage of at least 1.23 V is required. Due to barriers such as activation energy and ion mobility, an over potential is usually needed for the production of hydrogen. Electrolysis is not as economical as steam reforming and it is therefore rarely used in industry. If the energy input can be obtained from a renewable source, such as solar energy, H₂ can then become a low-cost and clean energy alternative capable of powering our planet [Lewis (2006)]. There are several ways for solar hydrogen production from water: PV solar cells and electrolyzers, or using sunlight concentrators to drive thermally the reaction at 1500-2500 K are possible ways to split water. Anyway, with these technologies, keeping the price at a competitive level with fossil-fuel-derived H₂ is still challenging. Photocatalytic water splitting represents one of the most appealing approaches due to its large-scale potential application [Jiang (2002)]. The technology is simple: a powdered material is suspended in water and directly produces H₂ and O₂ in a single reactor by sunlight irradiation; however, it represents a comprehensive scientific fundamental challenge. This will be deeply described in paragraph 1.2.2.

1.1.2 The “water” problem

One of the leading problems in developing countries is water quality and scarcity, which seriously affect their economic and social development and human health. The great importance of the “water problem” is underlined by the fact that under the first Horizon calls for projects, approximately €165 million are provided to water-related projects and this topic remains a key objective under the new EU research and innovation funding program, Horizon 2020.

Although two-thirds of our world’s surface is covered by water, only 0.75% is available for the survival of all living creatures outside of the sea. 1.2 billion people lack access to safe drinking water, 2.6 billion have little or no sanitation, millions of people die annually from diseases transmitted through unsafe water or human excreta and around \$7.3million is spent on healthcare for waterborne diseases alone [Montgomery 2007]. The increase of global population within global warming seriously affects water quality and availability. In particular, access to water resources decreases due to water shortages, erratic rainfall, glaciers melting and sea level rise. As a consequence, the salinity of costal potable water sources will increase, affecting approximately a third of the world population in particular in developing countries. This problem rests more on women: they are forced to walk 3-4 hours for day to collect and carry back home contaminated water, thus avoiding them the possibility of attending school or holding a job and further reducing the family income and their economic independence. Water also strongly affects energy and food production, industrial development, and the environment quality, affecting the economies, health of population and social development of both developing and industrialized nations.

Within the high rate of population growth, the demand for fresh water is expected to increase, but its quality is seriously limited by anthropogenic activities: around two million tons of waste are produced by humans and disposed every day in water courses. In particular, emerging pollutants have caught the attention of environmental organization and research institutes due to their toxic effects and recalcitrant properties [Méndez-Arriaga (2010)]. The mass use of cosmetic, cleaning and pharmaceutical products increases the level and variety of water pollutants, that are not removed by conventional wastewater treatment, affecting aquatic ecosystems and drinking water sources. Considering the limited water sources, the potential scarcity of water, the low efficiency for organic compounds removal in conventional water treatment systems, and emerging pollutants, highly efficient and compact systems, that minimize the use of chemical and the amount of residual products, are needed, In the following paragraphs the main classes of water contaminants are reported within a deep description of conventional and emerging methods for water purification.

1.1.2.1 Water Contaminants

The different types of water pollutants along with their sources and impact are given in Table 1A.

Table 1A Different water pollutants, sources and their effects

Pollutants	Sources	Effects
Organic pollutants	Industrial waste (Dyes, pesticides, chlorinated compound, pharmaceuticals)	Mutagenicity, pH, COD,
Inorganic pollutants	Soil-erosion, power plants (Metals/Metalloids, nitrates, phosphates)	Acidity, hardness,
Microorganisms	Sewage, animals excrement, (E-Coli, bacillus subtilis, pseudomonas aeruginosa, enterococcus faecalis, giardia lamblia)	Waterborne disease

- **ORGANIC CONTAMINANTS**

Natural organic matter (NOM) is referred to a broad group of organic materials including aquatic humic substances, carboxylic acids, phenols, amino acids, proteins, hydrocarbons, carbohydrates, and trace organic compounds, that are produced from the decomposition of living materials and anthropogenic activities. The composition and properties of NOM may vary with source (origin), age, fate, and season. [Aiken (1985)]. The removal of NOM is of great interest for the scientists since it can reduce the aesthetic qualities of drinking water by imparting colour to water; it is a substrate for microbial growth interfering with water treatment processes (i.e. membrane fouling), competing with other pollutants for adsorption sites and reacting with common disinfectants as chlorine producing a variety of toxic by-products [Zularisam (2006)]. Usually NOM is removed by coagulation followed by an advanced treatment process, such as membrane filtration, ion exchange/adsorption, and ozonation/biodegradation. These methods allow to concentrate or transfer it from water to another phase; recently, the photocatalytic process has been investigated as an alternative method for complete mineralization of organic matter [Bekbolet (1996)].

- **INORGANIC CONTAMINANTS**

Most of the surface and ground water sources are contaminated with many heavy and radioactive metals due to anthropogenic sources or geological reasons. These metal ions are accumulated in the biosphere and edible items. They also enter the human body through food chain and are also

responsible for their biomagnification. The different techniques used for metal removal are adsorption, chemical precipitation, coagulation, flocculation, ion exchange, and membrane filtration.

- **MICROORGANISMS**

An overarching goal for providing safe water is to disinfect water from traditional and emerging pathogens, without creating more problems due to the disinfection process itself. Waterborne pathogens have a devastating effect on public health, especially in the developing countries of sub-Saharan Africa and Southeast Asia. Disinfection methods currently used are based on halogenated compounds that are efficient, but they cause the formation of harmful disinfection byproducts (DBPs). Therefore, innovative approaches that enhance the reliability and robustness of disinfection while avoiding DBP formation are needed [Buccheri (2016)].

Recently, the use of UV or Visible light has been considered as a promising method to photochemically inactivate pathogens. Anyway, UV light alone is not effective for inactivating viral pathogens; in presence of photocatalytic materials such as titania (TiO_2), active species (i.e. hydroxyl radicals and superoxides) capable of inactivating viruses are generated. In addition, photocatalytic material can be appropriately modified to be active under visible light, so ideally it will be possible to use sunlight for virus inactivation [Li (2008)]. This aspect is highly important for developing countries. In this regard, it is mandatory to improve the understanding of the mechanisms for the interactions of pathogens, in particular virions, with excited photocatalyst surfaces and active species aiming to the design of selective materials.

1.1.2.2 Methodologies for water purification

New methods to detect toxic compounds and decontaminate water are urgently needed. These methods should be specific on the particular pollutant classes relevant to a specific water source and these should be “safe” or, in other words, they should not introduce new toxic by-products. Furthermore, they should take into account the available social and economic resources of each countries. These goals present exciting opportunities for the research community.

Water contaminants can be physically removed from water or can be converted into biodegradable compounds. Looking at the existent technologies for water and wastewater treatment, the most common methods are reported in Table 1B and briefly described in the following paragraphs.

Table 1B Current methods for water treatment

	METHODS	DESCRIPTION
Conventional Methods	Adsorption	Transfer of contaminants to a different phase without degradation. The efficiency is limited by surface area and there is a lack of selectivity. The regeneration is expensive and results in loss of the adsorbent
	Coagulation and Flocculation	Simple, economically feasible but high sludge production, handling and disposal problems
Established Methods	Membranes	Physical barrier based on size exclusion, commonly associated with high energy consumption (when pressure is the driving force). They produce a high-quality treated effluent. The performance is highly dependent on the type of membrane material.
	Ion Exchange	Ion exchange is a reversible chemical process in which an ion from solution is exchanged for a similar charged ion attached to an immobile solid particle or composite film. They are efficient but require high costs.
Emerging Technology	Chemical Oxidation	Molecular structural modification of contaminants by an oxidizing agent (i.e. chlorine, ozone). Rapid and efficient process. No sludge production, little or no consumption of chemicals, efficiency for recalcitrant dyes. Formation of mutagenic and carcinogenic by-products may bring additional risk for human health.
	Microfiltration Ultrafiltration Nanofiltration Reverse Osmosis	High efficiency in removing pollutants, but fouling increases the cost of energy for pumping and replacement of the membranes.
	Biological treatments	Decomposition of organic compounds through living systems (i.e. bacteria, algae, plants). Usually safe and low cost, the disadvantage is the high production of sludge when compared to the volume of treated water.

Conventional water treatment systems are capable of removing suspended solids, oil and fat, degrading organic matter and, depending on the technologies, removing nitrogen and phosphorus from urban wastewater. However, these systems display low efficiency for removing organic compounds and micro-pollutants. They also require sequential processes in order to reach the minimal

standards of water quality increasing the cost of the treatment due to high energy consumption, and high maintenance and operating costs [Shannon (2008)].

Advanced technologies, including UV light, ozone, membrane filtration and advanced oxidation processes (AOPs), have been studied for oxidation of different water pollutants showing remarkable results in the degradation of complex compounds.

This thesis work focused mainly on two methodologies for water purification: adsorption process and AOP, the latter including the use of photocatalytic materials. In the following paragraphs, these methodologies are deeply described.

- **Adsorption**

Adsorption is a process in which a substance (adsorbate), in gas or liquid phase, accumulates on a solid surface. Physical adsorption is achieved by weak chemical interactions between the adsorbate and the adsorbent i.e. Van der Waals forces, dipole interactions, and hydrogen binding. Physical adsorption is a non-specific and a reversible process. Chemical adsorption results from the chemical link between adsorbent and adsorbate molecules, therefore it is specific as well as irreversible, this means that chemical as well as electronic properties of adsorbent are changed.

The adsorption process involves the mass transfer of the adsorbate molecules across the liquid layer to the surface of the adsorbent particles followed by their transport and adsorption into the active sites. The most important properties of adsorbent, which determines its use, are the pore structure (shape, size and number) and the specific surface area.

Water purification by adsorption on activated carbons (AC) is very widely used, most often as a post treatment. Activated carbons is a solid, porous, black carbonaceous material that can be produced from either synthetic or natural C-based solid precursor. Activated carbons have high internal surface area and pore volume that make it very convenient to be used as adsorbent, catalyst, or catalyst supports [Radovic (2001)]. The high porosity of AC mainly derives from its structure composed by microcrystalline (amorphous) graphitic-like sheets, called “basal planes”, which are randomly cross-linked and surrounded by a number of unpaired electrons. The adsorption capacity of AC depends also on the chemical nature of its surface, i.e. by the presence of surface functional groups like acidic (carboxylic, lactones and phenols) or basic (ethers, carbonyls) groups. The main disadvantages of using AC are related to costs and their regeneration that is usually achieved at high temperature (>900°C) within the loss of about 15% of the initial activated carbon. Furthermore, their application as powder makes themselves a waste. For these reasons, the use of AC is restricted to the removal of low concentrated pollutants.

An evolution of carbonaceous adsorbents analogous to AC are graphene, carbon nanotubes and graphene oxide. The last one is deeply described in the second chapter.

- **Filtration**

The first attempt to use membrane technologies for water purification started in 1960, with the development of high performance synthetic membranes. Recently, more advanced membranes made from new materials and various configurations are employed for water treatment [Amjad (1993)]. These include microfiltration (MF), ultrafiltration (UF), reverse osmosis (RO), and nanofiltration (NF) membranes (Figure 1.1). MF membranes have the largest pore size and typically reject large particles and various microorganisms. UF membranes have smaller pores than MF membranes and, therefore, in addition to large particles and microorganisms, they can reject bacteria and soluble macromolecules such as proteins. RO membranes are effectively non-porous and, therefore, exclude particles and even many low molar mass species such as salt ions, organics, etc. NF membranes have pores with dimensions on the order of ten angstroms or less, and performance between that of RO and UF membranes.

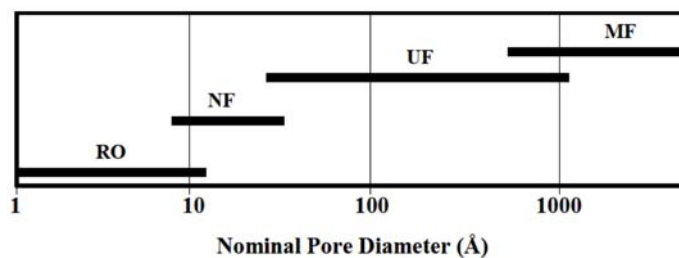


Figure 1. 1 Range of nominal membrane pore sizes.

Typical MF and UF polymers include poly(vinylidene fluoride), polysulfone, poly (ether sulfone), poly(acrylonitrile) and poly(acrylonitrile)-poly(vinyl chloride) copolymers, cellulose acetate-cellulose nitrate blends, nylons, and poly(tetrafluoroethylene). RO membranes are typically either cellulose acetate or polysulfone coated with aromatic polyamides. NF membranes are made from cellulose acetate blends or polyamide composites like the RO membranes, or they could be modified forms of UF membranes such as sulfonated polysulfone. Membranes can also be prepared from inorganic materials such as ceramics or metals [Baker (2004)]. Ceramic membranes are microporous, thermally stable, chemically resistant, and often used for microfiltration. However, disadvantages such as high cost and mechanical fragility have hindered their widespread use. On the contrary, polymeric membranes exhibit an excellent separation performance, while often show poor tolerance to high temperatures, organic solvents and corrosive environments.

The main drawback of filtration is fouling which occurs when pollutants such as salt and suspended solids clog membrane pores. This reduces the lifetime of membranes and membrane modules, increases the energy consumption and the complexity of the filtration process. Another major challenge of the membrane technology is to selectively set the trade-off between membrane selectivity and permeability. The final aim is to have efficient and resistant materials whose energy consumption in pressure driven processes is reduced.

The use of block copolymer architectures is under investigation for producing mechanically strong membranes, with a good trade-off between permeability and selectivity and reduced fouling. This aspect will be deeply discussed in Chapter 4 of this thesis. Besides copolymer architecture, also the incorporation of functional nanomaterials into membranes offers a great opportunity to improve the membrane permeability, fouling resistance, mechanical and thermal stability, as well as to render new functions for contaminant degradation and self-cleaning. Results related to the latter issue will be reported in Chapter 4.

- **Advanced Oxidation Processes (AOPs)**

Advanced oxidation processes (abbreviation: AOPs) refers to a set of chemical treatment procedures performed at normal pressure and temperature to degrade aqueous organic (or inorganic) pollutants into CO₂, water and mineral acids by reaction with hydroxyl radicals ($\cdot\text{OH}$). Their potential (2.8 V) is higher with respect to other species used in water treatment, such as ozone (2.07 V), H₂O₂ (1.78 V), HOCl (1.49 V) and chlorine (1.36 V) [Ibhadon (2013)]. Hydroxyl radicals are produced with the help of one or more primary oxidants (e.g. ozone, hydrogen peroxide, oxygen) and/or energy sources (e.g. ultraviolet light) or catalysts (e.g. titanium dioxide). Precise, pre-programmed dosages, sequences and combinations of these reagents are applied in order to obtain a maximum $\cdot\text{OH}$ yield. Actually, AOPs still have not been put into commercial use on a large scale (especially in developing countries) mostly because of the relatively high costs and low selectivity. Anyway, they are used as tertiary treatment for recalcitrant pollutants. There are many types of AOPs processes according to different mechanisms of $\cdot\text{OH}$ generation (Table 1C).

After the formation of $\cdot\text{OH}$, all the processes consist in the initial attacks on target molecules by $\cdot\text{OH}$ and their breakdown to fragments that are subsequently mineralized [Ibhadon (2013)]. Currently there is no consensus on the detailed degradation mechanisms of $\cdot\text{OH}$: since these are radical species and should behave like a highly reactive electrophile, hydrogen abstraction and/or addition are supposed to occur as initial attacks. As long as there are sufficient $\cdot\text{OH}$ radicals, they continue to react until the

fragments are completely mineralized. It is mandatory to underline that such processes may still be subject to a myriad of possible and partially unknown mechanisms.

Table 1C. List of homogeneous AOPs

Method	Key reaction	Drawbacks
UV /H ₂ O ₂	$H_2O_2 + UV \rightarrow 2 \cdot OH$	1) Absorb $\lambda < 300$ nm, a lesser component in solar radiation. 2) pH dependence. 3) Continuous supply of feed chemicals are required.
UV /O ₃	$O_3 + HO^- \rightarrow HO_2^- + O_2$ $O_3 + HO_2^- \rightarrow HO_2 \cdot + O_3^{-\cdot}$ $O_3^{-\cdot} + H^+ \rightarrow HO_3 \cdot$ $HO_3 \cdot \rightarrow \cdot OH + O_2$	1) Absorb $\lambda < 300$ nm, a lesser component in solar radiation. 2) pH dependence 3) Continuous supply of feed chemicals are required. 4) Process is expensive.
UV /O ₃ /H ₂ O ₂	$O_3 + H_2O_2 \rightarrow HO \cdot + HO_2 \cdot + O_2$	1) Absorb $\lambda < 300$ nm, a lesser component in solar radiation. 2) Applicable over a wider pH range.
Fe ³⁺ /H ₂ O ₂ (Photo Fenton)	$H_2O_2 + Fe^{2+} \rightarrow Fe^{3+} + \cdot OH$ $Fe^{3+} + UV + H_2O \rightarrow Fe^{2+} + \cdot OH + H^+$	1) Sludge disposal problem formed during the process. 2) Continuous supply of feed chemicals are required. 3) Process is expensive.

AOPs effectively allow to eliminate organic or inorganic pollutants from any aqueous phase, rather than being collected or transferred into another phase as in conventional methods. In some AOPs designs, heavy metals could also be removed in forms of precipitated M(OH)_x and disinfection could also be achieved. Furthermore, the complete reduction product of ·OH is H₂O, so AOPs theoretically do not introduce any new hazardous substances into the water.

The main drawbacks of AOPs concern high costs and low selectivity due to the high reactivity of radical species. Table 1D reports comparative costs of some AOPs. Only wastes with relatively small COD contents (≤ 5 gL⁻¹) can be suitably treated by means of these processes [Munter (2001)] since higher COD contents would require the consumption of too large amounts of expensive reactants. Given the potential costs, AOPs are usually deployed in the final stage after primary and secondary treatment have successfully removed a large proportion of contaminants.

Tabella 1D Comparative cost of some AOPs (Adapted from Munter [Munter (2001)])

Process	Cost of oxidant	Cost of UV
O ₃ /UV	High	Medium
O ₃ /H ₂ O ₂	High	0
H ₂ O ₂ /UV	Medium	High
Photocatalytic oxidation	Very low	Medium

Recent trends are the development of new, modified AOPs that are efficient and economical. In this regard, photocatalysis has been recognised for its high capability to mineralize organic compounds. In the following paragraph, photocatalytic process for water purification is described focusing on the enhancement of the photocatalytic activity promoting the production of hydroxyl radicals.

1.2 Photocatalysis

Since 1972, the number of publications about photocatalysis has increased dramatically. This trend not only aligns with the increase in the number of research projects about photocatalysis itself, but also to the multidisciplinary applications of this technology in a variety of fields such as semiconductors physics, surface science, photo-chemistry, material science and chemical engineering [Herrmann (2010)]. Photocatalysis is a process that uses light of the appropriate wavelength to activate a substance that modifies the rate of a chemical reaction without being involved itself. This substance is called photocatalyst: either II-VI compound semiconductors (CdS, ZnS) or semiconductor oxides (TiO₂, ZnO, ZrO₂, SnO₂) are used as photocatalysts. In a semiconductor, the combination of atomic orbitals gives rise to a series of molecular orbitals whose overlap results in the formation of the valence band, filled by the electrons, and the conduction band, empty and at higher energy. The energy difference between the two bands is known as a band gap and its width varies according to the type of semiconductor. Irradiation with light equal or higher than the energy gap of the semiconductor causes electron excitation from the valence band to the conduction band, generating electron-hole pairs (Figure 1.2). The pair generated can undergo various processes [Westwood (2011)]:

- Recombination, dissipating the initial energy in the form of heat (iib);

- Migration of holes from the valence band and electrons from the band conduction to the active sites on the surface (iia);
- Participation in redox chemical reactions occurring on the surface (iii): the holes are oxidizing agents, while the electrons reducing agents.

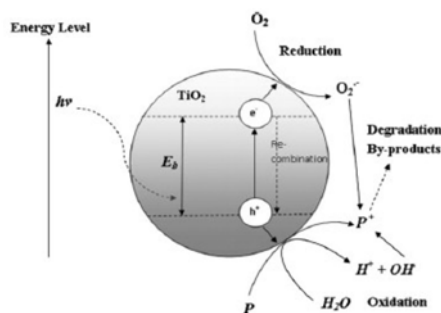


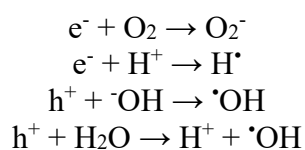
Figure 1. 2 Main processes in a photocatalytic semiconductor subsequent to the creation of an electron-hole pair induced by the incident radiation. Reported from [Chong (2010)].

Recombination time (about 10^{-9} s) is lower compared with time required to activate chemical reactions (10^{-8} - 10^{-3} s); as a consequence, only a small number of electrons (<1%) and holes do not recombine and this leads to a reduction in the efficiency of the process. The electrons-holes recombination can be avoided by different procedures that are described in Chapter 3. The reduction and oxidation reactions are the basic mechanisms of photocatalytic hydrogen production and photocatalytic water/air purification, respectively. Nano-sized semiconductors can enhance both surface adsorption as well as photocatalytic reactions, since a more reactive surface area is available. Both photocatalytic water/air purification and photocatalytic hydrogen production require essential photogeneration of hole/electron pairs. However, their utilization of holes/electrons as well as the system processing are different. In photocatalytic water/air purification, valence band (VB) holes are the key elements that induce decomposition of contaminants. On the other hand, when photocatalysis is applied to perform water splitting for production of hydrogen, the reducing CB electrons become important as their role is to reduce protons to hydrogen molecules.

1.2.1 Photocatalytic process for water purification

Photocatalytic studies have been focused on degradation of pollutants in air and water. Photocatalytic reactions occur at the interface of the solid (catalyst) and the media (water) in seven general steps [Herrmann (1999)]: (i) External mass transfer (diffusion) of reactants from the bulk fluid phase to the external surface of the solid photocatalyst, (ii) internal mass transfer (internal diffusion) of the

reactants from the external surface of the photocatalyst through the pores to the interior surface of the photocatalyst, (iii) adsorption of reactants, (iv) reaction in the absorbed phase, (v) desorption of products, (vi) internal counter-diffusion of the products through the pores to the external surface of the photocatalyst and (vii) external counter-diffusion of products from the external surface of the photocatalyst to the fluid media. The reaction in the absorbed phase (step iv) consists on a multiple sub-steps resulting in the formation of reactive hydroxyl radicals:



The oxidation of organic compounds can occur by reaction with photoholes or generated hydroxyl radicals. Without the presence of water molecules, the highly reactive hydroxyl radicals (OH•) could not be formed impeding the photodegradation of organic compounds.

The transfer process of charge carriers to any organic or inorganic species surrounding the semiconductor, is favoured if these species are adsorbed on the surface of the semiconductor itself. In addition, the probability of the process is highly dependent on respective positions of valence and conduction band of the semiconductor, and the levels of redox potential of the adsorbed species [Li (2016)]. The energy of the conduction band edge (E_c) corresponds to the potential of the photogenerated electrons, whereas the energy of the valence band (E_v) corresponds to the potential of the holes. For the degradation of organic compounds, the VB should be lower than the potential level of the donor species so it can transfer an electron to the VB. The CB level should be higher than the potential of the acceptor species so this can subtract the electron from the CB. For this reason, the knowledge of the relative edge positions of the bands and of the energetic levels of the redox couples is essential to establish if thermodynamics allows the occurrence of the reactions. The band positions for some important semiconductors (at pH = 7 in aqueous solution) and their potential applications are illustrated in Figure 1.3. Thus, the more negative conduction band positions of semiconductors are beneficial for reduction reactions, while the more positive valence band positions of semiconductors are favorable for oxidation reactions.

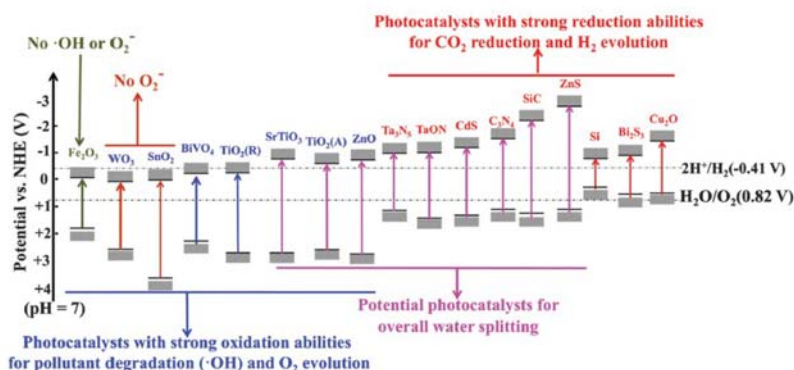


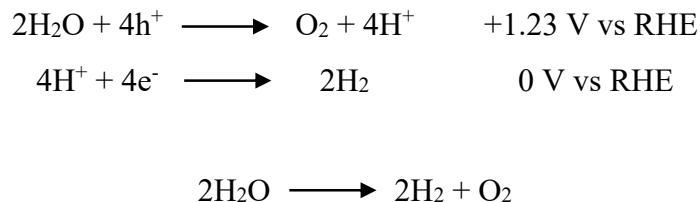
Figure 1.3 Band positions and potential applications of some typical photocatalysts at pH 7 in aqueous solutions [Li (2016)].

1.2.2 Photocatalytic process for hydrogen production

Storing solar energy in the form of transportable chemicals and fuels using an abundant raw material as water is a highly desirable scientific and economic goal [Schultz (2014)]. Photocatalytic water splitting has attracted significant interest in recent decades as it offers a clean and environmentally friendly route for the production of hydrogen. A key challenge remains the development of systems that employ abundant, non-toxic and inexpensive materials to dissociate water efficiently using sunlight. All of our energy needs may be satisfied by taking advantage of approximately 0.01% of the total solar energy irradiation [Takanabe (2014)]. Photovoltaic and electrochemical solar cells that convert solar energy into electricity can reach up to 55% ~ 77% efficiency but remain uneconomical because of high fabrication costs, insufficient light absorption and inefficient charge transfer. Photocatalysis, which directly converts solar energy into H₂-based chemical energy, may serve as an alternative way to utilize the solar spectrum. In addition, the water splitting reaction driven with nothing more than sunlight using a photoelectrochemical (PEC) cell or a photocatalyst does not involve the production of toxic gases. As just said, photon energy of at least 1.23 eV is required ($\lambda \cong 1000$ nm) to drive the water splitting reaction from a thermodynamic perspective. However, considering the overpotential required to overcome the activation energy of the redox reactions and other unavoidable efficiency losses in the system, the practical lower limit is often quoted to be closer to 2.5 V. Such energy is contained in the solar spectrum.

A semiconductor with a band gap larger than 1.23 eV can be, in principle, used for driving water-splitting reaction. The conduction band and valence band must straddle the formal potentials for the hydrogen evolution reaction (HER) and the oxygen evolution reaction (OER): the CB level must be more negative than the standard potential for HER and the VB must be more positive than the standard

potential for water oxidation. If these requirements are satisfied, holes and electrons generated upon light absorption can act as oxidizing species, leading to oxygen production, and as reducing species, leading to hydrogen evolution, respectively.



The total amount of hydrogen generated is mainly determined by the amount of excited electrons in the water/photocatalyst interface; any other processes that consume excited electrons should be avoided in order to maximize the efficiency of the hydrogen generation of the photocatalytic system. On the contrary, any process that generates excited electrons should be considered to act in a possible way to improve the efficiency. In this process, the choice of the semiconductor material is fundamental: considering all the steps involved in the photocatalytic process described in previous chapter, this is based on light absorption and charges generation, their separation and transfer to active sites where redox reactions occur.

The semiconductor photocatalyst should have a low band gap to absorb as much light as possible, and reflection or scattering of light by the photocatalyst should be minimized. Typically, the solar energy spectrum is defined to have a total energy of 1000 W m^{-2} accumulated to 4000 nm wavelengths. The UV-region accounts for 4% of the total sunlight with an integrated irradiance of almost 90 W m^{-2} . Visible light constitutes more than 50% of the solar spectrum with an integrated irradiance of about 524 W m^{-2} ($\lambda \leq 700 \text{ nm}$). Therefore, we can deduce that the use of materials capable of absorbing visible light respect to UV light is more convenient since visible photons are the most abundant in the solar spectrum. In addition, solar photons satisfy the required energy of at least 1.23 eV. Furthermore, the use of solar radiation for photocatalytic hydrogen production makes this process suitable on industrial scale.

Metal oxide semiconductor photoelectrodes have attracted interest since the first paper of Fujishima [Fujishima (1972)] on the use of TiO_2 for photoelectrochemical water oxidation. More than 130 inorganic materials have been demonstrated to exhibit photocatalytic performance for water-splitting [Osterloh (2008)]; with particular interest in large band gap semiconductors such as TiO_2 , $\alpha\text{-Fe}_2\text{O}_3$ and WO_3 because of their band energies which are suitable for the evolution of O_2 and their stability under conditions in which photoelectrochemical water oxidation occurs. However, under solar illumination, the efficiency of current photocatalytic devices is still well below the commercially

viable level. Therefore, in the last 40 years the synthesis of new materials and the surface modifications of existing semiconductors have been widely investigated with the aim of increasing their efficiency in particular under solar light [Chen (2010)]. A deeper understanding of the mechanisms involved in photo assisted water splitting would allow researchers to accurately engineer new and more efficient materials.

The other reason for the low efficiency of photocatalytic water splitting process is that the water-splitting reaction has very slow kinetics, as it is a process involving four electrons/holes as shown in the above reported reactions. The time from the generation of the electron-hole pairs to the activation of the HER and OER is significantly longer than the typical electron-hole lifetime in semiconductors [Tang (2008)]. Efficient charge separation and fast charge transport, avoiding any bulk/surface charge recombination, are fundamentally important for photocatalytic hydrogen generation through water splitting. Another important factor that affect the amount of produced hydrogen, is the back reaction of H_2 and O_2 to form H_2O . This reaction is normally called “surface backreaction (SBR)” and if it occurs, the amount of produced hydrogen is reduced. There are two main approaches to suppress SBR: one involves the addition of sacrificial reagents into the photocatalytic reaction environment and the second creates a separation of the photoactive sites on the surface of the photocatalysts [Chen (2010)].

There are mainly two types of water-splitting photocatalytic devices: the photoelectrochemical (PEC) cell and the so-called powdered device. In a cell device, the photocatalyst is one of the two electrodes, for example a photo-anode, while a metal (i.e. platinum) forms the other electrode. The generated electrons and holes can travel to the cathode and anode, and activate the HER and OER respectively. In addition, a bias voltage can be applied to this device between the cathode and the anode. This bias voltage can shift the band edge positions of the photocatalyst relative to the water redox levels in the solution; so materials with a band gap larger than 1.23 eV but unfavorable CB or VB positions may still be used. Anyway, a large bias voltage should be avoided to reduce the energy consumption; for this reason, photocatalysts are still required to have its CB and VB position close enough to redox potentials for water splitting.

In a powdered device, the photocatalyst in the powdered form is directly put into the solution. By light irradiation, the generated electrons-holes can travel to different places at the photocatalyst-solution interface, where they activate the HER and OER respectively. The powdered device has a good potential in practice, since it is simpler than the PEC cell device, and it is easy to be scaled up. The disadvantage of this device is that no bias voltage can be applied on it, indicating that the requirement of the band edge position should be strictly satisfied. In addition, unlike the PEC cell,

the powdered device generates H₂ and O₂ at the same particles, so it requires a gas separation step that is non-trivial.

1.2.3 Parameters affecting the photocatalytic process

An ideal photocatalyst should be characterized by high photo-stability, chemical and biological inertness, good availability and low cost, high capability to adsorb reactants under efficient photonic activation ($h\nu \geq EG$) [Gaya (2008)].

The efficiency of photocatalytic reactions, including water splitting for H₂ production and the decomposition of contaminants for environmental purification, strongly depends on three factors: efficient optical absorption by the photocatalyst, efficient creation of charge carriers, and efficient use of the charge carriers in the photocatalytic processes. Let us consider now the main operational parameters affecting the photocatalytic process [Gaya (2008)].

- *Light intensity*

The photocatalytic reaction rate (r_i) is directly dependent on the light intensity (I), as is expressed by

$$r_i = k_i C_i I^n$$

where k_i is a rate constant, C_i is the concentration of the substrate or pollutant and n is the kinetic order given by the light intensity. At light intensity lower than 25 mW/cm², the production of electron-hole pairs is limited and they are totally consumed during the photocatalytic reaction, therefore, the reaction is considered a first order with a value of n equal to 1. Light intensity higher than 25 mW/cm², on the other hand, generates excess of electron-hole pairs with a high rate of recombination, and as a result, the reaction is a half order, and the value of the kinetic order in this case is 0.5 ($n=0.5$).

The first parameter affecting the photocatalytic process is the radiation absorption efficiency of the photocatalyst. The overall quanta of light absorbed by any photocatalyst is given by Φ_{overall} , the quantum yield:

$$\Phi_{\text{overall}} = \text{rate of reaction} / \text{rate of absorption of radiation}$$

Some studies revealed an increase in the degradation rate with increasing the light intensity, but it is important to consider all the phenomena involved in the interaction of light with a material, i.e. reflection, transmission and energy loss as heat and, in particular in solid-liquid regime, the light scattering is also significant. Another factor limiting photonic efficiency is the thermal recombination between electrons and holes. A practical and simple alternative for comparing process efficiencies consists in defining a relative photonic efficiency ζ , defined as the number of reactant molecules transformed divided by the number of incident photons:

$$\zeta = N_{\text{mol transformed}} / N_{\text{ph incident}}$$

- *Nature and concentration of the organic pollutant*

The degradation of organic compounds occurs by electrons and/or holes transfer to them; therefore, their adsorption on the photocatalyst surface plays a key role in their photocatalytic degradation. The chemical and physical surface properties of the contaminants (i.e. substituent groups, surface charge etc.) and all parameters influencing these properties (i.e. pH) affect their adsorption and their degradation. In the present thesis work, we have investigated the role of direct interaction of the contaminant with the photocatalyst by comparing the degradation ability of polymeric nanocomposites against two dyes differing for superficial charge. This effect is also investigated by changing the pH of the solution.

- *Nature and concentration of the photocatalyst*

A very important parameter influencing the performance of photocatalyst is its surface morphology, the particle size and agglomerate size. For instance, smaller nano-particle size is reported to give higher photocatalytic efficiency. There is an optimum value of photocatalyst concentration to obtain the maximum photodegradation efficiency. Generally, decomposition increases with catalyst loading due to a higher surface area of the catalyst that is available for adsorption and degradation. However, above a certain concentration, the solution opacity increases (due to increased light scattering of the catalyst particles) causing a reduction of light penetration in the solution and a consequent rate decrease. For photocatalyst immobilized systems, there is also an optimal thickness of the catalyst film: the interfacial area is proportional to the thickness of catalyst; on the other hand, the internal mass transfer resistance for both organic species and photogenerated carriers will increase with

increasing thickness. This increases the recombination possibility of the electron-hole pair and, as a consequence, the degradation performance is reduced [Carp 2004].

- *pH*

Considering the above mentioned parameters, the pH of the solution dictates the surface charge properties of the photocatalyst, its stability and size of aggregates it forms, and the chemical and physical surface properties of the contaminant. This aspect has been investigated during the research activity carried out for this thesis and the results are reported in Chapter 4. It is important to underline that during photocatalytic reactions, the pH can vary due to the production of by-products and, therefore, the adsorption of the pollutants and the surface properties of the photocatalyst can change through the reaction.

- *Temperature*

Generally, the increase of temperature enhances the recombination of charge carriers and desorption process of adsorbed reactant species, resulting in a decrease of photocatalytic activity. This is in conformity with Arrhenius equation, for which the apparent first order rate constant K_{app} should increase linearly with $\exp(-1/T)$.

- *Presence of electrons or holes acceptors*

One practical problem in using semiconductors as photocatalysts is the energy lost in the electron hole recombination that results in low degradation efficiency. One approach used to prevent electron-hole recombination is to add electron acceptors into the reaction media; molecular oxygen has been employed as an effective electron acceptor in most photocatalysis applications. Another example is H_2O_2 : this avoids recombination of electrons-holes by accepting the conduction band electrons and increases the concentrations of the hydroxyl radical [Bertelli (2006)]. Sacrificial agents, as methanol or ethanol, boost hydrogen yields by acting as reducing agents, holes scavengers and extracting the oxygen from water preventing the backwards reaction, as reported in [Melian (2013)].

1.3 Nanotechnology for water purification and hydrogen production

Nanomaterials are typically defined as materials smaller than 100 nm in at least one dimension. At this scale, materials often possess novel size-dependent properties different from their

large counterparts. Some applications in water and wastewater treatment utilize the smoothly scalable size-dependent properties of nanomaterials that relate to the high specific surface area, such as fast dissolution, high reactivity, and strong sorption. Others take advantage of their discontinuous properties, such as super paramagnetism, localized surface plasmon resonance, and quantum confinement effect. Furthermore, nanotechnology provides unprecedented opportunities to advance the development of clean and renewable energy technologies [Fromer (2013)].

These novel functional materials can be processed into various form factors including water-soluble supramolecular hosts, particles, fibers and membranes. Chapter 2 and 3 report some examples of nanomaterials that are currently being utilized as building blocks to develop the next generation of sustainable products and technologies in water purification, energy generation, conversion and storage.

The main advantage of nanomaterials for photocatalytic application is the high surface-to-volume ratio that increases dramatically as the size of a material decreases. This property facilitates reaction/interaction between the photocatalyst and the molecules adsorbed on the photocatalyst surface. Furthermore, reducing particles size the diffusion length from the point in which the photocarriers are generated to the surface where redox reactions occur is reduced resulting in a decreasing of recombination. Surface-structuring on the micro- or nanoscale can increase the degree of light distribution in the materials via light scattering or reflection, in this way multiple interactions of light with the nanostructured materials increase the light optical path and the probability of photocatalytic processes.

1.3.1 Nanomaterials for water purification

The efficiency of conventional adsorbents is usually limited by the surface area or the availability of active sites, the lack of selectivity, and the adsorption kinetics. The extremely high specific surface area and associated sorption sites, the short intra particle diffusion distance, the tunable pore size and surface chemistry of nanomaterials make them high capacity and selective adsorbents for water pollutants [Qu (2013)]. Overall, carbon and metal oxides nanomaterials can be a good alternative for activated carbon as wide-spectrum adsorbents. As their surface chemistry can be tuned to target specific contaminants, carbon nanomaterials have unique applications in polishing steps to remove recalcitrant compounds or in pre-concentration of trace organic contaminants for analytical purposes. Metal oxides nanoparticles have been explored to remove a variety of heavy metals such as arsenic,

lead, mercury, copper, cadmium, chromium, nickel. In addition, adsorption of water pollutants as ions on these nanomaterials can be easily reversed by changing the solution pH. This aspect is really important considering that regeneration is an important factor that determines the cost-effectiveness of adsorbents. Metallic and metal-oxide nanoparticles, such as Ag and TiO₂, and carbon nanomaterials are among the most promising nanomaterials with antimicrobial properties [Buccheri (2016)]. Furthermore, the increased photocatalytic activity shown by nano-sized metal-oxide in combination or not with carbon nanomaterials has been investigated for water purification. A deeply description of carbon nanomaterials and inorganic nanomaterials for water purification by adsorption or photocatalysis is reported in Chapters 2, 3.

1.3.2 Polymeric nanocomposites for water purification

In recent years, polymeric nanocomposites (PNCs) have attracted the attention of scientists and technologists in water purification due to improved processability, surface area, stability, tunable properties, and decontamination ability with high selectivity and cost effectiveness. Nanocomposite membranes are considered a new effective approach for water purification, combining the advantages of membrane technology, nanoparticles and photocatalysis.

Nanocomposites are multi-phasic materials, in which at least one of the phases shows dimensions in the nano range (10–100 nm). Nowadays nanocomposite materials have emerged as suitable alternatives to overcome limitations of different engineering materials. They can be classified according to their dispersed matrix and dispersed phase materials (Figure 1.4).

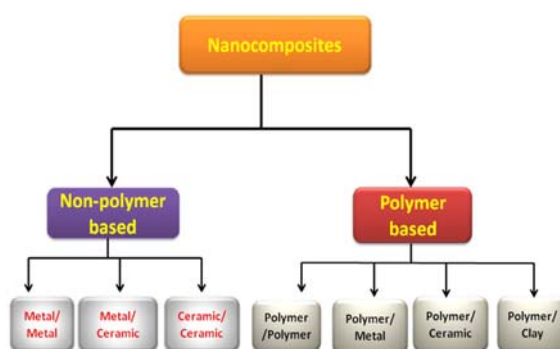


Figure 1. 4 Classification of nanocomposites.

PNCs have a lot of advantageous properties such as film forming ability, dimensional variability, and activated functionalities [Lofrano (2016)]. The choice of the polymers is usually guided mainly by their mechanical, thermal, electrical, optical and magnetic properties. However, other ones such as hydrophobic/hydrophilic balance, chemical stability, biocompatibility, opto-electronic and chemical functionalities have to be considered in the choice of the polymers. The nanofillers not only provide mechanical and thermal stability, but also new functionalities that depend on their chemical nature, structure, size, and crystallinity. Furthermore, the properties of nanocomposites depend on the interaction between the polymeric matrix and the nanofillers. It is possible to classify PNCs in two classes (Figure 1.5): Class I hybrid materials are those that show weak interactions between the two phases, such as van der Waals, hydrogen bonding or weak electrostatic interactions; Class II hybrid materials are those that show strong chemical interactions between the components [Kickelbick (2007)]. Another important property of these materials is their processing. Contrary to pure solid-state inorganic materials that often require a high temperature treatment for their processing, hybrid materials show a more polymer-like handling. Hence, these materials can be shaped in any form in bulk and in films by very low-cost methods.

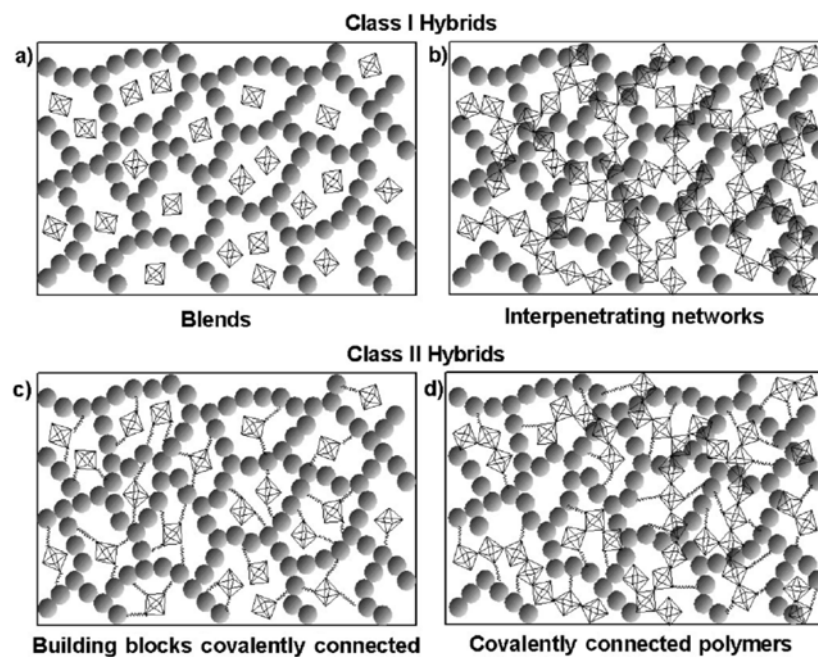


Figure 1. 5 The different types of polymer-matrix nanocomposites [Kickelbick (2007)].

The dispersion of inorganic materials inside a polymeric matrix will enhance its performance for filtration. [Rahimpour (2008)] reported that the dispersion of titanium dioxide inside PES membranes followed by UV irradiation is a way to increase the flux and enhanced fouling resistance when compared the system without UV radiation. This is ascribed to the photocatalytic property of the

inorganic semiconductor. Furthermore, the addition of titanium dioxide inside PVDF increased its permeability and antibacterial activity [Damodar (2009)]. Titania poly(ethersulfone) composite membranes showed higher fluxes and enhanced antifouling properties [Yang (2007)].

PNCs have extensively been used for adsorptive removal of various toxic metal ions, dyes, and microorganism from water/wastewater; these were prepared by adding inorganic nanoparticles onto different polymers as alginate, cellulose, porous resins, and ion-exchangers [Pandey (2017)]. The adsorption of a molecule depends on ionic or surface interaction, which needs selective interaction site. These sites can be available on the polymeric matrix. Another important strategy to optimize adsorption behaviour is to opportunely tune the hydrophobic and hydrophilic behaviour in composite matrix [Yeo (2012)]. For example, well defined sulfonated block copolymers composed of hydrophilic sulfonated polystyrene and cross-linkable hydrophobic hydrogenated isoprene chains allow to optimize charge densities of the membrane, water molecule transport rate, and mechanical integrity under water purification conditions. These polymers showed a high efficiency in removing multivalent cations and monovalent ions, a higher water permeability and mechanical stability. A description of this new class of polymers within their application in water purification by photocatalysis is reported in Chapter 4.

The tunable surface and catalytic properties of PNCs also find huge potential to remove dyes. Many polymer nanocomposites have been used as dye adsorbents and this are reviewed in [Pandey (2017)]. Some polymeric resins suitable as adsorbents through ion exchange mechanism are sulfonated polystyrene, sulfonated phenolic resin, phenolic resin, polystyrene phosphonate, polystyrene amidoxime, polystyrene-based trimethyl benzyl ammonium, epoxy-polyamine, and aminopolystyrene. Membranes loaded with photocatalytic nanoparticles have also been use for photocatalytic degradation of water contaminants [Petronella (2017)]. The use of titania in polymeric nanocomposites for dyes degradation has been investigated within this research activity and the results are shown in Chapter 4. Nanocomposites are potential materials to replace current chemical disinfectants [Zhang (2016)]. Polymeric nanocomposites with metallic or metal oxides nanoparticles or with carbon nanomaterials have been used efficiently for removing wide spectrum of bacterial strains up to 99.9%.

In addition to the above mentioned advantages, the dispersion of photocatalytic materials inside a polymeric matrix also allows to overcome all the problems of using powders in solutions (i.e. effects on human health and ecosystems due to their release, stability, dissolution, and retention time) leaving unaltered the catalytic activity of the nanomaterial. In some case, the polymeric matrix is also able to enhance the degradation activity of the nanomaterial itself [Filice (2015)]. Another important aspect about the use of PNCs in water purification is biodegradation. In this regard, a wide spectrum

biopolymer-based nanocomposite are explored for dye removal: chitosan, alginate, starch based-nanocomposites have been widely used for the removal of different dyes [Pandey (2017)].

1.3.3 Nanomaterials for hydrogen production

The discovery of water photoelectrolysis at illuminated TiO₂ electrodes in 1972 by Fujishima and Honda [Fujishima (1972)] established the use of photoelectrochemical cells for ‘artificial photosynthesis’. Later, Arthur Nozik formulated the concept of ‘photochemical diodes’ [Nozik (1978)]: basic functions of a photoelectrosynthetic cell (light absorption, charge separation, water electrolysis) could be copied in suspended micro- or nanoscale particles that would split water under illumination. The proposed basic device configurations consist of a Schottky type device, in which a photoanode material is fused to a cathode material, and the other configuration is a Tandem or Z-scheme device, with a photoanode coupled to a photocathode material.

The underlying physical principles of these devices are not covered here, but have been subject of several reviews [Osterloh (2008)]. Even though these catalysts worked reasonably well in the presence of a chemical bias (using sacrificial electron donors and acceptors), overall water splitting with them was not achieved. The most prominent examples of nanostructured photoelectrodes are based on nanostructured Fe₂O₃, which in combination with a nanoscale IrO₂ co-catalyst, supports photocurrents of up to 3.0 mA cm⁻². Performance enhancements have also been observed with the use of nanostructured WO₃, MnO₂, BiVO₄, and carbon nitride, and with many co-catalyst materials, including MoS₂ and with several noble metals. The improved efficiency is due to an increase in surface area and to a shortening of charge transport pathways between the material interior and the surface [Osterloh (2008)].

There are two main approaches for achieving water splitting using visible light (Figure 1.6). One approach is a two-step system, the Z-scheme. In this system, the water splitting reaction is broken up into two stages: one for H₂ evolution and the other for O₂ evolution; these are combined by using a shuttle redox couple (Red/Ox) in the solution. Over a H₂ photocatalyst, the photoexcited electrons reduce water to H₂ and holes in the valence band oxidize the reductant. The as generated oxidant is reduced back to the reductant by photoexcited electrons generated over an O₂ photocatalyst, where the holes oxidize water to O₂. This system lowers the energy required for photocatalysis, allowing visible light to be used more efficiently than in conventional water-splitting systems. For example, visible-light responsive oxides such as WO₃ can be used as O₂ photocatalysts if they can reduce the oxidant to a reductant. Similarly, non-oxide photocatalysts (e.g., sulfides, oxynitrides, and dyes) can

be used as H₂ photocatalysts if they can oxidize the reductant to an oxidant. Consequently, various semiconductor materials can be used in the Z-scheme even if they do not satisfy all the stringent requirements for a one-step system. Another advantage of Z-scheme systems is the ability to separate production of H₂ and O₂ by employing a separator, such as a porous glass filter. Meanwhile, the Z-scheme systems have a significant disadvantage: it requires a number of photons two-fold larger than the one-step system to achieve water splitting.

The other approach for achieving water splitting using visible light is to split water into H₂ and O₂ using a single visible-light responsive photocatalyst (a one-step system), as illustrated in Figure 1.6 b. Band engineering of semiconductors is required to artificially develop new photocatalytic materials that can be used under visible light irradiation.

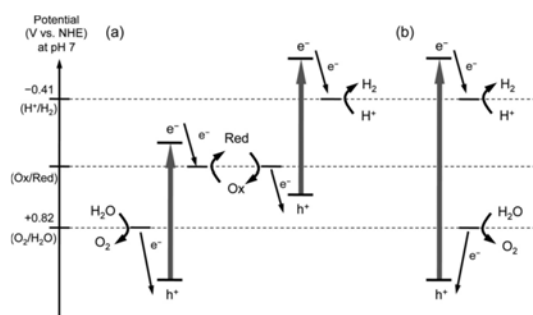


Figure 1. 6 Schematic energy diagrams of photocatalytic water splitting systems: (a) two-step photoexcitation system and (b) conventional one-step system. Reported from [Osterloh (2008)].

Chapter 2

LASER IRRADIATION OF GRAPHENE OXIDE SOLUTIONS FOR WATER PURIFICATION APPLICATIONS

Graphene oxide (GO) has become one of the most extensively studied materials of the last decade, in the fields of chemistry, physics and materials science. GO is not only a precursor for graphene, but it is a unique and valuable material, both from fundamental science perspectives and for practical applications. On the contrary of graphene, GO can be easily produced on large scale using water or organic solvents. In addition, it can be easily modified introducing different functional groups that alter its properties. All these qualities make it very attractive for photocatalytic applications ranging from air and water purification to hydrogen production by water splitting. In this Chapter, the results concerning the investigation of GO antibacterial properties and its use for dye removal are reported. Furthermore, laser irradiation of GO samples is investigated for further enhancing these properties.

2.1 Graphene oxide (GO)

GO is a two-dimensional (2D) material that is derived from the parent graphene backbone by introducing several oxygen functionalities. While GO is only one carbon layer thick, the lateral size of the flakes can vary from hundreds of nanometers through the tens and even hundreds of micrometers. The oxygen atoms are covalently bonded to carbon atoms, converting them from the sp^2 hybridized state into the sp^3 hybridized state. These oxygen functionalities can be considered as defects introduced into the graphene plane [Dreyer (2010)] that affect its properties; for example, GO is an insulator respect to graphene that is electrically conductive. However, on the other hand, the oxygen functionalities provide GO some advantages respect to graphene, for example GO is characterized by a high hydrophilicity, oxygen moieties confer to the material a tunable bandgap that is responsible for unique optical and electronic properties, and these groups can be easily functionalized to create a selective material. All these parameters are fundamental for its application in water purification or water splitting.

GO is prepared by chemical oxidation of graphite [Dreyer (2010)] that occurs mainly by two steps (Figure 2.1): firstly, graphite powder is oxidized to produce graphite oxide introducing hydroxyl and epoxide groups across the basal planes of graphite oxide and carbonyl and carboxyl groups located at the edges. Secondly, the bulk graphite oxide can be exfoliated by sonication to form colloidal suspensions of monolayer, bilayer or few-layer GO sheets in different solvents. The critical point of

preparing GO is the selection of suitable oxidizing agents to oxidize graphite; three main procedures are known for GO preparation i.e. Brodie, Staudenmaier and Hoffman methods [Dreyer (2010)].

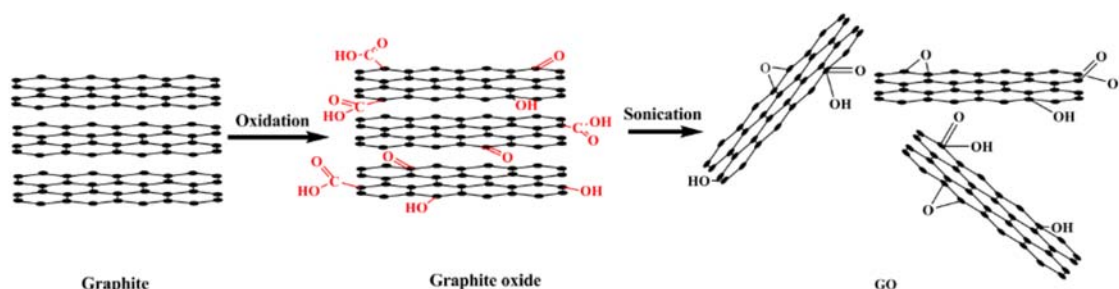


Figure 2. 1 Fundamental steps in GO preparation from [Dreyer (2010)]

Brodie was the first to synthesize GO in 1859 [Brodie (1859)]: graphite is treated with potassium chlorate and fuming nitric acid at 60 °C. About 40 years later, Staudenmaier [Staudenmaier (1898)] modified the Brodie method by using concentrated H₂SO₄ and fuming HNO₃ as the oxidizing agents for graphite. KClO₃ is slowly added to the mixture kept in an ice bath. Hummers and Offeman [Hummers (1958)] for the first time successfully applied permanganate as an oxidant for the formation of GO within sodium nitrate in concentrated sulfuric acid.

The Brodie GO samples are the purest and the most stable ones; especially, the Hummers–Offeman samples are contaminated with a considerable amount of sulfur. Compared to the Brodie–Staudenmaier methods, the Hummers method requires less than 2 h for completion at temperatures below 45° and can be carried out safely. However, all three reactions involve the liberation of toxic gas NO_x and/or ClO₂. The chemical composition of the various samples shows a great variation, but there is a trend in the degree of oxidations: the C/O ratio decreases in the order Brodie > Staudenmaier > Hummers–Offeman. Regarding the production cost, the oxidation process itself is not the most critical step in GO production. The bottleneck is the purification steps that follow the oxidation.

According to the LK model reported in Figure 2.2 [Lerf (1998)], GO planes consist of two different types of randomly distributed domains: (i) areas of pure graphene with sp²-hybridized carbon atoms, which have survived the oxidation, and (ii) areas of oxidized and thus sp³-hybridized carbon atoms. The oxidized GO domains contain epoxy and hydroxyl (tertiary alcohol) functional groups. The edges of the flakes are terminated by carboxyl and hydroxyl groups. In addition to intact graphene domains and oxidized domains, nanometer-sized holes were observed in GO flakes.

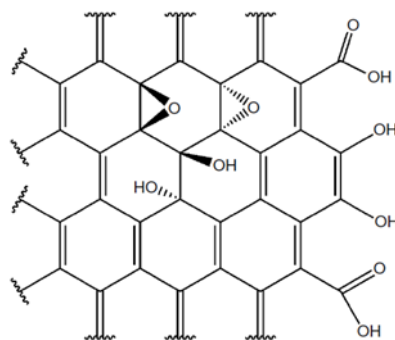


Figure 2. 2 Simplified version of the Lerf–Klinowski GO structural model, from [Lerf (1998)].

Considering the study on GO acidity, a new structural model of GO, the “dynamic structural model” (DSM), was proposed [Dimiev (2012)]. In aqueous solutions GO constantly interacts with water; as a consequence, tertiary alcohols slowly transform into enols and ketones by generating hydronium ions (Figure 2.3).

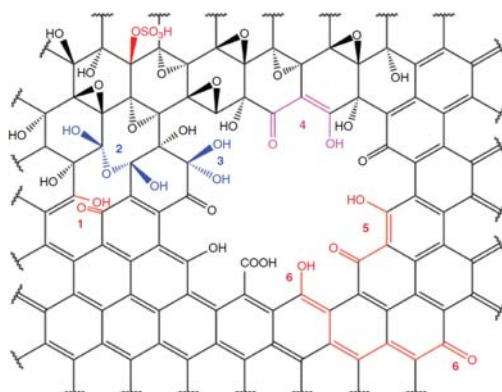


Figure 2. 3 The “dynamic structural model”. From [Dimiev (2012)].

The GO fragment contains a hole situated on the border between the graphitic domain and the oxidized domain. The main functional groups on the basal planes are epoxides and tertiary alcohols, in accordance with the LK model. However, the basal planes also contain numerous points of C–C bond cleavage with ketones and enols at the newly formed edges. In aqueous solutions, ketones can be converted into *gem*-diols (hydrates). *gem*-diol can also be converted to a hemiacetal. This structural model explains many of the known GO properties, including its acidity. The fine chemical structure of GO in aqueous solutions is different from that in the dry solid state, in particular enols are not formed. Drying GO solution, it is possible that enols convert into ketones. demonstrating the mobility of oxygen functional groups on GO planes, and their ability to transform into each other.

One of the main properties of graphene oxide is its acidity that makes this material suitable for application as adsorbent in water purification. As a consequence, GO demonstrates extremely high

cation exchange capacity (CEC), a property that can be ascribed to oxygen groups, both on the basal plane and at the edges. Depending on the concentration, the pH of GO solutions varies from 2.0 through 4.0 [Dreyer (2010)]. This acidity can be ascribed to carboxylic groups, phenols and enolic groups on the basal plane that is increased by conjugation with ketones and the other double bonds in the graphitic domains. In addition, these groups are reactive and can be easily transformed in many other groups to confer high selectivity and specific properties to GO itself.

2.1.1 GO functionalization and reduction

GO can undergo noncovalent or polar interactions (i.e. hydrogen bonding). Since approximately 50% of the C atoms of GO are sp^2 carbon, a non-covalent interaction with π conjugated molecules should be possible. Also polar interactions can be exploited to molecules adsorbed on GO. The covalent chemistry of GO is acted by oxygen functional groups that are located on the basal planes and at edges of the flakes or of defect sites, respectively. Nucleophiles react with carboxylic acids in acid–base reactions or with carbonyl groups located at edge groups. Carboxyl groups can be activated and subsequently converted to esters or amides. Ester or ether formation with hydroxyl groups will proceed at tertiary hydroxyl groups and the more phenol-like hydroxyl groups located at edges, where the reaction is sterically possible. In addition to small molecules, polymers have also been attached to the surface of graphene oxide. These attachments are typically made by either grafting-onto or grafting-from approaches. The epoxy groups can be easily modified through ring-opening reactions under various conditions. A likely mechanism for this reaction involves nucleophilic attack at the α -carbon by the amine [Dreyer (2010)].

GO is actually the best precursor for the preparation of graphene layers due to its low cost, high processability and the similarities between reduced graphene oxide (RGO) and pristine graphene in terms of their electrical, thermal, and mechanical properties, as well as surface morphology. However, with typical GO, the original graphene network is never fully restored. This is because GO itself is already highly defective. Two different types of species remain on the RGO planes after reduction: (i) holes and (ii) some oxygen functionalities i.e. carbonyls. GO reduction can be achieved through chemical, thermal, or electrochemical reduction pathways. The quality and the amount of oxygen that can be removed of RGOs depends on the reduction methodology.

The most popular chemical reductant for GO is hydrazine. Anyway, hydrazine does not completely reduce GO and nitrogen is introduced. This affects the electronic structure of the resulting graphene,

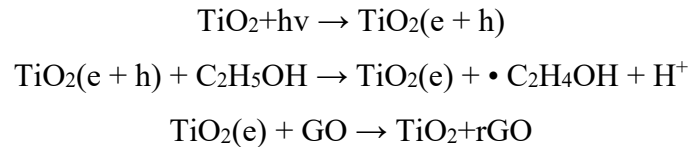
functioning as n-type dopants. The mechanism of reduction by other reducing agents is even less studied. It is thought, in general, that sodium borohydride (NaBH_4) is a more effective reducing agent than hydrazine. The use of borohydride has the additional advantage of introducing few, if any, heteroatoms to the graphene structure following reduction [Dreyer (2010)].

Electrochemical reduction is very attractive for its efficiency and “green” approach; but it might occur only on the surface of the negatively charged electrode, but not in the bulk solution. To reduce GO in bulk solution, one needs to find a proper system with a mediator that will transfer electrons from the electrode to GO by traveling through the solution [Dreyer (2010)].

Oxygen groups on GO sheets can be removed by thermal annealing within the restoration of sp^2 domains and the formation of carbon dioxide and carbon monoxide. The last effect results in the formation of small graphene like sheets and/or structural damages to graphene sheets. These defects inevitably affect the electronic properties of the product [Pei (2012)]. An alternative way is to exfoliate GO in the liquid phase before the thermal process. The main parameters to be controlled for thermal reduction of GO are the heating temperature and the reducing atmosphere. The main decomposition of GO occurs in the 160–300 °C temperature interval, where epoxides and alcohols are almost completely eliminated. At temperatures above 500 °C, carbonyls are removed. Finally, the carbon grid is restructured at temperatures above 700 °C. Since the etching of oxygen will be dramatically increased at high temperatures, oxygen gas should be excluded during annealing. As a result, annealing reduction is usually carried out in vacuum, or an inert or reducing atmosphere [Pei (2012)]. In particular, because of the high reducing ability of hydrogen, the reduction of GO can be realized at a relatively low temperature in H_2 . The exposure of rGO to carbon source such as ethylene at a high temperature (800 °C) is a way to heal the holes [Pei (2012)]. Despite structural defects introduced during thermal process, bulk conductivities of 1000–2300 S m^{-1} were measured [Dreyer (2010)]. The main disadvantages that makes the thermal reduction not the best process for large scale production of graphene are (i) large energy consumption and critical treatment conditions; (ii) the heating should be slow to avoid the expansion of GO structure generating holes and defects. This means that high time and high process costs are required; (iii) finally, due to high temperatures, this reduction method cannot be used for GO films on substrates with a low melting-point, such as glass and polymers, limiting its applicability.

The same principle applies to the base of GO “reduction” by light. In the same way as heat, light triggers the disproportionation reaction, leading to the same products. The role of heat, light, radiation, etc. in this transformation is to provide the energy to overcome the activation barrier [Pei

(2012)]. Another method is the irradiation, generally with UV light, of GO in the presence of a photocatalyst. The photocatalysts reduce GO nanosheet by the photogenerated electron in the conduction band during the irradiation. A mixture of GO and colloidal TiO₂ in ethanol was subjected to UV irradiation: upon UV irradiation of TiO₂ colloids in the presence of ethanol, the holes are scavenged to produce ethoxy radicals and electrons accumulate within the TiO₂ particles and interact with the GO sheets to reduce them (see following equations).



Intense light irradiation methods will also have the same disadvantage as the heat-treatment method, since it is based on the photothermal effect, that is, the heat-treatment effect in principle. Thus, the development of a simpler reduction process that employs mild conditions is desirable for extending the applications of GO. In this regard, laser irradiation is proposed to reduce or modify GO as shown in the following paragraphs.

The first effect of GO reduction usually results in a black precipitation from the original yellow–brown suspension, which is probably a result of an increase in the hydrophobicity of the material caused by a decrease in polar functionality on the surface of the sheets [Pei (2012)]. The related change can be also observed by optical microscopy of GO/rGO sheets lying on SiO₂/Si wafer. The GO sheets are almost transparent with low optical contrast with the substrate. After reduction, the rGO sheets show much improved contrast with the substrate, which is the same as that of pristine graphene sheets lying on the same substrate [Pei (2012)]. The effectiveness of reducing agents can be assessed based on the two main parameters: C/O ratio of obtained RGO, and its electrical conductivity [Pei (2012)]. For what concerning conductivity, it depends not only on the amount of oxygen functional groups on the RGO layers but also on the amount of sp² domains restored. In fact, chemical reduction alone never yields highly conductive graphene-like materials due to the presence of remaining oxygen functionalities and defects. To improve conductivity, the as-obtained RGO needs to be annealed at around 900–1000 °C to restore sp² domains. Most importantly, the conductivity of RGO depends not only on the effectiveness of the reduction method, but also on the quality (density of defects) of the GO precursor.

2.1.2 Modification of GO by laser irradiation

Laser irradiation is a modern nontoxic tool for local and/or large-area GO modification [Trusovas (2016)]. Laser irradiation of GO transfers energy to the material as local heating and electron excitation, that can be responsible of the break of existent bonds or of the formation of new bonds. In other words, laser irradiation can be used for GO reduction: high energy photons are capable of cleaving C-O bonds and, in some cases, of restoring C-C bonds. With respect to classical reduction methodologies, laser irradiation is a greener and cheaper technique since it allows to avoid the use of chemical reducing agents, high temperatures and high pressure; the extent of reduction is quite high compared to other approaches; it is a tunable and scalable process according to the laser parameters.

[Zhang (2010)] proposed the use of femtosecond laser irradiation for GO reduction for GO films with a conductivity of 256 S/cm, and the rGO film patterns can be drawn directly by a pre-programmed laser on the GO film to form more complicated and delicate circuits. [Sokolov (2013)] reported the reduction of freestanding GO sheet with thickness 5–8 μm using excimer laser irradiation in oxygen-free environments. The best sheet resistance was 100 Ω/sq and C/O ratio was 40.

Different lasers have been applied for GO reduction as UV lasers, femtosecond, picosecond, CO_2 lasers, etc. Anyway, it was shown that photon energy exceeding 3.2 eV (387 nm) is required for GO photoreduction; for laser wavelength larger than 390 nm, GO reduction occurs mainly due to the increasing of temperature within irradiation [Trusovas (2016)]. During GO ablation with nanosecond (532 nm and 355 nm) and CW (532 nm) lasers, it was observed the production of electron–hole plasmas within material removal (as CO , CO_2 and H_2O) and heating. This plasma plume can nucleate the formation and growth of new graphene sheets. In the case of femtosecond lasers, the reduction occurs due to electronic excitation and consecutive recombination within heat release [Trusovas (2016)]. In each case, the GO reduction degree can be controlled by varying the laser power or the laser fluence, since they determine the local temperature. Other critical factors are the ambient conditions (vacuum, gases or liquids) and, in the case of reduction of GO flakes, the supporting substrate. This can influence the heating or can dope rGO by releasing some atoms from its surface. The effect of the substrate can be avoided by performing the laser process on GO suspension. Laser reduction of a GO suspension in ammonia was compared with chemical reduction by hydrazine [Ghadim (2014)]. Upon laser irradiation for 10 min, the obtained reduced GO was similar to the one obtained by chemical reduction. Chemically prepared GO colloid in water was reduced by using the second harmonic (532 nm) radiation of a pulsed laser Nd:YAG system [Spanò (2014)]. It was shown

that this method is able to finely tune the degree of reduction and tailor both the hydrophilicity and the spectroscopic features of the final rGO suspension. Such a method is greener than other approaches, it is tunable and involves the graphene oxide sheets directly in solution.

Besides chemical reaction, also irradiation of GO in the presence of other chemicals is a way to functionalise it. As an example, an ultrashort pulsed laser with two different wavelengths of 532 nm and 800 nm was employed for favouring the interaction between GO and metal porphyrins of Cu, Sn, and Zn. The as formed GO–metal-porphyrin composites had different absorption behaviour as compared to those of pure porphyrins or pure GO [Trusovas (2016)]. The electronic properties of GO were changed by the pulsed laser ablation of bulk graphite in tetraethylethoxisilane resulting in Si–H doping and the formation of by-products as polyynes [Trusovas (2016)].

2.1.3 GO for water purification application

As explained in the first chapter, adsorption is a wide used methodology for the removal of many water contaminants. The wide use of activated carbon has been restricted because of its costs and the difficulty in its regeneration. As an alternative to it, carbon nanomaterials such as graphene oxide and reduced graphene oxide have been developed. Carbon nanomaterials are perfect candidate as adsorbent due to their high surface area; in particular, GO shows tunable surface chemistry and selectivity due to its functional oxygen groups, and scalable production. The oxygen atoms themselves are responsible for ion-exchange and electrostatic interaction with metal ions. In addition, they can be functionalised for selective adsorption. For example, GO revealed a higher adsorption capacity for Pb(II) compared to pristine graphene [Perreault (2015)]. All the parameters affecting the surface chemistry of GO also affect its adsorption ability, i.e. ionic strength, pH, number and quality of oxygen-containing groups of GO. For example, it was shown that the adsorption ability towards Zn(II) was decreased after addition of NaNO₃, NaCl, and KCl to GO suspension: this is ascribed to the competition of electrolytes and metal ions for GO active sites [Perreault (2015)]. In addition, electrolytes may affect the electrical double layer of hydrated particles, changing the interaction with active sites. Similarly, pH affects the adsorption behaviour of GO affecting its surface properties or the charged nature of the adsorbates. For example, it was demonstrated the removal of Cu(II), Zn(II), Cd(II), and Pb(II) ions at pH 5.0, while Co(II) and Cd(II) removal occurred at pH 6.0 [Perreault (2015)].

Taking advantage of the oxygenated functional groups on GO, selective adsorbents have also been prepared by modifying graphene materials: for example, the number of adsorption sites can be improved by grafting compounds such as ethylenediamine triacetic acid (EDTA) and chitosan

[Perreault (2015)]. The dispersability and adsorption capacity of rGO for Pb(II) was remarkably improved after grafting with poly- (acrylamide) (PAM) through the carboxylic groups of GO sheets. The graphene like materials can be used also for the removal of anions (e.g., F⁻, Cl⁻, Br⁻, sulphates, phosphates etc.) by interaction with electron-deficient aromatic ring on graphene layer [Perreault (2015)].

Graphene materials have also been applied as absorbents for the removal of organic pollutants, such as dyes, antibiotics, hydrocarbons, crude oil, pesticides, and natural organic matter [Perreault (2015)]. The adsorption capacity of GO, rGO, or pristine graphene sheets for an organic compound might be different since this depends on its structural properties (i.e. molecular conformation, dipole moment, presence of functional groups). The adsorption of organic compounds by graphene-based materials occurs by five different molecular interactions, which include electrostatic interaction, hydrophobic effect, p-p bonding, hydrogen bonding, and covalent bonding [Perreault (2015)]. The adsorption of cationic dyes such as methylene blue and methyl violet by GO over a wide pH range (6–10) is mediated through electrostatic interactions between exfoliated GO and the dye molecules [Perreault (2015)]. In general, graphene sheets can be used as a physical support to stabilize magnetic or photocatalytic nanoparticles, facilitating their recycling and reuse and avoiding their aggregation. The use of GO for photocatalytic applications is reported in the following paragraphs.

Graphene-based materials have also shown promising antimicrobial properties [Hegab (2016)]: they can induce inactivation of bacterial cells upon direct contact by physical and oxidative damage to cell membranes [Hegab (2016)]. The physical damage of the cell membrane by GO seems to be the major mechanisms of bacterial inactivation and this was demonstrated by different techniques, in particular electron microscopy on bacteria being in contact with GO showed evident damaged cell membranes. Due to its stronger mechanical properties, rGO may induce more membrane damage compared to GO [Buccheri (2016)].

Graphene sheets can be adsorbed on the membrane surface, penetrate across or be integrated into the lipid bilayer, or taken up in vesicular structures [Hegab (2016)]. Recent studies also indicate that oxidative stress is involved in the antimicrobial activity of GO and rGO nanomaterials [Hegab (2016)]. The presence of defects may be responsible for induced oxidative stress in bacterial cells. Actually there is a limited knowledge of the required graphene-based material features for efficient antibacterial activity. The structural chemical and physical characteristics, i.e. nanosheets thickness and size, dispersibility and oxidation capacity, affect this property. An accurate and comprehensive evaluation with regard to these factors is essential for prospective studies on the bactericidal properties of graphene-based materials.

Recently, GO has been used as filler in polymeric membranes to improve water permeability, antimicrobial properties and mechanical strength. It is fundamental to determinate the exact amount of GO to be added: it has been shown that integrating GO sheets at around 1 wt% directly into the polymer solution can increase the Young's modulus of polysulfone membranes from 150 MPa to up to 218 MPa [Perreault (2015)]. Further increase in the GO concentration, however, weakens the membrane due to an incomplete dispersion and distribution of GO in the polymer matrix.

GO/PVDF, GO/PES and GO/PSF membranes have been prepared showing increased water flux, salt rejection, mechanical stability, antibacterial and antifouling properties. GO can be directly bound to the surface of the polymeric membrane by existing functional groups or by using an intermediate coating compound to provide reactive sites [Perreault (2015)].

2.1.4 GO for photocatalytic application

Graphene oxide and its reduced counterpart, r-GO, have been proven to be promising materials for photocatalytic applications.

The electronic structure of graphene makes it a zero band-gap semiconductor; tuning the electronic properties of graphene by introducing heteroatoms or functionalities extends the applications of graphene to photocatalytic processes [Yeh (2013)]. The introduction of oxygen on the graphene layers results in the generation of a band gap in graphene that depends on the quantity and quality of oxygen groups as shown in Figure 2.4; fully oxidized GO is an insulator, in contrast to partially oxidized GO and graphene that are a semiconductor and a conductor, respectively. GO is a p-doped material but a simple replacement of oxygen functionalities with N atoms transforms GO into an n-type semiconductor [Yeh (2013)]. In other words, the amount and quality of functional groups on GO layers can be used for tuning its electronic properties i.e. its photocatalytic properties. The structure of GO according to the LK model has been described in the previous paragraph.

GO materials with different oxidation levels were tested as photocatalysts for H₂ generation from water and a mixture of water and methanol [Yeh (2010)]. These materials have energy gap ranging from 2.4 to 4.3 eV and they are able to produce hydrogen without degrading. GO sheets have a large exposed area for extensive contact with water molecules: carbon atoms on GO sheets are easily accessible to protons due to the highly dispersion of GO sheets in water. These protons readily transform to H₂ by accepting photogenerated electrons from the carbon atoms. However, no O₂ evolution was observed. During the irradiation of GO samples for hydrogen production, these are reduced as evidenced by the formation of aggregates in the solution. The GO reduction narrows their

band gaps. However, this did not affect H₂ generation under irradiation underlining that the oxygen functional groups that participate in the H₂ production are still active. Electrons and holes are generated by adsorption of UV light, the photogenerated electrons form defect carbon sites by reducing oxygen functional groups. These are the active sites for water reduction to H₂. The holes may oxidize the defect carbon atoms to form CO₂ gas, resulting in photocorrosion of the GO sheets. Modifications of GO sheets to avoid photocorrosion are necessary for the direct use of GO as photocatalysts in water splitting. The same materials were tested for hydrogen evolution under visible light irradiation but with a low efficiency. However, the positive response to visible-light irradiation suggests to plan further studies on the potential use of GO for solar-energy conversion.

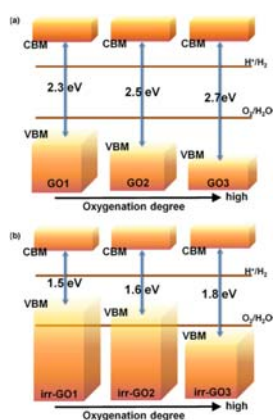


Figure 2. 4 The VBM and CBM positions of GO sheets (a) varying oxygenation degrees or (b) after mercury-lamp irradiation. The VBM upward shifts after irradiation, while the CBM position of the GO sheets remains unchanged. Reported from [Yeh (2013)].

As an alternative to noble metals that are costly, carbon materials are good electron capture agents because of their high conductivity. Due to its large exposed area and an excellent electronic mobility thanks to its p-conjugation structure, graphene is a viable co-catalyst to accept electrons for exciton separation [Yeh (2013)]. As shown in Figure 2.5, when graphene-coupled semiconductors are excited under light irradiation the photoinduced electrons quickly transfer to the surface of graphene and this can suppress electron-hole recombination. In this way a p-n junction is created in which GO acts as an electron sink, improving the separation of photogenerated charges. Commonly, graphene/semiconductor composites are prepared by reduction of graphene oxide/semiconductor composites due to the higher processability and hydrophilic character of graphene oxide respect to graphene. In this case, an important parameter is the loading of GO in the composite. Since a single sheet of GO can absorb 2.3% of visible light, increasing GO content in the nanocomposites will affect the light absorption ability of the photocatalyst itself in the nanocomposite, resulting in a low quantum efficiency. As a consequence, the correct amount of GO in the specific nanocomposite should be evaluated experimentally according to the specific application.

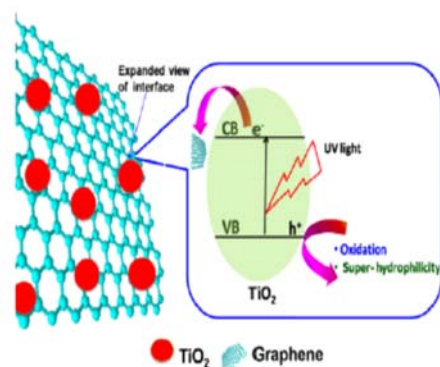


Figure 2. 5 Schematic illustration of photogenerated charge carrier transfer between a photocatalyst and graphene. Reported from [Yeh (2013)].

Besides being an electrons sink, GO and rGO also enhance the adsorption capacity and tune the light absorption range of the inorganic semiconductor [Zhang (2015)]. Owing to its high surface area and adsorption properties, graphene and its derivatives act as ideal scaffold materials for contaminants adsorption favouring their contact with the photogenerated active species (e.g., electrons, holes, hydroxyl radicals, and superoxide radicals). Moreover, graphene like structure are able to extend the light absorption range from the UV to visible light region of wide-band gap semiconductor photocatalysts. For example, integrating TiO₂ (P25) nanoparticles with RGO through a one-step hydrothermal method has shown to be a good way for extending the light response range of titania into the visible light region [Zhang (2015)].

These hybrid materials have been used for hydrogen production by photocatalytic water splitting. GO-TiO₂ nanocomposites synthesized by different methods as sol-gel and hydrothermal method catalysed H₂ evolution from an aqueous solution with higher efficiency with respect to the use of titanium dioxide alone [Yeh (2013)]. For what concerns O₂ evolution, GO in combination with BiVO₄ has shown to be able to improve the charge separation and electron transport in photoanodes for O₂ evolution. The composite photoanode showed a photocurrent of 65 mAcm⁻² that is higher than the one observed for the free photocatalyst (8 mAcm⁻²) at +0.75 V bias [Yeh (2013)].

These hybrid nanocomposites have also been used for photocatalytic degradation of water contaminants. RGO-TiO₂ thin films via deposition of GO sheets on TiO₂ thin films followed by annealing and a UV-Vis light-assisted reduction process have been utilized for photoinactivation of *E. coli* in an aqueous solution under solar light irradiation [Zhang (2015)]. With the appropriate addition of RGO, the composite displays significantly enhanced bactericidal activity in comparison with blank TiO₂.

Loading graphene into Bi_2O_3 is a way to obtain a composite with enhanced photocatalytic activity toward the degradation of methyl orange and methylene blue. Bi_2O_3 -reduced graphene oxide ($\text{Bi}_2\text{O}_3/\text{RGO}$) composites were synthesized by a solvothermal technique using modified Hummers method for graphene oxide. The as-prepared material reveals as a good photocatalyst for water purification, since it showed higher efficiency for the photocatalytic degradation of organic dye molecules and the destruction of harmful bacteria compared with the pristine material [Suresh (2016)].

2.2 GO and irradiated GO: study of antibacterial properties and toxicity

Disinfection methods currently used in drinking water treatment are efficient but the main drawback is the formation of harmful by-products [Li (2008)]. Therefore, new clean approaches and materials for water disinfection are needed. Among these materials, graphene-based nanomaterials have been found to show antibacterial properties. The toxicity and antimicrobial properties of GO and laser irradiated GO (iGO) are shown in the following paragraph.

GO in aqueous suspensions was synthesized by a modified Hummers method [Hummers (1958)]. Powdered graphite flakes and solid sodium nitrate (2:1) are stirred in concentrated sulfuric acid in an ice bath. Under vigorous stirring, the potassium permanganate is slowly added, keeping the temperature below 20 °C. Then the temperature of the suspension is increased to 35 °C, and kept at that temperature for 30 minutes. The now pasty suspension is then diluted by adding water, causing a temperature increase. After holding the temperature constant for 15 minutes the mixture is diluted with more water and the residual permanganate reduced with hydrogen peroxide. The obtained graphite oxide is then purified by repeated washing in water and then it is dried in a vacuum oven at 60 °C for 48 h before use.

For the laser irradiation process, GO solutions were irradiated by the second harmonic of a pulsed Nd:YAG laser (532 nm) with a pulse duration of 5 ns a repetition rate of 10 Hz. The laser beam size was around 28 mm² and the GO solutions (20 ml) were homogeneously irradiated, without any focusing lens, at a constant fluence of 0.32 J/cm². For antibacterial tests, 180 mg/l GO solutions were irradiated as described for different times ranging from 1 to 4 hours, named iGO15, iGO1, iGO2, iGO3 and iGO4, respectively.

Figure 2.6 shows the optical absorbance spectra of the GO solution (magenta curve) prepared by the Hummers method and consequently diluted. The spectra were acquired by the instrument reported in Appendix A1. The peak at about 230 nm is related to the π - π^* transitions of C=C bonds; the shoulder

at around 310 nm is due to the $\sigma-\pi^*$ transitions of the C=O bonds [Wang (2009)]. The red and wine curves are related to the irradiated samples for three and four hours, named iGO3 and iGO4, respectively. The effect of laser irradiation results mainly in three differences visible in the spectra reported in Figure 2.6: (1) a slight red shift of the $\pi-\pi^*$ absorbance peak position, less than 5 nm after four hours of irradiation; (2) an enhanced light absorption in the visible region; (3) the shoulder at 310 nm becomes indistinguishable from the main peak. In particular, the increased absorption in the visible region is consistent with the darker color of solutions after irradiation as shown in the inset of Figure 2.6 (from yellow to brown). This effect is associated to GO reduction of its oxygen functionalities [Li (2014)] and to the reduction of the flakes size, as shown by the morphological characterization.

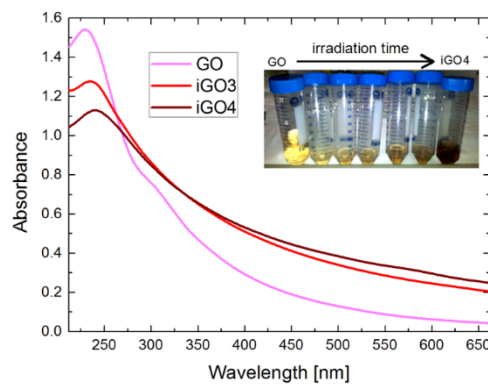


Figure 2. 6 Absorbance spectra of the as prepared GO (pink curve) and iGO solution at different laser irradiation time (3 and 4 hours). The picture in the inset shows the as prepared solution, from left to right as the irradiation time is increased. Reported from [Buccheri (2016)].

The Raman spectra of GO (magenta curve), GO irradiated for one hour (iGO1) and for three hours irradiation (iGO3), wine and red curves respectively are displayed in Figure 2.7. These were acquired by the procedure reported in Appendix A2. The main characteristic vibrational modes of carbonaceous structures are the D and G bands at about 1360 and 1590 cm^{-1} , respectively and the 2D band between 2700 and 3300 cm^{-1} [Claramunt (2015)]. The G and 2D bands are associated to the E_{2g} mode of crystalline graphene and these are the only peaks present in the Raman spectrum of pure graphene. The D band, related to the A_{1g} breathing mode, arises from the introduction of defects (such as oxygen functional groups) on the basal plane structure of graphene. Considering this aspect, the G (or 2D) band is used to measure the order in the structure, while the D band is a measure of the disorder. To be more precise, the ratio I_D/I_G is an index of the defectiveness of the material. The calculated I_D/I_G ratio is about 1.20 for the as prepared GO and this values remains unchanged after laser irradiation process. This is not surprising although one could expect a reduced I_D/I_G value after reduction. We can explain this considering that laser reduction on one side can reduce the amount of

oxygen functional groups but, on the other side, does not restore sp^2 domains (in this case I_G will not increase) and, furthermore, induces an increase of the edges due to the reduction average size of the graphene flakes. XPS, DLS measurements and morphological characterization confirm this hypothesis, as shown in the following discussion.

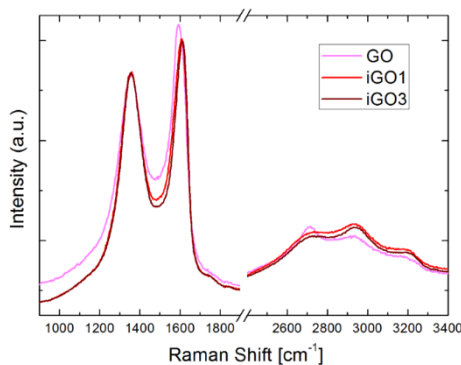


Figure 2. 7 Raman spectra of GO (pink curve), iGO1 (red curve) and iGO3 (wine curve). Reported from [Buccheri (2016)].

The Raman spectra of iGO samples show a less defined 2D band with respect to the one of initial GO and an upshift of the G band at 1615 cm^{-1} . This shift could be related to the disordered-induced phonon mode due to crystal defects or to a double vacancy corresponding to pentagonal and octagonal carbon rings, named 5-8-5 defects [Claramunt (2015)], that generate a Raman signal at 1620 cm^{-1} . Furthermore, the reduced definition of the 2D band can be explained hypothesizing the presence of a small fraction of pure graphene in the initial GO that disappears after visible laser irradiation.

Figure 2.8 shows the C1s and O1s XPS spectra of GO and iGO3 acquired according to the procedure in Appendix A3. From these spectra it is possible to deeply understand the effect of laser irradiation on GO and the grade of its reduction. This analysis allows to get information on the oxygen content and the kinds of C-C and C-O bonds. The elemental analyses of GO confirm the presence of O and C and a small fraction (less than 1 at%) of Na, S and N as contamination deriving from the synthetic procedure. The calculated O/C ratio is 41.7% for the initial GO and 38.7% for iGO3 sample. Despite of the increasing of temperature, the O/C value reduction for iGO3 is not so high as expected, due to the presence of water during irradiation, that induces an oxidizing effect on GO; in other words oxygen functional groups are not completely removed from GO surface by the irradiation process.

The C1s signal of GO (Figure 2.8 a) presents two main peaks at about 285 and 287 eV. After three hours of irradiation (Figure 2.8 b), the intensity of the peak at 287 eV decreases. The deconvolution of these spectra allows to distinguish different structural configurations present on the GO surface [Chen (2012)]. According to this reference, C1s XPS profiles were deconvoluted considering the sp^2

and sp^3 carbon domains at 284.2 and 284.5-285.0 eV, (magenta and orange curves); hydroxyl and epoxyde groups between 286.0 and 287.0 eV, respectively (dark yellow and green curves); C=O bonds between 287.7-288.7 eV (blue curves); carboxyl groups at 289.0-290.5 eV (cyan curves). O1s XPS spectra (Figure 3.3 c,d) can be deconvoluted considering two characteristic contributions, due to the O-C and O=C bonds, located at about 531 and 533 eV, respectively. The O-H bond (water) is reported at 535 eV.

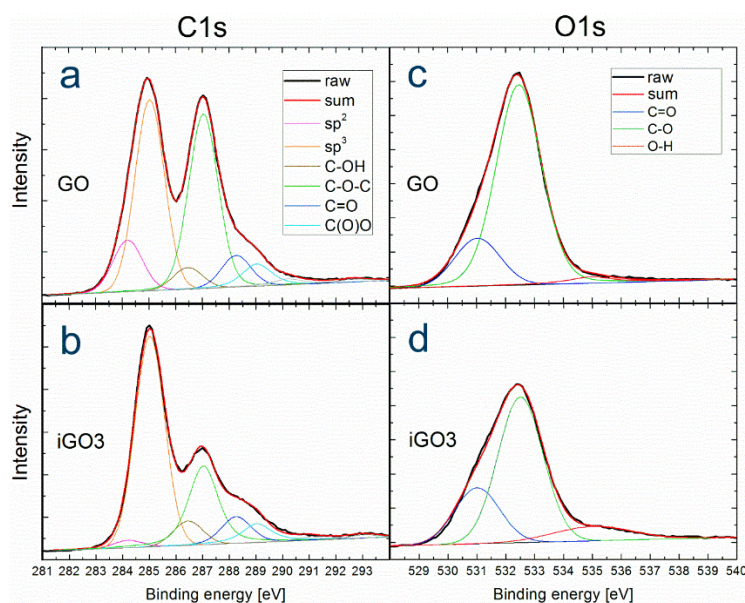


Figure 2. 8 XPS spectra of C1s in GO (a) and iGO3 (b) and O1s for GO (c) and iGO3 (d). Reported from [Buccheri (2016)].

Fitting the XPS spectra as described, the amount of each functional groups for GO and iGO3 is calculated and reported in Table 2A. After irradiation, the sp^2 fraction decreases and this is unusual for any GO reduction process. Epoxides decrease as expected for reduced GO. However, the total oxygen concentration is quite similar to the one of initial GO. The C=O, COOH and C-OH groups show a slight increase, and, since these are stable at the edge of GO sheets or bound to defects, the increase of defected sites and edges can be deduced as an effect of laser irradiation. The positions and the areas of the de-convoluted peaks calculated from O1s XPS spectra are given in Table 2B. In agreement with the results from C XPS spectra, the total contribution due to the C-O bonds decreases, and, in particular, the areas of the peaks related to the C=O and O-H configurations show a slight enhancement.

Table 2A C1s XPS peak position and intensity for GO and iGO3

peak	Position [eV]	Area % (GO)	Area % (iGO3)
sp^2	284.2	10.4	1.9
sp^3	285.0	37.5	53.4

C-OH	286.5	4.2	6.2
C-O	286.9	36.1	24.3
C=O	288.1	6.5	7.6
COOH	288.9	5.3	6.6

Table 2B O1s XPS peak position and intensity for GO and iGO3

peak	Position [eV]	Area % (GO)	Area % (iGO3)
C=O	531.0	17.7	24.7
C-O	532.5	78.8	64.2
O-H	535.0	3.5	11.1

In summary, pulsed visible laser irradiation of aqueous GO mainly creates defects in the GO structures instead of a large reduction of the oxygen content. This is confirmed by the shift of G band position (connected to the introduction of new defects) and the small decrease of the I_G/I_D ratio in the Raman spectra. XPS analysis confirm the introduction of defects showing a reduction of the sp^2 component within the increase of signals related to the oxygen configurations that are stable on defects (C=O, COOH and C-OH). This is compatible with the presence of more edges and, therefore, with a size reduction of GO flakes. In order to check a change in the size distribution of GO flakes, SEM and Dynamic Light Scattering investigations were performed, according to the procedure reported in Appendix A4 and A5, respectively.

DLS was already applied to GO solutions [Liu (2011)] for the estimation of average size of non-spherical objects. In this case, DLS technique estimates the hydrodynamic diameter of the hypothetical hard sphere that diffuses with the same diffusion coefficient of the nanoparticle under examination. Before the measurements, the solutions undergo sonication to reach a complete dispersion of GO and iGO3. It was shown that laser irradiation has the effect of reducing the stability of GO in water: while GO is stable for several months, the iGO particles started to agglomerate after one month. The hydrodynamic diameters are reported in Figure 2.9 for GO and iGO3 after different times of sonication. At the starting point, the GO and iGO3 have the same dimension due to iGO3 agglomeration. Probably, the agglomerates are formed by stacked sheets and the hydrodynamic diameter of the aggregates depends only on the largest dimension. After sonication the aggregates dissolve and particles with a smaller size are observed. The saturation of measured hydrodynamic diameter occurs after 20 minutes of sonication. The size reduction due to laser irradiation is confirmed since the average size of iGO3 is about half the value (140 ± 10 nm) of GO (305 ± 15 nm).

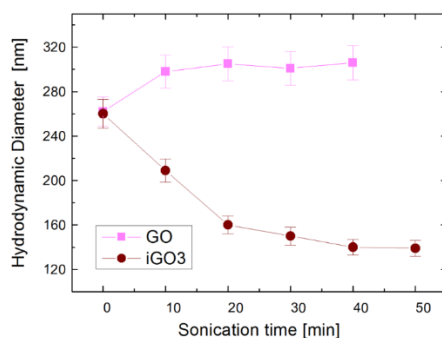


Figure 2. 9 Hydrodynamic diameter of the GO (magenta squares) and iGO3 (red circles) in water as a function of the sonication time of the solutions. Reported from [Buccheri (2016)].

The SEM images of initial and irradiated samples were acquired as reported in Appendix A5 and these are shown in Figure 2.10. GO sheets have a typical regular shape with an average area of several μm^2 ; after laser irradiation, the sheets are smaller, with irregular edges. The morphological characterization confirms the introduction of defects in GO flakes with reduced dimensions and irregular shape after the irradiation process.

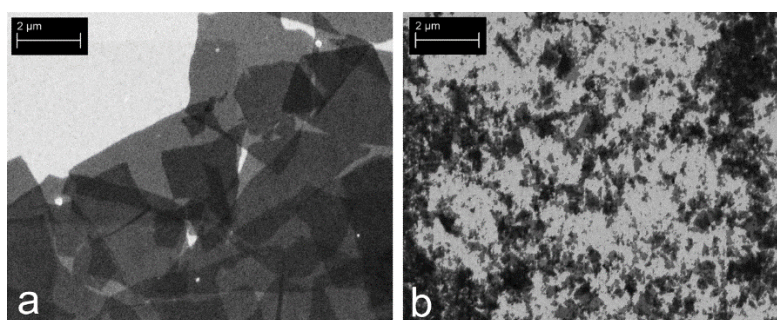


Figure 2. 10 Scanning electron microscopy of the GO flakes (a) and GO flakes after 3 hours of laser irradiation (b). Reported from [Buccheri (2016)].

The antimicrobial properties of GO and iGO were studied using *Escherichia coli* ATCC25922 as a model organism according to the procedure reported in Appendix A6. GO and iGO showed different antimicrobial activities as shown in Figure 2.11. After 1h exposure to GO, 90% of bacteria was still surviving, even at the highest nanomaterial concentration. While the results for iGO1 and iGO2 are the same as GO, iGO3 displayed higher antibacterial activity: at a final concentration of 10 $\mu\text{g/ml}$, bacterial survival is about 38% after 1h exposure. Doubling the iGO3 concentration, *E. coli* survival was reduced to 18%. Surprisingly, continuing to increase material concentration did not improve the result, due to iGO3 flakes precipitation. Similar results were obtained with iGO4. For what concerns the time of exposures the best results were obtained after one-hour treatment, while longer exposures

did not improve the results. This means that the mechanisms leading to bacterial inactivation act quite fast and this is independent from the contact time.

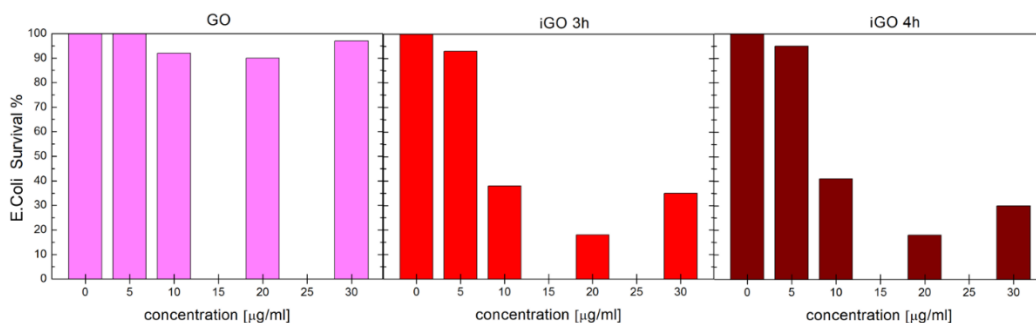


Figure 2.11 Relative *E. coli* survival rate measured by CFU count after 1h exposure to GO, iGO3 and iGO4 at different final concentrations. Data were normalized to the untreated sample run in parallel. Reported from [Buccheri (2016)].

Bacterial metabolism is tested by WST-8 assay (see Appendix A7). As for the previous analysis, the best antibacterial activity is recorded for iGO3 and iGO4 (Figure 2.12): after 1h exposure to the nanomaterials at the final concentration of 20µg/ml, metabolism rate is reduced down to 54% and 62%, respectively.

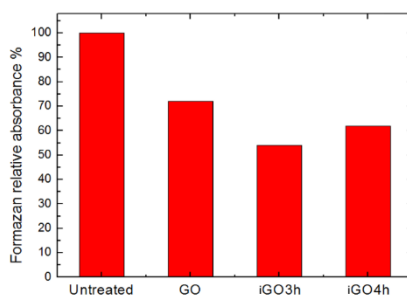


Figure 2.12 Results of WST-8 Assay showing relative absorbance levels after 1h exposure to GO, iGO3h and iGO4h at different final concentrations. Data were normalized to the untreated sample run in parallel. Reported from [Buccheri (2016)].

Laser irradiation of GO confers to it an antibacterial activity; in order to understand the correlation between GO modifications induced by laser irradiation and the resulting antibacterial activity we evaluated lipid peroxidation. Recent studies suggest that graphene-like materials exhibit antibacterial activity by mechanical damage towards the bacterial membrane and oxidative stress [Liu (2011)]. The possible generation of reactive oxygen species (ROS) induces lipid peroxidation of the bacterial membrane. The oxidation level of bacterial membranes was measured by the level of malondialdehyde (MDA), through the TBARS Assay, during exposure to GO and iGOs samples (see Appendix A8). The reaction was carried out in the presence of D-mannitol: this is a scavenger of the hydroxyl radical (OH·), allowing to investigate a possible role of this radical in the oxidative stress

generated [Cai (2014)]. Anyway, MDA levels do not change after GO and iGOs exposure (Figure 2.13). As a result, lipid peroxidation or oxidative stress is not the main mechanism of antibacterial activity.

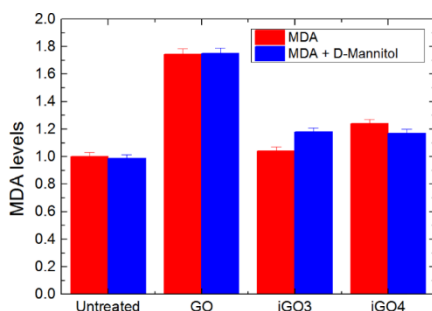


Figure 2. 13 MDA levels generated by GO, iGO3 and iGO4. Reported from [Buccheri (2016)].

As a consequence, mechanical damage is responsible for the higher antibacterial activity of iGO3 and iGO4. As show by SEM characterization (Figure 2.10), laser irradiation of GO reduced GO flakes dimensions that acquire irregular edge shapes. The dimensions of GO flakes are reduced from tens microns to few microns by laser irradiation and these are very close to the size of *E. coli* bacteria. The as modified GO flakes may seriously damage bacterial membrane by contact. This is demonstrated by acquiring SEM images of bacteria in contact with GO and iGO, respectively. These images were acquired according to the procedure reported in Appendix A9. As shown in Figure 2.14 a,b, untreated samples of *E.coli* or the same in contact with GO show a regular shape and bacterial membranes do not display any damage. On the other hand, iGO planes (Figure 2.14 c) are directly in contact with the bacteria damaging their membranes as clearly visible.

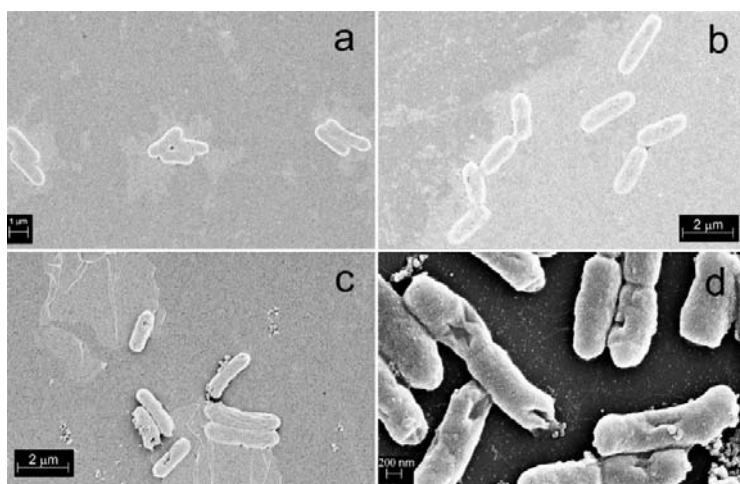


Figure 2.14 SEM images of untreated *E. Coli* (a) and of *E. Coli* after 1 h of exposure to 30 mg/l of GO (b) or to 30 mg/l of iGO3 (c and d). Reported from [Buccheri (2016)].

Considering the possible application of these materials in water purification, their toxicity was investigated through the Fish Embryo Toxicity (FET) test by evaluation of viability, growth (larval length), brain morphology, pharyngeal arches and jaw, other craniofacial structures, heart, fins, notochord, somites, tail, body shape, cardiovascular function, yolk sac and locomotor function and touch response (see Appendix A10). This test was performed for different GO and iGO concentrations (from 10 to 160 mg/l). The test showed that the tested GO and iGO solutions did not affect viability or any other parameter in Zebrafish larvae (Figure 2.15). Although iGO3 and iGO4 solutions with a concentration of 20 mg/l showed antibacterial activity, these materials are not toxic even at concentration of 160 mg/l.

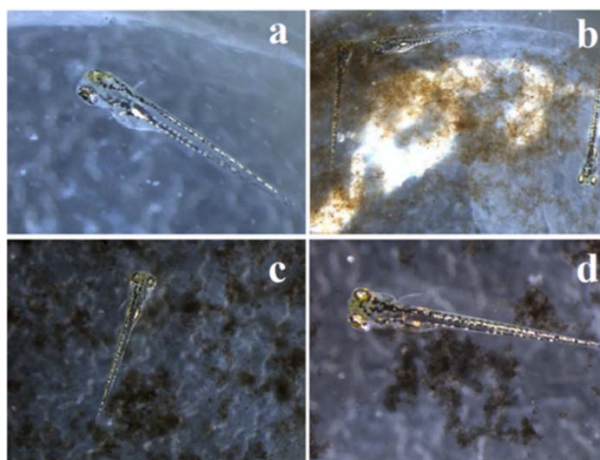


Figure 2.15 Zebrafish larval 72 hpf, 32x. Untreated (a); GO, 160mg/l (b); iGO2, 160 mg/l (c); iGO4, 160 mg/l (d). Reported from [Buccheri (2016)].

The absent toxicity of these materials makes them suitable for water purification application. In this regard, GO, laser modified GO (hereafter named rGO) and their hybrid composites with P25 have been tested for adsorption or photocatalytic removal of MB from water.

2.3 Laser irradiated GO and titania for dye removal

Laser irradiation process was used to modify the properties of graphene oxide (GO) sheets dispersed in water by finely tuning the amount of oxygen functionalities and, therefore, the degree of reduction. In this way both the hydrophilicity and the spectroscopic features of the GO suspension can be changed. The same procedure is tested for the synthesis of GO(rGO)-TiO₂ composite materials. These hybrid compounds were realized to increase the photocatalytic activity of titania.

GO was prepared by a modified Hummers method, described in Paragraph 3.1.1. Different solutions of GO at 100 mg/l were irradiated by the second harmonic of a pulsed Nd:YAG laser (532 nm) with a pulse duration of 5 ns a repetition rate of 10 Hz. The laser beam size was around 28 mm² and the

GO solutions were homogeneously irradiated, without any focusing lens, at a constant fluence of 0.32 J/cm^2 for 15, 60 and 180 minutes (samples named hereafter rGO15, rGO60 and rGO180, respectively). Aqueous GO-P25 and rGO180-P25 solutions were prepared mixing the GO (rGO180) and P25 Titania (>99,5% Sigma–Aldrich) with atomic ratio of 1:9 until a final concentration of 100 mg/L . These solutions were irradiated by pulsed laser for 15 minutes in the same conditions used for GO reduction.

Hybrid nanocomposites were investigated by SEM (see Appendix A4), and the images of the irradiated GO-P25 and rGO180-P25 samples are reported in Figure 2.16 a,b, respectively. As just shown in the previous paragraph, the rGO layers appear to be smaller and more irregular than the GO ones as a consequence of laser irradiation; considering the smaller sizes, TiO_2 particles results in a more homogeneously distribution on the surface of rGO while the GO surface are partially uncovered.

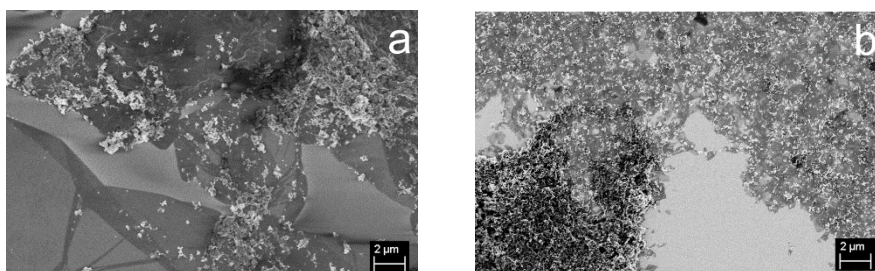


Figure 2.16 SEM images of GO-P25 (a) and rGO180-P25 (b) composites obtained by pulsed laser irradiation for 15 minutes. Reported from [Filice (2015)].

The absorbance spectra of hybrid compounds are shown in Figure 2.17 and compared with the initial samples without P25. The spectra were acquired with the instrument reported in Appendix A1. GO and rGOs show the main peaks just explained in the previous paragraph. For the mixed GO-P25 and rGO180-P25 solutions, the maximum peak initially located at 230 nm is shifted to 250 nm and a shoulder at 320 nm is observed. This shoulder is ascribed to the presence of the P25 nanoparticles, as clearly shown by the comparison with the P25 absorbance spectrum reported in the same figure.

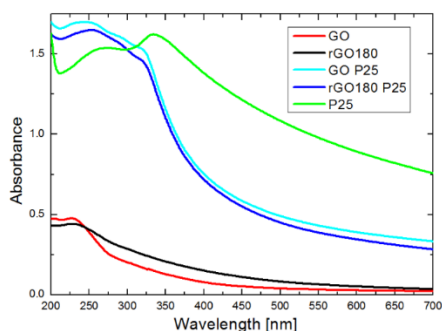


Figure 2.17 Uv-Vis absorbance spectra of 10 mg/l GO and rGO180 solutions, 100 mg/l GO/rGO180-P25 solutions and 90 mg/l P25 solution. Reported from [Filice (2015)].

Figure 2.18 compares the Raman spectra of GO and laser modified GO with the spectra of hybrid materials, acquired according to the procedure reported in Appendix A2. All the spectra report the characteristic peaks for the graphitized structures, as explained in the previous paragraph. Also in this case, the D band is the same while the G band at 1615 cm^{-1} is shifted slightly to 1635 cm^{-1} after the laser irradiation process. In addition, the Raman spectra of the composites show the characteristic peaks of anatase at 400 , 523 and 653 cm^{-1} . As previously shown for GO and laser modified GO, the ratio I_D/I_G is quite the same also for the composites, confirming that no sp^2 domains are formed due to laser irradiation, and the effect of this process is only to change the quantity and quality of oxygen content on graphene layers. Furthermore, the peaks characteristic of anatase phase are more visible in the rGO-P25 composite than in GO-P25, this is in agreement with morphological characterization: TiO_2 nanoparticles cover almost completely rGO sheets, whilst the coverage of GO sheets is only partial. This difference arises from the smaller dimension of rGO flakes induced by laser irradiation.

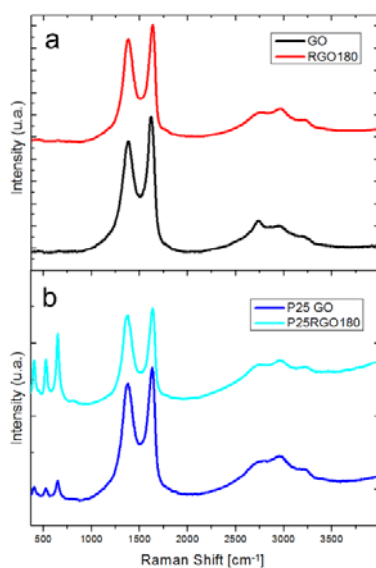


Figure 2.18 Raman spectra of GO and rGO180 solutions (a) and GO/rGO180-P25 solutions (b). Reported from [Filice (2015)].

Figure 2.19 compares the XPS spectra (see Appendix A3) of hybrids materials with the GO samples treated in the same way as composites but in absence of titania. The last two (i.e. GO and rGO) are described in the previous paragraph. In the case of hybrid composites, a lower amount of O-related contributions in the C1s peak is shown, suggesting an increase of the reduction effect of laser irradiation in presence of titania. This is better underlined by comparing XPS spectra of initial GO, and GO or mixed GO P25 irradiated for 15 minutes (Figure 2.2). The effect of laser irradiation is not only a reduction of oxygen amount but also a modification of the nature of oxygen groups. The Table 3C shows the percentage of functional groups and their relative position obtained by the fitting of the XPS spectra. It is evident that epoxy groups decrease in favour of an increase of hydroxyl groups, in particular in the presence of titanium dioxide. Instead, the areas of the bands associated with the C=O, COOH and C–OH configurations show a slight increase, suggesting the increase in defected sites and edges.

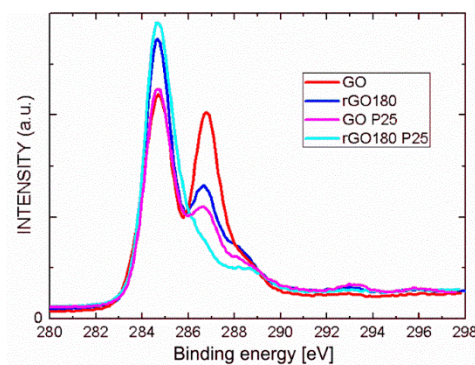


Figure 2.19 XPS spectra of C 1s for GO and rGO180 solutions and GO/rGO180-P25 solutions. Reported from [Filice (2015)].

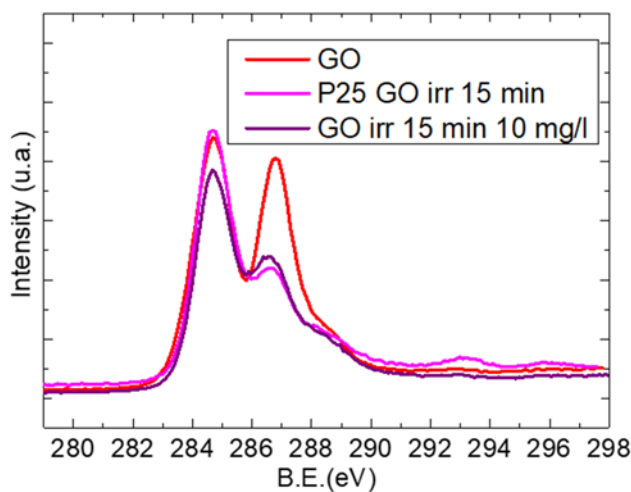


Figure 2.20 XPS spectra of C 1s for GO itself and GO or mixed GO P25 irradiated for 15 minutes.

Table 3C Percentage of functional groups and their relative position obtained by the fitting of the XPS spectra.

Peak	Position [eV]	% GO	% GO 10 mg/l irr 15 min	% P25 GO 100 mg/l irr 15 min
sp2	284,2	10,43	3,22	3,94
sp3	285	37,48	49,68	53,42
C-OH	286,5	4,22	13,78	9,69
C-O-C	287	36,05	21,00	18,45
C=O	288,3	6,48	6,67	6,05
COOH	289	5,34	5,36	6,6

The as prepared materials are tested for the removal of a cationic, thiazine dye, Methylene blue, according to the procedure reported in Appendix A11. The optical characteristics of this dye are reported in Appendix B. Dye cations are adsorbed on GO flakes via electrostatic interactions with negative oxygen moieties and π - π interactions with sp^2 conjugation system. Since the first one is the main interaction, one experimental parameter to be controlled is the pH of the solutions. Both GO and rGO have pH value of 3.8 while the mixed solutions of GO-(rGO)-P25 show a pH of about 5 (see Appendix A11). These values are constant during the experiments.

It is possible to get information on the surface properties of a material by observing the changes in the absorbance spectrum when in contact with MB. For this reason, the efficiency of GO and its laser reduced forms for the adsorption of MB in water is investigated to get information on the modifications induced by laser irradiation on the surface of GO flakes.

Figure 2.21 reports, respectively, the absorbance spectra for MB after 30 minutes in the presence of GO at different concentrations (0.01 – 0.07 – 0.1 g/L) and a comparison among the spectra of the same concentrated solutions of GO and laser modified GO for different reduction times (15, 60 and 180 min) in the bottom.

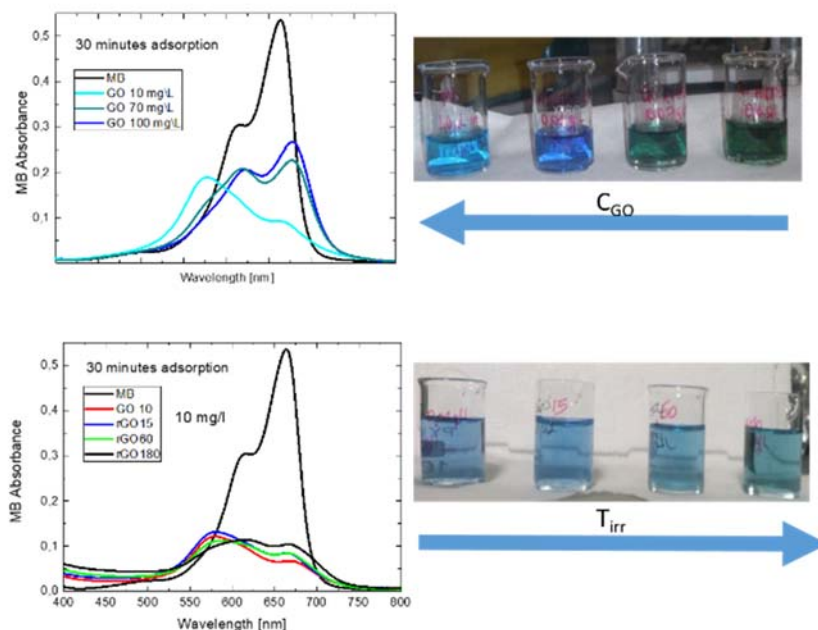


Figure 2.21 UV-Vis absorbance spectra of MB in (on the top) GO solutions with different concentration values and (right) GO 10 mg/l before and after different laser reduction times (15, 60 and 180 minutes). The figures in the inset show the GO solutions with increasing concentration (left) or increasing reduction time (in the bottom).

In both the images, we can observe that the concentration of MB rapidly dropped down within a shift of the absorbance maxima towards lower wavelengths, indicating the formation of MB aggregates when the dye is in contact with GO and laser modified GO. For what concerns the dependence of MB aggregation on GO concentration, the aggregation decreases with increasing GO concentration. For GO solutions 10 mg/l, MB trimer are formed and evidenced by the peak at 577 nm and the shift of the monomer peak to 668 nm. For the highest concentrated GO solution, the peak related to the trimer disappears and the peaks of dimer and monomer are predominant. For 70 mg/l GO, trimers are still present and evidenced by a shoulder at 577 nm. MB adsorption occurs by three consecutive steps depending on MB concentration: initially isolated MB molecules electrostatically interact with the O-functional groups on GO flakes and are adsorbed, in this stage the number of active sites on GO flakes is higher than the number of dye molecules; as the MB concentration increases the number of active sites on GO surface is comparable or lower than the number of dye molecules, the probability of self-interaction increases and dye molecules start to aggregate. The last step is MB saturation of GO surface and subsequent precipitation.

It is obvious that these three steps depend on the relative concentration of GO layers and MB molecules; considering a fixed MB concentration and increasing GO concentrations (as for Figure 3.21 in the bottom) the trend is the opposite of what explained above. For less concentrated GO

solutions, the numbers of layers and active sites is lower than the number of MB molecules and these tend to aggregate, When GO concentration is high enough, i.e. the number of active sites is high enough, MB molecules can distribute homogeneously on its surface without aggregation. The figure 2.21 in the bottom better explains the dependence of MB aggregation on the number and quality of active sites on GO flakes.

For a fixed GO concentration, the formation of MB aggregates decreases in favour of monomers with increasing the laser irradiation time for the following reasons: (i) the size of GO flakes reduces after laser irradiation, that is similar to the situation of increasing the number of GO flakes and the spatial distribution of adsorption sites; (ii) epoxides are converted to hydroxyls, as shown by XPS investigation and, therefore, the larger distances between negative neighbouring sites cause relatively larger distances between adsorbed cations.

The adsorption and photocatalytic activity of hybrid samples were also tested for the removal of MB. Table 3D reports the residual MB concentration for dye solutions where P25 alone or mixed with GO and laser modified GO were immersed in dark or under irradiation for 30 minutes. P25 is not able to absorb MB (only 6%) and degradation increased under irradiation up to 42%. The combination of P25 with carbon nanostructures increases the MB removal efficiency: both the composites adsorb the 69% of initial MB concentration and their degradation efficiency is increased of 16 and 22%, respectively, under irradiation. For composite materials the efficiency is higher due to the synergic activity of both materials: GO increases the adsorption efficiency of the composite with respect to titania, while this one is mainly responsible of the degradation under irradiation. Figure 2.22 reports the UV-Vis absorbance spectra of MB without catalysts or in contact with GO-P25 and rGO-P25 composites, both in dark for 30 minutes or under irradiation for 30 minutes. Also in this case, the spectra underline the formation of MB higher aggregates as evidenced by the peak at 570 nm. This peak is more evident in the case of photocatalytic experiments than for adsorption tests, maybe because irradiation of adsorbed MB is able to degrade monomers more than dimers and higher aggregates.

Table 3D MB residual concentration after 30 minutes of adsorption or irradiation in presence of P25 and the composites GO(rGO)-P25

Sample	% MB residual concentration after 30 min adsorption	% MB residual concentration after 30 min irradiation
P25	94	58
GO-P25	31	16
rGO-P25	31	22

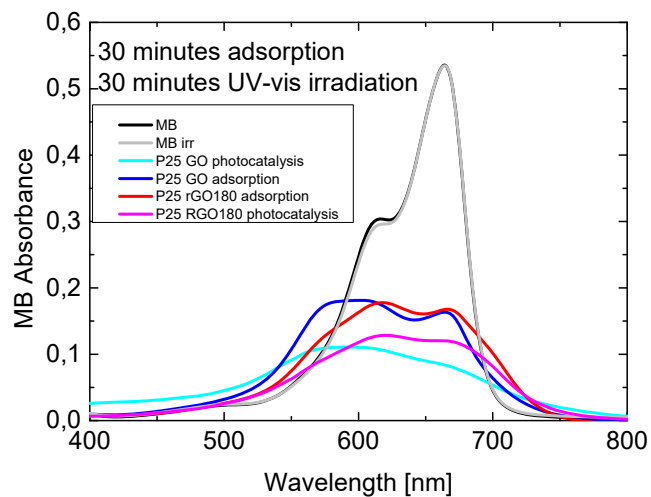


Figure 2.22 UV-Vis absorbance spectra of MB without catalysts, MB in contact with laser irradiated GO-P25 solution and laser irradiated rGO180-P25 solution, both in dark for 30 minutes or under irradiation for 30 minutes. The used lamp is reported in Appendix C. Reported from [Compagnini In press]

Chapter 3

LASER IRRADIATION OF INORGANIC SEMICONDUCTORS FOR PHOTOCATALYTIC WATER SPLITTING

3.1 Pulsed Laser Irradiation in Liquid (PLIL)

Laser processing is emerging as a powerful technique for material manipulation. Continuous wave or pulsed lasers, as optical energy sources, are available in a wide range of wavelengths (IR to deep UV), a broad variation in pulse widths (down to femtoseconds) and laser beam fluences varying from $\mu\text{J cm}^{-2}$ to several J cm^{-2} . Laser irradiation of liquids or solids allows the transfer of energy from the energy source to the materials leading to the break or the formation of chemical bonds and to a local increase of temperature. The amount of transferred energy can be easily tuned due to the great deal of freedom in the selection of laser parameters favouring specific chemical transformation to occur. Laser irradiation in liquid has been investigated for the introduction of defects in the titania and bismuth based photocatalysts; vacancy-rich photocatalysts display extended optical absorption, facilitate charge separation and enhance the selective chemisorption of reactants, which all result in improved photoreactivity.

In the past decade, nanoparticles (NPs) with different optical, electromagnetic, and chemical properties have been prepared by laser processing. The high tunability of this technique allows to prepare NPs of different sizes, shapes, morphologies, and chemical compositions for specific applications. Laser ablation of a target in the liquid phase has been used for the preparation of many metallic or not nanoparticles, but the main disadvantages of this technique still remain the particle-size control and homogeneity [Barcikowski (2013)]. These arise from the consideration that the laser formed NPs by primary ablation still continue to interact with the laser during the experiment, creating a very complicate situation.

Also colloidal solutions can be used as initial target for the generation of NPs by laser modification of their initial size, shape, chemical composition, and morphology [Pyatenko (2005)], [Pyatenko (2007)]. With respect to laser ablation in liquid, more homogeneous irradiation conditions for each nanoparticle are achieved by non-focused laser beam. During laser irradiation, laser photons are absorbed or scattered by the particle electrons. The effect of laser irradiation on NPs are different according to their metallic or not nature. If these particles are metallic, the interaction with the laser results in the collective motion of all electrons; with non metallic NPs, this interaction involves the perturbation of dipoles by interaction with the electron orbits. As a consequence, metallic NPs can

rapidly be heated to very high temperatures (5000–7000 K) by energy transfer from the laser. Two phenomena can follow this situation: the particles will transfer this energy to the lattice and finally evaporate or melt; in the second option, if the energy remains on the particles, electrons can be ejected from them and the particle may explode due to the Coulomb force [Pyatenko (2013)]. For non-metallic NPs, as inorganic semiconductors, the first hypothesis is the most accredited. In addition, it was demonstrated, comparing the time required for energy transfer to the electrons (usually picoseconds) and the pulse duration of nanosecond lasers (usually 10 ns), that when NPs are irradiated by this type of laser, the particle is intensively heated by the absorbed laser energy.

In pulsed laser irradiation in liquid, it is assumed that laser energy is adsorbed by particles resulting in particle heating, melting and evaporation [Pyatenko (2013)]. In such a case, the laser energy absorbed by a particle is written as:

$$Q_{\text{abs}} = J\sigma_{\text{abs}}^{\lambda}(d_p) \quad (1)$$

where J is the laser fluence, d_p is the diameter of the particle, and $\sigma_{\text{abs}}^{\lambda}$ is the particle absorption cross-section, which can be calculated by classical Mie theory using the complex refractive index of the bulk material. All the energy absorbed by the particle is consumed in heating and melting, which can be expressed as

$$Q_{\text{abs}} = \rho_p \frac{\pi d_p^3}{6} [C_p^s (T_m - T_0) + \Delta H_m] \quad (2)$$

where ρ_p , T_m , T_0 , C_p^s , ΔH_m are the density of the particle, the melting temperature, the ambient temperature, the heat capacities of the material and the enthalpy of melting ΔH_m respectively. By combining the above equations, the relationship between particle diameter and critical laser energy density is achieved [Pyatenko (2013)]. It is important to consider the heat loss during the process: heat loss can occur by radiative cooling or by transfer to the solvent. This heat loss generates particle cooling and solidification after melting. It was shown that solidification time and cooling time range from 10^{-5} s to 10^{-6} s. Anyway, for nanosecond, picosecond or femtosecond lasers, the heat loss time is longer than pulse duration, so heat losses can be neglected during the laser irradiation. On the other hand, the time between two consecutive nanosecond laser pulses is sufficient for particle solidification and complete cooling [Pyatenko (2013)]. This phenomenon of heating and cooling of nanoparticles is responsible for the change of particles morphology and size during laser irradiation in liquid.

PLAL fabrication of NPS is to be preferred with respect to classic method since it requires less chemical agents and no vacuum equipment. The pulsed laser irradiation in liquid allows to prepare sub-micrometer crystalline nanoparticles using low fluences [Ishikawa (2013)]. Gold NPs prepared by laser ablation in liquid were transformed into sub-micrometer spherical gold particles with a diameter of 200–300 nm by irradiation with a non-focused Nd:YAG laser [Pyatenko (2013)]. Large gold particles were melted during laser irradiation and consecutive cooling and solidification resulted in bigger, spherical particles. The average size of spherical particles increases with increased laser fluence. To modify the dimension of semiconductor in the range of sub-micrometer spherical particles, it results suitable for optical applications such as scatterers and nonlinear optical crystals, because their size is comparable to the wavelength of visible light [Ishikawa (2013)].

Zinc oxide (ZnO) crystalline spheres were obtained by laser irradiation of ZnO aqueous colloids by nanosecond Nd:YAG laser. The obtained particles had spherical shape and increased dimension from nano to sub-micrometer [Wang and Pyatenko (2014)]. These spheres showed higher sensitivity towards ultraviolet light with respect to initial particles. It was also shown that a key role in this process is acted by particle aggregation [Ishikawa (2013)]. To have particles with increased dimension with respect to the initial ones, nanoparticles aggregation is needed. This is ascribed to the fact that the process consists in consecutive cycles of particles melting and solidification, lower is the dispersion of nanoparticles higher is the aggregation and thus the melted material. During each nanosecond pulse, the agglomerates start to melt becoming bigger particles after solidification (Figure 3.1). These particles have spherical shape if the melting is complete, if not they acquire irregular shapes. Small particles continue to aggregate within bigger particles and to melt. The probability of collision decreases within increasing the number of formed bigger particles. Therefore, while the formation of large particles is fast at the beginning, the particles growth becomes slower with irradiation time. The process finishes when all particles are melted.

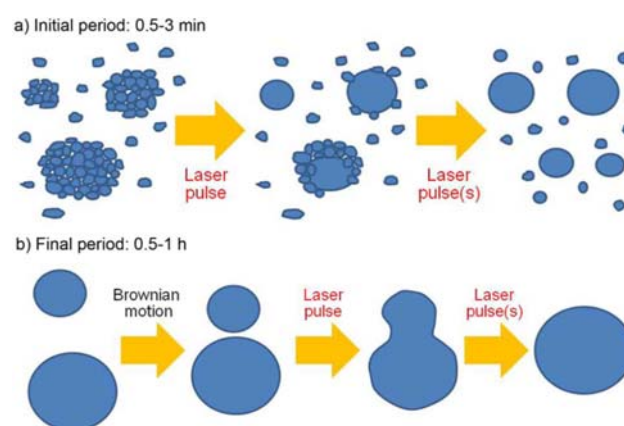


Figure 3. 1 Large particles formation from [Pyatenko (2014)].

Considering this explanation, a change of the dielectric constants of the solvents obtained by adding electrolytes (i.e. changing the dispersion properties) affects the sizes of the spherical particles produced. The production of sub-micrometer spheres is affected by the characteristic of the target material and solvent. For example, the irradiation of Boron particles led to sub-micrometer spheres of Boron itself if the irradiation occurred in water, and if an organic solvent like ethanol was used, spheres of carbide B₄C were obtained [Ishikawa (2007)]. On the contrary, for copper oxide CuO, spherical metallic particles were obtained in acetone, whereas spherical oxide particles were obtained in water [Wang (2010)].

Single-crystalline hollow spheres of Titanium dioxide were prepared by laser irradiation and these showed tunable light scattering over a wide visible-light range [Wang (2011)]. So these spheres were introduced in a dot-sensitized solar cells (QDSSCs) achieving an increasing of solar to energy conversion of 10%. The formation of these spheres is similar to the one described above (i.e. particles aggregation, melting and solidification), but many voids due to the penetration of the solvent are considered to exist inside the agglomerates (Figure 3.2).

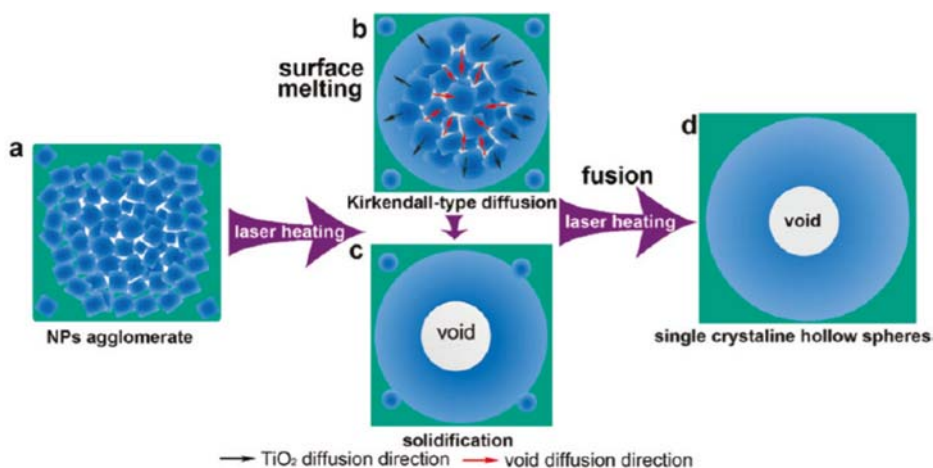


Figure 3. 2 Single-Crystalline TiO₂ hollow sphere formation by laser processing reported from [Wang (2011)].

The same technique has been demonstrated to be an interesting method to easily increase the photocatalytic activity of TiO₂ [Chen (2015)] for the enhanced degradation of rhodamine B. By laser irradiation, bigger spheres of titania were formed and these also showed the presence of reduced titanium. Ti³⁺ or oxygen vacancy increase the photocatalytic efficiency of titania in the visible region, as described in the following paragraph. The as modified material showed a better performance in degrading rhodamine B with respect to unmodified titania.

3.1.1 Laser irradiation of inorganic semiconductor

Laser irradiation has been explored as a methodology to introduce defects in inorganic semiconductors in order to improve their photocatalytic properties. All chemical functions of semiconductors, such as catalysis, adsorption or sensing behaviors, are dominated by their electronic structures and surface properties and vacancies or point defects in a material allow to manipulate the electronic structure, surface properties, charge transportation, reactivity. In particular, in contrast to the exploration of novel photocatalytic materials, vacancy engineering of traditional photocatalysts comprising earth-abundant elements represents an effective method for enhancing photocatalytic performance without introducing other elements [Long (2017)].

Vacancy engineering has many advantages for high performance photocatalysts: (1) increased activity without the introduction of impurities; (2) a promising low-cost method using simple synthetic techniques if compared to traditional doping described in the following paragraph for titania. Besides oxygen vacancies, other vacancies have been developed and can be classified in anion and cation vacancies or combinations of both [Long (2017)]. The anion vacancies in photocatalytic materials are most often oxygen, nitrogen, sulfur, and halogen vacancies. Cation vacancies are acceptors and always induce p -type conductivity. Vacancies function as active sites and enhance the adsorption of reactants (e.g., oxygen, water, or organic molecules), promote electron migration from materials to adsorbates, increase the mobility of electrons and interfacial transfer of charge carriers, which suppresses recombination and enhances the photocatalytic activity and can even directly participate in specific photocatalytic or photochemical reactions.

Studies on oxygen vacancies (VO) in photocatalysis increased dramatically in the 2000s when their role in enhancing the visible light photocatalytic activity of TiO_2 was shown [Nakamura (2000)]. Pure TiO_2 samples synthesized from conventional preparation methods are mostly oxygen-deficient non-stoichiometric compound. As a consequence, oxygen vacancies as well as Ti interstitials in TiO_2 make it an n -type semiconductor. When the proportion of O atom in TiO_2 rises, the TiO_2 may be identified as the p -type semiconductor taking holes as the main charge carriers. Although VO occur naturally in materials, higher density VO can be generated by treatment under vacuum or under reducing conditions, hydrogen plasmas, chemical reduction by aluminum, zinc, NaBH_4 etc. and electrochemical reduction [Chen (2015)]. These methods inevitably involve high processing temperatures (400–700 °C), vacuum systems, long processing times and multistep operations. For these reasons, it is exceptionally desirable to explore simple and economic strategies to synthesize stable active defective Titania photocatalysts.

In particular, hydrogen treatment (HT) (i.e. hydrogen thermal treatment, high-pressure pure hydrogen treatment, ambient or low-pressure pure hydrogen treatment, ambient hydrogen–argon treatment, hydrogen plasma) was applied to TiO₂ nanoparticles and found to be effective in improving their photo-oxidation performance. Recently, the exciting results with black TiO₂ make HT an important area of research for the introduction of VO and defects on the surface of inorganic semiconductors [Chen (2015)]. The reaction pathways and thus the final properties of the hydrogen treated TiO₂ nanomaterials will be different depending on the hydrogen treatment conditions and on the morphology and surface properties of initial material. Apparently, the hydrogenation condition played a critical role in the final color and optical properties of modified samples. Titania samples subjected to high-pressure pure hydrogen treatment change their color from white to yellow, grey, blue, deep purple and black according to the exposure time to H₂, the exposed titania facets, the gas atmosphere, H₂ concentration and to the temperature.

Independently from the synthetic procedure, the distinctive signal of defective titania is the change of typical white coloration to yellow, grey, blue, deep purple and black. Defective TiO₂ nanoparticles showed common features. First of all, their structure is formed by a well crystallized lattice core surrounded by an amorphous shell [Chen (2015)]. This shell was believed to host the possible hydrogen dopant, forming the Ti–H and O–H bonds, and contributed to the mid-gap states and the black color of the hydrogenated samples. Hydrogen occupied the interstitial sites between titanium–oxygen octahedra in the lattice and the energy barrier for hydrogen incorporation was lower through the anatase (101) surface than that through (001). Secondly, oxygen vacancies have been constantly reported in defective TiO₂ nanomaterials independently from the synthetic procedure [Chen (2015)]. For what concerns the change of colour, it is commonly associated to the introduction of Ti³⁺ ions. Anyway, depending on the synthetic conditions of defective TiO₂ nanomaterials, Ti³⁺ ions can be observed or not seen experimentally [Chen (2015)]. The same consideration also occurs for the OH and Ti-H contents. This means that the change of colour after treatment of titania samples, only suggests a change in the optical and electronic properties of the material whose origin is still not completely understood.

The change in optical properties results in an improved photocatalytic performance of defective samples and this can be ascribed to three main functions acted by defects:

- (1) to modify the band energy structure of the pristine TiO₂ as the defect states,
- (2) to trap charge carriers in the migration pathways as the electron pool or recombination center,
- (3) to influence the adsorption of reactants (e.g., H₂O, O₂, CO₂, and organic pollutants) as the active sites.

Bismuth vacancies (VBi) are also ubiquitous in nonstoichiometric bismuth oxide compounds [Xu (2016)]. Various bulk defects, including VO and VBi, were observed increasing the photocatalytic performance. Halogen vacancies (VH) are easily generated in bismuth oxyhalides, which have unique layered structures consisting of positively charged $[\text{Bi}_2\text{O}_2]^{2+}$ layers with negative halogens among them [Long (2017)]. However, although VH can easily be created in layered structural bismuth oxyhalides, there are concerns about the stability of these compounds, especially in the aqueous phase, which greatly restricts their application in water purification.

A black defective $(\text{BiO})_2\text{CO}_3$ catalyst was synthesized by heat treatment of pure $(\text{BiO})_2\text{CO}_3$ in a vacuum [Dong (2015)]. The obtained samples consisted of the $(\text{BiO})_2\text{CO}_3$ phase, Bi element phase and Bi^{5+} , within the generation of oxygen defects. The black $(\text{BiO})_2\text{CO}_3$ is active in the dark for NO removal at room temperature. Under visible light irradiation, highly efficient activity for NO removal was achieved, which is attributed to the synergy of thermocatalysis and visible light photocatalysis.

3.2 Titanium dioxide

One of the most used photocatalyst for the removal of environmental pollutants is TiO_2 , due to its low cost, the inert nature and photostability [Gaya (2008)]. The photocatalytic activity of this inorganic semiconductor finds application in many different areas as the removal of organic pollutants in gaseous phase or water, as coating materials used in medical field, as antibacterial material or to inactivate tumoral cells. Many other applications are possible for TiO_2 also in alimentary, pharmacological and automotive industries. The overall photocatalytic activity of TiO_2 is determined by its crystalline structure, surface area, density of surface hydroxyl groups and adsorption/desorption characteristics.

An ideal photocatalyst should be characterized by the following attributes [Gaya (2008)]:

- ❖ Photo-stability
- ❖ Chemically and biologically inert nature
- ❖ Availability and low cost
- ❖ Good interaction with molecules to be degraded.

TiO_2 satisfies quite well the above mentioned requests [Gaya (2008)] and it is the most studied semiconductor in the field of chemical conversion and storage of solar energy thanks to its ability to combine the high refractive index with the high degree of transparency in the region of the visible spectrum. Anyway, its main drawback is the fact that its efficiency under visible irradiation is low

due to its large band gap; it can absorb only the UV radiation that is about the 5% of solar radiation and this limits its use on large scale.

Titanium dioxide belongs to the family of transition metal oxides and it occurs in nature as amorphous or well-known minerals rutile, brookite and anatase (Figure 3.3). The amorphous forms of titania is photocatalytically inactive.

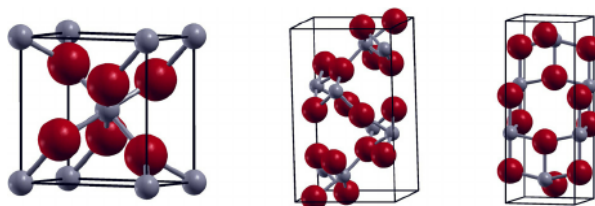


Figure 3. 3 The primitive cells of rutile, brookite and anatase (from left to right) [Tracy (2006)].

In all the three crystalline structures, the TiO_6 octahedra are the basic structural unit: each Ti^{4+} ion is surrounded by an octahedron of six O^{2-} ions. The difference among these forms are in number of shared octahedra, i.e. two for rutile, three for brookite and four for anatase. It is very difficult to obtain it in the pure form and it is less used for photocatalytic application respect to the other two forms. The rutile and anatase are the forms most widespread in nature and most commonly used. Usually, amorphous titania crystallizes into anatase around 400°C , which is further converted into rutile from 600 to 1100°C . The two crystal structures differ by the distortion of each octahedra and by the assembly pattern of the octahedral chain. The octahedron in rutile is not regular, showing a slight orthorhombic distortion. The octahedron in anatase is significantly distorted so that its symmetry is lower than orthorhombic. In rutile structure each octahedron is in contact with two sharing edge oxygen pairs and eight sharing corner oxygen atoms while in the anatase structure each octahedron is in contact with four sharing an edge and four sharing a corner [Tracy (2006)].

In general, anatase ($E_g = 3.2$ eV) gives better photocatalytic results than rutile ($E_g = 3.0$ eV). This is due to a more negative conduction band of anatase than that of rutile, which produces photo generated electrons with higher reduction potential [Tracy (2006)]. In addition, normally rutile is obtained by the calcination of amorphous titania at a higher temperature than that for anatase, increasing the possibility of particles agglomeration decreasing the surface area. Mixing anatase and rutile has shown to have synergistic effects for photocatalysis, which have been attributed to longer electron hole lifetimes [Hurum (2003)]. The most used form of titanium dioxide in photocatalytic studies is a mix of anatase and rutile, i.e. Degussa P25. This material possesses a high specific surface area (50

m^2g^{-1}), and it is formed by 80% of anatase and 20% of rutile. Electron microscopy showed P25 containing single particles of anatase or rutile, crystallites composed of anatase in close contact with rutile, as overlayers or as crystallites partly fused. This particular structure arises from the manufacturing procedure, i.e. Aerosil process. According to this, a titanium compound undergoes hydrolysis in the vapor phase at an elevated temperature. Under such conditions, the particle growth occurs on the external surface, resulting in the formation of an anatase core surrounded by the most thermodynamically stable phase (i.e. rutile).

The first hypothesis explaining the higher activity for mixed phase particles concerns the transfer of an electron from anatase to rutile reducing the recombination rate (Figure 3.4a), leading to more efficient electron-hole separation [Hurum (2003)]. This explanation is not satisfactory if we consider the electronic structure of anatase and rutile, respectively. The anatase trapping site has been shown to be 0.8 eV lower in energy than the anatase conduction band, and it is below the rutile one. In the work of [Hurum (2003)] a new model is proposed (Figure 3.4b) in which rutile acts as antenna and subsequent charge separator. Rutile can absorb a higher amount of solar radiation due to its lower band gap, so, mixed with anatase, it acts as an antenna increasing the spectral range of activity of the total catalyst. Anyway, the conduction band of anatase is lower in energy respect to rutile, so electrons migrate to it lowering their recombination rate. For enhancing this type of mechanism, small size of the rutile particles in P25 and the intimate contact with anatase are crucial.

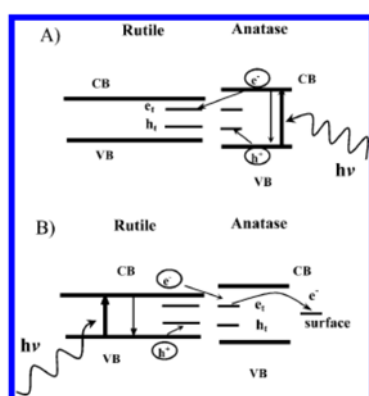


Figure 3. 4 (A) Previously speculated model of P25 activity where charge separation occurs on anatase and rutile acts as an electron sink. (B) Proposed model of a rutile antenna and subsequent charge separation. Reported from [Hurum (2003)].

Computational calculations [Scanlon (2013)] confirmed this model and showed that, despite having the same chemical composition, the differences in the coordination environments, and hence chemical bonding, of rutile- and anatase- structured TiO_2 result in very different ionization potentials and electron affinities. The valence band edge of both materials is dominated by O 2p, and the conduction band edge is formed by Ti 3d. According to electron paramagnetic resonance data, excess electrons are centered on the d states of cations, whereas holes are centred on 2p states of oxygen. Furthermore,

the model predicted a difference of 0.47 eV between rutile and anatase ionization potentials (7.83 and 8.30 eV respectively), with the rutile valence band higher in energy than anatase. The electron affinity of rutile is lower than anatase (4.80 and 5.10 eV respectively), indicating that the conduction band of anatase is lower in energy respect the one of rutile (Figure 3.5a). This means that photogenerated conduction electrons will flow from rutile to anatase. Due to the direct contact of the two phases in P25, band alignment occurs varying the energy difference between conduction bands to 0.4 eV (Figure 3.5b). In this way, the band gap of mixed materials is lowered and efficient electron-hole separation is achieved. This is responsible of the increased photoactivity of anatase-rutile composite materials over their individual counterparts.

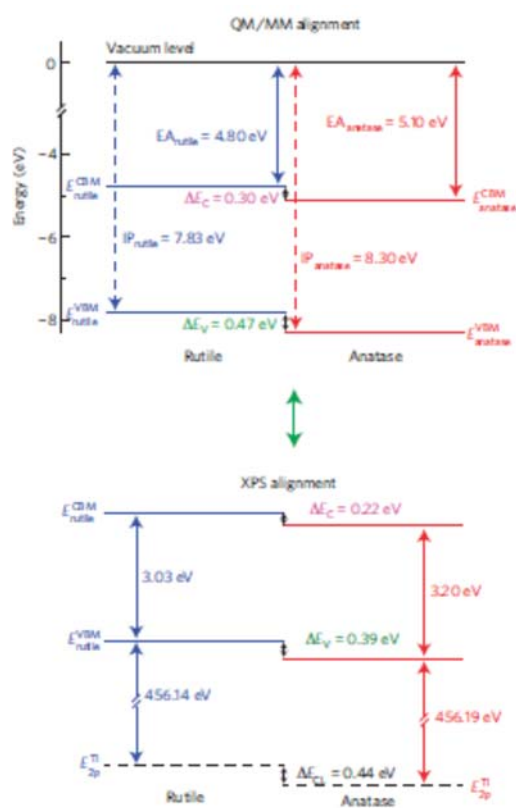


Figure 3. 5 (a) Calculate electronic affinities and ionization potentials for rutile and anatase. (b) Band alignment between rutile and anatase. Reported from [Scanlon (2013)].

3.2.1 Enhancement of TiO₂ photocatalytic activity

The photoactivity of nano-TiO₂ can be improved by optimizing particle size and shape, by reducing e⁻/h⁺ recombination by different methods and by surface treatment to enhance contaminant adsorption. The final aim is to avoid the recombination of holes with electrons and enlarge the light

absorption of TiO₂ in the visible region. In the introduction, the effect of reducing catalyst dimension to nanoscale on the photocatalytic activity has been discussed.

The high efficiency of titania is limited to the absorption of light in the UV region based on its wide band gap. Solar light consists of around 5% of UV light and 45% of visible light, this means that TiO₂ is inefficient when sunlight is used as light source to drive the photocatalytic reactions. For a potential real application of titanium dioxide photocatalytic activity on industrial scale, TiO₂ has to be active under visible light irradiation. For this purpose, it has been modified by various strategies such as the formation of heterojunctions, doping or dye sensitization.

When p-type and n-type semiconductors are brought into close contact, an internal electric field forms at the interface. The photoinduced electrons migrate from the CB of the semiconductor with the more negative value to the CB of the other semiconductor, and the holes migrate from the VB of the semiconductor with the more positive edge to the VB of the other semiconductor. As a result, the photoinduced electrons and holes are effectively separated, thus enhancing the photocatalytic activity of photocatalysts [He (2014)]. An example of p-n junction for titanium dioxide is its composite with GO.

Extensive research on metal ion doping method for enhancement of TiO₂ photocatalytic activities has been carried out especially for water/air cleaning applications [Reddy (2016)]. The incorporation of transition metals (e.g., Cu, Co, Ni, Cr, Mn, Fe, Ru) in the titania crystal lattice may result in new energy level produced in the band gap of TiO₂, near the conduction band. Deposition of noble metals like Ag, Au, Pt and Pd on the surface of TiO₂ is a way to enhance its photocatalytic efficiency under visible light by delaying electrons and holes recombination. This is due to the fact that the Fermi levels of these noble metals are lower than that of TiO₂: photo-excited electrons can be transferred from CB to metal particles deposited on the surface of TiO₂, while photo-generated VB holes remain on the TiO₂. On the other hand, some noble metal nanoparticles (NPs) such as Ag and Au, exhibit strong UV-vis absorption due to their plasmon resonance, produced by the collective oscillations of surface electrons [Reddy (2016)]. For example, under visible irradiation, gold nanoparticles can absorb light and transfers photogenerated electrons to the conduction band of TiO₂. Actually, the industrial application of the metal doping methods is not convenient due to the high costs and the fact that the enhancement of photocatalytic activity depends on the nature and the amount of doping agent. Possible limitations are photocorrosion and promoted charge recombination at metal sites.

Non-metal doping with N, C, F and S has shown great promise in achieving visible light active photocatalyst [Reddy (2016)]. The non-metal doping results in the introduction of energy levels higher in energy respect to the valence band of TiO₂ and consequently absorption of visible photons. In addition, the presence of trap sites within the TiO₂ bands reduces the photogenerated carriers

recombination. The main disadvantages of this method concern short-term stability; high cost for their preparation and low efficiency due to the possible formation of oxygen vacancies in the bulk, acting as recombination centers. Many results, up to now, describe nitrogen doping as substitutional element on the oxygen lattice sites or at interstitial lattice sites. Nitrogen can be easily introduced in the TiO₂ structure, due to its comparable atomic size with oxygen, small ionization energy and high stability. For the efficient incorporation of nitrogen into TiO₂ either in the bulk or as a surface dopant, both dry and wet preparation methods have been adopted, including sol-gel, sputtering, ion implantation, and plasma-enhanced chemical vapor deposition method [Reddy (2016)].

Fluorine doping promotes charge separation, not shifting the TiO₂ band gap, but improving the surface acidity and reduction to Ti³⁺ ions [Reddy (2016)].

Carbon, phosphorous and sulphur as dopants have also shown positive results for visible light activity in TiO₂ [Reddy (2016)]. Sulfur is easier to be inserted into the Titania lattice than nitrogen, due to its larger ionic radius. The formation of Ti-based composite with carbon nanostructures is a way to increase the photocatalytic activity of Titania; this is explained reporting some examples in previous chapter.

Dye-sensitization consists in the coupling of TiO₂ photocatalysts with dye molecules (as erythrosine B, porphyrins, thionine and phtalocyanine) able to absorb visible light [Reddy (2016)]. The dye absorbs visible photons causing the excitation of an electron from the highest occupied molecular orbital (HOMO) to the lowest unoccupied molecular orbital (LUMO). The excited dye molecule subsequently transfers electrons into the conduction band of TiO₂, while the dye itself is converted to its cationic radical. Advantages of the dye-sensitized reactions are the fast injection of electrons to the semiconductor and slow backward reaction. The main disadvantage is dye degradation occurring during the process that can decrease the photocatalytic activity.

The introduction of defects for increasing Titania photocatalytic activity in the visible region is explained in the previous paragraph.

3.2.2 TiO₂ photocatalytic application

The photocatalytic mechanism can be successful applied in the air purification [Mamaghani (2017)]. Indoor air quality (IAQ) has a significant impact on human health, comfort and productivity. VOCs, nitrogen oxides (NO_x), carbon monoxide (CO), and particulate matter are among the main indoor air pollutants. TiO₂ is able to oxidize gaseous pollutants in quantum yields ranging from 1% to over unity: in presence of O₂ and UV illumination, gaseous organic substrates can be completely degraded

into CO₂, H₂O, and mineral acids on a TiO₂ thin film. The removal rate is influenced by numerous parameters as explained in the first Chapter.

Over the past few decades, the visible light activated photocatalytic disinfection of water has received significant attention, with research focus moving from laboratory studies to potential applications [Zhang (2013)]. A visible light-activated palladium-modified nitrogen-doped titanium oxide (TiON/PdO) photocatalyst has been demonstrated to have good visible light adsorption and a superior efficient photocatalytic disinfection effect on *Fungi*.

Titania has also been used for water purification [Fujishima (2008)]. Decontamination of industrial, agricultural, and municipal wastewater by Titania under solar irradiation has been studied at the pilot-plant scale, using compound parabolic collector (CPC) reactors and TiO₂ slurry photocatalysts. They observed the complete mineralization of organic matter at concentrations of ca. 50 mg L⁻¹ within hours under sunlight. Since the first report [Fujishima (1972)], Titania has also been studied for photocatalytic water splitting application.

3.2.3 Visible laser irradiation of titania colloids

The photocatalytic activity of titania colloids and laser modified ones was investigated for hydrogen production by water splitting. In the first chapter, the fundamental aspects of photocatalysis and photocatalytic water splitting are reported. The use of “in liquid” laser irradiation technique is here proposed for generating defects within titania colloids and improving their photocatalytic activity.

25 mg of anatase, rutile (both from Sigma Aldrich) or P25 (from Areoxide by Acros) nanopowders, with nominal particle size well below 100 nm, were dispersed in 40 mL of water by sonication for 5 minutes and these were continuously stirred during the irradiation process. For such a process, titania colloids were irradiated by the second harmonic (532 nm) radiation of a Nd:YAG pulsed laser system (Continuum, Surelite II model) operating with a pulse duration of 5 ns and a repetition rate of 10 Hz. The laser beam size was around 28 mm², and it was directed toward the titania solution without any focusing lens. The samples were irradiated for 30 min at a constant laser power increased up to 1.45 Watt (0.5 J/cm²), far below the ablation threshold (around 0.8 J/cm²); in fact, no plasma emission has been detected during the irradiation. In the first minutes of the irradiation process, the initially white samples turn toward blue.

It was observed that the effects of laser irradiation on samples morphology is independent on initial crystalline phase; so, for a clearer discussion, the morphological characterization is discussed

hereafter only for one of the investigated sample. Figure 3.6 reports SEM images of the sample before and after the irradiation process, acquired according to Appendix A4. Commercial samples exhibit sizes below 50 nm and a random polyhedral shape. The morphology is quite different after the irradiation process: sub-micrometric, perfectly spherical particles are formed with a concentration linearly depending on the irradiation fluence or the irradiation time. Under laser irradiation, aggregated particles melt and rapidly cool down generating bigger particles within a spherical shape to reduce the surface tension.

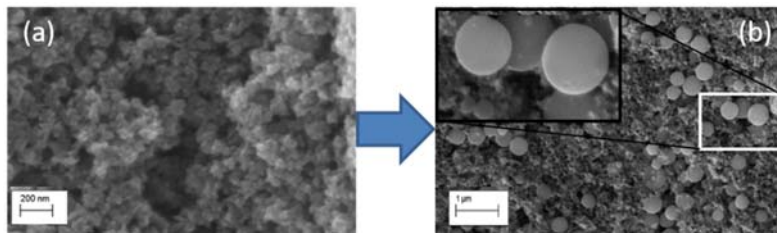


Figure 3. 6 Typical SEM images for some titania nanoparticles before (a) and after (b) the irradiation (here at 0.4 J/cm²) showing the changes in size and shape.

TEM images reported in Figure 3.7 also show the formation of sub-micrometer spherical particles, while the nanocrystals seem morphologically less regular with respect to the initial well-defined shape (see Appendix A12).

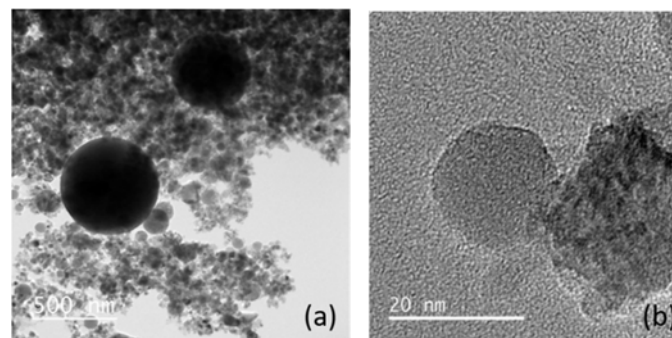


Figure 3. 7 TEM images of the irradiated samples at two different magnifications.

TEM images also suggest a moderate increase of porosity due to the high pressure conditions during laser irradiation [Li (2011)], as confirmed by BET analysis showing a porosity increase of 20% (Figure 3.8).

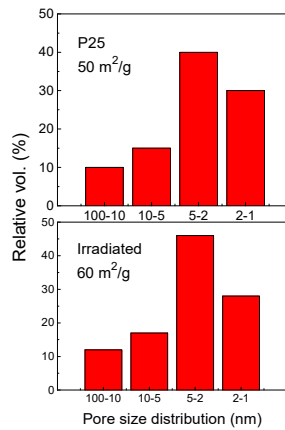


Figure 3. 8 Pore size distribution of P25 sample before (on the top) and after (in the bottom) the irradiation process (see Appendix A13). Reported from [Filice (2016)].

If the morphology changes induced by laser irradiation are independent on the initial crystalline phases, these are modified during the process differently for each sample as shown by Raman analysis (Figure 3.9). In particular, after laser irradiation, the anatase sample has been found in a mixed rutile/anatase phase derived from partially conversion of anatase into rutile. On the contrary, the rutile and P25 crystalline structure remained essentially unaltered. In the present study, four Raman-active modes of E_g (140 cm^{-1}), B_{1g} (395 cm^{-1}), A_{1g} (515 cm^{-1}) and E_g (635 cm^{-1}) are observed for anatase TiO_2 . Rutile also gives three signals: multi-photon (230 cm^{-1}), E_g (445 cm^{-1}) and A_{1g} (610 cm^{-1}). E_g , B_{1g} and A_{1g} are caused by symmetric stretching, bending and antisymmetric O-Ti-O motion respectively [Ohsaka (1978)]. These signals are in agreement with group theory and literature: the anatase structure belongs to the tetragonal space group of $I4(1)/amd$ and six Raman transitions ($1A_{1g}$, $2B_{1g}$ and $3E_g$) are allowed; the rutile structure is characterized by the tetragonal space group of $P4(2)/mnm$ and five Raman transitions (B_{1g} , multi-photon process, E_g , A_{1g} and B_{2g}) are allowed [Ohsaka (1978)]. After the laser irradiation process Raman peaks are shifted and broader as reported in Figure 3.9 and Table 3E [Filice (2016)]. This is ascribed to lattice distortions and the bonds length (r) can be calculated starting from the Raman frequencies (ν) according to the following law [Filice (2016)]:

$$\nu = 772e^{-1.55(r-1.81)}$$

The initial samples show characteristic bonds lengths as reported in literature; while irradiated samples show a shift of the Raman peaks correlated to a nanoparticles size change. In particular, the anatase peak at 140 cm^{-1} strongly depends on nanoparticles dimensions due to quantum confinement effects [Filice (2016)]. After laser irradiation, the observed spectra reveal a partial conversion of anatase into rutile as shown by the appearance of the peak at 445 cm^{-1} in the laser irradiated anatase

sample. It is possible to estimate the amount of anatase, by comparing the Raman signal at 140 cm^{-1} and 445 cm^{-1} , that are characteristic for anatase and rutile, respectively. The spectra reveal a conversion of 73% of anatase into rutile. This value was estimated by comparing the intensity ratio of 145 and 445 peaks with the ones reported in a calibration curve for known concentrated mixture of anatase and rutile.

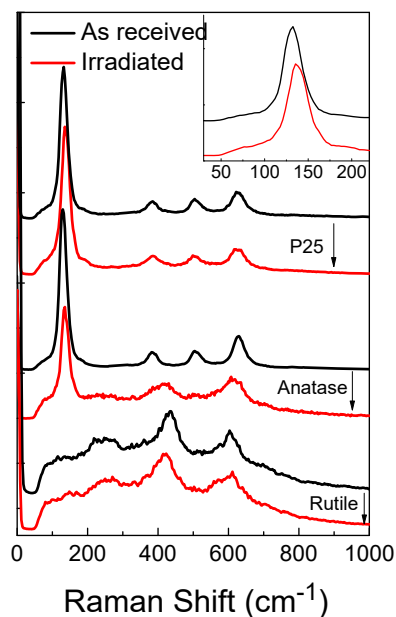


Figure 3. 9 Typical Raman spectra of as received and irradiated TiO_2 nanoparticles showing a definite change of the crystalline phase for the anatase particles. The inset shows a detailed Raman feature for P25. Reported from [Filice (2016)].

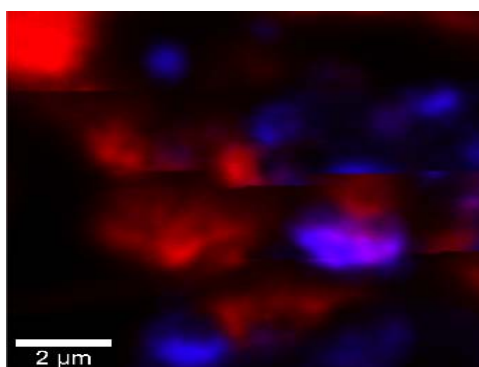


Figure 3. 10 Raman map of the anatase sample after the irradiation process reporting the signal at 140 cm^{-1} for anatase phase (blue) and the signal at 445 cm^{-1} for rutile phase (red). Reported from [Filice (2016)].

Table 3E Calculated bonds length. Reported from [Filice (2016)].

	COMMERCIAL SAMPLE			LASER IRRADIATED SAMPLES		
	Raman Shift [cm ⁻¹]	FWHM [cm ⁻¹]	Bond length [Å]	Raman Shift [cm ⁻¹]	FWHM [cm ⁻¹]	Bond length [Å]
RUTILE	435	56	2.136	423	60	2.154
	603	37.4	1.925	611	71	1.917
ANATASE	136.35	24.2	2.885	142	24.6	2.858
	390		2.206	422		2.162
	510.55		2.033	624		1.903
	634		1.893			
P25	139.5	25	2.870	142	28	2.859
	391.7	30	2.204	391.7	39	2.204
	511	30	3.460	511	33	3.460
	633	38	1.899	633	42	1.899

Figure 3.10 reports the Raman map of anatase sample after irradiation showing the anatase and rutile phases, respectively in blue and red. Temperature increases within laser irradiation, favouring the phase transition from anatase to the most thermodynamically stable rutile phase and, this explains while rutile sample remained unaltered. For what concerns P25, one could expect a phase transition to occur since P25 is formed mainly (80%) by anatase. Anyway, the Raman analysis denies this hypothesis (Figure 3.9). As explained in [Filice (2016)], the transformation of P25 into pure rutile under thermal treatments occurs at higher temperatures with respect to anatase. Previous studies show that anatase conversion to rutile occurs starting from the surface and if this is covered with other materials like for example small metals or rutile as in the case of P25 itself, the conversion occurs at higher temperatures.

As previously mentioned, the first observable effect of laser irradiation on titania samples is that the samples become blue suggesting the formation of Ti^{3+} vacancies. The chemical composition of titania samples before and after the laser irradiation processes are investigated by XPS (Figure 3.11), according to Appendix A3. The observed effects are similar for all the samples and only the XPS spectra of P25 are shown for a clearly discussion. In Ti 2p spectra, peaks at 458.4 and 464.1 eV are assignable to $2p_{3/2}$ and $2p_{1/2}$ of Ti^{4+} [Chen (2015)]. After irradiation, these peaks are broader due to the partial reduction of Ti^{4+} to Ti^{3+} . In fact, deconvoluted XPS spectra show the three main contributions centered at around 455, 458 and 457 eV and related to Ti^{2+} , Ti^{3+} and Ti^{4+} , respectively [Chen (2015)]. Their calculated percentages are reported in Table 3F: the ratio of $\text{Ti}^{3+}/\text{Ti}^{4+}$ is the same for the commercial products and it slightly increases after the irradiation process.

Figure 3.11 b reports the O1s XPS spectra for initial and modified sample. XPS peak at 529.5 eV is related to Ti-O bonds present and the tail at higher binding energies (531,9 eV) indicates the presence of surface hydroxyl group [Chen (2015)]. This is in agreement with the blue coloration of irradiated samples and the formation of oxygen vacancies. It is important to underline that the hydroxyl surface groups are not absorbed on TiO_2 (in this case these would be easily removed under the ultrahigh vacuum condition of the XPS system), but these are strongly bound to surface and are produced by the irradiation process.

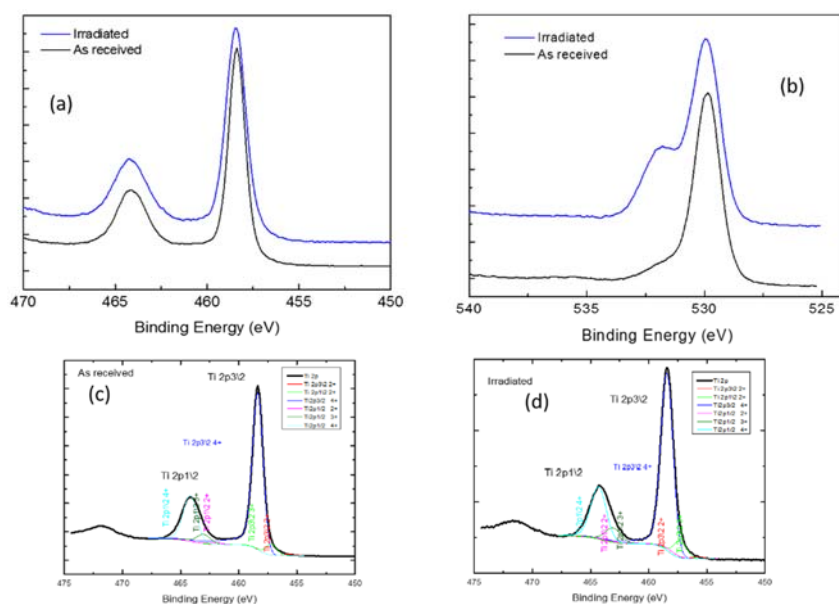


Figure 3. 11 Typical Ti2p (a) and O1s (b) XPS signals for as received and irradiated samples. Deconvoluted XPS Ti $2p_{3/2}$ peak for a typical samle before (a) and after (b) the laser process are also shown. Reported from [Filice (2016)].

Table 3F The percentages and binding energy of different oxidation states of titanium. Reported from [Filice (2016)].

	RUTILE		IRRADIATED RUTILE		ANATASE		IRRADIATED ANATASE		P25		IRRADIATED P25	
	% Ti	Peak BE (eV)	% Ti	Peak BE (eV)	% Ti	Peak BE (eV)	% Ti	Peak BE (eV)	% Ti	Peak BE (eV)	% Ti	Peak BE (eV)
Ti²⁺	0,88	455,7	0,9	455,7	0,85	455,7	0,54	455,7	0,99	455,7	1,3	455,7
Ti³⁺	6,5	457,19	8,78	457,3	6,32	457,3	6,38	457,16	6,34	457,2	8,62	457,08
Ti⁴⁺	92,61	458,37	90,32	458,44	92,83	458,55	93,08	458,6	92,66	458,47	90,08	458,28

The effects of the introduction of defects is that of increasing the photocatalytic activity of titania samples, in particular under visible light irradiation. Qualitatively, the energy gap calculated by UV–vis reflectance spectra of initial and modified samples using the Tauc plot suggests a higher photocatalytic activity of irradiated samples under visible light. In fact, the calculated bandgap decreases of about 0.2 eV after irradiation (Figure 3.12 reports these spectra for one of the samples). The spectra were acquired according to Appendix A14.

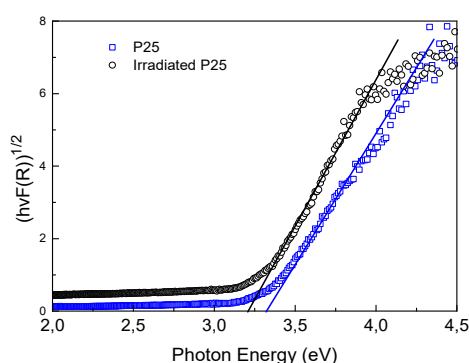


Figure 3. 12 Tauc plot for commercial and laser irradiated P25 samples. Reported from [Filice (2016)].

All the modifications induced by laser irradiation result in an enhanced photocatalytic activity for the production of hydrogen by water splitting (see Appendix A15), in particular under UV irradiation at 365 nm. Figure 3.13 reports the curve of produced hydrogen versus irradiation time for initial P25

and modified one. The same curves are obtained for rutile and anatase samples, what is different among the three materials is the final amount of produced hydrogen reported in Figure 3.14.

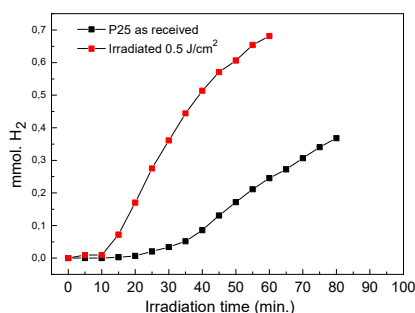


Figure 3. 13 Evolution of hydrogen versus irradiation time under UV irradiation for modified and as received samples. Reported from [Filice (2016)].

All the curves present three main steps: for the first 10 minutes the production is zero and this is ascribed to an initial induction period; then hydrogen evolution starts to linearly increment until a maximum and finally a moderate decrease of the production rate after about one hour of irradiation is observed. The first step is certainly due to the stabilization of lamp radiation and the saturation of water with evolved gases. The final plateau i.e. the stop of hydrogen production is consistent with two fundamental effects [Ni (2007)]: the recombination of photo-generated electron/hole pairs and the fast backward reaction of hydrogen and oxygen into water.

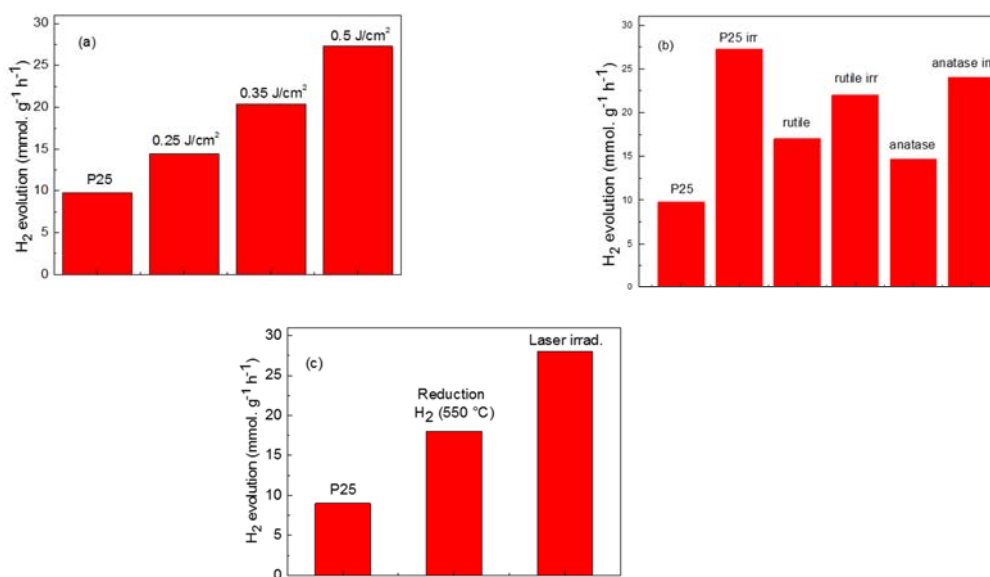


Figure 3. 14 Total amount of produced hydrogen for P25 (a) with increasing laser fluences and for all colloids before and after laser irradiation (b). A comparison for the P25 sample modified by the laser and by an heating treatment in hydrogen atmosphere (c). Reported from [Filice (2016)].

In Figure 3.14 a, it is evident that laser irradiation has the effect of increasing the total amount of produced hydrogen and this linearly depends on laser fluence. In general, laser irradiation has a positive effect on the photocatalytic performance of all titania samples which we correlate to higher concentration of defects and morphology modifications. On the other hand, it is possible to exclude a contribution of crystalline phase changes with the increased activity since P25, which does not exhibit any relevant change in the crystalline phase, shows the best performance. Figure 3.14b also evidences a higher rutile activity with respect to anatase as known from theoretical study [Zhao (2014)], but this activity is inverted after irradiation process. In addition, the hydrogen production yield for irradiated P25 nanoparticles is compared with that obtained after a standard reduction procedure at 500°C for 1h in hydrogen atmosphere (Figure 3.14c). The best performance is recorded for laser modified sample. These results confirm laser irradiation as a simpler, green, tunable technique for titania reduction with respect to conventional methods.

The P25 sample has been tested for consecutive repeated runs showing a moderate decrease of the maximum rate efficiency and a good data reproducibility. The maximum rate has been always found after 20 minutes of irradiation (Figure 3.15).

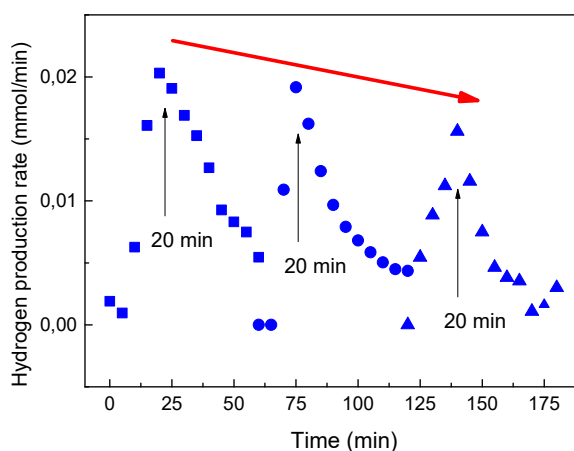


Figure 3. 15 Hydrogen production rate of laser modified P25 sample for three consecutive processes. Reported from [Filice (2016)].

The laser modified samples were also tested for hydrogen production under visible light irradiation (the emission spectrum of the lamp is reported in Appendix C): an enhancement of the hydrogen production for laser modified samples is obtained also in this case. Figure 3.16 reports the result for P25 as an example. In this case, the H₂ production rate has a more pronounced decrease with time respect to the sample under UV irradiation. This effect is due to a quicker recombination of photo-

generated electron/hole pairs. Furthermore, the total amount of produced hydrogen under visible light is considerably lower than that found with UV irradiation. This is in agreement with measured energy gap: after laser irradiation this value decrease but it is still high for the application of this materials in solar driven photocatalytic process. For all these reasons further investigations on the laser irradiation process for enhancing titania photocatalytic activity under visible light are necessary. Preliminary results are reported in the following paragraph.

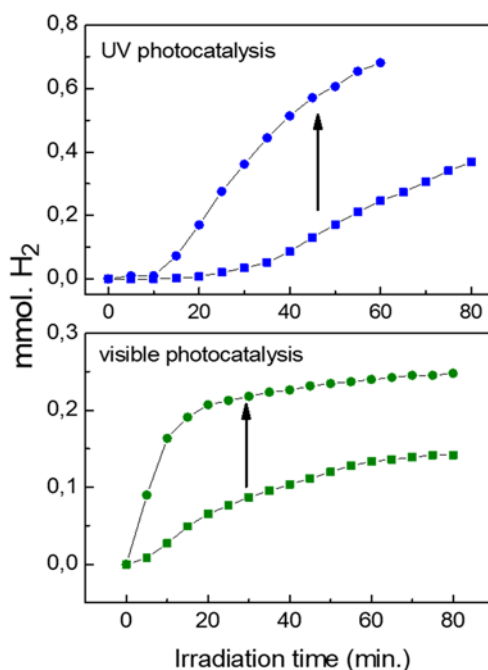


Figure 3. 16 Comparison of hydrogen production for initial and laser modified P25 samples versus irradiation time in a UV (top) or Visible (bottom) photocatalytic experiment, respectively. Reported from [Filice (2016)].

3.2.4 UV laser irradiation of titania colloids

The final aim of this activity is that of producing solar driven photocatalytic materials, so, starting from above results, modified anatase samples have been prepared by changing the laser wavelength and fluence as well as the liquid environment in which the irradiation is conducted. This is a preliminary study whose results are reported below.

In a typical experiment, anatase titania nanoparticles (25 nm by Sigma Aldrich) were added to 10 mL of distilled water or ethanol irradiated under continuous stirring after 5 minutes sonication. In this case, the samples were irradiated by the third harmonic (355 nm) radiation of a Nd:YAG pulsed laser

system operating with a pulse duration of 5 ns and a repetition rate of 10 Hz. Also in these experiments, the laser beam size was around 28 mm², and it was directed toward the titania solution without any focusing lens. Different concentrated anatase suspensions were irradiated homogeneously at a constant laser power increasing up to 700mW (250mJ/cm²) for 15 min. No plasma emission has been detected during the irradiation. The most homogeneous samples, in terms of particles size distribution, were obtained by laser irradiation of 3 mg of titania nanoparticles into 10 mL of solvent for 15 minutes at a constant fluence of 140 mJ/cm².

Figure 3.17 reports the typical morphologies of the irradiated nanoparticles obtained by SEM microscopy (see Appendix A4). After the irradiation process, both the samples show the formation of sub-micrometric, perfectly spherical particles with dimension below 200 nm. Anyway, brighter particles, having sizes below 25 nm and a random polyhedral shape are present in anatase modified in water: these particles are unmodified anatase suggesting that the conversion of this sample is not complete in water.

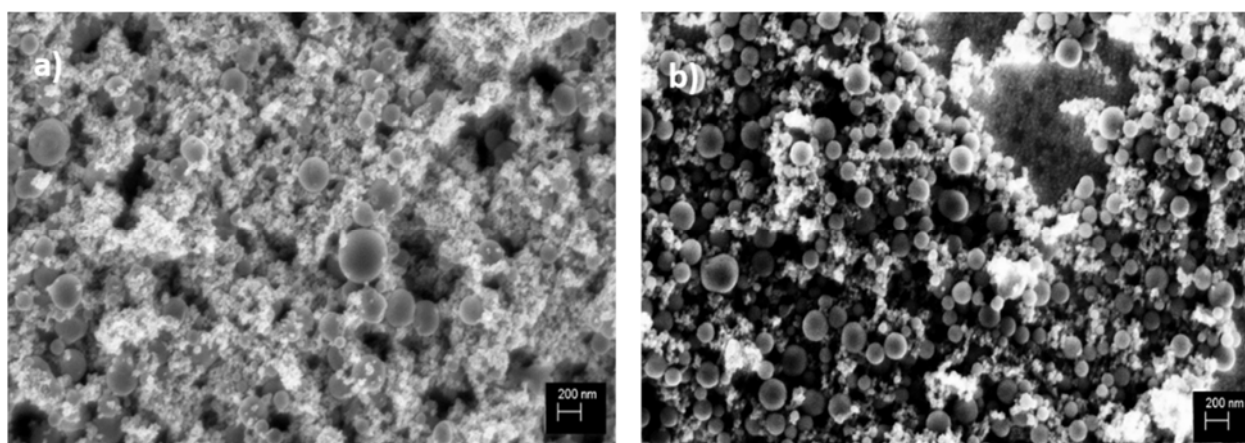


Figure 3. 17 SEM images of laser irradiated titania nanoparticles dispersed in water (a) or (b) ethanol.

The formation of these sub-micrometer spherical particles is described in the previous paragraph. According to this, the fluence of 140 mJ/cm² is capable of melting the original titania particles that, finally, solidify into much bigger particles of 200 nm without vaporization. In addition, a moderate increase of porosity confirmed by BET surface area measurements was recorded (see Appendix A13): the commercial anatase has a surface area of 55 m²/g and this value is increased up to 61 m²/g and 76 m²/g, respectively for laser modified sample in water and ethanol. On the contrary, with respect to the experiments described in the previous paragraph, this UV laser irradiation process did not affect the crystal phase of anatase samples, as confirmed by Raman spectra (not shown here). Maybe this is

ascribed to a different values of laser fluence, i.e. 140 and 250 mJ/cm² for UV and Visible laser irradiation, respectively.

Figure 3.18 shows the hydrogen production versus irradiation time for the investigated anatase samples under UV and Solar light lamps. Laser modified samples show a higher activity compared to commercial TiO₂ anatase, with the sample irradiated in ethanol providing the best performance: under UV irradiation this sample exhibits a two times higher hydrogen production compared to commercial anatase. A further increase of hydrogen production was obtained using ethanol as sacrificial agent. As described in Chapter 1, ethanol is a holes scavenger that reduces electrons-holes recombination reaction. A more interesting result is obtained for hydrogen production under solar light irradiation: laser modified samples displayed 6 and 3 times higher activity, respectively for sample modified in ethanol and water. This result points out the effectiveness of the laser modification strategy to obtain an efficient visible light photocatalyst. The better performance shown by anatase modified in ethanol can be ascribed to the better morphology homogeneity compared to the sample laser irradiated in water.

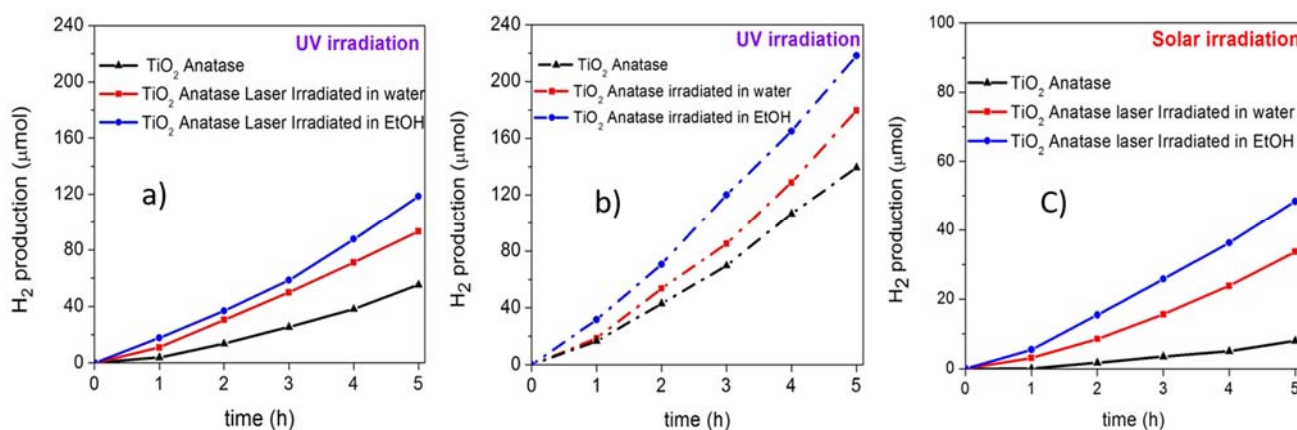


Figure 3. 18 Micromoles of H₂ produced versus irradiation time for the initial samples and the laser modified samples under UV irradiation (a); in presence or absence of ethanol as holes scavenger (b); under solar irradiation in a water-ethanol reaction mixture (c).

In addition, these results suggest that laser irradiation affects the electronic structure of anatase and the effects are different according to the solvent used during the laser irradiation process. Further investigation on the electronic structure of laser modified samples will clarify this aspect.

3.3 Bismuth oxide and Bi-based materials

Bismuth oxide-based materials have attracted considerable attention as photocatalysts, owing to their narrow band gap and high activity in the visible light range, as well as the relative abundance of

elemental bismuth [He (2014)]. For this reason, Bi-based compounds and composites have attracted much research interest in terms of their synthesis and characterization. The band gap, conduction band (CB) and valence band (VB) energies of typical Bi-based semiconductors range from 1.3 to 3.6 eV and these are reported in [He (2014)]. These semiconductors are promising visible light photocatalysts; while the valence band of titania is composed only by O 2p orbitals, the valence band of bismuth-based materials consists of hybrid orbitals of O 2p and Bi 6s; the last one increases mobility of photogenerated charge carriers and decreases the bandgap at values lower than 3.0 eV [He (2014)].

Bi sulfide Bi_2S_3 has a narrow band gap of 1.3–1.7 eV, it usually exists in an orthorhombic phase and have a layered structure. According to the preparation methods, it can assume different morphologies, i.e. nanoplates, nanorods, and nanowires, and different band gaps [He (2014)].

Bi-based multi-component oxides i.e. $\text{Bi}_4\text{Ti}_3\text{O}_{12}$, Bi_2WO_6 , BiVO_4 , and Bi_2MoO_6 etc., are hybrid oxides composed of Bi_2O_3 and metal oxides such as TiO_2 , W_2O_3 , V_2O_5 , and Mo_2O_3 etc. These have a layered Aurivillius structure, i.e. $[\text{Bi}_2\text{O}_2]^{2+}$ layers intergrown with metal oxide layers along the c axis [He (2014)].

For example, Bi titanates have a narrower band gap of 2.5–2.8 eV, and can thus be easily excited by visible light for higher photocatalytic activity [He (2014)]. This arises from the fact that the VB of Bi titanates consists of a $6s^2$ filled orbital and an O 2p orbital, and the CB consists of a Ti 3d empty orbital.

Bi oxyhalides including BiOF, BiOCl, BiOBr, and BiOI have anisotropic layered structures with $[\text{Bi}_2\text{O}_2]^{2+}$ layers intercalated by X^- ions ($X = \text{F}, \text{Cl}, \text{Br}, \text{I}$). Between these two portions, an internal electric field is formed and this can promote the separation of photoinduced electrons and holes and thus enhance their photocatalytic activity [He (2014)].

Bi_2O_3 is a common oxide semiconductor widely used in the fields of chemical engineering and electronics. Bi_2O_3 has several crystal structures including α - Bi_2O_3 (monoclinic), β - Bi_2O_3 (tetragonal), γ - Bi_2O_3 (body-centered cubic), δ - Bi_2O_3 (cubic) and ω - Bi_2O_3 (triclinic), with an indirect band gap ranging from 2.6 to 2.9 eV, depending on different crystal structures [Azhar (2017)]. The crystal structure of α - Bi_2O_3 and β - Bi_2O_3 structures are reported in Figure 3.19. The α phase is stable at relatively low temperatures, δ phase is only stable at temperature between 729 °C and 825 °C and a large hysteresis has been observed on cooling from a high temperature to room temperatures, with the possible occurrences of two intermediate metastable phases with β or γ phase.

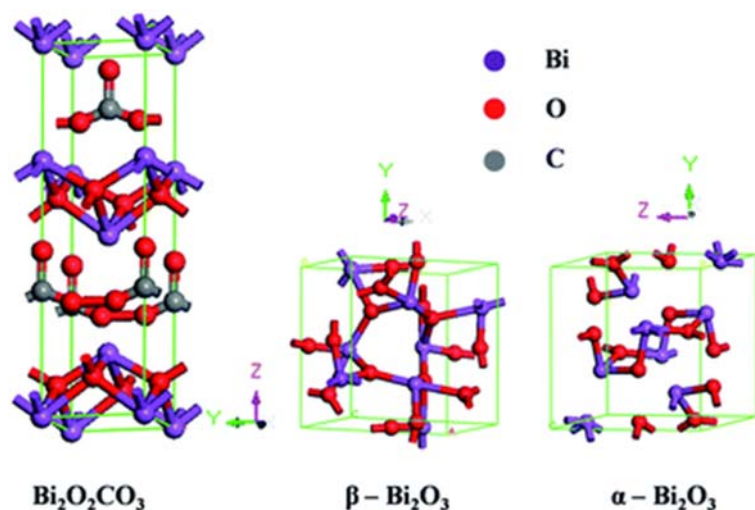


Figure 3. 19 Schematic crystal structures of $\text{Bi}_2\text{O}_2\text{CO}_3$, $\alpha\text{-Bi}_2\text{O}_3$ and $\beta\text{-Bi}_2\text{O}_3$. Reported from [Jiang (2015)]-

$\text{Bi}_2\text{O}_2\text{CO}_3$ has a Sillen layered structure consisting of $[\text{Bi}_2\text{O}_2]^{2+}$ layers intercalated by CO_3^{2-} groups where the large Bi^{3+} cation with 8-coordinate shows stereo active lone pair behaviour that may result in a Bi-O polyhedron with a large distortion [Jiang (2015)], as shown in Figure 3.19. $\text{Bi}_2\text{O}_2\text{CO}_3$ is widely used as an industrial additive, and is a raw material used in stomach medicine. Recent studies indicate that it has also a promising photocatalytic activity [He (2014)]. The band gap of $\text{Bi}_2\text{O}_2\text{CO}_3$ is dependent on the preparation method, the structure, and the morphology. Enhanced photocatalytic activity was observed for $\text{Bi}_2\text{O}_2\text{CO}_3$ compared to P25. $\text{Bi}_2\text{O}_2\text{CO}_3$ hollow microspheres were obtained by a template-free hydrothermal method [Dong (2011)]. These showed an increased photocatalytic removal of indoor NO respect to P25, C-doped TiO_2 , and $\text{Bi}_2\text{O}_2\text{CO}_3$ particles.

3.3.1 Bi_2O_3 photocatalytic application

The photocatalytic properties of semiconductors are highly dependent on their morphologies and their sizes. Bi-based materials are generally classified as one dimensional (1D) materials (including nanowires, nanorods, nanotubes), two dimensional (2D) materials (including nanoplates, nanobelts, thin films), and three dimensional (3D) materials (including nanospheres, nanoflowers, hollow microspheres) [He (2014)].

Bismuth oxide has been used for photocatalytic degradation of water pollutants. The photocatalytic activity of bismuth oxide was reported by [Zhang (2006)] for Bi_2O_3 nanopowders prepared via a simple sonochemical route. This was able to degrade methyl orange by 86% within 100 min under visible light illumination ($\lambda > 400 \text{ nm}$). $\beta\text{-Bi}_2\text{O}_3$ was prepared directly under microwave irradiation, and it changed into $\alpha\text{-Bi}_2\text{O}_3$ when calcined at higher temperature. $\beta\text{-Bi}_2\text{O}_3$ showed higher

photocatalytic activity than α - Bi_2O_3 , which was due to its lower band gap energy and higher optic absorption in wider visible light region [Huang (2011)]. As for titania, several methods have been used to improve the photocatalytic activity of Bi_2O_3 .

Bi-photocatalyst have also been used for the removal of gaseous contaminants like NO [Dong, Li (2014)]. Bi deposited BiO_2CO_3 microspheres were fabricated via hydrothermal method by using thiourea for Bi^{3+} reduction to metallic Bi. The as prepared Bi/BOC samples showed outstanding visible light photocatalytic activity for NO photo-oxidation due to the cooperative contribution of surface plasmon resonance (SPR) effects, efficient separation of electron-hole pairs, and prolonged lifetime of charge carriers by Bi nanoparticles.

Bi/ Bi_2O_3 composite film, prepared by electrolysis treatment of Bi_2O_3 film, showed hydrogen evolution ability under visible light irradiation with an external bias voltage. Under light irradiation, the current density of Bi/ Bi_2O_3 electrode was in milliamperere range, much higher than that of Bi_2O_3 electrode [Li (2012)].

Bi-based co-catalysts have proven beneficial for TiO_2 -based photocatalytic pollutant degradation [Xu (2017)]. Bi_2O_3 -QDs decorated TiO_2 photocatalyst was prepared by impregnation and calcination method obtaining samples composed by Bi- Bi_2O_3 -anatase-rutile TiO_2 multi-junction. The corresponding H_2 production was 73 times higher than pure TiO_2 . Under light irradiation, Bi_2O_3 -QDs can easily be reduced to metallic Bi, and this is responsible of the enhanced H_2 -production activity helping the transfer and separation of photogenerated charge carriers of TiO_2 [Xu (2017)]. The addition of bismuth oxide to titania increased its activity in photocatalytic water splitting [Xu (2017)] due to the formation of a p-n junction. The CB and VB potentials of Bi_2O_3 are calculated to 0.10 and 2.38 eV (vs. NHE, pH = 7), respectively. This means that the photogenerated electrons will spontaneously transfer from the CB of TiO_2 (-0.6 eV, vs. NHE, pH = 7) to that of Bi_2O_3 .

Similar to Au and Ag, Bi has been found to exhibit plasmonic properties [Toudert (2012)]. Bi is an interesting element because of its rich electronic band structure. It is a semimetal that presents a particularly high mean free path (in the micrometer range at room temperature), a long de Broglie wavelength (about 50 nm) and a low effective mass. Electronic confinement effects have been observed in monocrystalline Bi thin films and Bi nanowires, resulting in a thickness- or diameter-controlled conductivity and allowing a semimetal-to-semiconductor transition at thicknesses or diameters of a few tens of nanometers [Toudert (2012)]. The strong SPR-mediated effect with semimetal Bi has been exploited in many applications, including sensors, fluorescence and surface enhanced spectroscopy [Toudert (2012)]. The Bi element has also been applied in photocatalysis based on its photosensitization or narrow energy band gap. Bi nanoparticles were prepared by a facile

chemical solution method and these showed SPR properties in the near ultra-violet and visible range. This property confers to the material an admirable and stable photocatalytic activity towards removal of NO under 280 nm light irradiation [Dong (2014)]. In addition, Bi/(BiO)₂CO₃, Bi/g-C₃N₄, Bi/TiO₂, and Bi/BiOCl have been developed and have exhibited upgraded photocatalytic performance due to the presence of metal Bi, which can promote charge separation.

3.3.2 Laser irradiation of β -Bi₂O₃ nanospheres in different liquid environments: reactivity and structural changes

For the first time, laser process in liquid is investigated for inducing tunable chemical or morphological modifications in bismuth oxide for improving its photocatalytic performance.

3 mg of β -Bi₂O₃ nanoparticles (Sigma Aldrich, 90-210 nm particle size, 99.8% trace metals basis) were irradiated by the third harmonic of Nd:YAG laser (355 nm) in 10 ml of water (BOW) or ethanol (BOET). Before irradiation, the samples were stirred for 5 minutes at 5000 rpm and sonicated for 10 minutes. Each solution was irradiated under continuous stirring by the third harmonic of a Nd:YAG laser (355 nm) operating with a pulse duration of 5 ns and a repetition rate of 10 Hz for 15 minutes. The laser beam was homogeneously directed toward the solution without any focusing lens. The investigated fluence was of 140 mJ/cm² for BOW and at 35, 70 and 140 mJ/cm² for BOET (sample BOET35, BOET70 and BOET140). All the investigated fluences are below the ablation threshold. After the irradiation at highest fluence, the colour of both initial solutions changes from yellow (Figure 3.20 a,b) in a different way according to the solvent: BOW solution turned into white (Figure 3.20 c) while BOET into yellowish-grey with a black precipitate (Figure 3.20 d).

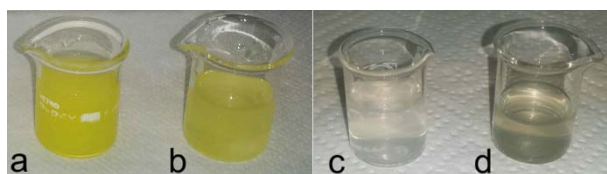


Figure 3. 20 BOW and BOET solutions before (a,b) and after (c,d) the UV pulsed laser irradiation for 15 minutes.

As just reported for titania samples, the first effect of laser irradiation on inorganic semiconductors is shown on their morphology. This effect depends on the dispersing medium and laser parameters as wavelength and fluence. Figure 3.21 reports the SEM images of initial bismuth oxide nanoparticles

and the same after the laser irradiation process in water and ethanol, respectively (see Appendix A4). The initial particles (BO) have spherical shape with diameter ranging from 50 nm to 250 nm and bigger objects with diameter above 500 nm (Figure 3.21 a). For BOW sample, after the UV laser irradiation in water, nanoparticles shape changes from spherical to irregular two-dimensional sheets (Figures 3.21 b) with lateral dimension ranging from hundreds of nanometers to a few microns. On the contrary, the same process on the BOET sample induces the formation of a more complex morphology constituted by a dense network of particles with size of few nanometers (these particles are evident in Figure 3.21 d as roughness on the surface of the larger ones) within localized regions with spherical nanoparticles of the same dimension or larger than commercial β - Bi_2O_3 . These larger nanoparticles are generated by the fusion of initial particles followed by solidification as an effect of laser irradiation process (this aspect is deeply described in previous paragraphs): during laser irradiation, nanoparticles acquire energy as heat that causes their melting or evaporation, depending on the amount (i.e. laser fluence) of transferred energy from the laser to the solution. The fluence of 140 mJ/cm^2 is thus enough to generate the melting and evaporation of initial particles as evidenced by the formation of bigger and smaller particles. The density of larger particles is much lower than the density of the smaller nanoparticles and these increase with increasing laser fluence. Different morphologies are shown by irradiated samples according to the solvent medium. The morphology exhibited by samples irradiated in ethanol is due to a melting process followed by solidification, within a reduction of bismuth oxide to elemental bismuth thanks to the reductant environment created by ethanol. In water, we observe the formation of planes since bismuth oxide can interact with the dissolved carbon dioxide and transform to bismuth subcarbonate ($\text{Bi}_2\text{O}_2\text{CO}_3$) [Huang (2011)]. Elemental Bi is absent, no smaller particles are observed, since water is not a reductant. These chemical evolutions of bismuth oxide are confirmed by further analysis, as reported below.

As for titania samples, the heat generated in the irradiated solutions could modify the crystalline phase of initial nanoparticles; this aspect was investigated by XRD analysis (see Appendix A16). The XRD peaks of BO (red curve), BOW (black curve) and BOET (blue curve) nanoparticles and, at the bottom, as a reference, XRD peak positions of β - Bi_2O_3 (orange bars, PDF#27-0050), $\text{Bi}_2\text{O}_2\text{CO}_3$ (cyan bars, PDF#41-1488) and rhombohedral Bi (green bars, PDF#44-1246) crystal phases are reported in Figure 3.22. No modification of crystalline phase was observed for the samples irradiated in ethanol, but the XRD peaks are broader suggesting a decrease of the mean nanoparticles size after laser irradiation. These dimensions were calculated by the Debye-Scherrer formula applied to the (201), (220) and (222) diffraction peaks at 27.95° , 32.69° and 46.22° of the β - Bi_2O_3 phase, respectively, and by considering the wavelength of the Cu $K\alpha$ radiation (0.1547 nm) and the shape factor equal to $0.89 \pm$

0.03 for spherical objects. The estimated size of $\beta\text{-Bi}_2\text{O}_3$ is of 39 ± 1 nm in BOET, while the initial BO nanoparticles have dimensions ranging between 90 and 210 nm. These results are in agreement with the SEM observations reported in Figure 3.21c.

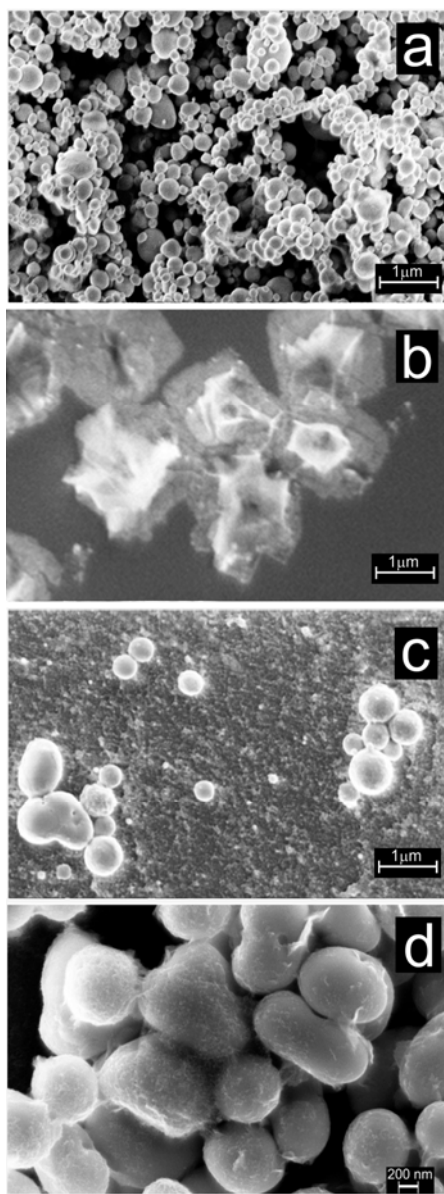


Figure 3. 21 SEM images of the as-received $\beta\text{-Bi}_2\text{O}_3$ nanoparticles (a) and the same after UV pulsed laser irradiation for 15 minutes in water (b) or in ethanol (c and d) solutions.

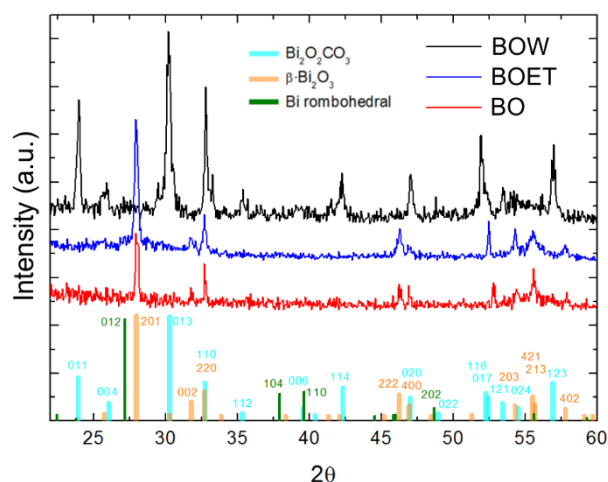


Figure 3. 22 XRD patterns of BO (red curve), BOW (black curve) and BOET (blue curve) nanoparticles. The reference XRD peaks of β -Bi₂O₃ (orange bars, PDF#27-0050), Bi₂O₂CO₃ (cyan bars, PDF#41-1488) and rhombohedral Bi (green bars, PDF#44-1246) crystal phases are reported at the bottom.

The XRD spectrum of BOW sample evidences the formation of the Bi₂O₂CO₃ phase, as suggested by the presence of the bi-dimensional particles observed after the process by SEM analysis (Figure 3.21b). According to [Huang (2011)], Bi₂O₃ nanoparticles interact with the CO₂ dissolved in the deionized water, producing a phase transition by the following reaction:



To confirm this hypothesis, we compare the as obtained subcarbonate particles with the ones obtained by heating aqueous bismuth oxide solutions at 80°C under stirring. The as formed nanoparticles have a more rectangular singular shape (Figure 3.23) with respect to the ones obtained by laser irradiation that have a petal-like shape above the center of each rectangular sheet (Figure 3.32 d) and require only 15 minutes of processing. The rose like morphology has also been observed for Bi-based materials obtained by process at higher pressure and temperature [He (2014)]; these conditions are reached during the laser irradiation process.

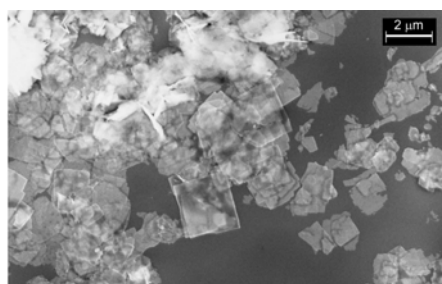


Figure 3. 23 Bi₂O₂CO₃ sheets formed by the phase transition of β -Bi₂O₃ nanoparticles dispersed in water at 80 °C for 2 hours under continuous stirring.

The chemical compositions of initial and laser modified samples are investigated by XPS analyses of BO, BOW and BOET nanoparticles reported in Figure 3.24 (see Appendix A3). For the unmodified sample, the characteristic Bi $4f_{7/2}$ and $4f_{5/2}$ peaks for the oxidized state Bi^{3+} are observed at binding energies of 159.2 and 164.4 eV, respectively [Barreca (2001)]. These peaks are shifted of 0.5 eV towards higher binding energy for BOW sample, this is due to the transformation of Bi_2O_3 into $\text{Bi}_2\text{O}_2\text{CO}_3$ after laser irradiation. For samples irradiated in ethanol, the presence of metallic Bi (Bi^{0+}) is evidenced by peaks at 157.8 and 163.3 eV. Metallic Bi amount is higher than over the Bi_2O_3 phase, since the calculated $\text{Bi}^{0+}/\text{Bi}^{3+}$ intensity ratio is 1.2 ± 0.1 .

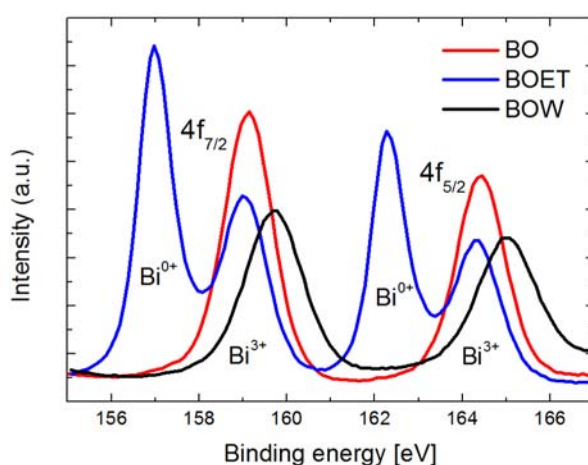


Figure 3. 24 XPS signals of Bi 4f of BO (red curve), BOW (black curve) and BOET (blue curve) nanoparticles.

The presence of metallic Bi was not observed in XRD analysis, therefore, the structure of the metallic bismuth created after irradiation in ethanol solution was identified by HR-TEM analyses (see Appendix A12). Figure 3.25 shows the bright-field TEM image of BO nanoparticles (Figure 3.25 a) and BOET nanoparticles (Figure 3.25 b,c).

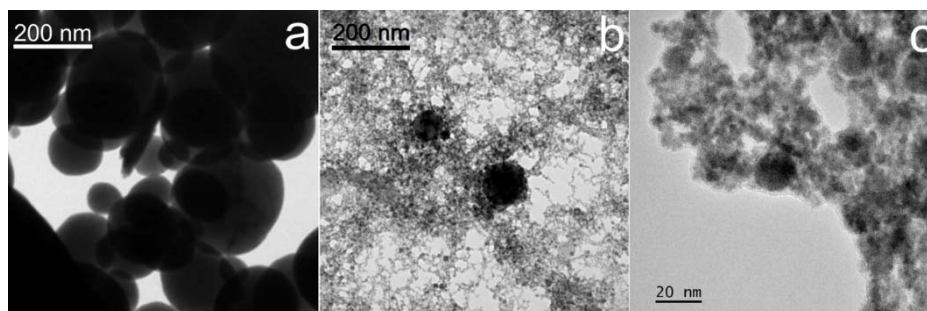
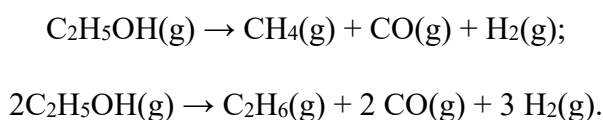


Figure 3. 25 Bright-field TEM images of BO nanoparticles (a) and BOET nanoparticles at two different magnifications (b,c).

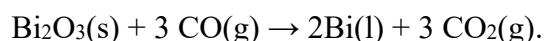
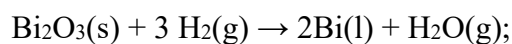
The commercial β -Bi₂O₃ particles have a spherical-like symmetry and show a faceted surface (Figure 3.25a) and size from a few tens to a few hundreds of nanometers. After the laser irradiation in ethanol, we can observe dark spherical object in Figure 3.25b that are β -Bi₂O₃ particles and the formation of smaller nanoparticles with size from a few to tens of nanometers, connected by a fine irregular particulate network, as shown in detail in Figure 3.25c.

The nanoparticles with dimension of about ten nanometers show a crystalline fluctuation with time under electron beam irradiation, as shown by TEM images of a 10 nm nanoparticles acquired at two different times (Figure 3.26a,b). During the first acquisition (Figure 3.26a), rhombohedral metallic Bi is observable by the (110) and (015) diffraction spots associated to the interplanar distances at 2.27 Å and 2.03 Å, respectively. During the second acquisition (Figure 3.26b), the diffraction spots associated to the interplanar distance of (012), (024) and (107) planes at 3.27 Å, 1.65 Å and 1.56 Å, respectively, of rhombohedral metallic Bi appear. The core of the nanoparticles shows interplanar distances of 2.37 Å, as highlighted in the rectangular box of Figure 3.26b. It is known [Wu (2016)] that metallic Bi nanoparticles with size between 4 and 15 nm undergo a crystalline / non-crystalline fluctuation, while the Bi nanoparticles show a non-crystalline structure below 4 nm and a crystalline one above 15 nm. Figure 3.26c shows the crystallization of another amorphous region of the BOET sample under the 200 keV electron beam. In fact, the diffraction spots obtained from this region and shown in Figure 3.26d are characteristic of rhombohedral metallic bismuth: these spots are associated to the interplanar distance of (012), (110) and (104) planes at 3.27 Å, 2.27 Å and 2.37 Å, respectively [Wu (2016)]. Figures 3.26e,f show the same region observed at the TEM within increasing time: the formation of crystal rhombohedral Bi is clearly observed and confirmed by diffraction patterns in the insets. This crystallization process is influenced by the dose of electron beam as supposed but not verified by [Wu (2016)]. The presence of metallic Bi evidenced by XPS analysis was in contrast with the results obtained by XRD analysis. This apparent contradiction is explained by HR-TEM analysis: these shows the presence of amorphous metallic Bi, confirming the XPS results and explaining the absence of this phase in XRD spectra as due to the amorphous nature of the synthesized Bi.

The reduction of Bi³⁺ can be ascribed to the reductant character of ethanol as reported in previous work [Korkmaz (2016)]. The following reactions occurs if the temperature is enough to decompose ethanol molecules:



The generated H₂ and CO can reduce bismuth oxide to bismuth producing water and CO₂:



Since the temperature reached during irradiation is enough to melt bismuth oxide leading the formation of bigger spheres ($T > 875^\circ\text{C}$), this means that it is also enough for ethanol decomposition ($T = 375^\circ\text{C}$) and we can assume the previous reactions as responsible for Bi_2O_3 reduction in ethanol.

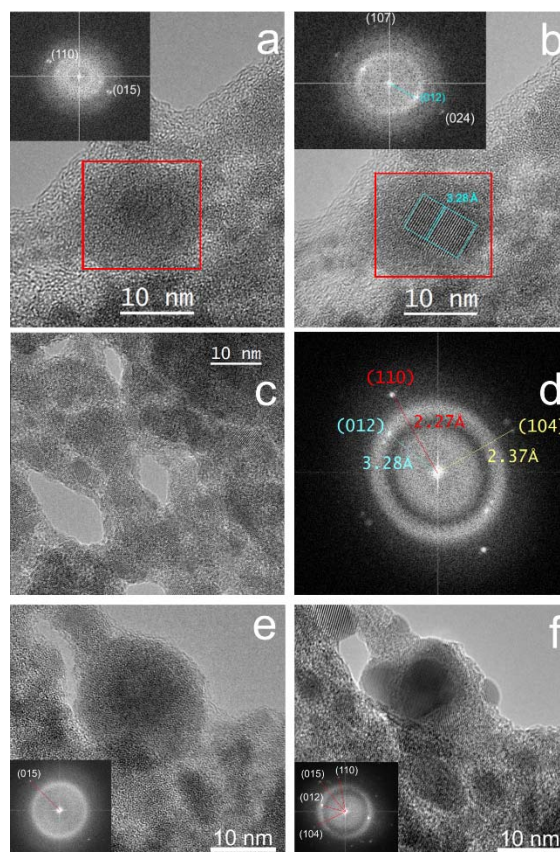


Figure 3. 26 HR-TEM images of BOET sample. The same zone acquired in different times (a) and (b) show the crystalline/non-crystalline fluctuation of a metallic Bi nanoparticle of 10 nm size. The figures in the insets are the corresponding FFT images. Another region after 1 minutes of 200 keV electron beam irradiation (c) and the corresponding FFT image (d) that shows diffraction spots of the (012), (104), (110) family planes of rhombohedral Bi with interplanar distance of 3.27, 2.37 and 2.27 Å, respectively. A further zone before (e) and after (f) electron beam irradiation for 2 minutes with the FFT in the inset.

Both the $\text{Bi}_2\text{O}_2\text{CO}_3$ and the mixed $\text{Bi}/\text{Bi}_2\text{O}_3$ phases are promising materials for application in photocatalytic processes for water splitting and dye degradation, in particular the presence of metallic Bi will increase the photocatalytic activity of Bi-based photocatalysts also in the visible wavelength range. For this final aim, the complete characterization of the optical properties of modified bismuth oxide is under investigation.

Chapter 4

POLYMERIC NANOCOMPOSITES FOR PHOTOCATALYTIC APPLICATIONS

4.1 Sulfonated polymers in water purification

As described in previous chapters, recently nanotechnology products as nanoparticles and/or nanofiltration have been shown to be the best solution for many of the issues involving water quality. The main disadvantage of using these materials as powders directly dispersed in water is given by the difficulties in their recovery at the end of the process without contaminations. In addition, it is not possible to wash and reuse them as powders. The combined use of membrane technology and nanomaterials is expected to overcome these problems. Sulfonated polymers have many properties that make them good candidate for the preparation of polymeric nanocomposites and their application in water purification. These properties will be described in the following paragraphs for two commercial sulfonated polymers and their use for dye removal will be reported.

4.1.1 Nafion

From its development by DuPont in the 1960s, Nafion (Figure 4.1) has found application in liquid and gas separations, fuel cells, and the chloralkali industries, due to its thermal and chemical resistance, ions exchange properties, selectivity, mechanical strength, and insolubility in water. Taking advantage of these properties, a new option of using Nafion composite membranes is shown in this thesis with the investigation of its photocatalytic properties under UV/visible light illumination.

Nafion is a perfluorosulfonate ionomer membrane consisting of a hydrophobic fluorinated long main chains and short side chains that terminate by a hydrophilic polar group SO_3H . These constituents are responsible for the morphological structure of the membranes.

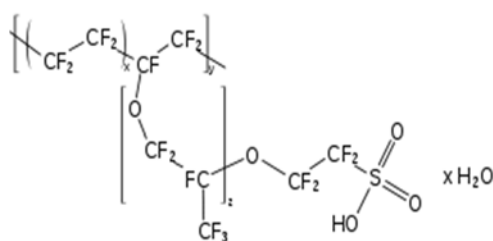


Figure 4. 1 Nafion structure

The synthesis of the monomers as well as that of the membranes involves dangerous reactions under conditions of high pressure and temperature [Doyle (2003)]. These materials are generated by copolymerization of tetrafluoroethylene (TFE) with a perfluorinated vinyl ether co-monomer with sulfonyl acid fluoride (Figure 4.2). The synthesis of this co-monomer (perfluoro sulfonyl fluoride ethyl propyl vinyl ether PSEPVE) involves numerous steps with low yields. These factors contribute to the cost of these materials. SO_3 reacts with tetrafluoroethylene (TFE) to form a cyclic sultone. A rearrangement of the cyclic compound yields the so-called rearranged sultone (RSU), which is reacted with hexafluoropropylene oxide (HFPO) to produce sulfonyl fluoride adducts. Heating these compounds in the presence of sodium carbonates yields the co-monomer PSEPVE. Hot aqueous NaOH converts these sulfonyl fluoride ($-\text{SO}_2\text{F}$) groups into sulfonate groups ($-\text{SO}_3^-\text{Na}^+$). This form of Nafion, referred to as the neutral or salt form, is finally converted to the acid form containing the sulfonic acid ($-\text{SO}_3\text{H}$) groups. Industrial production of Nafion membranes is costly due to several factors: firstly, the monomers used are expensive to manufacture, since the synthesis requires a large number of steps and the monomers are dangerous to handle. The precautions for safe handling are considerable and costly. Secondly, the PSEPVE monomer is not used for other applications, which limits the volume of production. The most significant cost driver is the scale of production. When compared to large-scale production of polymers like Nylon, the perfluorinated ionomer membrane is a specialty polymer produced in small volumes.

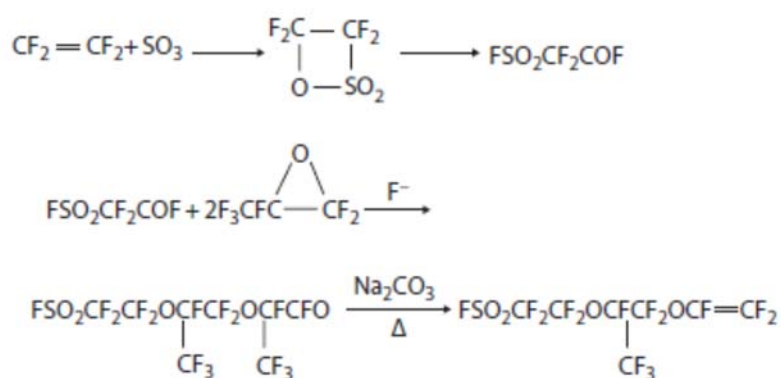


Figure 4. 2 Synthesis process for Nafion membrane co-monomer PSEPVE. Reproduced from [Doyle (2003)].

The combination of the stable Teflon backbone with the acidic sulfonic groups makes Nafion highly conductive to cations, making it suitable for many membrane applications; highly resistant to chemical attack and to temperature and highly mechanically stable.

The main characteristics for Nafion application on large scale industry are its strong acidity, with $pK_a \sim -6$, its selectively and highly permeability to water. Its proton conductivity is up to 0.2 S/cm depending on temperature and hydration state. For these characteristics, Nafion is the most used polymer as proton exchange membrane in fuel cell application [Enotiadis (2012)]. Two mechanisms are involved in Nafion proton conductivity: the vehicle mechanism according to which proton transfer by hydrogen bonds within water molecules, and the Grotthuss mechanism, or protons hopping through the acid groups. The vehicle mechanism occurs by the formation of an ion adduct composed of a proton and a diffusible carrier molecule (e.g., H_2O). The Grotthuss-type mechanism is the transport of protons from site to site without a carrier molecule, and its activation energy depends on the hydrogen bond breaking energy and the distance between sites. In most cases, these two proton-conducting mechanisms are not entirely separate from one another.

A controversial debate is still open on Nafion structure; its structure is made by an alternation of hydrophobic and hydrophilic domains and this is responsible of its mechanical stability conjugated with its high hydrophilicity and stability in water. Ionic clustering is present in Nafion, however, details on the arrangement of these clusters have not fully been realized. The hydrophobic region is composed of the polymer fluorocarbon backbone while the hydrophilic region contains the ionic groups and their counter ions.

The cluster-network model of Gierke is the “starting point” in the interpretation of Nafion structure [Mauritz (2004)]. According to small-angle X-ray scattering (SAXS) studies and several assumptions, it is possible to identify an inverted micellar structure (Figure 4.3a) with 40 Å -in-diameter clusters ending with sulfonilic groups. Proposed pores or channels that are 10 Å in size connect these micelles. These hydrophilic channels are responsible of the high proton conductivity of Nafion.

In the following years, further studies have been conducted on the Nafion structure. The Yeager Three Phase Model is based on a three-phase clustered system with interconnecting channels within the polymer (Figure 4.3b) [Mauritz (2004)]. The three regions consist of (A) a fluorocarbon backbone, some of which is microcrystalline, (B) an interfacial region of relatively large fractional void volume containing some pendant side chains, some water, and sulfonilic groups and counter ions which are not in clusters, and (C) the clustered regions where the majority of the ionic exchange sites, counter ions, and sorbed water exists. As compared with the model of Gierke et al., the clusters do not have a strict geometrical definition and their geometrical distribution has a lower degree of order. Most importantly, there are transitional interphases between hydrophilic and hydrophobic regions, a concept that is becoming increasingly accepted. From small-angle x-ray scattering (SAXS) analysis it has been determined that the phase-separated morphology is on the order of 30-50 Å Bragg spacing.

However, upon hydration, Nafion can increase its dry weight by as much as 50 percent or more, cluster diameter and the number of exchange sites increase, leading to fewer, larger clusters.

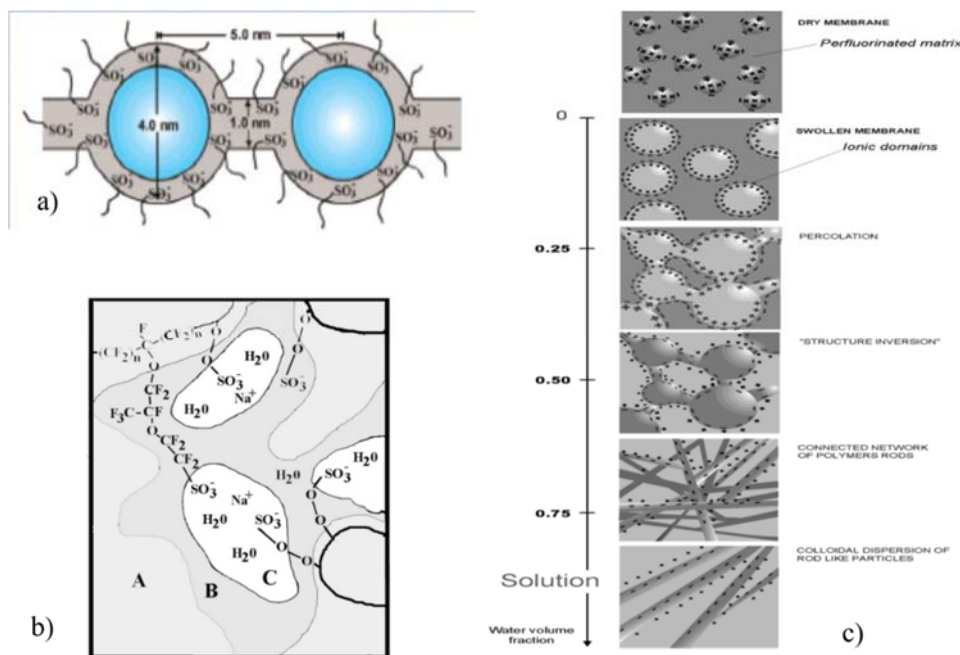


Figure 4.3 (a) Inverted micellar structure of Nafion. (b) The Yeager 3 Phase Model of Nafion Clusters (c) Conceptual model for the morphological reorganization and continuity of the ionic domains in Nafion as the dry membrane is swollen with water to the state of complete dissolution. Reported from [Mauritz (2004)].

Gebel proposed a conceptual description for the swelling and dissolution process [Mauritz (2004)] showed in Figure 4.3c. In dehydrated Nafion, the dry cluster diameter is smaller than the inter-cluster distance (1.5 and 2.7 nm respectively), which explains the extremely low ionic conductivity observed at anhydrous state. With the absorption of water, the clusters increase their dimension until the formation of spherical ionic domains connected with cylinders of water dispersed in the polymer matrix. This increase the connection of spherical cluster exposing the sulfonic groups and as a consequence the ionic conductivity also increases. Continuing to increase water adsorption until a threshold value, an inversion of the structure occurs and the membranes correspond to a connected network of rod-like polymer aggregates. If the amount of water continues to increase, the membrane “dissolves” into solution, yielding a colloidal dispersion of isolated rods. A more convenient and simple explanation for the swelling behaviour of Nafion was proposed by Litt [Mauritz (2004)]. Nafion has a layered structure whose basic element is a “sandwich”. The outer part or shell consists of the side chains, including the sulfonic acid groups, and the “core” consists of water molecules. The sandwiches are distributed linearly with contiguous core that constitute the water channels for proton transport. The distance between each lamella increases with absorption of water and the swelling behavior is completely reversible, thus eliminating the requirement of morphological reorganization.

Due to its high proton conductivity, mechanical, thermal and chemical stability and due to its acid character, the main application of Nafion is as proton exchange membrane in fuel cell application for both vehicle applications and local on-site power generation systems in the future. Nafion allows high hydrogen ion transport while preventing electron conduction. Anyway, this high proton conductivity is critically dependent on the presence of water. Since fuel cell generally should operate in a temperature range up to 120-130°C, Nafion nanocomposite with hydrophilic nanofillers, such as titania, zirconia, silica, alumina, clays, zeolites, and carbon nanomaterials have been used to enhance its water retention property [Enotiadis (2012)]. GO functionalized with aliphatic amine derivatives containing various functional groups, such as sulfonic, carboxyl, and hydroxyl groups, were tested as nanofillers for the creation of novel hybrid Nafion nanocomposites. The as prepared composite membranes showed high water diffusion coefficients over a wide range of temperatures (25–140 ° C) and a higher hydration level with respect to filler-free Nafion, as revealed by water uptake measurements. Nanocomposite membranes were able to retain water for several hours at temperatures as high as 140 ° C without any further humidification. Finally, the mechanical investigation of the nanocomposites indicated that the nanofiller increased the mechanical property of membranes respect to the filler free.

Nafion was also reported as support for photocatalyst as TiO₂. Due to its chemical, thermal and mechanical stability, it is a stable matrix to control the size and inhibit the agglomeration of nanoparticles during their growth. For this reason, nitrogen doped titania nanoparticles were directly synthesised in the Nafion matrix by solvothermal method and tested as photocatalyst for methylene blue degradation [Han (2009)]. The structure of Nafion also enhanced the surface acidity of TiO₂ and increased the pollutant adsorption and thus the contact chance between the photocatalyst and the contaminant. From the point of practical application, the use of polymeric nanocomposite is better than photocatalytic powder to overcome all the problems linked with powder recovery and reuse.

For all these reasons, Nafion nanocomposites have been prepared and investigated as photocatalyst during this research activity and the results are reported in the following paragraphs.

4.1.2 Nexar

Nexar is a sulfonated pentablock copolymer (s-PBC) that has recently found numerous application mainly thanks to the block architecture and the functionalization with sulfonilic groups that allow to this polymer to get a good trade-off between hydrophilicity and mechanical stability.

Block copolymers are opening new perspectives in polymer application and could overcome some drawbacks of homopolymer membranes. The main advantages of block copolymers for membrane manufacture are the possibility of morphology control and of high porosity within a much narrower pore size distribution. Charged block copolymers have been explored as proton exchange membranes for fuel cell application [Nunes (2016)]. They offer the possibility of controlling swelling and electroosmotic transport, while keeping proton conductivity high. As non-porous membrane, block copolymers are used as coatings for fouling minimization [Nunes (2016)]: for example, the use of coating by amphiphilic copolymers with side chains of hydrophilic poly ethylene oxide (PEO) blocks and hydrophobic blocks of polystyrene (PS) and polyisoprene (PI) showed a decrease of biofouling by increasing the amount of PEO [Nunes (2016)].

What makes block copolymers so interesting is the possibility of tuning their morphologies that affect their properties and finally applications. Most membrane manufacturing processes are based on solution, and the final morphology is in most cases a non-equilibrium, kinetically trapped structure. In this case, self-assembly is a relevant aspect and the interactions between different blocks and a variety of possible solvents and solvent mixtures have to be taken into consideration. The reported main structures are spherical micelles, cylinders or wormlike micelles, vesicles, bicontinuous rods, bilayers, and more complex structures. The copolymer concentration is an important factor for the morphology. In the range of 10–20%, spherical micelles order forming a lattice. The lattice geometry depends on copolymer concentration and the solvent-blocks and block-block interactions. Face-centered (fcc) or body-centered cubic (bcc) geometries are possible, and the transition between them can be induced by temperature.

Actually, one of the main used polymer in the field of water purification is polyamide for desalination. Anyway, its performance highly declines due to oxidative degradation aqueous chlorine-based chemicals. As a consequence, improved membranes more robust and durable (i.e. resistant to oxidation by chemicals, such as the chlorine-based disinfectants used in water treatment, highly pH tolerant, and more resistant to fouling) but at the same time characterized by high flux and high salt rejection are needed. One approach is choosing polymers with robust, stable backbones but these are often rather hydrophobic (i.e., polysulfone, polystyrene, etc.) and therefore are not sufficiently permeable to water. A way to overcome this problem is adding charged groups (i.e., carboxylate or sulfonate groups) to the hydrophobic polymer resulting in a higher hydrophilicity and water permeability. Sulfonated poly(arylene ether sulfones) have been studied as potential desalination membranes [Geise (2010)]. The amount of charged groups on the polymer backbone is known as ion exchange capacity (IEC). In sulfonated polymers, polymer charge or IEC influences salt transport and rejection, water permeability and water uptake. High degrees of sulfonation can lead to excessive

swelling decreasing the polymer mechanical strength. Both crosslinking and block copolymer architectures restrict water uptake preventing highly sulfonated polymers from dissolving in water. The investigated polymer (Figure 4.4) is prepared by Kraton Performance Polymers, Inc. using anionic polymerization to synthesize the base block copolymer, catalytic hydrogenation of the residual isoprene C=C bonds, and final a post-polymerization sulfonation process [Willis (2010)].

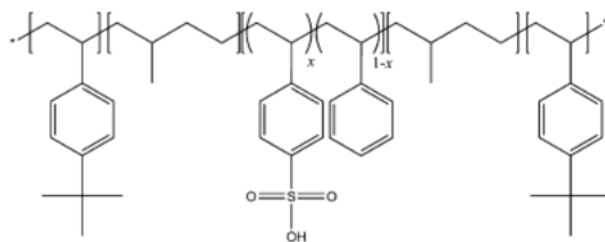


Figure 4. 4 Nexar structure from [Geise (2010)]

Nexar, as commercially known, is a symmetric pentablock copolymer comprised of poly[*t*-butyl styrene-*b*-hydrogenated isoprene-*b*-sulfonated styrene-*b*-hydrogenated isoprene-*b*-*t*-butyl styrene] (tBS-HI-SS-HI-tBS), in which the sulfonated midblock provides the ionic character while the outer blocks provide the strength of a high T_g material and the flexibility of a low T_g material. Unlike sulfonated poly(styrene-*b*-hydrogenated butadiene-*b*-styrene) or SEBS materials, in this new polymeric architecture the sulfonation is limited to the middle block, resulting in a polymer with controlled swelling and good mechanical properties in the hydrated state [Geise (2010)]. On the contrary, in SEBS architecture the sulfonation of the styrene end blocks is uncontrollable leading to swelling and, thus, poor mechanical properties when hydrated. In this new architecture, the tert-butyl group and the polymer backbond protect the favourable para- and ortho- positions of the phenyl avoiding sulfonation of styrene end blocks. The hydrogenated isoprene block gives the copolymer additional toughness. The film structure, physical properties, and transport characteristics are dependent upon casting solvent, sulfonation level, and processing method.

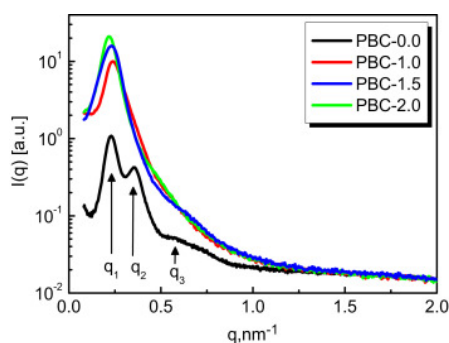


Figure 4. 5 SAXS curves of pentablock copolymers with different sulfonation levels reported from [Fan (2014)].

As shown in Figure 4.5, the SAXS profiles of unsulfonated pentablock copolymer reveal three main peaks, q_1 0.230 nm^{-1} ($d_1=27.3 \text{ nm}$) and q_2 0.356 nm^{-1} ($d_2=17.6 \text{ nm}$) and a weak higher-order peak at q_3 0.675 nm^{-1} ($d_3=9.31 \text{ nm}$). These scattering peaks are close to nq , suggesting a lamella morphology for PBC-0.0. With increasing sulfonation levels, the q_3 shifts to lower values and the other two principal peaks merge into a single broad peak. The scattering intensity and average d -spacing increased with IEC. In other words, no long-range order in structure is present, which is attributed to ion aggregation and domain formation. This results in a decreasing of polymer chain mobility, thus an increase in the distance between ion domains. The lack of organized structure suggests that these materials are non-equilibrium materials, which may be attributed to processing method and solvent system.

As noted by [Choi (2010)], the sulfonated pentablock copolymer solutions form spherical micelles with a core of SS and a corona of solvated HI-tBS in cyclohexane/heptane mixtures (Figure 4.6).

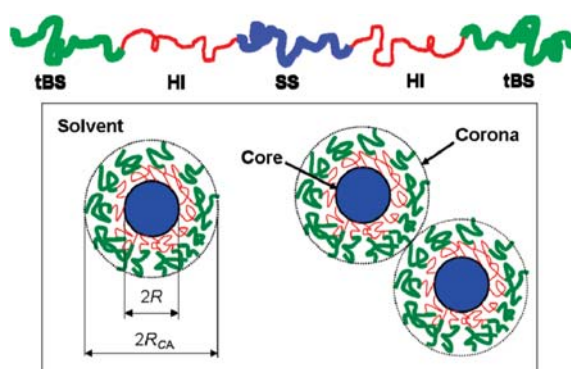


Figure 4. 6 Monodisperse, spherical micelles containing dense cores of SS and coronas of HI-tBS swollen by solvent. Reported from [Choi (2010)].

This hypothesis was confirmed by TEM images. Due to the incompatibility between ionic (SS) and non-ionic (tBS and HI) blocks, both the radius of the micelle core and the radius of the micelles increase with increasing IEC, while the number of micelles per unit volume decreases with increasing IEC. These findings are important for establishing appropriate processing conditions considering also that this morphology may persist when polymer solutions are quickly dried into a film. During membrane formation by solvent casting, the spherical micelles compact as the cyclohexane/heptane evaporates and the HI-tBS coronae merge to form discrete SS microdomains. However, as the sulfonation level of the polymer is increased, the volume fraction and the size of SS microdomains increase, such that upon solvent casting the SS microdomains transform to a bicontinuous morphology with interconnected SS microdomains [Choi (2012)].

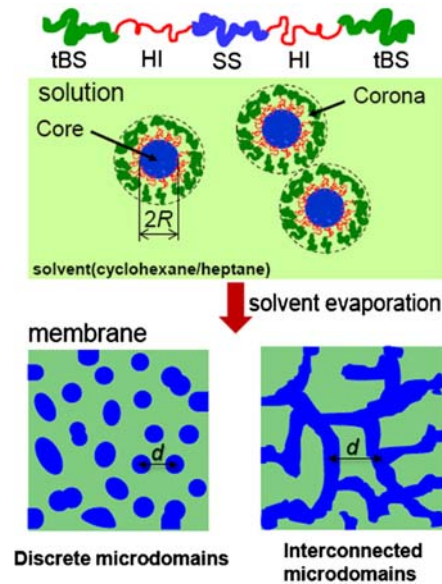


Figure 4. 7 Schematic illustration of morphological changes when membranes are cast from solution [Choi (2012)].

For what concerns solvent casting, using polar solvents, inverted micelles with exposed sulfonilic groups occur forming connected ionic domains [Mineart 2015]. While membranes prepared from cyclohexane solution displayed ion-rich spherical microdomains, those cast from THF exhibited coexisting nonpolar cylinders and lamellae; thereby providing a continuous pathway through which ions and other polar species can diffuse.

The reported studies confirm that understanding the size and shape of self-assembled structures is critical to the correlations between the molecular structure, morphology, and properties of these sulfonated pentablock copolymer membranes. Salt and water permeability, water uptake, and salt diffusion were studied [Geise (2010), Geise (2013)] for water desalination applications. This polymeric architecture was investigated as desalination membrane material by the preparation of different membranes changing the degree of sulfonation, the block molecular weights, and film casting technique; the final aim was to tune transport properties [Geise (2010)]. Both water uptake and water permeability increase with degree of sulfonation, in particular a jump in both water permeability and the apparent water diffusion coefficient was observed for membranes with IEC 0.7 and IEC 1.0. At equal values of IEC, the size of hydrophobic end block reduced the water uptake. Additionally, as the water content of the material increases, a plasticization of the polymer is induced determining an increase of the water diffusion coefficient. The sodium chloride salt permeability of the sulfonated pentablock copolymer materials increases with the salt concentration. This may be due to Donnan exclusion, that is, an electric potential acts to exclude anions from the polymer matrix [Geise

(2010)]: as salt concentration decreases, sorption of chloride ions in the polymer matrix decreases reducing salt permeability. Increasing salt concentration, the salt permeability increases, since the ionic strength of the solution increases and overcome the Donnan exclusion effect. Higher salt permeability was observed for materials with higher water content i.e. higher sulfonation degree or lower hydrophobic degree. Anyway, the larger hydrophobic blocks restrict swelling and result in a material with increased selectivity. The results also showed a dependence of material transport properties by the casting method; this is due to the complex morphology of this kind of material as explained in the previous paragraph. This aspect is still under investigation. In another study [Geise (2013)], the same author investigated the sodium chloride diffusion properties in steady state of sulfonated polymers with those of an uncharged hydrogel. In the configuration of the system, the thin, nonporous polymeric film was in contact with two different salt concentration solutions: the concentration gradient leads the diffusion of cations and anions from the more concentrated solution to the lower one. On the contrary, compared to uncharged polymers. the salt diffusion coefficients of sulfonated polymers increase markedly as salt concentration increases. Further study is required to fully understand such trends. Fan et al. [Fan (2014)], [Fan (2013)] studied sulfonated and unsulfonated pentablock copolymer ionomers with respect to gas (CO_2 , O_2 , and CH_4), to liquids and to ions transport in order to evaluate their potential application as a polymer electrolyte membrane. Phase separation was observed in all PBC ionomers due to incompatibility between blocks: as sulfonation levels increase, the sulfonated PBC ionomers lose their long-range structure as compared to unsulfonated ionomer. This is attributed to tBS and PS mixing with sPS in order to create ionic domains. The effect of sulfonation was that of increasing the gas solubility and, as a consequence, their transport with respect to unsulfonated polymer. In particular, CO_2 has a higher solubility suggesting a greater affinity with the material. Water uptake, methanol permeability and proton conductivity increase with IEC values. The higher water content within sulfonated PBC ionomers results in swelling that improves methanol transport because sulfonated domains become increasingly connected. In conclusion, Fan et al observed that gas transport properties are slightly IEC dependent, so gas permeability dependences more on the unsulfonated domains. On the contrary, proton and methanol transport is through sulfonated hydrophilic domains. Therefore, for the application of this polymer as filter or proton exchange membranes a structure favouring the interconnection of sulfonic domain is highly desirable. This aim can be achieved by varying the membranes preparation procedure. In the following paragraph, a description of the structure of this polymer is reported underlying the relationship of its morphology with synthetic procedure, sulfonation levels and possible applications.

4.2 Nafion hybrid nanocomposite membranes for water purification applications

4.2.1 Materials preparation and characterization

Taking advantage of Nafion high acidity and structure, for which it is very stable in water but it has a high value of water uptake, we have tested for the first time Nafion® (DuPont) nanocomposites for water purification application. Titania has been dispersed inside it to confer photocatalytic activity and investigate the role acted by the polymer itself in this process. GO and a chemical modified GO with sulfonic groups (hereafter as GO_{SULF}) have been added in this matrix to increase the polymer acidity and water uptake. These aspects have a key role in both adsorption and photocatalytic processes. To the best of our knowledge, the possibility of using organo-modified graphene oxide as catalyst in water purification was not explored before our work, whereas it was limited mainly to fuel cells applications [Enotiadis (2012)].

Hybrid nanocomposite Nafion membranes containing different fillers such as anatase-type TiO₂ nanoparticles, graphene oxide (GO) (Figure 4.8 left) or organo-modified graphene oxide (GO_{SULF}) (Figure 4.8 right) were prepared by the solvent casting method.

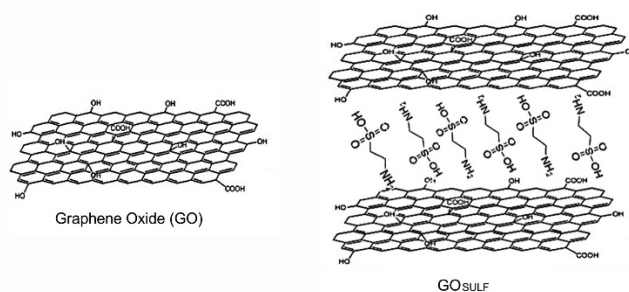


Figure 4. 8 GO and organo modified GO structures, respectively on the left and on the right.

Aqueous dispersions of GO were produced using a modified Staudenmaier's method [Staudenmaier (1898)] from graphite powder. In a typical synthesis, powdered graphite (10 g, purum, powder <0.2 mm; Fluka) was added to a mixture of concentrated sulphuric acid (400 mL, 95–97 wt%) and nitric acid (200 mL, 65 wt%) while cooling in an ice-water bath. Potassium chlorate powder (200 g, purum, > 98.0%; Fluka) was added to the mixture in small portions while stirring and cooling. The reaction was quenched after 18 h by pouring the mixture into distilled water, and the oxidation product was washed until the pH reached 6.0 and finally dried at room temperature. According to elementary analysis data, the C/O atomic ratio of the resulting product was 2.6.

For the preparation of organo-GO nanofiller (GO_{SULF}), GO (100 mg) was dispersed in water (100 mL), followed by the addition of 300 mg of 3-amino-1-propanesulfonic acid (denoted SULF from Sigma Aldrich) in 40 mL of water. After stirring for 24 h, the organo-modified GO was washed with water, separated by centrifugation, and air-dried by spreading on glass plates. The modification of graphene oxide occurs by the replacement of epoxy functionalities by amine derivatives ending with a sulfonic groups. This synthetic procedure has the advantage of occurring without the formation of intermediate products.

For membranes preparation, fillers were directly dispersed in Nafion commercial solution (20 wt% dispersion in water and lower aliphatic alcohols from Sigma Aldrich), ultrasonicated for 1 day and stirred for another day at room temperature until a clear solution was obtained. After that, the dispersion was cast on a petri dish at 30° C overnight to remove the solvents. The hybrid membranes (Figure 4.9) were removed from the petri dish by immersing the glass plate in deionized water for several minutes. To reinforce the membrane, it was sandwiched and pressed between two Teflon plates and placed in oven at 150° C for about 25 min. As far as it concerns pristine Nafion membranes, an appropriate amount of Nafion solution was dried at about 60° C and then re-dissolved in the dimethylformamide (DMF) until a clear solution was obtained. Finally, the suspension was cast on a petri dish at 80° C overnight.

All composite and Nafion membranes produced by casting were subsequently treated by rinsing in: (1) boiling HNO_3 solution (1 M) for 1 h to oxidize the organic impurities; (2) boiling H_2O_2 (3 vol%) for 1 h to remove all the organic impurities; (3) boiling deionized H_2O for 40 min three times; (4) boiling H_2SO_4 (0.5 M) for 1 h to remove any metallic impurities; and again (5) boiling deionized H_2O for 40 min twice to remove excess acid.



Figure 4. 9 From left to the right: Nafion, Nafion- TiO_2 and Nafion with GO-based materials.

In order to study the membrane morphology and to get qualitative information as far as it concerns surface and cross-sectional details, SEM analysis was performed on hybrid polymeric systems (see Appendix A4). Figure 4.3 shows the cross-sections of all the nanocomposite membranes: Nafion (Figure 4.10a), Nafion- TiO_2 (Figure 4.10b,c,d), Nafion-GO (Figure 4.10e,f), Nafion- GO_{SULF} (Figure

4.10g,h). Nafion pristine membrane is quite smooth and homogeneous; in composites we can observe nanoparticles homogeneously dispersed through the entire volume of polymeric matrix both for titania (Figure 4.10b,c,d) and for GO-based materials (Figure 4.10e,f,g,h). Furthermore, in the case of GO and GO_{SULF} nanocomposite membranes, a wrinkled and spongy structure is shown within well visible graphitic planes in the polymeric matrix. The presence and the chemical composition of the fillers in the membranes is confirmed by EDX analysis shown in [Filice (2015)]. The homogeneous dispersion of titania in the polymeric matrix section is confirmed, while, in the case of nanocomposites with GO-based fillers, some regions show a higher concentration of C and O atoms due to the presence of graphene oxide flakes. Fourier Transform infra-red (FT-IR) spectroscopy performed on GO_{SULF} showed the reduction of the epoxy groups along with the appearance of the signals related to CH₂ on amine groups; the functionalization of GO with the amine derivate was also confirmed by TGA/DTA analysis and calculated as 22% [Enotiadis (2012)].

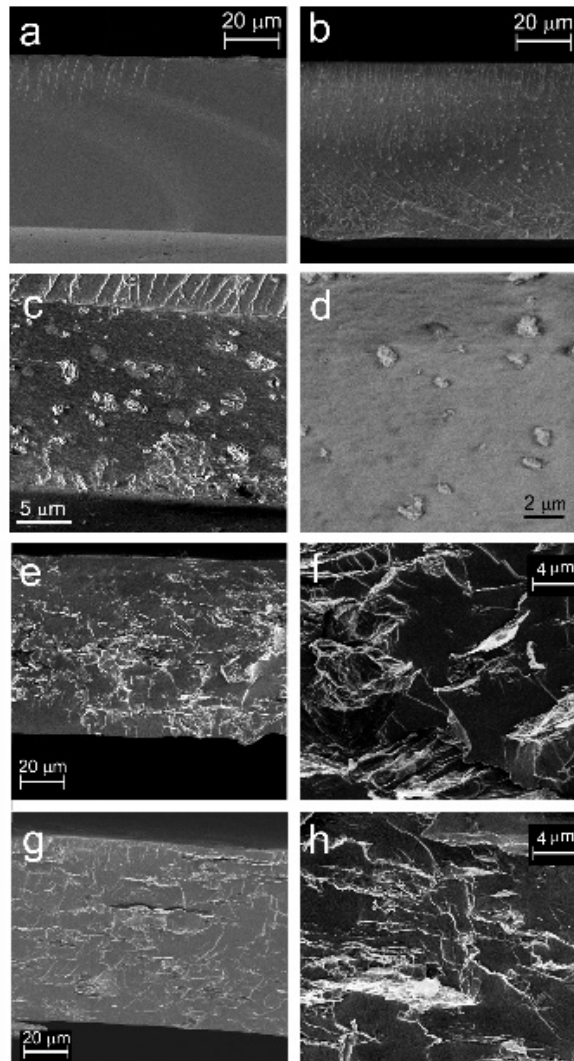


Figure 4. 10 Cross-sectional SEM images of Nafion membrane (a) and hybrid nanocomposite Nafion membranes loaded with 3% of TiO₂ (b–d), GO (e, f) and GO_{SULF} (g, h). More details are visible in the images at higher magnification (b, f, h). Reported from [Filice (2015)].

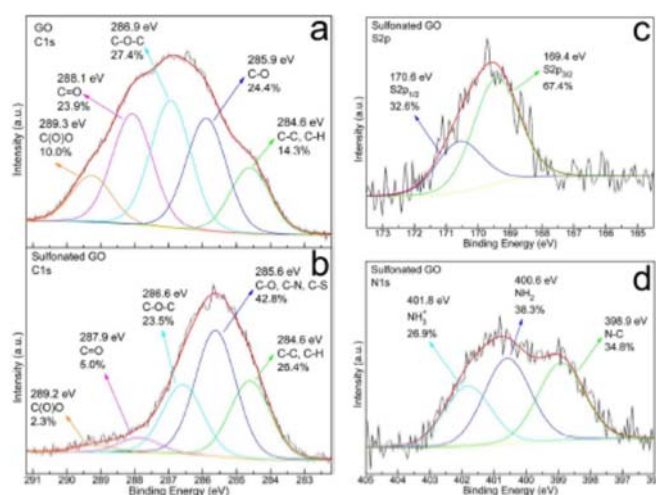


Figure 4. 11 X-ray photoemission spectra of (a) C1s core level for starting GO and (b) C1s, (c) S2p and (d) N1s for sulfonated GO. Reported from [Scalese (2016)].

Figure 4.11 reports the C1s XPS spectra for starting GO and sulfonated GO (a,b). Each spectrum is deconvoluted by mixed Gaussian–Lorentzian functions into five components, reported in Table 4A (see Appendix A17).

Table 4A XPS peaks assignment

Peak position [eV]	Peak assignment	
	GO	GO _{SULF}
284.6	C-C, C-H	C-C, C-H
285.6-285.9	C-O	C-O, C-N, C-S
286.6-286.9	C-O-C	C-O-C
287.9-288.1	C=O	C=O
289.2-289.3	C(O)O	C(O)O

The above reported contributions within the fact that the contribution to the total C1s integrated intensity of the first two peaks is significantly enhanced upon sulfonation confirm the successful functionalization of GO. According to the chemical functionalization, the insertion of additional C-C, C-H, C-N and C-S bonds is confirmed by the increase in the intensity of the first two peaks reported

in the table: a 26.4% contribution for C-C/C-H and 42.8% for C-O/C-N/C-S is observed for GO_{SULF}, with respect to the 14.3% and 24.4% of the starting GO, respectively. These findings are confirmed by the observations of N1s and S2p XPS spectra of GO_{SULF} (Figure 4.4 c,d): in the first one, the three observed signals are related to C-N and N-H bonds of amines; in the S2p spectrum the peak is related to sulfonates [Scalese (2016)].

Z potential measurements of GO and GO_{SULF} solutions (see Appendix A18) show that, at pH = 6.3 both materials are negatively charged: in particular, the zeta potential of GO is higher (-46 mV) than the zeta potential of GO_{SULF} (-42.8 mV). This means that GO_{SULF} is less negative than GO, as evidenced also in XPS spectra by the loss of O groups due to sulfonic functionalization.

4.2.2 Nafion hybrid nanocomposite membranes for cationic and anionic dye removal

The photocatalytic activity of all the prepared membranes was investigated according to the methodology reported in Appendix A19. The photocatalytic activity of titania is well known in literature and this is described in Chapter 3: excited dye molecules are generated upon absorption of visible photons and subsequently inject electrons into TiO₂ CB (ecb⁻). As a consequence, dye molecules degrade and ecb⁻ reacts with oxygen that acts as electron acceptor avoiding the recombination of dye^{•+} and ecb⁻. The overall rate of the dye degradation should be determined by the competition between the forward electron injection and the backward recombination. To favour the first one, the adsorption of dyes on the photocatalytic surface is needed in order to achieve dye degradation. In the case of Nafion nanocomposite membranes, the dye adsorption depends on the interactions of the dye with the membrane surface and on the water absorption equilibrium of the membranes. In addition, the absorption of water on polymer surface favours the interaction of electrons and holes with water molecules or hydroxyl ions forming reactive species able to degrade organic compounds, as shown in Chapter 1. According to this, the high water uptake show by Nafion membrane and nanocomposite plays a key role in the dye degradation ability shown by these materials. This aspect is deeply discussed in the following text.

In addition, dye adsorption (in dark conditions) for each membrane was also evaluated in order to discriminate between the contributions of the mere adsorption and the photocatalytic activity. For this purpose, it is necessary to consider the acid-base equilibria of the polymer and the dye. The equilibrium between acid and basic form of the used dyes is shown in Figure 4.12a, while the

equilibrium of protonation and deprotonation of sulfonic group in the polymer is shown in Figure 4.12b.

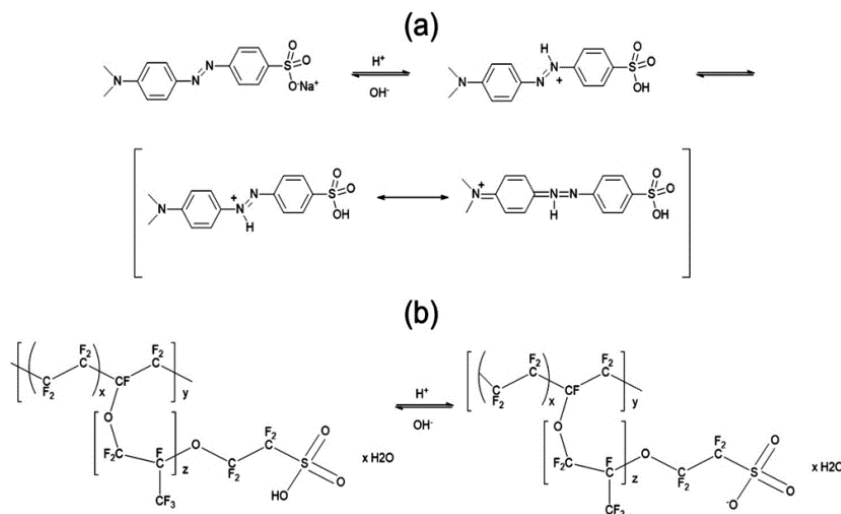


Figure 4. 12 Acid-base equilibria of MO (a) and Nafion (b). Reported from [Filice (2015)].

MO adsorption on Nafion based composite membranes should be hindered because of the electrostatic repulsions between the negative molecular charge of the dye and the negative sulfonic group in Nafion. After one hour of immersion (Figure 4.13a), all the Nafion membranes adsorb similar amounts of dye independently of the used filler with the exception of Nafion-GO_{SULF} that shows a slight decrease of the peak at 465 nm. After two and three hours (Figure 4.13b,c), the membranes continue to adsorb the dye and the absorbance band shifts to larger wavelength due to the decrease of the pH value of the solution. The changes in the shape of MO UV-Vis absorbance spectrum within pH values is reported in Appendix B. As shown in Figure 4.13d, in the first hour the pH value decreases more for Nafion-TiO₂, while in the second and third hour a larger pH decreasing is observed for the other membranes, especially for Nafion-GO_{SULF}. This pH reduction is ascribed to the acid base equilibrium described in the previous Figure. Nafion is a very strong Bronsted acid and when the membranes are immersed in the solution, the acid-base equilibrium of SO₃H groups shifts to the deprotonated form (SO₃⁻), while the equilibrium of MO shifts towards protonated forms (MO⁺). In this way, the electrostatic interaction between SO₃⁻ and MO⁺ is favoured and the adsorption increases within dipping time, accompanied by an increase of the solution pH value.

Under UVA/Vis light irradiation (see Appendix C), each membrane shows a different behaviour. In the presence of recast Nafion, the intensity at 465 nm of the MO absorbance gradually decreases and the peak position shifts towards higher wavelengths (up to 470 nm) with irradiation time (Figure 4.14). This shift is associated with the more acidic value of pH solution. Higher

degradation values are recorded, at the same time, for Nafion-TiO₂ and even more for Nafion-GO_{SULF}, while the worst performance among the composites is shown by Nafion-GO membrane that finally reaches the degradation value shown by Nafion itself. Also for the composites as for Nafion itself, the pH of solutions is acid, as evidenced by the shape of the absorbance spectra.

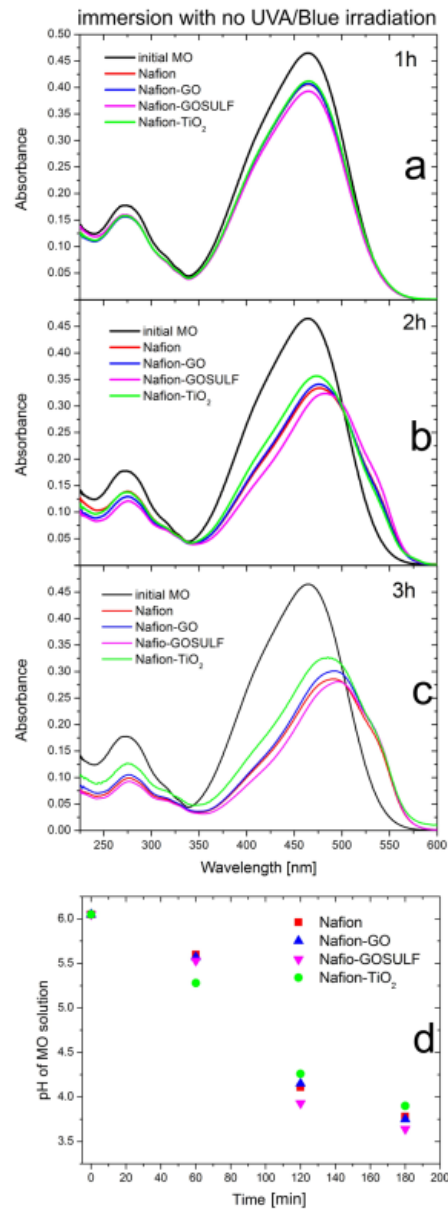


Figure 4. 13 UV-Vis absorbance spectra of methyl orange after immersing Nafion composite membranes in MO solution for one hour (a), two hours (b) and three hours (c). The Figure (d) shows how pH changes during the adsorption time. Reported from [Filice (2015)].

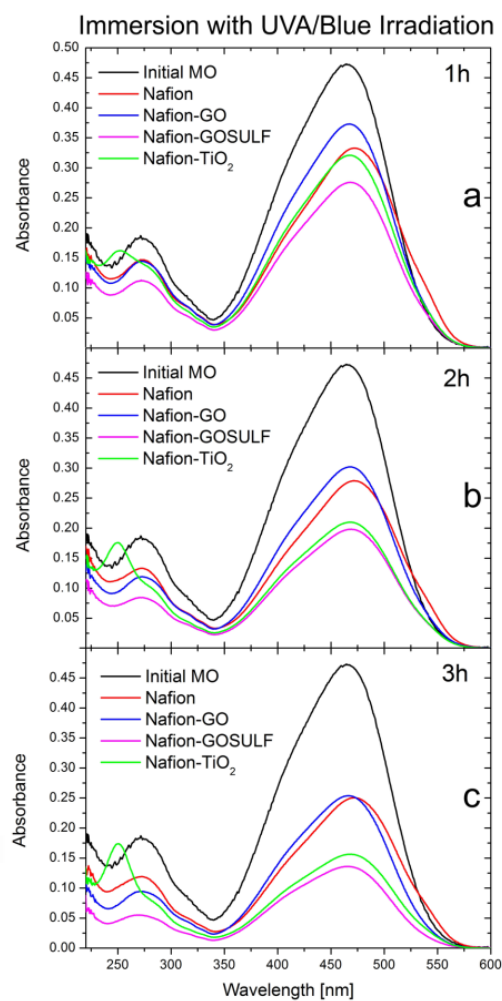


Figure 4. 14 UV-Vis absorbance spectra of methyl orange after immersing Nafion composite membranes in MO solution and irradiated with UVA-Vis light for one hour (a), two hours (b) and three hours (c). Reported from [Filice (2015)].

The above reported results evidence that sulfonation of GO greatly increase the degradation ability of GO itself due to an increase of the acidity and of water uptake (about 27 wt% Nafion-GO against about 50 wt% Nafion-GO_{SULF}). For what concerns the characteristic MO absorption peak at 270 nm, this decreases of almost the same amount for Nafion and the composite with GO-based materials after 1 hour of irradiation and then it remains constant. A different situation is observed for Nafion-TiO₂ with increasing irradiation time: the 270 nm peak not only decreases, but it also changes its shape and shifts towards shorter wavelengths (250 nm).

Figure 4.15 reports the curves of MO residual concentration versus dipping time in dark condition (a) or irradiation time (b). In dark, in the first hour the MO adsorption is almost the same (10%) for all the materials. In the following hours Nafion, Nafion-GO and Nafion-GO_{SULF} adsorb more than Nafion-TiO₂ with the best performance shown by Nafion and Nafion-GO_{SULF} (35%). A correlation

between the adsorption and the decreasing of pH versus dipping time is out of doubt: both show a great change during the second hour, likely due to an initial slow kinetic caused by the electrostatic repulsion between the negative charges of the dye and of the sulfonic groups.

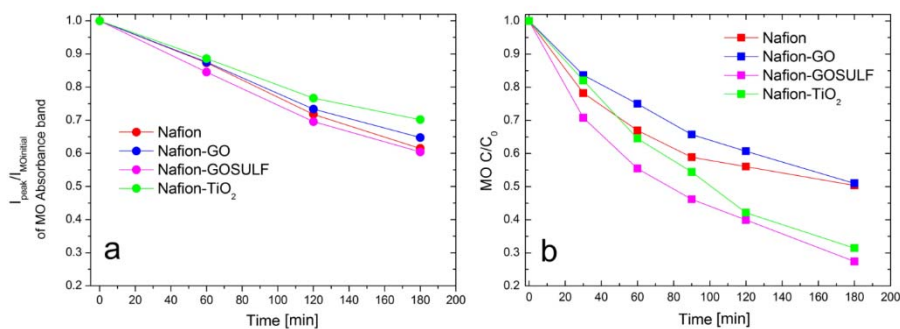


Figure 4. 15 The maximum value of MO absorbance during time due to the adsorption of the membranes (a) and the residual MO concentration during the UVA/Vis irradiation time (b). Reported from [Filice (2015)].

Under irradiation dye degradation (Figure 4.15b) is larger with respect to adsorption, in particular for Nafion-GO_{SULF} and Nafion-TiO₂. Table 4B reports the amount (%) of MO removed by each membrane after three hours irradiation and the rate constant k , calculated by fitting the experimental C/C_0 data of Figure 4.15b, considering $C=C_0 \exp(-kt)$. These results were expected for Nafion TiO₂ since its well known photocatalytic activity, while the GO_{SULF} performance, as good as titania, is shown here for the first time. In the following paragraphs GO_{SULF} properties and its application in dyes removal are deeply investigated.

Table 4B: Amount (%) of MO dye removed after 3 hours irradiation (initial concentration $C_0=2 \times 10^{-5}M$); the rate constant k is calculated by fitting the experimental C/C_0 data of Figure 23b, considering $C=C_0 \exp(-kt)$. Reported from [Filice (2015)].

Membrane	MO removed after 3h of irradiation (%)	K [$\times 10^{-3} \text{min}^{-1}$]	
		Value	Error
Nafion	47	4.6	0.4
Nafion-GO	46	4.1	0.2
Nafion-GO _{SULF}	71	7.7	0.4
Nafion-TiO ₂	67	6.7	0.2

Figure 4.16 reports in detail how MO UV-vis absorbance spectra change during three hours under irradiation, for the solutions where Nafion-TiO₂ (a) and Nafion-GO_{SULF} (b) are immersed. The best

performance is recorded for Nafion-GO_{SULF}. The shapes of reported MO spectra are different according to the composites immersed in the solution, suggesting that a different degradation mechanism occurs. For the solution containing Nafion-TiO₂, the 465 nm peak intensity decreases with time and a new peak at 250 nm appears in the first hour becoming more define with time. This peak indicates the formation of aromatic intermediate compounds as harmful as the original MO species [Baiocchi (2002)]. These are absent in the case of Nafion-GO_{SULF}, (the peak at 250 nm is not present) suggesting that this material is more safe to be used respect to Nafion TiO₂ for MO removal. In addition, the absence of this peak open a discussion on the degradation mechanism acted by Nafion-GO_{SULF}. A possible speculation, concerning the formation or not of the toxic by-products, should be based on two main hypotheses: MO is only adsorbed by Nafion-GO_{SULF} simply explaining the absence of 250 nm peak, or these by-products are formed but at the same time they are degraded by adsorption or photocatalysis on the same membrane. Further investigations will clarify this aspect.

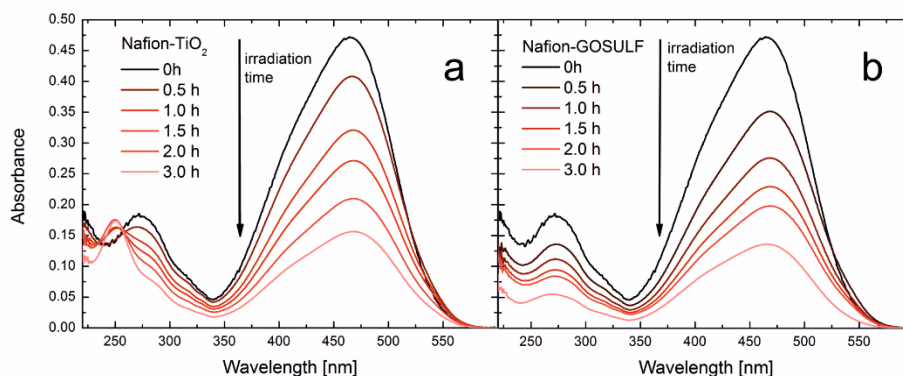


Figure 4. 16 UV-vis absorbance spectra of MO solution after irradiation for three hours in the presence of Nafion TiO₂ (a) and Nafion GOSULF (b). Reported from [Filice (2015)].

To have an idea of degradation mechanisms, Figure 4.17 compares the effect of adsorption and photocatalysis for Nafion-GO_{SULF} and Nafion-TiO₂ membranes on MO solutions where the membranes were dipped for 3 hours. As just described, the spectra are different: in dark, not only MO concentration decreases, but the peaks also result shifted towards larger wavelengths within a hump on the right of the peaks due to the protonation of MO (this aspect is explained in the previous text); on the contrary, under irradiation, the spectra of the solution show a larger decrease of dye concentration, without alteration of the shape of the peak at 465 nm. For what concerns the peak at 270 nm, a strong difference is observed between Nafion-TiO₂ and Nafion-GO_{SULF} and this is explained in the previous text. As a result, under irradiation Nafion-TiO₂ degrades MO following the same pathway of TiO₂ powder [Baiocchi (2002)], confirming Nafion membrane as a support to incorporate the catalyst. If we compare adsorption and photocatalysis for the same composite Nafion-

GO_{SULF}, the absorbance spectra are different, suggesting that the MO degradation acted by this material under irradiation is not only a removal effect due to adsorption.

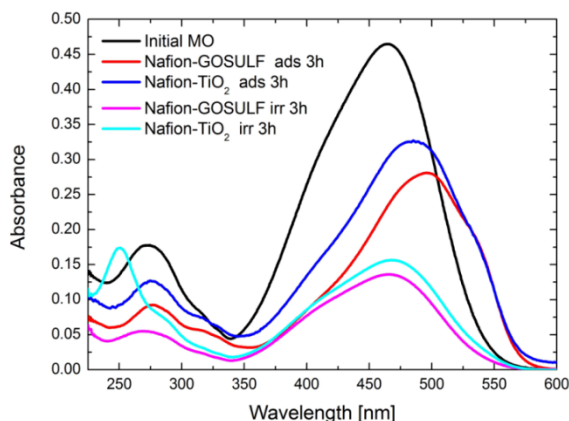


Figure 4.17 UV-Vis MO absorbance spectra for Nafion-TiO₂ and Nafion-GO_{SULF} after 3 hours of immersion in dark and after 3 hours of UVA-Vis irradiation. The initial absorbance spectrum of MO is reported as a reference. Reported from [Filice (2015)].

Mono- and di-hydroxylated species as by-products of MO degradation were individuated during MO degradation by titania powder, and the reported absorbance spectra show the same profile of MO spectrum, but with the maximum shifted to 470 nm [Baiocchi (2002)]. The absorbance peak for Nafion-GO_{SULF} is shifted from 465 nm to 470 nm after irradiation, therefore we hypothesize a mechanism concerning the formation of the above mentioned hydroxylated species as reported in Figure 4.18. Hydroxyl radicals are likely formed by Nafion-GO_{SULF} under irradiation, and added directly to MO phenyl ring, forming an intermediate radical; subsequently the removal of H-atom by oxidants (e.g. O₂) could lead to the hydroxylated species. This hypothesis is also validated by the fact that, under UV irradiation, hydroxylation of benzene can occur in the presence of a photocatalyst and acid catalysis [Park and Choi (2005)].

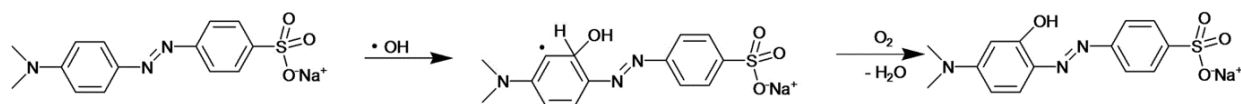


Figure 4.18 Proposed mechanism for MO degradation by GO_{SULF}. Reported from [Filice (2015)].

In order to verify the role acted by the polymeric matrix, we compare the degradation ability of polymeric nanocomposites with the ones shown by anatase TiO₂ nanoparticles or GO_{SULF} directly dispersed in MO solutions in the same concentration as that dispersed in 1 cm² of Nafion

nanocomposites (70 mg/l). Figure 4.19 shows that the photocatalytic efficiency of TiO_2 and Nafion- TiO_2 is almost the same up to three hours of irradiation and in both cases the formation of the same aromatic by-product is observed. In this case Nafion acts as a support for the filler, avoiding its dispersion in the environment. On the contrary, embedding GO_{SULF} in the Nafion matrix increases the MO photocatalytic reduction with respect to the powder itself from the 60 % to the 90% respectively.

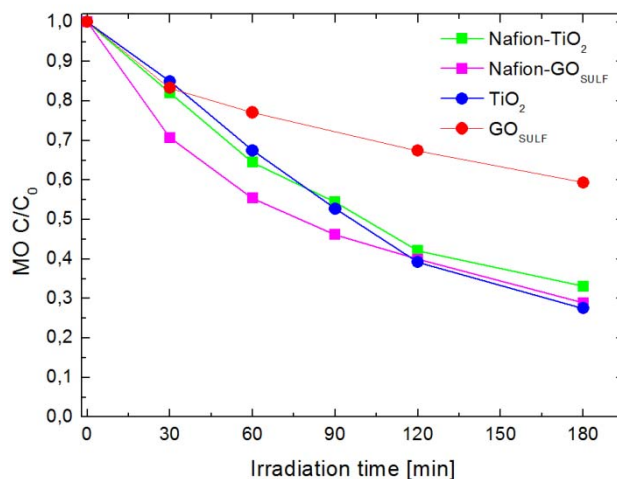


Figure 4. 19 Residual MO concentration as a function of the irradiation time for TiO_2 and GO_{SULF} directly dispersed in the MO solution or incorporated as fillers in the hybrid membranes. Reported from [Filice (2015)].

One of the main advantages of using polymeric nanocomposites respect to powders is the possibility to re-use them for several purification processes. In order to investigate this aspect, the Nafion- GO_{SULF} and Nafion- TiO_2 membranes were dipped in MO solution under irradiation for three different times, alternated with regeneration processes (described in Appendix A19). The MO concentration versus irradiation time for three consecutive uses of the nanocomposites is reported in Figure 4.20. After the first use and regeneration the performance reduces but, then, remains stable for the following cycles. This can be ascribed to a passivation of sulfonic groups after the first use. Other regeneration procedures will be investigated.

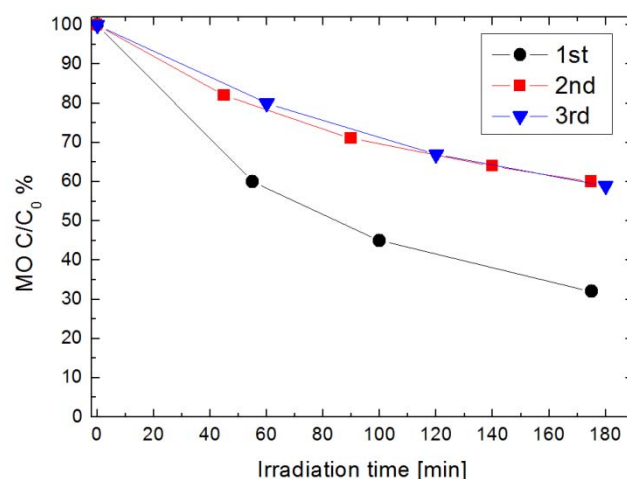


Figure 4. 20 MO concentration versus irradiation time for three consecutive photocatalytic processes using the Nafion-GO_{SULF} membrane. Second and third process took place after membrane regeneration step. Reported from [Filice (2015)].

Starting from the above reported results, Nafion, Nafion GO and Nafion TiO₂ were tested, in the same experimental conditions, for the removal of an anionic dye Methylene Blue, comparing these results with the ones reported for the removal of anionic dye. The activity of GO_{SULF} and Nafion GO_{SULF} composite in removing both cationic and anionic dyes is deeply investigated in the next paragraph. As just shown, the degradation ability of these nanocomposites mainly depend on the electrostatic interaction between the SO₃⁻ groups in Nafion and dyes: since the MB is a cationic dye, its adsorption is favored with respect to MO.

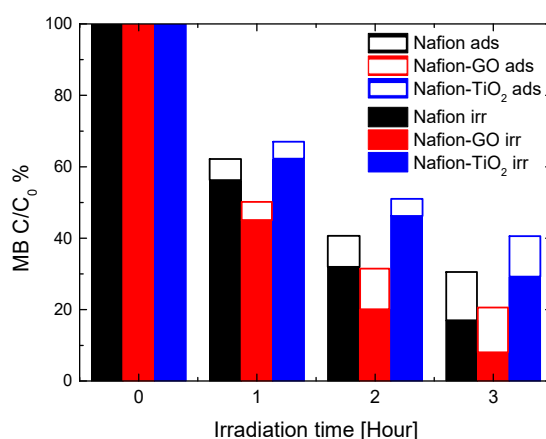


Figure 4. 21 Residual concentration (in percentage) of MB versus the time of contact with Nafion (black bars), Nafion-GO (red bars) and Nafion-TiO₂ (blue bars) membranes in the dark (empty bars) or under UV/blue light irradiation (full bars). The initial concentration of the dyes is 2×10^{-5} M in H₂O.

Figure 4.21 shows the residual concentration of MB versus the time of contact with Nafion, Nafion-GO and Nafion-TiO₂ membranes in the dark or under UV/blue light irradiation. We have reported in the previous paragraph that Nafion membranes was able to remove (after 3 hours) the 35% of MO by adsorption and the 55% under irradiation, Nafion TiO₂ the 30% and 70%, respectively and Nafion GO the 30% and 55% respectively. In the case of MB, the electrostatic interaction between sulfonic groups and dye molecules is favored increasing the degradation ability of these materials. Also for the removal of cationic dye, a higher degradation efficiency is achieved under irradiation respect to adsorption. After 3 hours, the residual concentration due to MB adsorption is 30%, whereas after 3h irradiation it is below 20%, showing that Nafion membranes possess photocatalytic properties. For what concerns Nafion-GO, we showed that, with respect to Nafion itself, the efficiency of this nanocomposite is quite similar to that of Nafion itself in removing MO, while this is more efficient in the degradation of MB. This can be ascribed considering the electrostatic interactions: Nafion GO composite has a higher density of negative charges with respect to Nafion that increases the adsorption of MB. Vice versa, the Nafion-TiO₂ is more efficient in the degradation of the MO and less effective in the degradation of MB compared to the pure Nafion membrane. The degradation activity of Nafion-TiO₂ under illumination are very similar in degrading both MO and MB, suggesting that the photocatalytic activity of TiO₂ nanoparticles predominates over the dye adsorption effect. The best observed performance is reported for the membrane of Nafion-GO that is capable of reducing by 92% the initial MB concentration of 2×10^{-5} M of after 3 hours of irradiation. The most interesting and promising results for MB removal are achieved by using GO_{SULF}. These are described in the following paragraph.

4.3 Effect of the GO sulfonation on the dye removal in water

The organo-functionalization of the GO surfaces with hydrophilic groups such as -SO₃H, improve both the acidity and the water uptake of the resulting nanocomposite membranes, but also their mechanical, chemical, and thermal strength [Enotiadis (2012)]. We expect that this functionalization increases the adsorption properties and selectivity of GO; for this purpose, GO_{SULF} powder is tested for the degradation of MO and MB and its activity is compared with GO itself (see Appendix A11). Figure 4.15a shows the absorbance spectra of MB solution containing GO_{SULF} powder with increasing concentration (10, 70 and 100 mg/l) in dark. GO_{SULF} is able to adsorb MB by electrostatic attraction between sulfonic groups and positive dye molecules. This adsorption increases with powder concentration and occurs immediately in the first minutes, causing the formation of MB-GO_{SULF} precipitates as shown by the inset photos of Figure 4.22a.

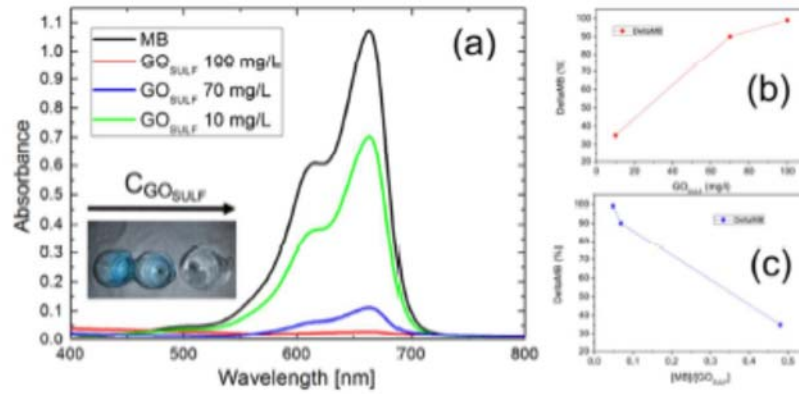


Figure 4. 22 (a) UV–Vis absorbance spectra of MB solution after adding GO_{SULF} powder with different concentrations: 10 mg/l (green curve) 70 mg/l (blue curve) and 100 mg/l (red curve). The initial absorbance of the MB is also reported (black curve). The photo in the inset shows the beakers containing the MB solutions with GO_{SULF} with increasing concentration (from left to the right). In (b) and (c) the removed MB (%) as a function of GO_{SULF} concentration or as a function of the [MB]/[GO_{SULF}] concentration ratio is reported, respectively. Reported from [Scalese (2016)].

In particular, a 35% decrease of MB due to adsorption is observed for a GO_{SULF} content of 10 mg/l (Figure 4.22b). This value is reduced down to ~1% of the initial value by increasing the GO_{SULF} concentration in solution by one order of magnitude (100 mg/l). The % decrease of MB is linearly dependent on GO_{SULF} concentration only in the region where the concentrations are comparable, then it seems to reach a plateau value. In Figure 4.22c the % of MB decrease is reported as a function of the ratio between dye and GO_{SULF} concentrations. The investigated MB concentration is 4.8 mg/l, comparable with the lower GO_{SULF} concentration (10 mg/l). The range [MB]/[GO_{SULF}] between 0.1 and 0.5 should be further studied in order to investigate the linearity of the trend.

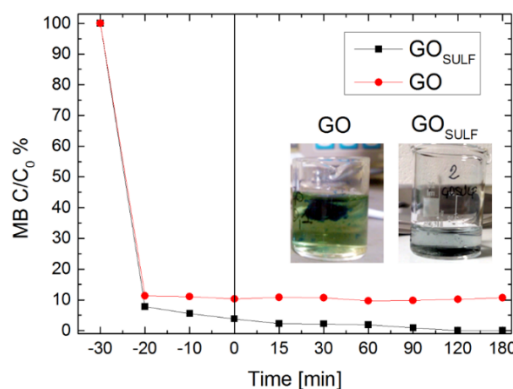


Figure 4. 23 MB residual concentration versus time of contact with GO and GO_{SULF} powders (both with a concentration of 70 mg/l). The UV-blue lamp irradiation starts after 30 min of adsorption in dark, as indicated by the vertical line at t = 0 min. The photos in the inset show the beakers containing the MB solutions with GO_{SULF} and GO after 10 min adsorption (t = -20). Reported from [Scalese (2016)].

In Figure 4.23 the residual concentration of MB in contact with a fixed concentration of GO_{SULF} is compared with GO powders (70 mg/l) versus contact time. After 30 minutes of adsorption in dark, the solution is exposed to UV-blue light irradiation (time zero) up to three hours (see Appendix C). The same experiments have been conducted under irradiation to test its photocatalytic properties. Before these tests, the photostability of GO and GO_{SULF} in water was investigated within the experimental irradiation conditions used in this work but in absence of dyes. Any evident variation in the UV-Vis absorbance spectra of GO materials was observed.

The adsorption occurs immediately for both the materials and is more efficient for GO_{SULF} than for GO, even if the first one is less negative than GO itself. This behaviour can be explained considering that the sulfonilic functionalization induces a larger distance between GO planes, as reported by XRD analysis [Enotiadis (2002)], and, therefore, the accessibility of the active sites to the dye molecules in the two materials is different. In addition, GO_{SULF} acidity is higher with respect to GO. In the first section of this chapter it is shown that GO immediately adsorbs MB and MB-GO flocculates appear in the solution. Furthermore, the MB adsorption on GO layers occurs within the formation of aggregates, according to its superficial properties (i.e. quality and quantity of oxygen moieties). On the contrary, this aggregation does not occur after amine functionalization; in fact, the characteristic peak of MB aggregates at 577 nm is not observed in Figure 4.23a. In addition, GO_{SULF} shows a slightly further MB decrease after adsorption within irradiation, while in GO no effect of irradiation is observed: the MB concentration reaches the minimum value after 10 min in dark and then it is constant. Anyway, we can conclude that the main MB removal occurs by adsorption for both the materials.

As just explained, the use of powders for water purification is not convenient, but the creation of a nanocomposite, which prevents photocatalyst release, is examined (see Appendix A19).

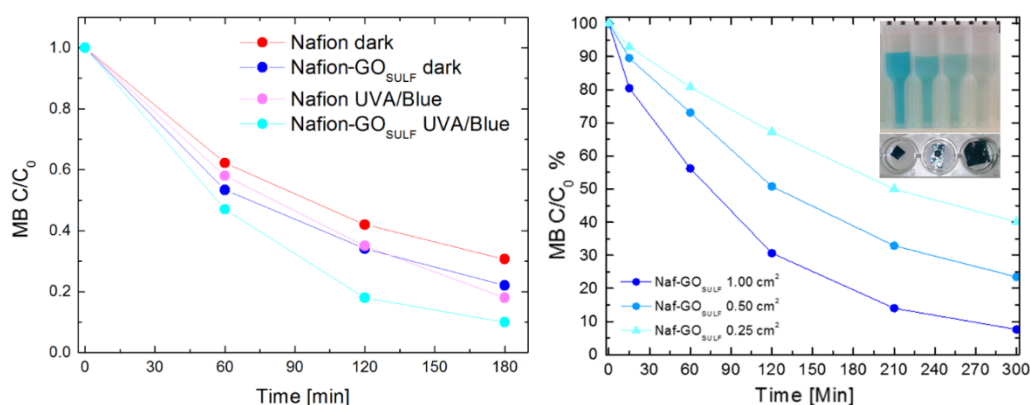


Figure 4.24 *On the left:* MB residual concentration versus time of contact with Nafion and Nafion- GO_{SULF} in dark (red and blue dots, respectively) and under irradiation (magenta and cyan dots, respectively). *On the right:* MB residual concentration versus contact time in dark with Nafion- GO_{SULF} membranes having different surface areas. In the inset we report the pictures of the membranes used for MB adsorption (from left to right: 0.25 cm², 0.5 cm², 1 cm²) and the cuvettes with initial MB solution (first on the left) and solutions after dipping the three Nafion- GO_{SULF} membranes for 5 hours. Reported from [Scalese (2016)].

Figure 4.24 on the left compares the MB degradation activity of Nafion and Nafion-GO_{SULF} membranes in dark and under UV-blue irradiation. In the previous section, it is just explained that Nafion itself can easily adsorb MB. Nafion-GO_{SULF} composite shows better performance than filler-free Nafion membrane, both in dark and under illumination. This result was expected considering that the presence of the filler increases the number of acid sites in the electrolyte (SO₃⁻) available for dye adsorption and also its water uptake and proton conductivity. Figure 4.24 on the right reports the MB degradation ability of Nafion-GO_{SULF} membrane as a function of its size (0.25, 0.50 and 1.00 cm²). The adsorption is linearly dependent on the membrane area as a consequence of the variation of the number of active sites. The highest adsorption i.e. solution decolourization is obtained for the membrane with the highest area, as shown in the photo in the inset. Comparing Figure 4.22 and 4.24, the degradation of MB is larger and faster for GO_{SULF} powders than for the composite, since in the former case the active sites are more accessible to MB molecule with respect to the case in which the MB molecules have to diffuse inside the polymeric matrix.

In order to investigate the role of polymeric matrix in the degradation ability of GO_{SULF}, the results above presented are compared with the ones obtained for the degradation of an anionic dye i.e. MO: in this case the contaminant is electrostatically repulsed by both the polymer and the filler. Figure 4.25 reports the absorbance spectra of MO solution where Nafion membrane, Nafion-GO_{SULF} membrane and GO_{SULF} powder were dipped for one hour in dark and under UVA/blue irradiation, respectively.

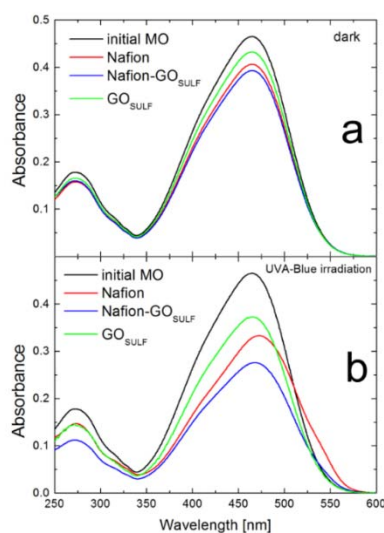


Figure 4. 25 UV-Vis absorbance spectra of MO after immersing Nafion (red curves), Nafion-GO_{SULF} (blue curves) composite membranes and GO_{SULF} powder (green curves) in MO solution for one hour in dark (a) or under UV/blue irradiation (b). Reported from [Scalese (2016)].

As expected, MO adsorption is quite small for all the materials due to electrostatic repulsion: GO_{SULF} powder is able to adsorb about the 6.5% of initial MO and this rises to 15.6 % in presence of the polymer. The MO degradation increases under irradiation, in particular for Nafion-GO_{SULF}. In

presence of filler free Nafion membrane, the absorbance spectrum is shift towards larger wavelength, as a consequence of MO protonation and this aspect is explained in the previous paragraph. In general, Figure 4.26 shows that dispersing the nano-additive inside the polymeric matrix results in an increased degradation activity by increasing the acidity and the water uptake capacity of the polymeric film. After one hour of irradiation, the MO degradation value is of 55% in the presence of Nafion-GO_{SULF} and 82% for GO_{SULF}. In all investigated cases, no toxic by-products, as shown for titania in the previous section, are formed; therefore, the use of Nafion-GO_{SULF} membrane for MO removal seems to be a safer method than the use of the same filler or a photocatalyst like titania as powders directly dispersed in water.

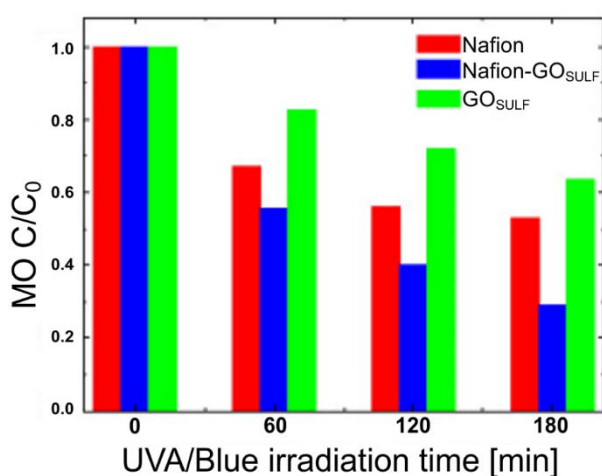


Figure 4. 26 Residual concentration of MO versus time of contact with Nafion (red bar), Nafion-GO_{SULF} (blue bar) and GO_{SULF} (green bar) under UV/blue light irradiation. Reported from [Scalese (2016)].

The irradiation effect has been followed in time and the results are reported in the histogram of Figure 4.26. The MO reduction is larger either in dark or under irradiation when the filler is embedded in the Nafion matrix, within the best performance of 70% for Nafion-GO_{SULF} after three hours. The possible degradation mechanism played by this material is described in the previous paragraph. The reported result is also explained considering that the polymer provides a larger number of active sites for MO absorption and this is also crucial for the photocatalytic process.

In previous paragraph, we showed the possibility to reuse Nafion GO or Nafion TiO₂ nanocomposites: after the first use, the membranes have been washed in water and their activity reduces but, then, it remains stable for the following cycles. This effect is ascribed to a passivation of sulfonic groups; the membranes preparation involves their activation by rinsing in acid media. Therefore, another regeneration process is tested by using 1% nitric acid in DI-water as described in the Appendix A19.

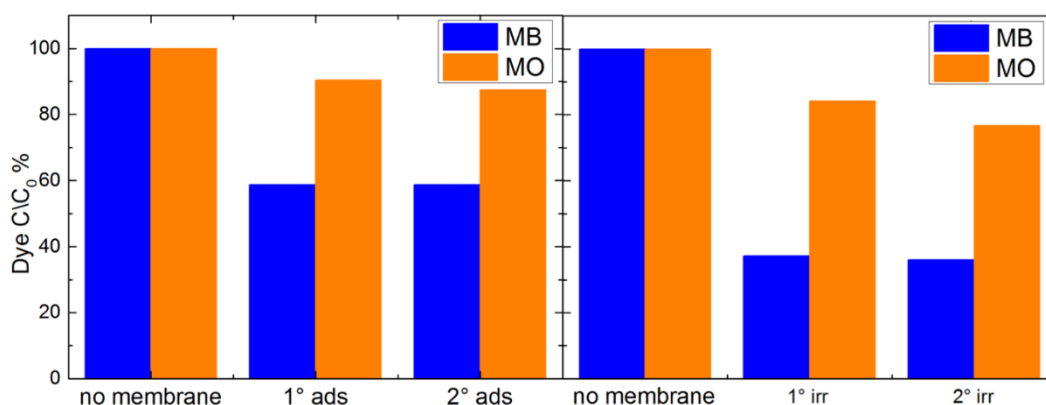


Figure 4. 27 MO and MB residual concentration versus two consecutive (a) adsorption processes for 3 hours in dark or (b) photocatalytic processes for 3 hours, using the same pieces of Nafion-GO_{SULF} membrane. Reported from [Scalese (2016)].

In Figure 4.27 we report MO and MB concentration for two consecutive uses of the same Nafion-GO_{SULF} membranes as adsorbent material in dark (a) or as photocatalytic material (b), after the regeneration process. Respect to the previous tested regeneration process, rinsing the membranes in acid water allows to obtain the same performance, confirming the possibility of regeneration and reuse of these membranes without efficiency loss.

4.4 Sulfonated pentablock copolymer for water purification applications

4.4.1 Materials preparation and characterization

A sulfonated pentablock copolymer (s-PBC) poly-(tBS-HI-sS:S-HI-tBS) solution with 10-12 wt% polymer in a cyclohexane/heptane mixed solvent, was provided by courtesy of Kraton Polymers LLC. The IEC value of the commercial polymer is 2.0 meq/g corresponding to a sulfonation degree of 52 mol%. The molecular weight is 112500 g/mol and the volume fraction (tBS-[sS:S]-HI) is 0.300-[0.226:0.208]-0.266. s-PBC membranes and hybrid s-PBC nanocomposite membranes containing as fillers P25 titania (>99.5%) nanoparticles (s-PBC-TiO₂), β-Bi₂O₃ (90-210 nm particle size, 99.8% trace metals basis) nanoparticles (s-PBC-BO) or GO (Graphenea 4 mg/ml) (s-PBC-GO) were prepared by the solvent casting method. In particular, 2.5 g of commercial s-PBC solution were dried at about 60 °C to get the evaporation of the commercial solvents and then dissolved in 10 mL of DMF (as revealed by the clear colour of the solution). Finally, the suspension was cast on a Petri dish at 60 °C overnight for the complete evaporation of the solvent. In the case of nanocomposites, the filler solution (12 mg of nanofiller completely dispersed in 10 mL of DMF) was added slowly to the DMF

polymer solution prepared as described above. This final solution was stirred for several hours to get a homogeneous mixture. Then it was stirred at 80°C until the final volume was around 10 mL and the solution was dense enough to be cast as described for the s-PBC membrane; afterwards the membranes were removed from the Petri dish by dipping the glass plate in deionized water for several minutes. The membranes were soaked and washed in deionized water (Millipore Advantage A10) at room temperature in order to remove eventual impurities, such as residual acids, until the soaking solution stabilized at neutral pH.

The membranes were morphologically and chemically characterized before testing their photocatalytic activity. SEM images of the nanocomposite membranes in cross section (see Appendix A4) within the relative photos in the insets are reported in Figure 4.28. The s-PBC membrane (a) is quite smooth and homogeneous; the presence of small irregular vertical lines is due to the breaking of the membrane intentionally produced for cross section analysis. In the case of s-PBC-BO (b), nanoparticles are not visible in the polymeric matrix neither at higher magnification. For comparison, Figure 4.28c reports the SEM image of commercial bismuth oxide, showing spherical particles mainly having a diameter in the range between 50 nm and 250 nm (particles with diameter above 500 nm are present in a lower amount). The fact that bismuth oxide nanoparticles are not evident in the nanocomposite suggests that the filler is completely and homogeneously dispersed throughout the entire volume of the polymeric matrix. In the case of s-PBC-GO (d) and s-PBC-TiO₂ (e) the filler is completely and homogeneously dispersed through the entire volume of the polymeric matrix, in the former one the nanocomposite membrane shows a spongy structure, with graphitic planes well visible; in the latter case some agglomerates of titania nanoparticles are evident. The thickness of all the membranes is about 100-110 μm. The presence and the chemical composition of the fillers in the membranes are verified by other analyses as shown below.

The first effect of dispersing nanomaterials inside the polymer is a change of the water uptake values with respect to filler-free s-PBC, as reported in table 4C.

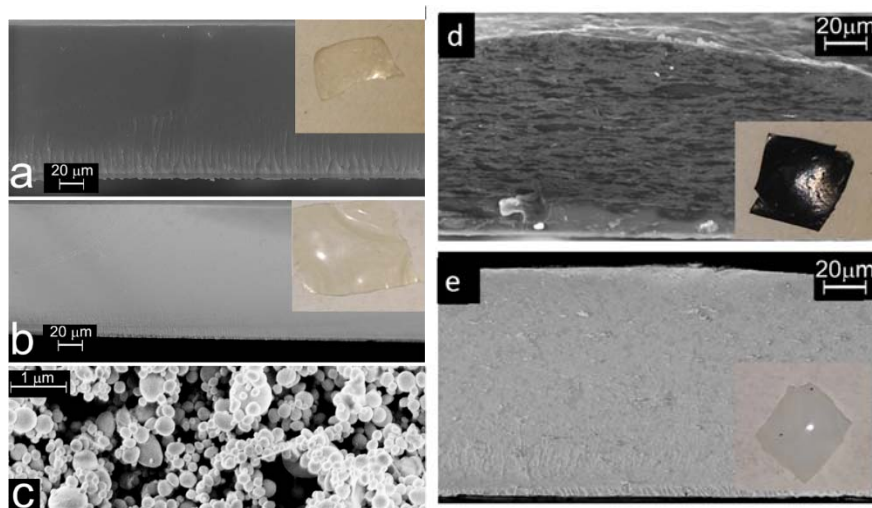


Figure 4. 28 Cross-sectional SEM images and relative photos of (a) s-PBC and (b) s-PBC-BO membranes, (c) SEM image of the as-received β -Bi₂O₃ nanoparticles. Cross-sectional SEM images and relative photos of (d) s-PBC-GO and s-PBC-TiO₂ (e) membranes.

Table 4C Water uptake values for s-PBC and nanocomposites.

s-PBC	201 %
s-PBC-GO	308 %
s-PBC-TiO₂	182 %
s-PBC-BO	224 %

The main effect is observed for s-PBC-GO due to its highly porous structure within the hydrophilic character of GO. On the contrary, for titania nanocomposites the water uptake value is lower with respect to the filler free polymer as a result of titania agglomeration inside the polymeric matrix. Figure 4.29 shows Raman spectra of s-PBC (black curve), s-PBC-TiO₂ (green curve) and s-PBC-GO (red curve) acquired according to Appendix A2. The spectrum of s-PBC-BO is not reported since this does not add any information. The Raman spectrum of s-PBC confirms that the polymer structure remains unaltered after film preparation although this is prepared re-dispersing the commercial polymer into the DMF polar solvent. The observed Raman peaks for s-PBC are in agreement with those reported in the literature [Fan (2013)]. The assignments are reported in the following table.

Table 4D – Assignment of the Raman peaks to the vibrational mode as reported in [Fan (2013)].

Raman shift [cm⁻¹]	Peak assignment
619	Aromatic ring deformation
641	$\delta(\text{SO}_2)$ of sulfone, sulfonate, and sulfonic acid
692	Skeletal stretch of <i>t</i>-butyl phenyl group
797	$\nu(\text{CS})$ and vibrational mode of phenyl group
1001	Aromatic ring $\nu(\text{CC})$
1031	$\nu_s(\text{SO}_3^-)$ of sulfonate ion and polystyrene
1110	<i>p</i>-substituted of aromatic ring
1127	$\nu_{\text{as}}(\text{SO}_3^-)$
1155	CC stretch
1198	Aromatic ring vibration

In the case of s-PBC-TiO₂, it is possible to observe the above mentioned peaks of the polymer itself within characteristic peaks related to titania at 136, 397, 515 and 638 cm⁻¹ (indicated by the magenta stars), associated respectively to the *E_g*, *B_{1g}*, *A_{1g}* & *B_{2g}*, and *E_{2g}* modes of the anatase phase. The latter peak is due to the superposition of two signals: the sulfonilic bending of the polymer and *E_{2g}* modes of titania. On the contrary, in the case of s-PBC-GO, only the characteristic G and D bands for GO [Filice accepted to RSC] are visible: the absorption coefficient of GO at the laser wavelength, block the incoming radiation and limits the detection of the overall Raman signal to few hundreds nanometers, thus limiting the collection of the polymeric Raman features.

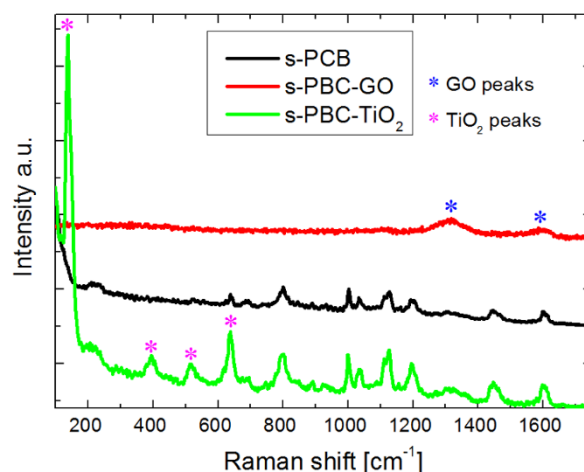


Figure 4. 29 Raman spectra of the s-PBC polymer (black curve) and of the hybrid composite with TiO₂ (green curve) and GO (red curve). The stars indicate the peaks associated to the graphene oxide and crystalline titania phase. Reported from [Filice accepted to RSC].

XRD analysis was performed, according to Appendix A16 in order to investigate the crystallinity degree of the organic–inorganic composite membranes and to have information on the grade of nanomaterial dispersion inside the polymeric matrix (Figure 4.30).

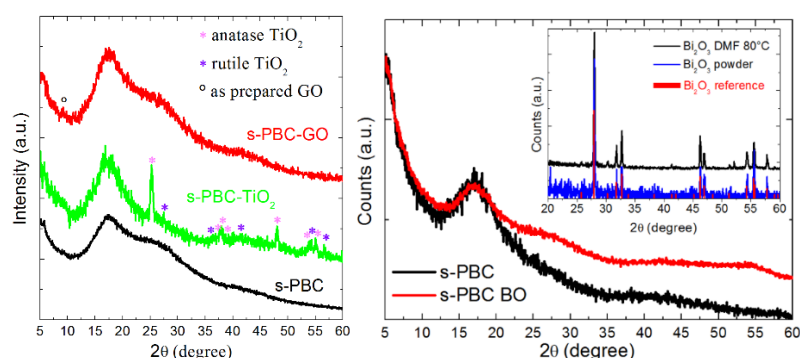


Figure 4. 30 *on the left*: XRD spectra of the s-PBC Polymer (black curve) and the hybrid composites s-PBC-TiO₂ (green curve) and s-PBC-GO (red curve). The pink and violet stars indicate the peaks associated to the anatase and rutile titania phases, respectively, while the circle evidences the diffraction peak related to GO. *on the right*: XRD patterns of the s-PBC Polymer (black curve) and the hybrid composites s-PBC-BO (blue curve). In the inset XRD patterns of commercial β-Bi₂O₃ nanoparticles (blue curve) and after being treated at 80°C in DMF.

Figure 4.30 shows the XRD spectra of filler free membrane and nanocomposites. In particular the XRD analysis of s-PBC-BO is reported in the graph on the right within a comparison with the XRD patterns of (i) the commercial β-Bi₂O₃ nanoparticles before (blue curve) and (ii) after being treated in DMF at 80°C in the same conditions used for membrane preparation (black curve), but without the polymer and (iii) the reference XRD peak positions of β-Bi₂O₃ (red bars, PDF#27-0050). These spectra are reported in the inset. According to [Filice,D’Angelo (2017)], all the polymeric membranes show a broad peak at 17° corresponding to a *d*-space value of 2.6 Å: this broad peak is typical of an

amorphous structure. In addition, XRD analysis are in agreement with morphological characterization. For s-PBC-TiO₂, the characteristic XRD peaks related to the anatase and rutile crystalline phases of the nanofiller are visible, confirming that titania is agglomerated inside the matrix. In the case of s-PBC-GO, on the contrary, the expected peak of GO at 10° is not clearly evident in the XRD spectrum, indicating that GO is completely dispersed and mixed within the polymer. Figure 4.30 on the right shows the comparison of crystalline phase of the composite s-PBC-BO with initial β -Bi₂O₃ nanoparticles and after being treated in the same conditions as composite preparation but without the polymer. It is shown that the solvent and the temperature do not modify the particles in absence of s-PBC. As for SEM characterization, the XRD pattern of s-PBC-GO does not contain the peaks of the β -Bi₂O₃ phase confirming its complete dispersion inside the polymeric matrix within a reduction of its dimension with respect to commercial particles. Anyway, the effective presence of Bi-based nanoparticles in the composite is confirmed by other analysis reported below. As a consequence, these results suggest a modification of the filler induced by the polymer during the preparation of membranes. Furthermore, another peak is evident for all the polymeric materials. The shoulder around 28°, that is more evident for s-PBC and s-PBC-GO with respect to s-PBC-TiO₂, is ascribed to the sulfonic groups inside the polymer, or in more detail, to the presence of water. These results are in good agreement with the water uptake values reported in table 4C: the peak at 28° is less evident for the materials with the lowest water uptake i.e. s-PBC-TiO₂. This can be explained considering that TiO₂ particles are aggregated inside the polymer and, probably, these interact with the sulfonic groups. Furthermore, s-PBC has a micellar structure that change depending on the choice of the solvent (polar or apolar) used. The interaction of micellae with nanofillers could depend on the morphology of the fillers (flakes vs spheres) and their chemical (electrostatic or hydrophobic) interactions with the polymers. These aspects result in a different distribution of nanofillers inside the polymer. Further specific morphological investigations will be conducted to better explain this aspect.

The presence and chemical composition of bismuth oxide is verified by comparing XPS spectra of s-PBC and s-PBC-BO acquired according to Appendix A3 and reported in Figure 4.31.

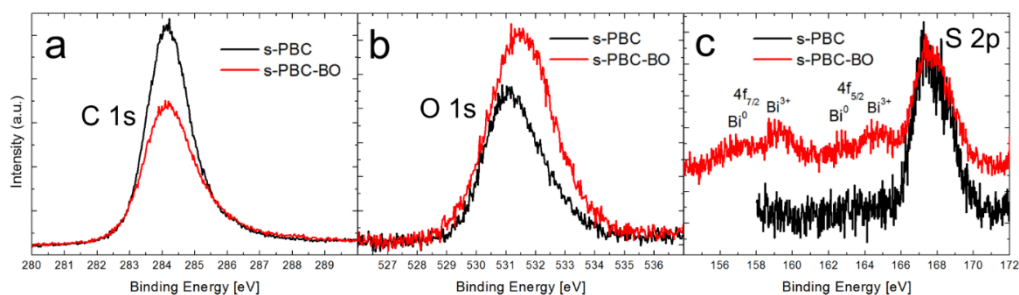


Figure 4. 31 XPS spectra of s-PBC (black curve), s-PBC-BO (red curve) membranes showing the (a) C1s, (b) O1s and (c) Bi4f and S2p peaks. Reported from [Filice submitted to Catalysis Today].

The peak at 284.2 eV in the C 1s XPS spectrum of both the s-PBC and the composite membranes is related to the carbon sp^2 bonds of the polymeric chain. The O 1s spectrum for s-PBC shows a large peak related to sulfonic groups (531.1 eV). For the composite, this peak is broader with respect to the one for s-PBC and shifted towards higher binding energy, 531.4 eV, due to the contribution of Bi-O bonds at 531.9 eV [Barreca 2001]. The S 2p peak is centered at 167.5 eV for both s-PBC and s-PBC-BO; for the composite we can observe other four peaks due to Bi 4f in the region 156 eV-166 eV [Barreca (2001)]: these peaks are related to the characteristic binding energies of Bi $4f_{7/2}$ and $4f_{5/2}$ of the oxidation state of Bi^{3+} and elemental Bi (Bi^0), the former at 159.2 and 164.4 eV and the latter at 157.8 and 163.3 eV, respectively. The measured Bi^0/Bi^{3+} intensity ratio is 0.6. XPS spectra confirm the presence of Bi_2O_3 inside the polymer within its reduction to elemental bismuth due to the acidity of sulfonic groups, as reported in [Li (2012)]. In fact, in the Bi 4f XPS spectrum of nanoparticles treated at 80°C in DMF without the polymer, no reduction related to the procedure in DMF was observed, thus confirming the role played by sulfonic groups acidity in reducing bismuth oxide (Figure 4.32). Furthermore, the intensity ratio S2p/C1s peaks for s-PBC-BO is reduced to a value of about 55% with respect to the s-PBC membrane confirming a loss of sulfonic groups in the composite membrane. In other words, sulphur is oxidized during composite preparation and released in the solution as a consequence of bismuth oxide reduction.

To summarize, the presence of bismuth inside the polymeric matrix is not evidenced by morphological and XRD characterization, but its presence is confirmed by XPS analysis, that also shows the reduction of Bi^{3+} to elemental Bi. Elemental Bi have dimension in the order of few nanometers, as shown by the results reported in Chapter 3, and this is the reason why they are not detected by SEM or XRD characterization. XPS spectra of s-PBC-GO and s-PBC- TiO_2 are not reported since they do not add useful information.

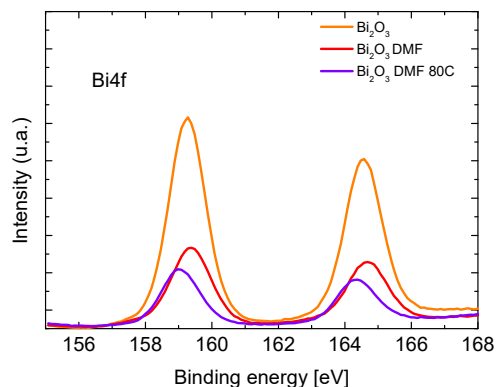


Figure 4. 32 Bi 4f XPS spectra of commercial bismuth oxide nanoparticles (orange curve), and the same dispersed in DMF at room temperature and at 80°C (red and purple curves, respectively).

The amount of elemental bismuth and bismuth oxide is also estimated by TGA analysis acquired according to Appendix A20 (Figure 4.33).

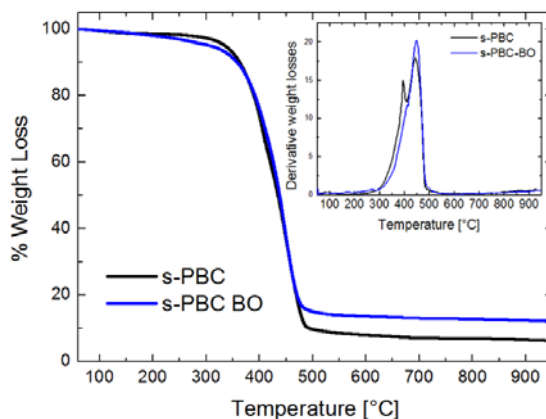


Figure 4. 33 TGA analysis showing the overall thermal weight losses and the derivative weight losses (see inset) as a function of temperature for s-PBC (black curves) and s-PBC-BO (blue curves) membranes. Reported from [Filice submitted to Catalysis Today].

s-PBC exhibits three distinct degradation steps (Figure 4.33): below 150°C, the small weight loss of about 5% is due to the removal of residual water within the membrane. The second weight loss between 260–400 °C is due to the de-sulfonation process and the last one, above 400 °C, is associated to thermal degradation of the polymer backbone. In the inset of Figure 4.33 the derivative of weight loss for the polymer and the composite between 50°C and 950°C is reported, showing two main peaks related to the above mentioned second and third steps. For s-PBC (black curve), the thermal degradation of sulfonic groups occurred rapidly and completely as suggested by the fact that the first peak at 395°C is very sharp, whereas the backbone degradation occurred at 444°C. The s-PBC-BO is more stable with respect to the filler free polymer: the thermal decomposition of the backbone

is slightly shifted to 450°C and the peak related to the sulfonic groups shows a lower intensity and/or a shift towards higher temperature. This confirms the previous hypothesis i.e. sulfonic groups are involved in the reduction process of bismuth oxide. The presence of elemental Bi is confirmed by the peak at 273°C visible in the DTGA curve of the composite within a different slope in the TGA curve in the same temperature range. The calculated amount of filler in the composite, is 5.7% weight percent with respect to the polymer, while the amount of elemental Bi is 2.55%. This means that 43.85% of initial Bi₂O₃ is converted to elemental bismuth during the membrane preparation. The Bi⁰/Bi³⁺ ratio has a higher value, 0.9, with respect to the one calculated by XPS analysis (i.e. 0.6). This is not surprising considering that XPS analysis is a surface technique while TGA gives information on the whole sample. For comparison, Figure 4.34 shows the TGA and DTGA curves for the other two composites, compared with s-PBC. As for s-PBC and s-PBC-BO, the TGA curves show the same three distinct weight step losses. Some differences are observable in the DTGA curves (Figure 4.34 b). For s-PBC-GO the thermal decomposition is shifted to 451 °C and the peak at about 395 °C is only a shoulder, suggesting a modification of the sulfonic contribution. On the contrary, for s-PBC-TiO₂, the curve shows a different shape with respect to the other ones: the first peak is as sharp as in the case of the polymer, but more intense, whereas a significant decrease of the second peak intensity is observed. This composite is more thermally unstable with respect to the other materials, maybe due to a different interaction of TiO₂ with the sulfonic groups. Therefore, thermogravimetric analyses confirms that the inorganic particles and the GO layers disperse in a different way within the polymeric matrix, in agreement with the XRD analysis.

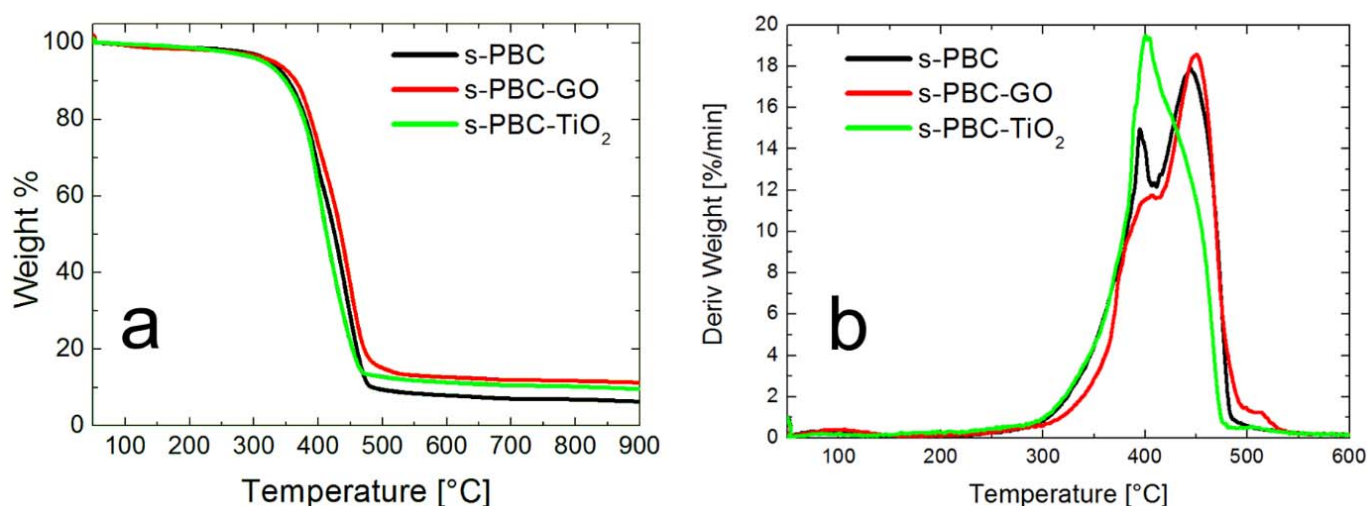


Figure 4.34 TGA analysis showing the overall thermal weight losses (a) and the derivative weight losses (b) as a function of temperature for s-PBC polymer (black curves) and hybrid membranes with TiO₂ (green curves) and GO (red curves). Reported from [Filice,D'Angelo (2017)].

4.4.2 s-PBC hybrid nanocomposite membranes for dye removal

The s-PBC polymer and its composites are investigated for the removal of cationic and anionic dyes, comparing these results with the ones obtained for Nafion materials. The s-PBC is not only cheaper than Nafion, but it has higher acidity and hydrophilicity: this is confirmed by the water uptake values (i.e. 24% for Nafion and 201% for s-PBC) and the IEC values (i.e. milliequivalents (meq) of sulfonic acid per gram of dry polymer) of the two polymers (i.e. 0.9 and 2.0 meq/g for Nafion and s-PBC, respectively). In other words, the density of the sulfonated groups is higher for s-PBC with respect to Nafion. Figure 4.36 shows the residual methylene blue concentration for the solutions where the s-PBC membrane and the composites were immersed for three hours in dark (blue bars) or under irradiation (cyan bars), as calculated by the variation of the dye monomer peak. The emission spectra of used lamps compared with the absorbance spectra of s-PBC materials are reported in Appendix C.

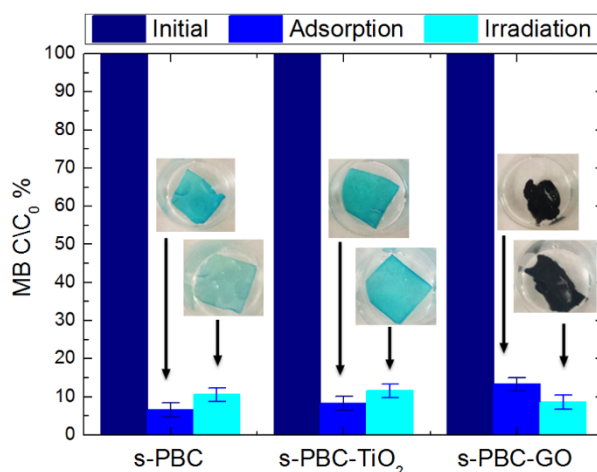


Figure 4. 35 Residual concentration of MB after three hours in contact with s-PBC, s-PBC-TiO₂ and s-PBC-GO in dark (blue bars) or under UVA/blue light irradiation (cyan bars). The navy blue bars represent the initial MB concentration (i.e. 1.5×10^{-5} M). Reported from [Filice,D'Angelo (2017)].

Membranes change their color to blue, due to the interaction with MB (photos of Figure 4.35) with the exception of s-PBC-GO, in this case no evident color change is observed since its initial color is black. On the contrary respect to the use of powders directly dispersed in water (shown in Paragraph 1 of this Chapter), MB is removed immediately and without the formation of any precipitates or flocculates. The results are explained considering the electrostatic attractions between MB positive superficial charge and the negative charge of sulfonic groups present on the membranes: all the materials are able to remove more than the 90% of the initial MB concentration either in dark or under irradiation. For s-PBC-GO, the degradation efficiency is higher under irradiation, while the s-PBC and the s-PBC-TiO₂ membranes show the best efficiency in dark. This aspect is better explained in

the following discussion by a more careful analysis of the absorbance spectra. Compared to the initial MB spectrum (blue curves), the shape of the absorbance spectra of the dye solutions changed after being in contact with the membranes in dark or under irradiation for three hours (Figure 4.36). In particular, for the adsorption process, MB dimers are predominant with respect to the peak of the monomer for all the membranes (see inset of Figure 4.36a) and the best performance is recorded for s-PBC. In the case of irradiation, monomers and dimers are almost the same except for s-PBC-TiO₂, in this case the monomer peak is higher than the one related to the dimers.

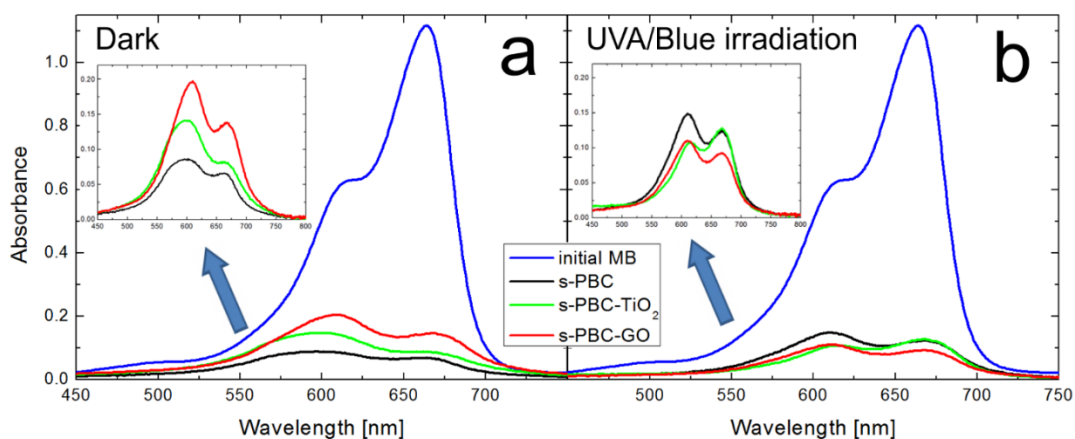


Figure 4.36 UV-Vis absorbance spectra of initial MB solution (blue curve) and of the dye solution after adsorption in dark (a) and after UVA/blue irradiation (b) for three hours in the presence of s-PBC (black curves), s-PBC-TiO₂ (green curves) and s-PBC-GO (red curves) membranes. In the insets, the magnification of the absorbance spectra for the three membranes after three hours are reported. Reported from [Filice, D'Angelo (2017)].

Observing all the spectra acquired for the adsorption and irradiation processes of all the materials with increasing contact time (Figure 4.37), it is possible to affirm that the kinetic of monomer and aggregates formation depends on the type of process and on the specific material. The MB absorbance spectra were deconvoluted in three main components related to monomers at 664 nm, dimers at 610 nm and higher order aggregates of the dye at 577 nm, respectively. Figure 4.38a shows an example of deconvolution of the MB UV-Vis absorbance spectrum in the aforementioned main components, while Figure 4.38b, c, d report the residual concentration of each of these components versus time of contact with s-PBC, s-PBC-TiO₂ and s-PBC-GO, in the dark (closed symbols) and under irradiation (opened symbols), respectively.

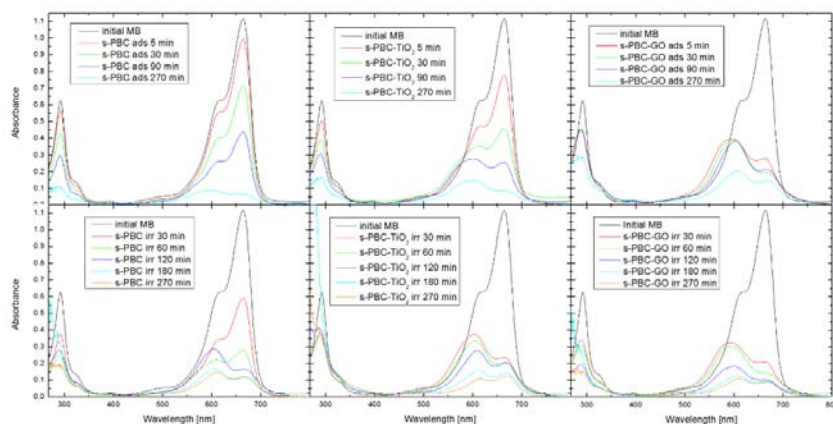


Figure 4.37 Uv-Visible absorbance spectra of MB solution with time in dark (top graphs) and under irradiation (bottom graphs) in the presence of s-PBC, s-PBC-TiO₂ and s-PBC-GO membranes. Reported from [Filice,D'Angelo (2017)].

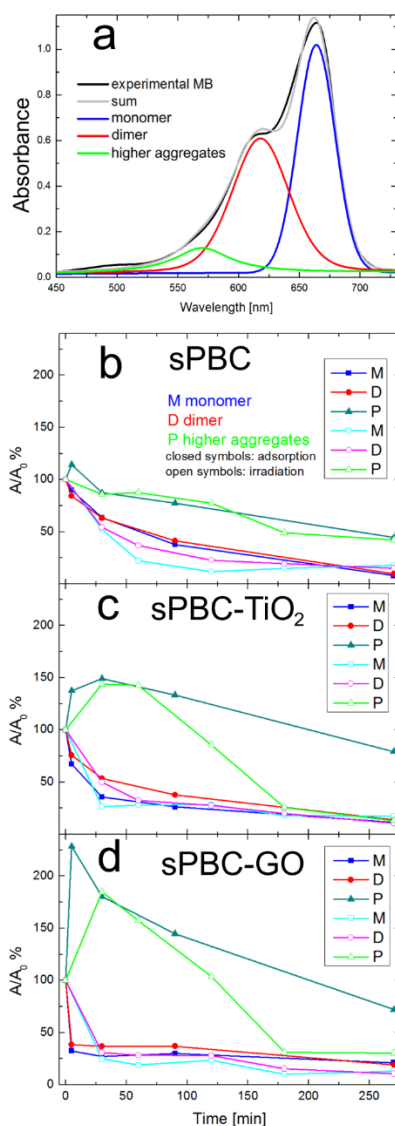


Figure 4.38 (a) Deconvolution of MB UV-Vis absorbance in three main components related to the monomer (M), dimer (D) and higher aggregates (P) forms of the dye. Residual concentration versus time of contact with s-PBC (b), s-PBC-TiO₂ (c) and s-PBC-GO (d) in the dark (closed symbols) and under irradiation (opened symbols) for dye monomers (M), dimers (D) and higher aggregates (P), respectively. Reported from [Filice,D'Angelo (2017)].

In the presence of s-PBC polymer (Figure 4.38b), during the adsorption process, MB monomers and dimers decrease linearly with time. In the first 5 minutes, higher order aggregates are formed and then they are adsorbed. Anyway, their final concentration in solution remains higher than the monomer and dimer ones. Under irradiation, the removal efficiency of monomers and dimers is the same as adsorption but it is faster at the beginning. For higher aggregates, the photocatalytic degradation is slower and very similar to the trend shown during adsorption.

Figure 4.38c,d show the kinetic of degradation/formation of monomers, dimers and higher aggregates in the case of s-PBC-TiO₂ and s-PBC-GO, respectively. As for s-PBC, monomers and dimers decrease with time due to their adsorption and finally, they reach almost the same residual concentration. Higher order aggregates are formed in the first minutes of contact with s-PBC-TiO₂ and even faster for s-PBC-GO. By comparison with the case of s-PBC, the higher aggregates formation is faster for the nanocomposites but their final concentration remains higher than the dimer and monomer concentrations. Under irradiation (open symbols), monomers and dimers decrease rapidly with time until the same final value, larger aggregates are formed in the first minutes but finally their removal efficiency is higher with respect to their adsorption.

In summary, all the membranes are able to remove monomers and dimers with time, independently on the specific process. On the contrary, higher order aggregates are formed in the first minutes of contact with the membranes, in particular for s-PBC-GO, where also GO favors dye aggregation, and then decrease. The higher efficiency in the removal/degradation of larger aggregates are shown by the nanocomposites under irradiation.

The presence/formation of aggregates larger than dimers is not evidenced in the results reported for Nafion nanocomposites. A possible explanation concerns the structural differences between the two sulfonated polymers and/or a modification of the ionic strength of dye solutions due to a possible release of ions by s-PBC membranes. Furthermore, Nafion is less efficient in MB removal with respect to s-PBC: the degradation efficiencies for MB removal in presence of Nafion is of 70% and 80% in dark or under irradiation, respectively. Otherwise, the s-PBC polymer is able to remove more than 90% of MB in the same experimental conditions. This higher efficiency within the formation of MB aggregates is ascribed to the higher density of sulfonilic groups in s-PBC with respect to Nafion. No evident difference are observed in the final value of adsorption efficiency for s-PBC and composites with titania and GO, since this process is fast and mainly ascribed to the negative charge of sulfonilic groups of the polymer. The main effect evidenced by the introduction of the fillers in s-PBC is an increased capacity to form MB aggregates (as shown in Figures 4.37 and 4.38), probably due to an increased porosity and surface area of the materials. Another explanation could be ascribed to the morphology of these materials: spherical or layers like nanoparticles can affect the re-

organization of polymer micellae and the orientation of sulfonic groups i.e. of the adsorption sites. These aspects will be the subject of future investigation.

Analogously to what explained for the case of Nafion membranes, the adsorption of MO on s-PBC membranes is hindered, due to the electrostatic repulsions between the negative molecular charge of the dye and the negative charge of sulfonic groups in the polymer. As shown in Figure 4.39 and in contrast respect the results obtained for Nafion nanocomposites, s-PBC and its composites are not able to adsorb the dye even after 24 hours in contact with MO solutions (Figure 4.39a). Under irradiation (Figure 4.39b), only a moderate (20%) degradation efficiency for the composite with titanium dioxide is obtained. Anyway, the degradation efficiency shown by this composite is low with respect to what expected considering the presence of titania. This means that dye molecules do not enter in contact with the photocatalyst as confirmed by adsorption tests. For this reason, the experiments were repeated at pH value of the dye solution down to 2 by adding hydrochloric acid, so MO has a positive charge derived from its protonation. This aspect is deeply explained in Paragraph 4.2.2. In fact, s-PBC membranes are able to adsorb protonated MO molecules and show a photocatalytic activity (Figure 4.40).

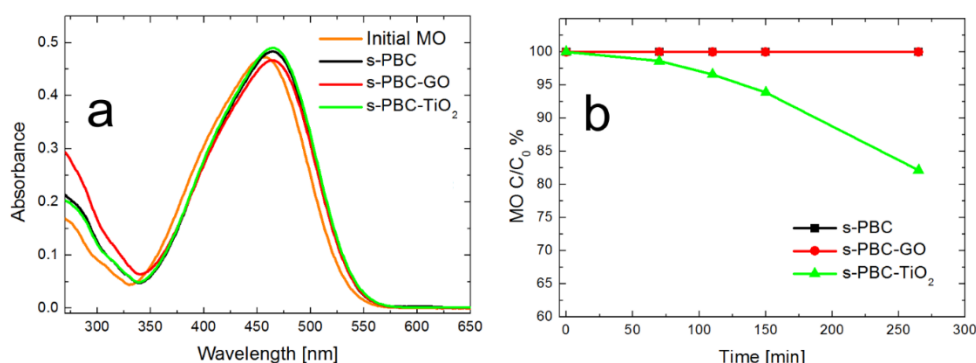


Figure 4. 39 (a) UV–Vis absorbance spectra of initial MO solution ($C = 2 \times 10^{-5}$ M) and of dye solutions in contact with s-PBC (black curve), s-PBC-TiO₂ (green curve) and s-PBC-GO (red curve) for one day in dark at pH 6. (b) Residual MO concentration versus time of contact of MO solutions at pH 6 with s-PBC (black curve), s-PBC-TiO₂ (green curve) and s-PBC-GO (red curve) under UVA-Blue light irradiation. Reported from [Filice,D’Angelo (2017)].

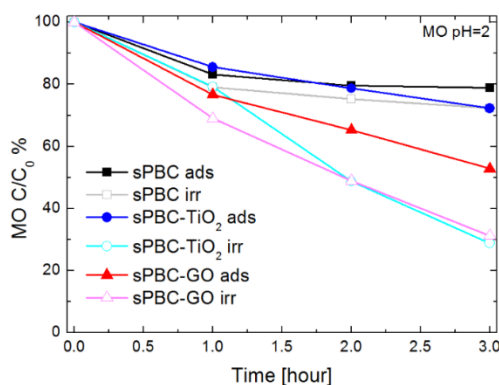


Figure 4. 40 Residual concentration of MO at pH=2 versus time of contact with s-PBC (squared symbols), s-PBC-TiO₂ (circular symbols) and s-PBC-GO (triangular symbols) in dark (closed symbols) or UVA/Blue light irradiation (open symbols). The initial MO concentration is 2×10^{-5} M. Reported from [Filice,D’Angelo (2017)].

At acid pH, s-PBC is able to adsorb more than the 20% of initial MO concentration after three hours, and a similar effect is observed for the membrane with TiO₂. GO enhances the MO adsorption that passes from the 20% for the filler free polymer the 50% for the composite. In particular, s-PBC-GO membrane shows the higher MO removal efficiency after one hour of irradiation. This is explained considering the highly porosity of s-PBC-GO (shown by SEM images) and by the measurement of the water uptake that is the highest one among the investigated samples. As for Nafion materials, irradiation has the effect of increasing both the total efficiency and the degradation rate for all the materials: the best performances are shown by both the composites with TiO₂ and GO that are able to remove about 75% of the initial dye concentration.

For a better understanding of the photocatalytic process, the UV-Visible absorbance spectra obtained for all the processes and investigated materials are reported in Figure 4.41 within the photos of the membranes tested after the adsorption and irradiation processes. As just said, s-PBC is able to reduce MO concentration in acid condition with a more significant effect under irradiation with respect to adsorption. In the former case, a slight increase of the absorbance curve below 300 nm is visible. After both processes, the s-PBC membranes changes its colour to red due to the contact with (and adsorption of) MO molecules. The absorbance spectra of the polymer before and after the adsorption process are reported in Figure 4.41d: after the adsorption process an absorbance peak the at 520 nm is visible, confirming that these are adsorbed into the polymeric matrix without any dye degradation. This means that the degradation of MO by the polymer is due mainly to an adsorption phenomenon that is enhanced under irradiation. For a comparison of the irradiance spectrum of the lamp used for the irradiation with MO absorbance spectrum see Appendix C.

The s-PBC-GO composite shows the best removal efficiency in removing MO, but no information are provided by the absorbance spectra of the membranes after the processes in MO (Figure 4.41e) due to the fact that initial membranes are black. In other words, GO dispersed in the polymer changes the optical properties of the polymer itself leading to the absorption of light in the whole investigated region.

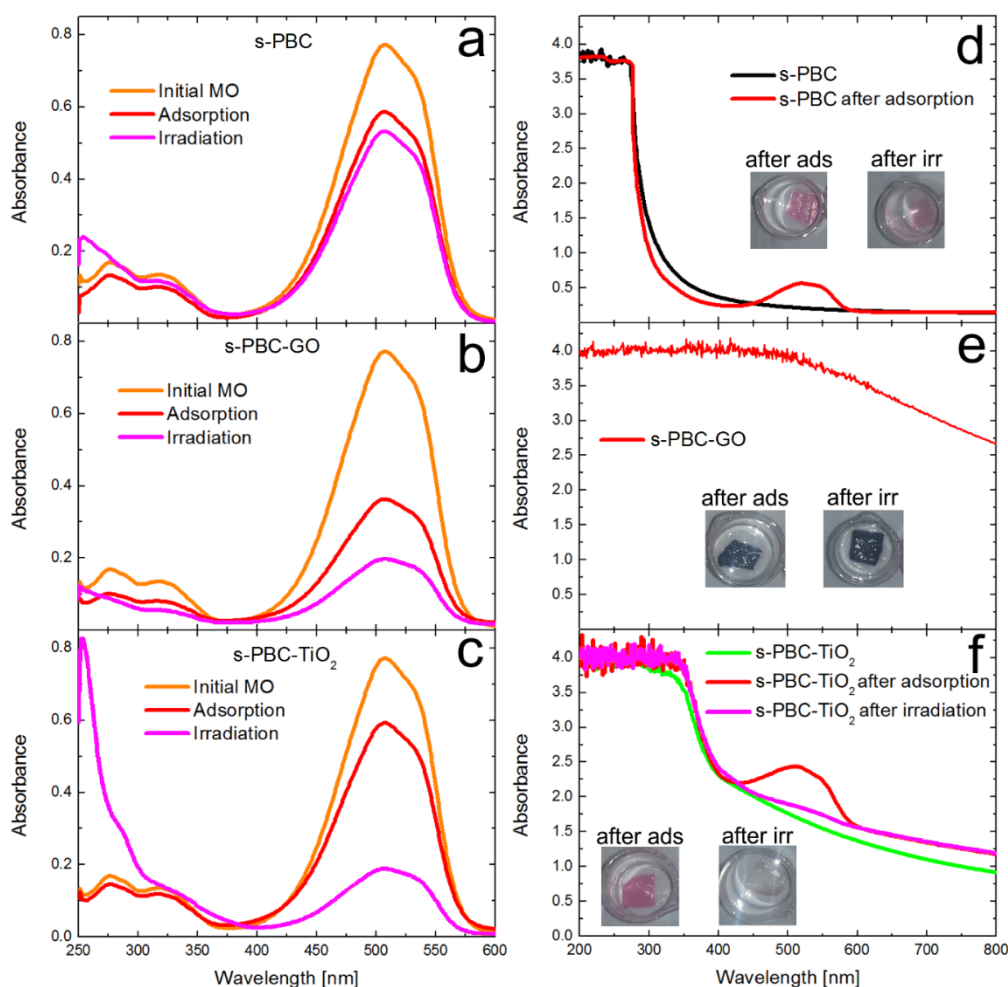


Figure 4.41 UV-Visible absorbance spectra of MO solutions where (a) s-PBC, (b) s-PBC-GO and (c) s-PBC-TiO₂ membrane were immersed at acid pH in dark or under irradiation. UV-Visible absorbance spectra and photos of (d) s-PBC, (e) s-PBC-GO and (f) s-PBC-TiO₂ membranes before and after the irradiation and the adsorption processes. Reported from [Filice,D'Angelo (2017)].

In the case of s-PBC-TiO₂ (Figure 4.41c), the best performance is recorded under irradiation within the appearance of a strong peak below 300 nm suggesting the formation of by-products generated by photocatalytic degradation (explained in Paragraph 4.2.2). The colour of the membrane put in contact with MO in dark turns to red, while the piece under irradiation remains almost unchanged. This experimental observation is in agreement with the recorded absorbance spectra of s-PBC-TiO₂ before and after being in contact with MO solution in dark and under irradiation. The nanocomposite absorbance spectrum shows an absorption edge at about 380 nm, while the filler-free polymer has an absorption edge at about 275 nm. The MO-related peak appears after the process in dark confirming the adsorption ability of the composite; this peak is not observed after the irradiation process, corroborating the evidence of photocatalytic degradation with no significant adsorption effect. For a clearer investigation of the degradation mechanisms, Figure 4.42 reports a comparison among the absorbance spectra of MO solutions (at pH = 2) put in contact with the two nanocomposites

showing the best performance. The initial MO spectrum at pH = 2 is also reported as a reference. The best performance in dark is recorded for the composite with GO, due to its high porosity and hydrophilicity with respect s-PBC-TiO₂. Under irradiation, the two nanocomposites show the same efficiency. However, in the case of s-PBC-TiO₂, the formation of aromatic toxic by-products is evidenced by the peak below 300 nm (explained in Paragraph 4.4.2). This confirms the photocatalytic degradation of MO. In the case of s-PBC-GO, these by-products are not observed, so MO dye removal from water is achieved in a safer way by using s-PBC-GO membrane instead of a s-PBC-TiO₂ membrane.

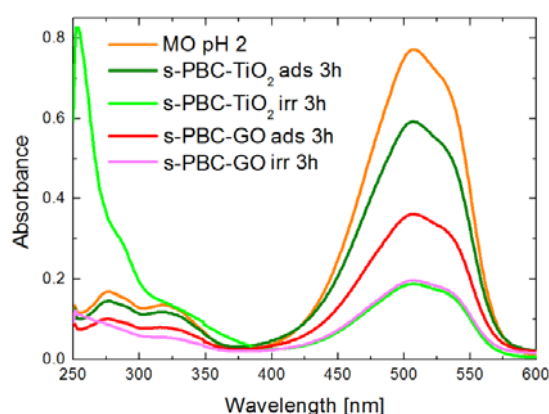


Figure 4. 42 UV–Visible absorbance spectra of MO solution at pH = 2 in dark or after irradiation for three hours in the presence of s-PBC-TiO₂ (green and light green curves) and s-PBC-GO (red and magenta curves). Reported from [Filice,D’Angelo (2017)].

In order to investigate the MO degradation mechanism for s-PBC-GO, a simple test was performed to discriminate between the two main hypothesis on the degradation pathway: (1) by-products are formed in solution but immediately removed by adsorption on the same membrane or (2) MO is just adsorbed without degradation (no by-products formation). For this purpose, s-PBC-GO was put in contact with two solutions containing the by-products (highlighted by the absorbance peak at about 300 nm) for one, two and three hours in dark or under irradiation. In this way is possible to investigate the effect of s-PBC.GO on in order to verify the effect on the by-products. The contaminated solutions were produced under 3 hours of irradiation in the presence of two pieces of s-PBC-TiO₂. Their UV–Vis absorbance spectra are reported in Figure 4.43a (dark condition) and Figure 4.43b (irradiation). The membranes are able to remove the MO molecules but are inefficient in removing toxic by-products both in dark and under irradiation. Therefore, the hypothesised mechanism for s-PBC-GO does not involve the formation of toxic by-products, confirming this material safer with respect to the use of s-PBC with titania for MO degradation.

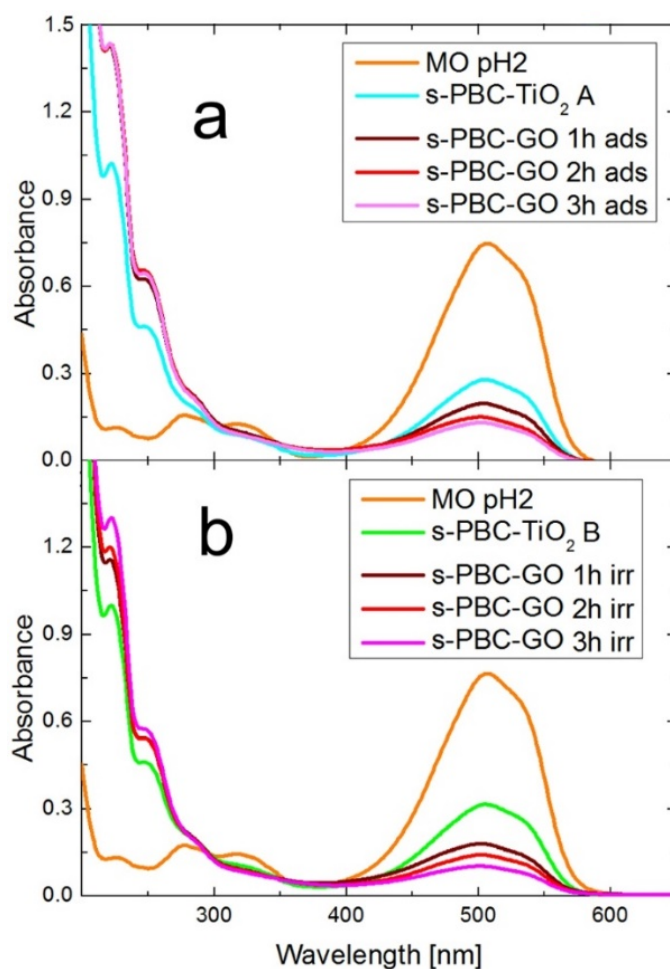


Figure 4.43 Figure XX UV-Vis absorbance spectra of MO solution after irradiation in the presence of two different pieces of s-PBC-TiO₂ membranes (named A and B) and subsequently in contact with s-PBC-GO in dark (a) or under irradiation (b) for one, two and three hours. Reported from [Filice,D'Angelo (2017)].

These results are in agreement with the ones reported for Nafion materials (see Paragraph 4.2.2). Table 4E reports the calculated rate coefficient k of MO degradation for the experiments in dark or under UV-visible irradiation, using the relation $-\ln(C/C_0) = k t$, where C and C_0 are the residual and the initial MO concentrations, respectively, and t is the time.

As just described, Nafion can adsorb a little fraction of MO (45% in the same experimental conditions) while the adsorption in s-PBC is negligible after 3 hours. This is due to the high electrostatic repulsion between s-PBC and MO, as a result of the higher density of sulfonic groups in s-PBC and their different structure. The correlation of dyes adsorption/degradation within structure of sulfonated polymers will be investigated in the future. Lowering the pH of MO solution (pH= 2), electrostatic interactions between protonated MO and negative sulfonic groups in s-PBC are favoured obtaining similar or better rate coefficients than for Nafion nanocomposite membranes. The s-PBC materials, showing comparable activity with Nafion nanocomposites, are proposed as a cheaper and safer alternative to Nafion, in particular considering also their preparation methodology.

Table 4E also shows an increase of degradation rate under irradiation and after dispersion of nanofillers inside both the polymeric matrixes (more significantly for s-PBC than for Nafion).

Table 4E Rate coefficient of degradation of MO at pH = 2 for the s-PBC membranes and at pH = 6 for Nafion membranes, as reported in [D'Angelo (2014)]. * pH 6

Membrane	k [x10 ⁻³ min ⁻¹]
s-PBC ads	1.6 ± 0.3
s-PBC irr	2.1 ± 0.3
s-PBC-GO ads	1.9 ± 0.1
s-PBC-GO irr	6.4 ± 0.4
s-PBC-TiO ₂ ads	3.6 ± 0.1
s-PBC-TiO ₂ irr	6.3 ± 0.1
Nafion irr *	3.8 ± 0.4
Nafion-GO irr *	4.1 ± 0.2
Nafion-TiO ₂ irr *	6.7 ± 0.2

Finally, the possibility to regenerate (according to the procedure in Appendix A19) and reuse the s-PBC membranes is tested and shown in figure 4.44. The s-PBC-GO composite shows stability in the performance, while s-PBC-TiO₂ even increases in the second cycle and then remains stable.

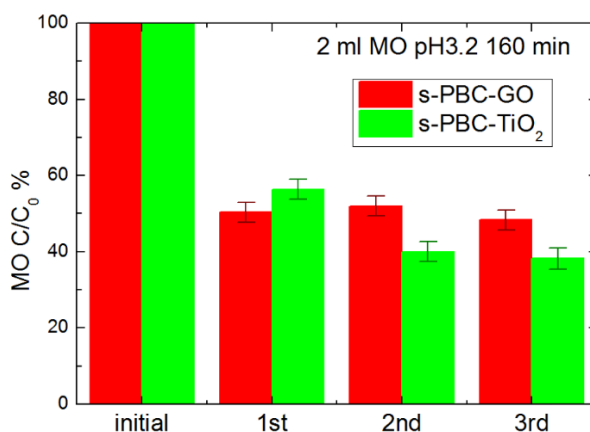


Figure 4.44 MO residual concentration versus three consecutive 3 hours irradiation processes, using the same pieces of s-PBC-GO (red bars) or s-PBC-TiO₂ (green bars) membranes. Reported from [Filice, D'Angelo (2017)].

4.4.3 Bi₂O₃/sPBC composite for visible photocatalytic applications

The use of this polymeric matrix is also tested for visible light photocatalytic application, by comparing the degradation ability of the polymer and the nanocomposite membrane with bismuth oxide for the removal of dyes in dark or under irradiation. The characterization of nanocomposite shows the formation of a mixture of Bi-Bi₂O₃ as an effect of the reduction of Bi₂O₃ during the membrane preparation and this can enhance photocatalytic activity under visible light irradiation, as reported in [Dong, Li (2014)].

As s-PBC and the other investigated nanocomposites, also s-PBC-BO shows immediately (few minutes) a strong decrease of MB concentration due to a simple adsorption phenomenon (Figure 4.45).

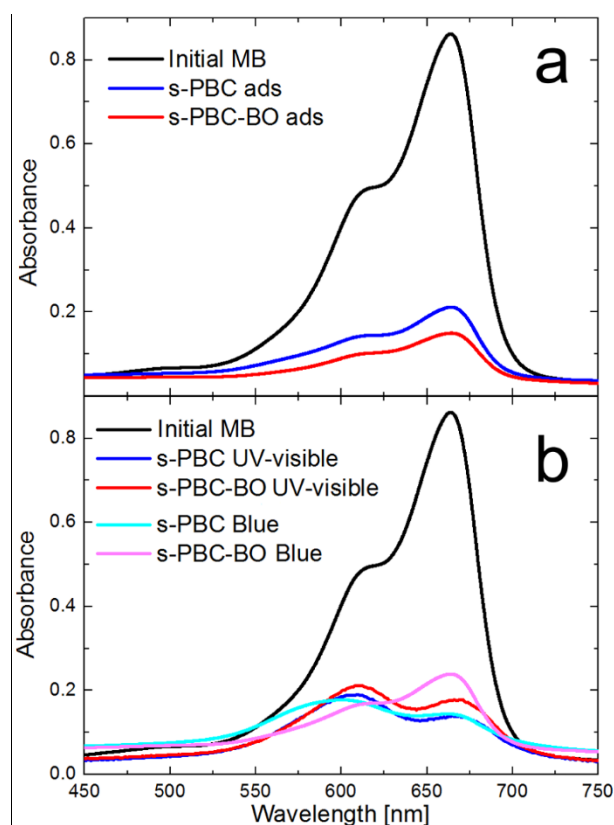


Figure 4.45 Absorbance spectra of MB at the initial concentration (i.e. 1.5×10^{-5} M) a) after being in contact with the membranes in dark conditions (only adsorption) and b) after 3 hours of irradiation with the two kinds of lamps (UV-Vis or Blue). Reported from [Filice submitted to Catalysis Today].

In particular, the dispersion of the nanofiller increased the adsorption efficiency of the polymer from 76.6% to 83.3% after three hours. The adsorption occurs due to the electrostatic attraction between the dye and the material. On the contrary, in the case of irradiation, it seems that the s-PBC is slightly more efficient to remove the dye with respect to s-PBC-BO. Furthermore, under irradiation with both lamps, the intensity of the peak at 610 nm is higher than the monomer peak after three hours,

suggesting the presence of MB aggregates comparable with the monomer species. In the case of adsorption, the main contribution is evident for the monomer with respect to the aggregates.

The MO adsorption on s-PBC membranes is hindered due to the electrostatic repulsions between the negative molecular charge of the dye and the negative charge of sulfonic groups in the polymer. As reported in previous paragraph, at pH 3, the membranes are able to adsorb MO as evidenced by the change of the colour of membranes from light yellow to red. Figure 4.46 compares the residual MO concentration of solutions in contact with the membranes in dark or under UVA □ Blue or Blue light irradiation for three hours, with the residual concentration of MO dye solutions irradiated by both the lamps in the absence of polymeric materials. While lamps irradiation does not affect MB, the acid MO solution absorbs light emitted by the Blue lamp, but it is not sensitive to the UV-Vis lamp. This explains why no degradation of acid MO occurred under UV-Vis lamp (orange bar) irradiation, while the 20% of initial acid MO solution is degraded under Blue lamp (magenta bar) in absence of polymeric materials (Figure 4.46).

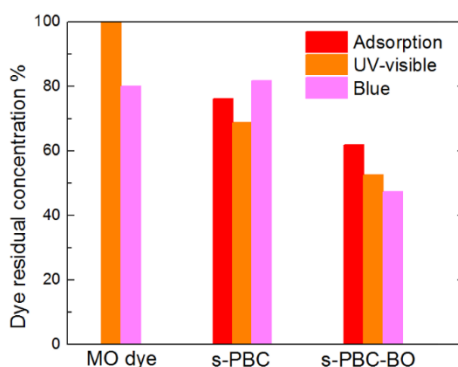


Figure 4.46 Residual MO concentration of solutions in contact with s-PBC and s-PBC-BO after adsorption or irradiation under UV-Vis and Blue lamp irradiation. As a reference, the MO dye concentration after irradiation with the two lamps (without contact with the membranes) is reported. Reported from [Filice submitted to Catalysis Today].

The dispersion of Bi_2O_3 inside the polymeric matrix increases the adsorption efficiency of the polymer (from 24% to 38%) in agreement with the increased value of water uptake. The dispersion of the filler in the membrane affects also its photocatalytic activity: under irradiation, the MO removal is significant only for the composite membrane (52.7%) and the larger effect is observed for the blue lamp irradiation after three hours. After photocatalytic experiments, the membranes were processed in order to release the adsorbed dye molecules and restore their properties (photos in Figure 4.47). The regeneration process is performed as described in Appendix A19. MB is not completely released as evidenced by the colour of membranes while the regeneration process is completely efficient for MO. Anyway, both the membranes show the same degradation efficiency for two consecutive dye removal processes.

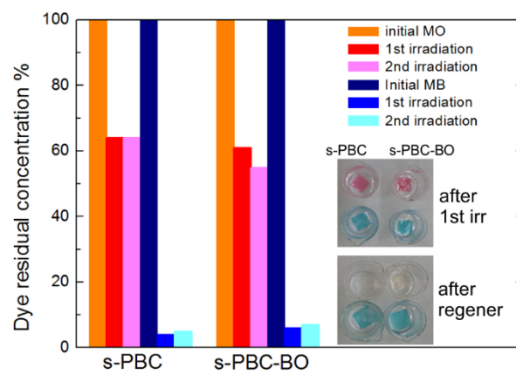


Figure 4.47 Residual MO and MB concentration of solutions in contact with s-PBC and s-PBC-BO after two consecutive photocatalytic tests. The photos of the membranes after a photocatalytic experiment (top) and after the regeneration processes (bottom) are shown. Reported from [Filice submitted to Catalysis Today].

CONCLUSIONS AND FUTURE PERSPECTIVES

In the last years the use of nanomaterials and nanocomposites has been considered more and more promising in providing new solutions for two of the main global sustainability challenges facing the world: sustainable energy production and water purification. In particular, photocatalytic processes involving nanomaterials and nanocomposites has recently been proposed as an efficient, green and sustainable approach to solve such problems.

Within this framework, this thesis work aims to propose, prepare and investigate new nanomaterials and/or nanocomposites able to remove organic pollutants with low cost, low energy consumption and low environmental impact. The photocatalytic process based on nanocompounds has been investigated as a green, low cost and efficient methodology for water purification application and the production of hydrogen by water splitting. The fundamental concepts regarding the global issues of clean energy production and water purification are introduced in the Chapter 1, and conventional methods are compared with photocatalysis. In the same Chapter, polymer nanocomposites are proposed as new efficient materials for water purification. Considering the complexity of water problem, the proposed materials allow to combine multiple approaches, as photocatalysis, nanotechnology and membrane technology, for appropriate solutions according to the specific problem and the natural and economic resources of the developing countries.

Development of novel and efficient antibacterial agents is vital for human health and wellbeing and it is urgently required due to the growing antibacterial resistance spectrum of bacterial infections. Carbon-based materials and, in particular, graphene-based nanomaterials have shown antibacterial properties making them promising materials for the filtration of microorganisms. In Chapter 2, graphene oxide (GO) and laser irradiated GO (iGO) were tested as antibacterial agents on *Escherichia coli*. Visible laser irradiation has shown to be a simple, cheap, green and tunable technique for inducing useful modifications of GO surfaces. Laser irradiation confers to GO antibacterial properties, as a result of the size reduction of its flakes: iGOs assumes a size comparable to bacteria that allows physical damages of bacteria membranes as shown by SEM characterization. XPS analysis on the samples also confirm that laser irradiation of GO in water affected the oxygen functional groups distribution on the GO surface but still maintaining enough hydrophilicity for its application in water.

As a consequence of this information, GO and laser irradiated GO were tested as adsorbents for the removal of dyes (in particular MB) from water showing an excellent adsorption capacity. The dye

adsorption occurs immediately within dye aggregation; in particular, the number and size of aggregates depends on the quantity and quality of oxygen moieties on GO surface. In other words, we can affirm that: GO can remove cationic dye by adsorption; the adsorption of MB is suitable for probing the layer charge density of GO; the GO surface properties can be selectively modified by laser irradiation process. GO was also tested for the photocatalytic degradation of MB.

In this regard, the laser irradiation process was also tested for the preparation of GO composites with titania, aiming to increase the well-known photocatalytic activity of this inorganic semiconductor by its interaction with GO as electrons sink. The results confirm the enhancement of degradation ability of titanium dioxide by combination with carbon nanostructures, confirming laser irradiation as a good technique for easy preparation of GO composites.

In Chapter 3, the fundamental characteristics of two semiconductor oxides, titania and bismuth oxide, were described and were proposed as good candidates for photocatalytic water splitting. In particular, bismuth trioxide (Bi_2O_3) is the simplest and most significant bismuth compound with a band gap that varies from 2.1 eV to 2.8 eV, (lower than the 3.05 -3.2 eV range for TiO_2) making it a viable visible-light-responsive photo-catalyst.

Furthermore, in Chapter 3, the modification of inorganic semiconductors by laser irradiation is described as a methodology to selectively modify them for photocatalytic applications. Different titania colloids modified by visible pulsed laser irradiation were tested for UV and visible photocatalytic water splitting and compared with initial samples. The induced modifications depend on laser process parameters (i.e. laser wavelength, fluence, solvent dispersing medium) as well as on the initial material characteristics (i.e. samples concentrations, crystalline phase). In all cases, under irradiation, sub-micrometer spherical particles are formed and their dimensions and numbers mainly depend on laser fluence. In addition, an increase of porosity was observed. Another common feature is the change of samples color from white to blue after irradiation. This is ascribed to the introduction of defects like reduced titanium and oxygen vacancies into titania structure that results in a slightly decreasing of energy gap. These induced modifications positively affect the photocatalytic activity of titania colloids for hydrogen production, even if results are still not satisfying for solar driven photocatalytic process. For this reason preliminary investigations have been conducted by irradiating anatase colloids in water or ethanol with UV laser. The most homogeneous sphere distribution were obtained for anatase samples dispersed in ethanol. The as obtained samples also showed the best performance in terms of H_2 production through photocatalytic water splitting under visible light irradiation.

The same irradiation process was used for the modification of bismuth oxide, resulting in larger or smaller Bi_2O_3 and affecting its chemical composition by reduction. This process depends on the used solvent and laser parameters as fluence and irradiation time. In particular, UV pulsed laser irradiation of $\beta\text{-Bi}_2\text{O}_3$ particles in water or in ethanol induces, respectively, the formation of $\text{Bi}_2\text{O}_2\text{CO}_3$ nanosheets or a mixed phase of $\text{Bi}/\beta\text{-Bi}_2\text{O}_3$ particles with a size smaller than the initial ones. The pulsed laser irradiation in liquid has shown to be a green, simple and tunable method for a massive and fast production of the bismuth subcarbonate and metallic Bi with respect to traditional methods that require high costs (due to the use of chemicals, high temperature and/or high pressure) and long processing time. Both the $\text{Bi}_2\text{O}_2\text{CO}_3$ and the mixed $\text{Bi}/\text{Bi}_2\text{O}_3$ phases are promising materials for application in photocatalytic processes for water splitting and dye degradation, in particular the presence of metallic Bi will increase the photocatalytic activity of Bi-based photocatalysts also in the visible wavelength range. For this final aim, the complete characterization of the optical properties of modified bismuth oxide is under investigation.

In [Chapter 4](#) hybrid polymeric membranes have been prepared to be used as adsorbent or photocatalyst for water purification. The investigated polymeric materials are sulfonated polymers, Nexar and Nafion, both characterized by high hydrophilicity and a structure for which they are stable in water but they can adsorb it. These materials are described at the beginning of [Chapter 4](#). The results reported in this chapter also confirmed that the use of polymeric nanocomposites is to be preferred with respect to nanomaterials directly dispersed in water. Polymeric nanocomposites can be easily removed at the end of the process without any dispersion of particles in the environment and they can be regenerated and used again. The comparison between the activity of nanomaterials dispersed in water with the activity of the same amount of nanomaterial but dispersed in the polymeric matrix also evidenced a synergic effect of the polymer in increasing the degradation activity of the filler.

Nafion has shown to be a good support for nanoparticles as GO, GO functionalized with sulfonic groups (GO_{SULF}) and titania, allowing to overcome all the problems shown by the direct use of powders dispersed in water. In addition, the polymer has shown to increase the degradation activity of GO_{SULF} . MO concentration is reduced by adsorption or photocatalysis in the presence of all the nanocomposites, with a stronger effect evidenced under irradiation. The best results are achieved for Nafion- TiO_2 and Nafion- GO_{SULF} . The photoactivity of GO_{SULF} has been shown for the first time: Nafion GO_{SULF} shows a residual MO concentration of less than 30% after three hours of irradiation as Nafion TiO_2 , without leaving any other harmful byproducts in solution. As a consequence, a new

material, obtained by the introduction of sulfonic groups on GO flakes, is proposed showing the same efficiency but less toxicity than titania. The presence of acid sulfonic groups on graphene oxide confers to the material highly hydrophilicity and acidity with respect to GO, resulting in an increasing of MB adsorption. For both dyes and all the materials, the possibility of regeneration and reuse of these membranes is confirmed suggesting as regeneration process to wash the membranes in diluted (1%) acid solution.

In the last part of [Chapter 4](#) a new sulfonated polymer (s-PBC) with block copolymer architecture is tested for the first time for dye removal from water. Nanocomposite s-PBC membranes were prepared by dispersing Bi₂O₃, GO and TiO₂ in the polymeric solutions using DMF as solvent. The use of s-PBC for this type of application within the possibility of using it combined with Bi₂O₃ for visible light photocatalytic applications is shown for the first time. TGA, XRD and Raman characterizations confirmed a different chemical interaction of the nanomaterials within the polymer. In particular, the dispersion of GO flakes increases the thermal stability of the polymer itself, while the dispersion of inorganic semiconductors has different effects. Titanium dioxide seems to interact mainly with sulfonic groups and its dispersion inside the polymer generates a destabilizing effect. For bismuth oxide, during the membranes preparation, the 43.85% of initial Bi³⁺ is reduced to elemental Bi, very probably due to the interaction with sulfonic groups.

The dye degradation activity of the nanocomposite membranes as adsorbents or photocatalysts is compared with the filler-free membranes. All the materials are able to remove more than the 90% of the initial MB concentration either in dark or under irradiation. This high efficiency is favored by the electrostatic interactions with the negatively charged sulfonic groups, and the dye is removed immediately (few minutes), without forming precipitates. An aggregation phenomenon is evidenced for all materials (while this was not observed for Nafion nanocomposites). In particular, the introduction of fillers in s-PBC accelerates the MB monomer and dimer adsorption rate while higher degree aggregates are quickly formed in the first minutes and efficiently removed under irradiation. Anyway, in the absence of fillers, the s-PBC polymer is more efficient than Nafion in the removal of MB. This can be explained by the larger IEC and water uptake values of sPBC.

Considering the electrostatic interactions of dye and sulfonic groups, the same polymer and its composites are able to adsorb MO only in acidic pH conditions (contrary to Nafion nanocomposites) thanks to the protonation of MO molecules. In particular, the MO degradation ability is increased under irradiation by a factor of 50% for the composite with TiO₂ and of 30% for the composite with GO, with respect to MO removal by adsorption. Finally, these two composites show the same degradation efficiency and toxic by-products are only observed for s-PBC-TiO₂, suggesting that for

s-PBC-GO membrane MO is removed by an adsorption process enhanced by irradiation. Therefore, MO dye removal from water is achieved in a safer way by a s-PBC-GO membrane instead of a s-PBC-TiO₂ membrane.

Furthermore, in the case of the composite with bismuth oxide, the formation of the Bi/Bi₂O₃ mixture confers to the polymer a photocatalytic activity under visible light as shown for MO degradation. The hypothesis of using sulfonated pentablock copolymer nanocomposites, as an efficient and low cost alternative to Nafion in water purification application, is confirmed.

In conclusion, within this dissertation, the use of new nanomaterials and nanocomposites in photocatalytic processes for water treatment and hydrogen production as an alternative to traditional methods is reported. In particular among nanomaterials graphene oxide, titania and bismuth oxide have been investigated for these purposes confirming them as good candidate for these applications. Laser irradiation processes are proposed as a new approach with respect to conventional methods to selectively tune the properties of above mentioned materials. The preparation of hybrid polymeric nanocomposites is confirmed being more efficient and clean materials for water purification. These results should be considered as a first step in developing efficient membranes with photocatalytic activity and filtration properties for removal of various pollutants and ions from water. Besides the photocatalytic activity, these membranes also have high proton conductivity suggesting their use as polymeric electrolyte in fuel cells or photoelectrochemical solar cells for hydrogen production.

REFERENCES

- N. S. Azhar, M. F. M. Taib, O. H. Hassan, M. Z. A. Yahya, A. M. M. Ali. *Mater. Res. Express*, 2017, 4, 3.
- G.R. Aiken, D. M. McKnight, R.L Wershaw, P. MacCarthy, *Humic Substances in Soil, Sediment, and Water: Geochemistry, Isolation, and Characterization*, John Wiley & Sons, Inc., 1985.
- Z. Amjad, Ed. *Reverse Osmosis: Membrane Technology, Water Chemistry, and Industrial Applications*; Van Nostrand Reinhold: New York, 1993.
- R. W. Baker, *Membrane Technology and Applications*, 2nd ed.; John Wiley & Sons, Ltd.: Chichester, 2004.
- C. Baiocchi, M.C. Brussino, E. Pramauro, A. Bianco, A. Prevot, L. Palmisano, G. Marci, *Int. J. Mass Spec.*, 2002, 214, 247-256.
- S. Barcikowski, G. Compagnini, *Phys.Chem.Chem.Phys.*, 2013, 15, 3022.
- D. Barreca, F. Morazzoni, G.A. Rizzi, R. Scotti, E. Tondello, *Physical Chemistry Chemical Physics*, 2001, 3, 1743-1749.
- M. Bekbolet, G. Ozkosemen, *Water Sci. Technol.*, 1996. 33, 189–194.
- M. Bertelli, E. Selli, *J. Hazard. Mater. B*, 2006, 138: 46–52.
- B.C. Brodie, *Phil. Trans. R. Soc. Lond.*, 1859, 149, 249–259.
- M.A. Buccheri, D. D'Angelo, S. Scalese, S.F. Spanò, S. Filice, E. Fazio, G. Compagnini, M. Zimbone, M. V Brundo, R. Pecoraro, A. Alba, F. Sinatra, G. Rappazzo, V. Privitera, *Nanotechnology*. 2016. 27, 245704 – 245716.
- O. Carp, C. L. Huisman, A. Reller, *Prog. Solid State Chem.* 2004, 32, 33-177.
- X. Chen, S. Shen, L. Guo, S. S. Mao, *Chemical Reviews*, 2010, 110, 6503.
- D. Chen, H. Feng, J. Li, *Chemical Reviews*, 2012, 112, 6027-6053.
- X. Chen, D. Zhao, K. Liu, C. Wang, L. Liu, B. Li, Z. Zhang, D. Shen, *ACS Appl. Mater. Interfaces*, 2015, 7, 16070-16077.
- J. H. Choi, A. Kota, K. I. Winey. *Ind. Eng. Chem. Res.* 2010, 49, 12093–12097.
- J. Choi, C. L. Willis, K. I. Winey. *J. Membr. Sci.* 2012, 394–395, 169–174.
- M. N. Chong, B. Jin, C. W. K. Chow, C. Saint, *Water Res.*, 2010, 44, 2997–3027.
- S. Claramunt, A. Varea, D. López-Díaz, M. M. Velázquez, A. Cornet, A. Cirera, *The Journal of Physical Chemistry C*, 2015, 119, 10123-10129.
- G. Compagnini *Laser micro-nano-nanomanufacturing and 3D microprinting* Springer In press

- D. D'Angelo, S. Filice, S. Libertino, V. Kosma, I. Nicotera, V. Privitera, S. Scalese, Proceedings of IEEE 9th Nanotechnology Materials and Devices Conference (NMDC), 2014, 54-57.
- R. A. Damodar, S. J. You, H. H. Chou, J. Hazard. Mater., 2009, 172, 1321–1328.
- Dimiev, L. Alemany, J.M. Tour, ACS Nano, 2012, 7 (1), 576–588.
- F. Dong, W. K. Ho, S.C. Lee, Z.B. Wu, M. Fu, S. C. Zou, Y. Huang, J Mater Chem, 2011, 21, 12428.
- F. Dong, T. Xiong, Y. Sun, Z. Zhao, Y. Zhou, X. Feng, Z. Wu, Chem. Commun., 2014, 50, 10386
- F. Dong, Q. Li, Y. Sun, WK. Ho, ACS Catal., 2014, 4 341–4350.
- F. Dong, T. Xiong, Y. Sun, H. Huang, Z. Wu, J. Mater. Chem. A, 2015, 3,18466.
- M. Doyle, G. Rajendran, Handbook of Fuel Cells: Fundamentals, Technology and Applications, Vielstich, W., Gasteiger, H.A., Lamm, A., eds., 2003, 3, John Wiley & Sons, Chichester, U.K., 351–395.
- D.R. Dreyer, S. Park, C.W. Bielawski, R.S. Ruoff, **Chem. Soc. Rev.**, 2010, **39**, 228-240.
- Enotiadis, K. Angjeli, N. Baldino, I. Nicotera, D. Gournis, Small, 2012, 8, 21, 3338–3349.
- Fan, Y.; Cornelius, C. J. Raman Spectroscopic and Gas Transport Study of a Pentablock Ionomer Complexed with Metal Ions and Its Relationship to Physical Properties. *J. Mater. Sci.* **2013**, *48* (3), 1153–1161.
- Y. Fan, M. Zhang, R. B. Moore, C. J. Cornelius, Journal of Membrane Science, 2014, 464, 179–187.
- S. Filice, D. D'Angelo, A. Scarangella, D. Iannazzo, G. Compagnini and S. Scalese, Highly effective and reusable sulfonated pentablock copolymer nanocomposites for water purification applications. RSC Advances, (2017), 7(72):45521-45534.
- S. Filice, G. Compagnini, R. Fiorenza, S. Sciré. L. D'Urso, ME Fragalà, P. Russo, E. Fazio, S. Scalese, *J Colloid Interface Sci.*, 2016, 489, 131-137.
- S. Filice, D. D'Angelo, S. Libertino, I. Nicotera, V. Kosma, V. Privitera, S. Scalese, Carbon, 2015, 82, 489-499.
- S. Filice, D. D'Angelo, S. F. Spanò, G. Compagnini, M. Sinatra, L. D'Urso, E. Fazio, V. Privitera, S. Scalese, Mater Sci Semicond Proc, 2015, 42, 50-53.
- N. Fromer, M.S, Diallo, J Nanopart Res, 2013, 15, 2011.
- Fujishima, K. Honda, Nature, 1972, 238, 37-38.
- Fujishima, X. Zhang, D. A. Tryk, Surface Science Reports, 2008, 63, 515–582.

- U.I. Gaya, A.H. Abdullah, J. Photochem. Photobiol. C: Photochem. Rev., 2008, 9, 1-12.
- G. M. Geise, B. D. Freeman, D. R. Paul. Polymer (Guildford). 2010, 51, 5815–5822.
- G. M. Geise, B. D. Freeman, D. R. Paul. J. Membr. Sci. 2013, 427, 186–196.
- E. Ghadim, N. Rashidi, S. Kimiagar, O. Akhavan, F. Manouchehri, E. Ghaderi, Appl. Surf. Sci. 2014, 301, 183.
- W. Han, P. Liu, R. Yuan, J. Wang, Z. Li, J. Zhuang, X. Fu, J. Mater. Chem., 2009, 19, 6888–6895.
- R. A. He, S. W. Cao, P. Zhou, J. G. Yu, Chin., J. Catal., 2014, 35, 989–1007.
- H. M. Hegab, A. ElMekawy, L. Zou, D. Mulcahy, C- P. Saint, M. Ginic-Markovic. Carbon, 2016, 105, 362-376.
- J. Herrmann, Catal. Today, 1999, 53, 115–129.
- J.M. Herrmann, J. Photochem. Photobiol. A Chem., 2010, 216,85–93.
- L. Huang, G. Li, T. Yan, J. Zheng, L. Li, New Journal of Chemistry, 2011, 35, 197-203.
- W.S. Hummers, R.E. Offeman, J. Amer. Chem. Soc., 1958, 80 (6), 1339–1339.
- D.C. Hurum, A.G. Agrios, K.A. Gray, T. Rajh, M.C. Thurnauer J. Phys. Chem. B, 2003, 107, 4545–4549.
- A.O. Ibhaddon, P. Fitzpatrick, Catalysts, 2013, 3,1,189–218.
- Y. Ishikawa et al., Appl Phys Lett, 2007, 91(16), 161110.
- Y. Ishikawa, Y. Katou, N. Koshizaki, Q. Feng, Chem. Lett. 2013, 42, 530531.
- X. Jiang, T. Herricks, Y. Xia, Nano Lett., 2002, 2, 1333–1338.
- H. Y. Jiang, P. Li, G. Liu, J. Ye, J. Lin, J. Mater. Chem. A, 2015, 3, 5119-5125.
- G. Kickelbick, Hybrid Materials. Synthesis, Characterization, and Applications. 2007, Wiley-VCH Verlag GmbH & Co. KGaA, Weinheim.
- Lerf, H. He, M. Forster, J. Klinowski, J. Phys. Chem. B, 1998, 102 (23), 4477–4482.
- Q. Li, S. Mahendra, D. Y. Lyon, L. Brunet, M. V. Liga, D. Li, P. J. J. Alvarez, Water Research, 2008, 42, 4591-4602.
- L. Li, *et al.* Appl. Surf. Sci. 257 (2011) 8006–8012.
- Li, J. Zhang, K. Liu, Int. J. Electrochem. Sci., 2012, 7, 5028-5034.
- Li, X. Zhang, P. Chen, X. Li, L. Wang, C. Zhang, W. Zheng, Y. Liu, RSC Advances, 2014, 4, 2404-2408.
- X. Li, J. Yu, M. Jaroniec, Chem. Soc. Rev., 2016, 45, 2603.
- S. Liu, T. H. Zeng, M. Hofmann, E. Burcombe, J. Wei, R. Jiang, J. Kong, Y. Chen, ACS Nano, 2011, 5, 6971-6980.

- G. Lofrano, M. Carotenuto, G. Libralato, R. F. Domingos, A. Markus, L. Dini, R. K. Gautam, D. Baldantoni, M. Rossi, S. K. Sharma, M. C. Chattopadhyaya, M. Giugni, S. Meric, *Water Res.*, 2016, 92, 22–37.
- M. Long, L. Zheng *Chinese Journal of Catalysis*, 2017, 38, 617–624.
- K. A. Mauritz, R. B. Moore, *Chem. Rev.*, 2004, 104, 4535-4585.
- F. Korkmaz, S. Cetinkaya, S. Eroglu, *Metallurgical and Materials Transactions B*, 2016, 47, 2378-2385.
- H. Mamaghani, F. Haghghat, C.S. Lee, *Appl. Catal. B: Environ*, 2017, 203, 247-269.
- P. Melian, O. Gonzalez Diaz, A. Ortega Mendez, C. R. Lopez, M. Nereida Suarez, J. M. Dona Rodriguez, J. A. Navio, D. Fernandez Hevia and J. Perez Pena, *International Journal of Hydrogen Energy*, 2013, 38, 2144.
- F. Méndez-Arriaga, S. Esplugas, J. Giménez, *Water Res.*, 2010, 44, 2, 589–95.
- K. P. Mineart, X. Jiang, H. Jinnai, A. Takahara, R. J. Spontak, *Macromol. Rapid Commun.* 2015, 36, 432–438.
- M. A Montgomery, M. Elimelech, *Environ. Sci. Technol.*, 2007, 41, 17–24.
- R. Munter, *Proc. Est. Acad. Sci. Chem*, 2001, 50, 2, 59–80.
- Nakamura, N. Negishi, S. Kutsuna, T. Ihara, S. Sugihara, E. Takeuchi, *J. Mol. Catal. A*, 2000, 161, 205–212.
- J. Nozik, *Annu. Rev. Phys. Chem.*, 1978, 29, 189–222.
- S. P. Nunes, *Macromolecules*, 2016, 49, 2905–2916.
- T. Ohsaka, F. Izumi, Y.J. Fujiki, *Raman Spectrosc.* 1978, 7, 321-324.
- D.F. Ollis, H. Al-Ekabi (Eds.), *Photocatalytic Purification and Treatment of Water and Air*, Elsevier Science, Amsterdam 1993.
- N. Pandey, S. K. Shukla, N. B. Singh, *Nanocomposites*, 2017, 3, 47-66.
- F. E. Osterloh, *Chem Mater*, 2008, 20 (1), 35-54.
- H. Park, W. Choi, *Catal. Today*, 2005, 101, 291–297.
- S. Pei, H.M. Cheng, *Carbon*, 2012, 50, 3210–3228.
- F. Perreault, A. F. de Faria, M. Elimelech, ***Chem. Soc. Rev.***, 2015, 44, 5861-5896.
- F. Petronella, A. Truppi, C. Ingrosso, T. Placido, M. Striccoli, M. L. Curri, A. Agostiano, R. Comparelli, *Catal. Today*, 2017, 281, 85–100.
- Pyatenko, M. Yamaguchi, S. Suzuki, *J. Phys. Chem.B*, 2005, 109, 21608.
- Pyatenko, M. Yamaguchi, S. Suzuki, *J. Phys. Chem. B*, 2007, 111, 7910.
- Pyatenko, H. Wang, N. Koshizaki, T. Tsuji, *Laser Photonics Rev.*, 2013, 7, 4, 596–604.

- Pyatenko, H. Wang, N. Koshizaki. *J. Phys. Chem. C*, 2014, 118, 4495–4500.
- X. L. Qu, P.J.J. Alvarez, Q.L. Li, *Water Res*, 2013, 47, 3931-3946.
- L. R. Radovic, C. Moreno-Castilla, J. Rivera-Utrilla, In *Chemistry and Physics of Carbon*, L. R. Radovic, Ed.; Marcel Dekker: New York, 2001, 27, 227-405.
- Rahimpour, S. S. Madaeni, A. H. Taheri, Y. Mansourpanah, *J. Membr. Sci.*, 2008, 313, 158–169.
- Reddy, P.A.K.; Reddy, P.V.L.; Kwon, E.; Kim, K.H.; Akter, T.; Kalagara, S. 2016, 91, 94-103
- S. Scalese, I. Nicotera, D. D'Angelo, S. Filice, S. Libertino, C. Simari, K. Dimos, V. Privitera, *New J. Chem.*, 2016, 40 (4), 3654–3663.
- Scanlon et al., *Nature Materials*, 2013, 12, 798 – 801.
- L. Schlapbach, A. Züttel, *Nature*, 2001, 414, 353-358.
- M. Schultz, T. P. Yoon, *Science*, 2014, 343, 1239176.
- M. Shannon, P. W. Bohn, M. Elimelech, J. G. Georgiadis, B. J. Mariñas, A. M. Mayes, *Nature*, 2008, 452, 7185, 301–10.
- S. Solomon, D. Quin, M. Manning, Z. Chen, M. Marquis, K.B. Averyt, M. Tignor, H.L. Miller, in *Climate change 2007: the physical science basis*, Cambridge University Press, 2007.
- D.A. Sokolov, C.M. Rouleau, D. B. Geohegan, T. M. Orlando, *Carbon*, 2013, 53, 81–89.
- S.F. Spanò, G. Isgrò, P. Russo, M.E. Fragalà, G. Compagnini, *Appl. Phys. A* , 2014, 117, 19–23.
- L. Staudenmaier, *Ber. Dtsch. Chem. Ges.* 1898, 31, 1481–1487.
- K. Takanabe, K. Domen, in *Heterogeneous Catalysis at Nanoscale for Energy Applications*, eds. F. F. Tao, W. F. Schneider and P. V. Kamat, John Wiley & Sons, Inc, Hoboken, NJ, 2014.
- J. W. Tang, J. R. Durrant, D. R. Klug, *J Am Chem Soc*, 2008, 130, 13885-13891.
- J. Toudert, R. Serna, M. J. Castro, *J. Phys. Chem. C*, 2012, 116, 20530.
- L. T., Thompson, J. T. Yates, *Chem. Rev.*, 2006, 106, 4428.
- R. Trusovas, G. Rac̄iukaitis , G. Niaura , J. Barkauskas, G. Valušis, R. Pauliukaite, *Adv. Optical Mater.*, 2016, 4, 37–65.
- M. V. Twigg, in *Catalyst Handbook*, Wolfe, London, UK, 2nd Edition edn., 1989.
- G. Wang, B. Wang, J. Park, J. Yang, X. Shen, J. Yao, *Carbon*, 2009, 7, 68-72.
- H. Q. Wang et al., *Angew Chem Int*, 2010, 49 (36), 6361–6364.
- H. Wang, M. Miyauchi, Y. Ishikawa, A. Pyatenko, N. Koshizaki, Y. Li, L. Li, X. Li, Y. Bando, D. Golberg, *J. Am. Chem. Soc.*, 2011, 133, 19102–191.

- H. Wang, A. Pyatenko, N. Koshizaki, H. Moehwald, D. Shchukin, *ACS Appl. Mater. Interfaces*, 2014, 6, 2241–2247.
- L. Westwood, *Carbon*, 2011, 49, 741–772.
- L. Willis, D. L. Handlin, S. R. Trenor, B. D. Mather, Sulfonated block copolymers, method for making same, and various uses for such block copolymers. US Patent 7,737,224 B2, June 15, 2010.
- S. Wu, Y. Jiang, L. Hu, J. Sun, P. Wan, L. Sun, *Nanoscale*, 2016, 8, 12282–12288.
- Xu, Y. Hai, X. Zhang, S. Zhang, R. He, *Applied Surface Science*, 2017, 400, 530–536.
- Y. Yang, H. Zhang, P. Wang, Q. Zheng, J. Li, *J. Memb. Sci.*, 2007, 288, 231–238.
- T.-F. Yeh, J. Cihlar, C.-Y. Chang, C. Chang, H. Teng, *Mater. Today*, 2013, 16, 78–84.
- J. Yeo, S. Y. Kim, S. Kim, D. Y. Ryu, T. H. Kim, M. J. Park., *Nanotechnology*, 2012, 23, 245703.
- L. S. Zhang, W. Z. Wang, J. Yang, Z. G. Chen, W. Q. Zhang, L. Zhou, S. W. Liu, *Appl Catal A*, 2006, 308, 105.
- Y. Zhang, L. Guo, S. Wei, Y. He, H. Xia, Q. Chen Q, *Nanotoday*, 2010, 5(1), 15–20.
- Zhang, Y. Liu, Q. Li, X. Zhang, J. K. Shang, *ACS Appl. Mater. Interfaces*, 2013, 5, 10953–10959.
- N. Zhang, M- Q. Yang, S. Liu, Y. Sun, Y.J. Xu, *Chem. Rev.*, 2015, 115, 10307–10377
- X. Zhang, J. Qian, B. Pan, *Environ. Sci. Technol.*, 2016, 50, 881–889.
- W.N. Zhao, Z.P. Liu, *Chem. Sci.*, 2014, 5, 2256–2264.
- A.W. Zularisam, A.F. Ismail, R. Salim, *R. Desalination*, 2006, 194, 211–231.

Appendix A: Characterization techniques

A1. The solutions of commercial and laser modified samples were analyzed by recording the absorbance spectra using an UV/Vis AGILENT Cary 50 spectrophotometer in a wavelength range between 200 and 800 nm. The concentration of GO flakes in water was evaluated by the intensity of the absorbance peak at 231 nm as described in the work of [Wang (2009)].

A2. All the solutions of commercial and laser modified samples were drop casted onto a double-side polished silicon substrates and heated on a hot plate at 80°C for 2h to evaporate the water and then characterized by Raman spectroscopy. Raman scattering has been excited by the 514.5 nm radiation of an Ar⁺ laser and analyzed by a Jobin Yvon 450 mm focal length monochromator equipped with a CCD camera detector cooled at 77 K. The incident laser beam was focused by a x100 objective. For polymeric materials, Raman analysis was performed using as excitation source a 785nm laser and spectra were collected in single spectrum mode with an integration time of 10 s, with a WITec alpha300R confocal instrument and a Nikon 100× objective.

A3. All the solutions of commercial and laser modified samples were drop casted onto a double-side polished silicon substrates and heated on a hot plate at 80°C for 2h to evaporate the water and then characterized by X-ray Photoelectron Spectroscopy (XPS). XPS analysis was performed by using a Thermo Scientific K-Alpha system with a monocromatic Al K α (1486.6 eV) source. The photoelectron spectra were collected by a CAE analyser using a pass energy of 200 and 50 eV for the survey and high resolution spectra respectively. A flood gun was used to decrease the effect of surface electrical charging. For polymeric materials, the chemical surface composition was determined by X-ray Photoelectron Spectroscopy (XPS) using a Kratos Analytical AXIS-HS X-ray photoelectron spectrometer, equipped with Vision 2 data system. The samples were analysed in fixed analyser transmission (FAT) mode using Al K α X-ray source at 1486.6 eV operated at 150 W (15 kV, 10 mA). The pass energy for general survey scan and core level spectra was set to 80 and 40 eV respectively. Low energy electrons flood gun for surface charge compensation was used.

A4. Field emission scanning electron microscope (Zeiss Supra35 FE-SEM) equipped with energy dispersive X-ray (EDX) microanalysis system (Oxford Instruments, X-MAX, 80 mm²) was used to investigate the morphology of investigated samples. Before SEM investigations, all the solutions of commercial and laser modified samples were drop casted onto a double-side polished silicon substrates and heated on a hot plate at 80°C for 2h to evaporate the water. In order to analyse the cross section of the membranes, they were dipped in liquid nitrogen, where they become stiff, and then they can be easily broken in two parts.

A5. Dynamic Light scattering measurements were performed by a homemade apparatus using quartz scattering cell, confocal collecting optics, a Hamamatsu photomultiplier mounted on a rotating arm, a BI-9100 AT hardware correlator (Brookhaven Instruments Corporation) and illuminating the sample with a 660 nm diode laser. The power ranged between 15 and 50 mW; low power intensity was used to avoid convective motions due to local heating. DLS measurements provided the auto-correlation function $g_2(t)$ of the scattered light intensity I with the light beating technique in homodyne mode. The auto-correlation function for spherical mono-disperse particles is a single exponential $\exp(-2\Gamma t)$ with a decay rate Γ . In poly-disperse solution, the autocorrelation function shows several exponential decay components and can be written as a sum of exponential decays. The auto-correlation functions are analyzed by cumulant analysis. This analysis is performed by taking the logarithm of the correlation function and expanding it in a power series of t : $\ln(g_2(t)) = -\langle \Gamma \rangle t + \dots$. The $\langle \Gamma \rangle$ is an average decay rate called the “first cumulant” and is related to the average diffusion coefficient of the particles $\langle D \rangle$ by the equation: $\langle \Gamma \rangle = \langle D \rangle q^2$, where q is the scattering vector defined as $q = (4\pi n/\lambda) \sin(\theta/2)$, n being the refraction index of the solvent, λ the light wavelength and θ the scattering angle.

A6. Antibacterial activity of GO and iGO was tested on *Escherichia coli* ATCC25922. Bacteria were routinely maintained by spreading on McConkey agar. To run tests, a single colony was inoculated in 50 ml of Luria-Bertani (LB) broth and grown overnight at 37°C by constant agitation at 180 rpm under aerobic conditions. The following day, the bacterial growth was measured by optical density at 600 nm. For the Colonies Forming Units (CFU) count, bacteria were diluted up to 10^6 CFU/ml and exposed either to GO or iGO at different concentrations in a final volume of 300 μ l. A control sample of untreated bacteria was run in parallel. Experiments were made in triplicates. Different final concentrations of GO or iGO were tested, ranging from 5 to 30 μ g/ml. Aliquots were collected at one hour (1h) or two hours (2h) respectively, conveniently diluted by serial dilutions 1:10 and plated in LB Agar Petri dishes. Plates were incubated overnight at 37°C. CFU were counted the following day.

A7. The WST-8 is a tetrazolium dye (2-(2-methoxy-4-nitrophenyl)-3-(4-nitrophenyl)-5-(2,4-disulfophenyl)-2H-tetrazolium monosodium salt), that is converted into formazan by dehydrogenases. The amount of formazan produced is directly proportional to the number of living cells, in addition formazan is orange so the presence of bacteria is immediately observable. For the WST-8 Assay, bacteria were diluted up to 10^8 CFU/ml and exposed either to GO or iGO at different concentrations in a volume of 200 μ l. Different final concentrations of GO or iGO were tested, ranging from 5 to 30 μ g/ml. Untreated samples were run in parallel as controls. After 60 min exposition to GO or iGO, 100 μ l were collected from each sample. WST-8 (10 μ l) was added to each collected sample. Samples were incubated at 37°C for 2h in a thermostatic bath. After incubation, the

amount of generated formazan was checked by measuring samples absorbance at 450 nm. Experiments were made in triplicates. WST-8 was purchased at Sigma-Aldrich (Cell Counting kit-8).

A8. For the TBARS Assay, bacteria were diluted up to 10^9 CFU/ml and exposed either to GO or iGO at different concentrations in a volume of 1000 μ l. Different final concentrations of GO or iGO were tested, ranging from 10 to 30 μ g/ml. Untreated samples were run in parallel as controls. Samples treated with Go or iGO and D-Mannitol at a final concentration of 1mg/ml were run in parallel as well. After 60 min exposition to GO, iGO, GO and D-Mannitol or iGO and D-Mannitol, 100 μ l were collected from each sample and transferred to a glass test tube. To each tube, 100 μ l of sodium dodecyl sulfate (SDS) solution and 2.5 ml of Thiobarbituric Acid (TBA)/Buffer Reagent were added. Samples were incubated at 95°C for 1h, then cooled in a bath ice for 10 minutes. After centrifugation at 3000 rpm for 5 min, supernatants were collected and their absorbance at 532 nm was measured by a spectrophotometer. Malondialdehyde (MDA) standards were treated in parallel in order to construct a standard curve against which unknown samples were plotted. The assay was carried out with the OXI-TEK TBARS Assay kit (Enzo Life Sciences).

A9. After 1h exposure to 20 mg/l of GO or iGO, bacteria were allowed to adhere to circular glass coverslips 13 mm in diameter (Electron Microscopy Sciences EMS, Fort Washington, PA). The samples were fixed in 2% glutaraldehyde in 0.1 M sodium-cacodylate (EMS) buffer, pH 7.2, for 1 hour at 4°C and then postfixed in 1% osmium tetroxide (EMS) for 1 hour at 4°C. After dehydration in ethanol, samples were air-dried. The coverslips were coated with vacuum-evaporated gold (Emscope-SM 300) and observed with a field emission scanning electron microscope (Zeiss Supra35 FE-SEM).

A10. Zebrafish of the AB strain (wild-type, wt) were obtained from the Center of Experimental Ichthyopathology of Sicily (CISS), University of Messina, Italy, where they are kept in a "Fish facility" (Stand Alone Unit, Tecniplast), a closed-loop system that allows the continuous monitoring of vital parameters. They were raised on a circulating aquarium system in an environmentally controlled room (28°C, 80% humidity), with the photoperiod adjusted to a 14 h light/10 h dark cycle. The larval and adult zebrafish were fed with brine shrimp (hatched from eggs in 10 mL in 2 L salt water) daily. For experiments, fertilized eggs were collected and chosen under a stereomicroscope (Leica M0205C, Multifocus) within 4 hours post fertilization (hpf). All embryos were derived from the same spawns of eggs. Fish Embryo Toxicity (FET) test was effectuated according to OECD (2006) and ISO 15088. Zebrafish embryos exposed to GO, iGO2 and iGO4 at different concentrations (10, 20, 40, 80, 160 mg/l) for 4–96 hpf were measured for toxic effects of a continuing observation period. The GO and iGO solutions were renewed and embryonic/larval mortality and hatching rate

were evaluated every 24 h. Healthy embryos were placed in 24-well culture plates (10 embryos in 2 ml solution/well). Each group had five replicate wells. Each experiment was replicated four times. During the exposure period (4–96 hpf), photographs of the embryos were captured under a stereomicroscope (Leica M0205C, Multifocus) and the percentage of abnormal embryos was counted every 24 h.

A11. The adsorption ability of GO, rGO, GO-P25, rGO-P25 and GO_{SULF} solutions at different concentration was evaluated by measuring the decrease of MB concentration starting from the initial value of $1 \cdot 10^{-5}$ M in water at room temperature. This was done by monitoring the absorbance signal at 664 nm by the Lambert-Beer law using a UV/Vis AGILENT Cary 50 spectrophotometer. The same experiments were conducted for all the solutions under irradiation using a 18 W UVA/blue DULUX OSRAM lamp. The pH of the solutions was measured by a SevenGO Duo pH-meter of Mettler Toledo.

A12. A drop of nanoparticles suspensions before and after the irradiation processes was placed into copper grids, on glass and silicon slides for morphological characterization. Each deposit was placed in a drier overnight. The grids were analyzed by JEOL JEM 2010F transmission electron microscope with a Schottky field emission gun operating at an acceleration voltage of 200 kV.

A13. The BET surface area measurements were performed by nitrogen adsorption-desorption measurements using a Sorptomatic 1990 instrument (Thermo Quest).

A14. Diffuse reflectance spectra were recorded on a Jasco spectrophotometer operating in the 600-200 nm range.

A15. Photocatalytic water splitting experiments were performed in a Pyrex jacketed reactor at 30°C (thermostated) under the irradiation of a 100 W mercury lamp (Black-Ray B-100A, 365 nm) or under the irradiation of a Osram Ultra Vitalux 300W E27 lamp, specially designed for sunlight simulation. The headspace of the reactor was connected to an inverted buret, filled with water at atmospheric pressure. This allows the measurement of the evolved gases. The evolution of H₂ was also confirmed by analyzing the effluent gases with an online gas chromatograph equipped with a packed column (Carboxen 1000) and thermal conductivity detector. Generally 25 mg of catalyst were suspended in deionized water under stirring. The suspension was then purged with a nitrogen flow for at least 30 min in order to remove dissolved air and then irradiated.

A16. X-ray diffraction (XRD) was performed by a Bruker-AXS D5005 diffractometer by using a Cu K α radiation with an incidence angle of 1.0° ; the detection angle 2θ was varied between 20° and 60° commercial and laser modified samples were drop casted onto a double-side polished silicon substrates and heated on a hot plate at 80°C for 2h to evaporate the water.

A17. X-ray photoelectron spectroscopy (XPS) measurements were performed under ultrahigh vacuum conditions with a base pressure of 5×10^{-10} mbar in a SPECS GmbH instrument equipped with a monochromatic MgK α source ($h\nu = 1253.6$ eV) and a Phoibos-100 hemispherical analyzer. All binding energies were referenced to the C1s core level at 284.6 eV. Spectral analysis included a Shirley background subtraction and peak deconvolution employing mixed Gaussian–Lorentzian functions, in a least squares curve-fitting program (WinSpec) developed at the Laboratoire Interdisciplinaire de Spectroscopie Electronique, University of Namur, Belgium.

A18. The surface charge of sulphonated graphene oxide and graphene oxide solutions was measured using an Horiba Scientific NanoParticle Analyzer SZ-100-Z.

A.19 The membranes photocatalytic activity was evaluated by measuring the degradation of methyl orange or methylene blue, with a concentration of $2 \cdot 10^{-5}$ M and $1.5 \cdot 10^{-5}$ M, respectively, in water solution under UV-Vis light irradiation carried out with a 18 W UVA/blue DULUX OSRAM lamp. During the photocatalytic experiment, one piece of membrane (about 1 cm²) was dipped into 2 mL of the above MO solution. The degradation of dyes was evaluated via the absorbance peak at 465 nm for MO and at 664 nm for MB by the Lambert-Beer law using a UV/Vis AGILENT Cary 50 spectrophotometer. Dye adsorptions (in dark conditions) for each membrane was also evaluated in order to discriminate between the contributions of the mere adsorption and the photocatalytic activity. Dyes solution pH was measured by a Mettler Toledo SevenGO duo SG23 pH-meter. The water content value of each membrane was determined using a microbalance and recorded as: $uptake\% = [(m_{wet} - m_{dry}) / m_{dry}] \times 100$, where, m_{dry} is the mass of membrane dried in oven at 60 °C for 2 h and then put to equilibrate in a desiccator before being weighted; m_{wet} is the weight of the membrane after immersion in distilled water at room temperature for at least 48 h and quickly blotted dry with a paper tissue in order to eliminate most of the free surface liquid. Regeneration processes were performed, after adsorption/photocatalysis experiments, by boiling the membrane in de-ionized water or diluted acid water (1% nitric acid) for 15 minutes, in order to release the adsorbed dye molecules. Then they were dried at 80°C on a hot plate for 30 minutes before each use.

For s-PBC-Bi₂O₃ membrane the photocatalytic activity was tested in the same conditions also under visible light irradiation by using a 18W Blue DULUX n.71 OSRAM lamp (producing mainly a broad-band blue light emission between 400 and 450 nm).

A20. Thermogravimetric studies were performed in a temperature range between 100°C and 1000 °C with a 10 °C/min ramp under nitrogen on a TA Q500 instrument.

Appendix B: Azo Dyes

Azo dyes are water contaminants derived from the textile industry, these or their by-products have shown to be toxic or carcinogenic causing many risks for human health as a consequence of their release in the environment [Ollis (1993)]. Many technologies have been developed for dye removal from aquatic environments, including physical, chemical, and even biological approaches. Among these approaches, absorption and photocatalytic degradation have been mainly investigated easy, efficient and economic processes [Filice, D'Angelo (2015)].

The investigated dyes are methyl orange (MO) and methylene blue (MB), whose structure is shown in Figure B1.

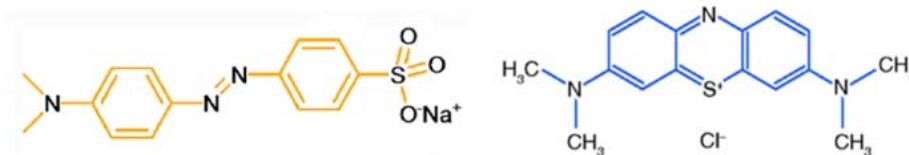


Figure B1 Chemical structure of methyl orange and methylene blue, respectively.

The UV–visible absorbance spectrum of MO dissolved in water shows two maxima. The absorbance at 270 nm is assigned to the benzene ring in MO, any variation of the 270 nm peak position is correlated to the formation of by-products as a consequence of the photodegradation of the azo dye. The absorbance at 465 nm is due to the azo linkage of MO and this was used to quantify the MO concentration reduction or degradation due to adsorption and Photocatalysis [Filice (2015)]. We have not observed any degradation of MO under UVA/blue irradiation for 1 hour as one can see in Figure B2; degradation of MO is only observed when the membranes are dipped in the solution and MO is incorporated in the polymeric matrix. Under Visible irradiation MO is reduced of about 20% of its initial concentration. Changing the pH by adding HNO₃ or NaOH did not result in a variation of MO absorbance spectra after irradiation, as one can see in Figure C3. UV-Vis spectra at pH 10.5 and at pH 6.0 are almost the same, while at acidic pH the absorbance bands shift towards larger wavelengths, and an additional feature (a hump) appears at larger wavelength on both peaks, due to the protonation of dye. MO solution is orange in basic medium and red in acidic medium, as highlighted in the photo of Figure B3 where the coloured MO solutions at acid, neutral and basic pH are in beakers numbered 5, 6, 7 respectively.

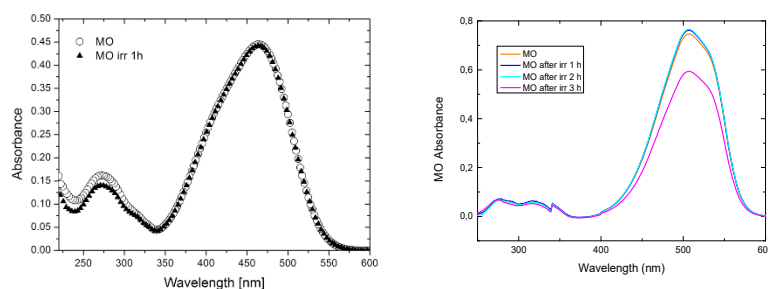


Figure B2 *On the left:* UV-vis absorbance spectra of MO ($C = 2 \cdot 10^{-5}$ M) before (open circles) and after irradiation for one hour (closed triangles) under UVA/Blue light. Reported from [Filice (2015)]. *On the right:* UV-vis absorbance spectra of MO ($C = 2 \cdot 10^{-5}$ M) before and after irradiation for three hours under Visible light.

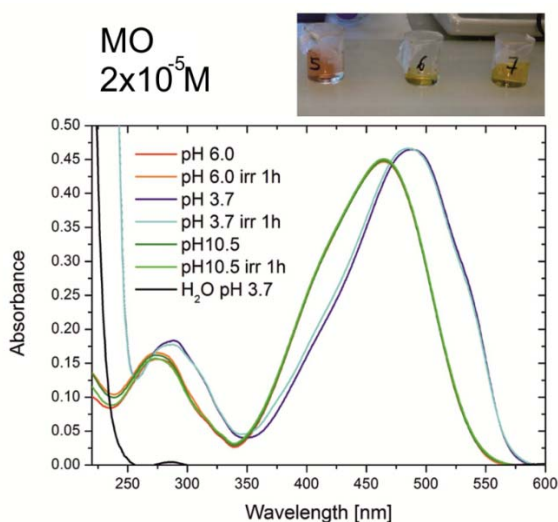


Figure B3 UV-Vis absorbance spectra of MO solution at different pH values in dark condition and after one hour irradiation. The photo above the graph shows the beakers containing the MO solution at different pH. Reported from [Filice (2015)].

Methylene blue is a cationic, thiazine dye, which absorbs light at 664 nm ($n-\delta^*$) (monomer) with a shoulder at 610 nm corresponding to the dimer; furthermore, in concentrated aqueous solutions, aggregation occurs (Figure B4). According to the exciton theory [Filice, D'angelo (2015)], when aggregation occurs some changes in the absorption spectra are visible and due to coupling between transition moments of chromophores. In particular, respect to monomer, H-aggregates with sandwich type clusters absorb light at higher energies, J-aggregates with a head-to-tail intermolecular association show a redshift. This means that the molecular aggregation is easily detectable by UV-Vis spectroscopy; in addition, if this aggregation occurs on a surface this depends on the surface properties of material. It has been checked that under UVA/Blue or Visible light irradiation in absence of investigated materials no degradation of MB takes place.

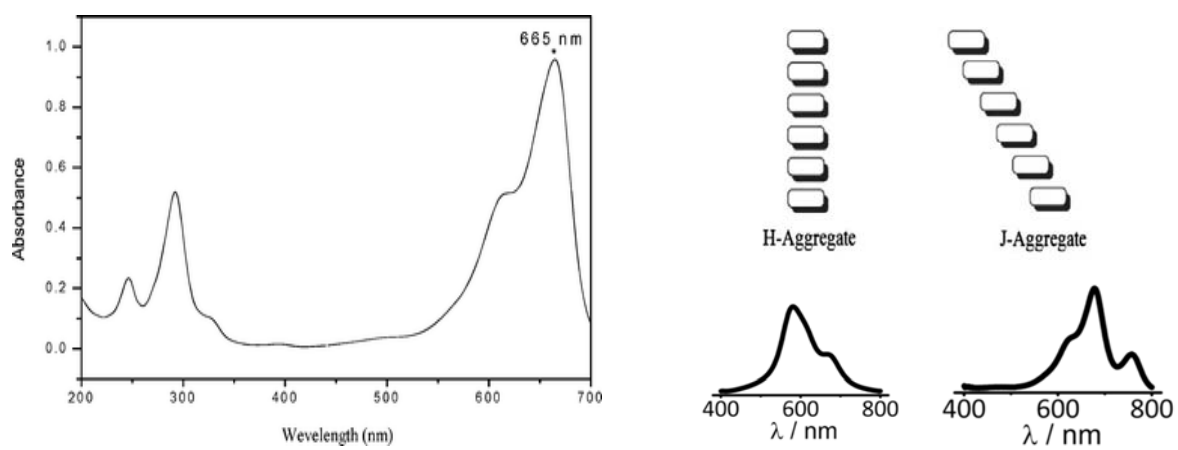


Figure B4 *On the left* Methylene blue UV-Vis absorbance spectrum. *On the right* H- and J- types of Methylene blue aggregates.

Appendix C: Irradiation Lamps

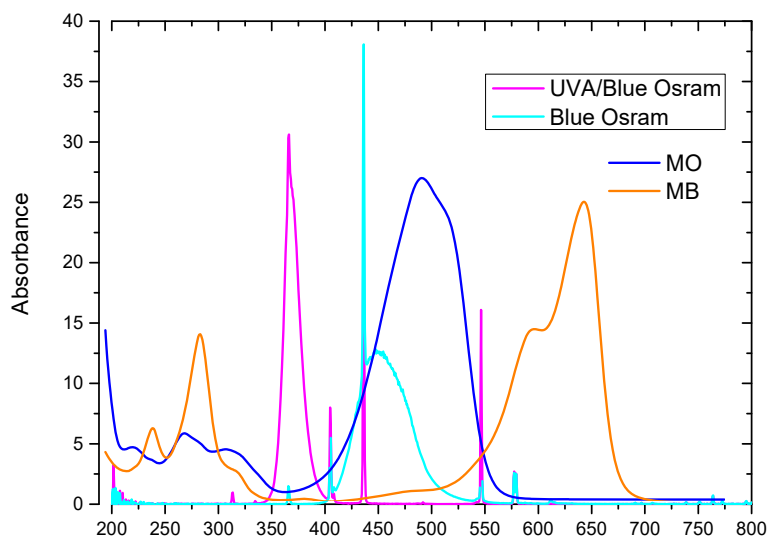


Figure C1 UV-Visible absorbance spectra of MO and MB compared with emission spectra of the two lamps used for the photocatalytic degradation of dyes.

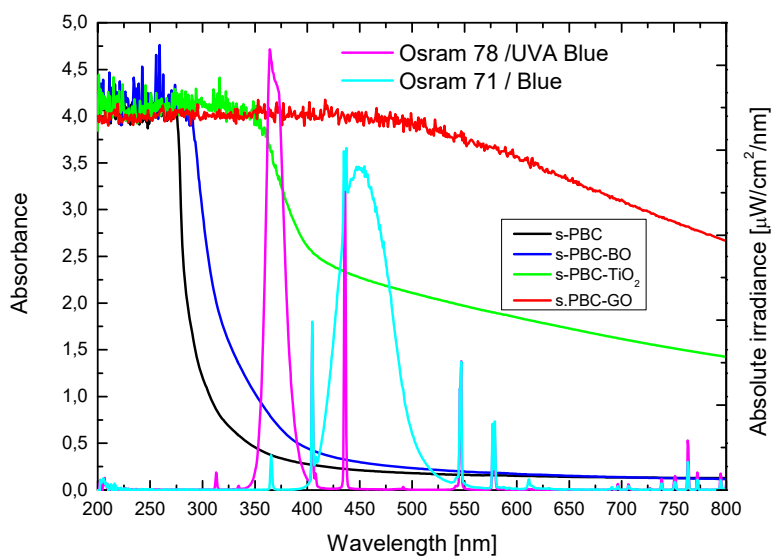


Figure C2 UV-Visible absorbance spectra of s-PBC materials compared with emission spectra of the two lamps used for the photocatalytic degradation of dyes.

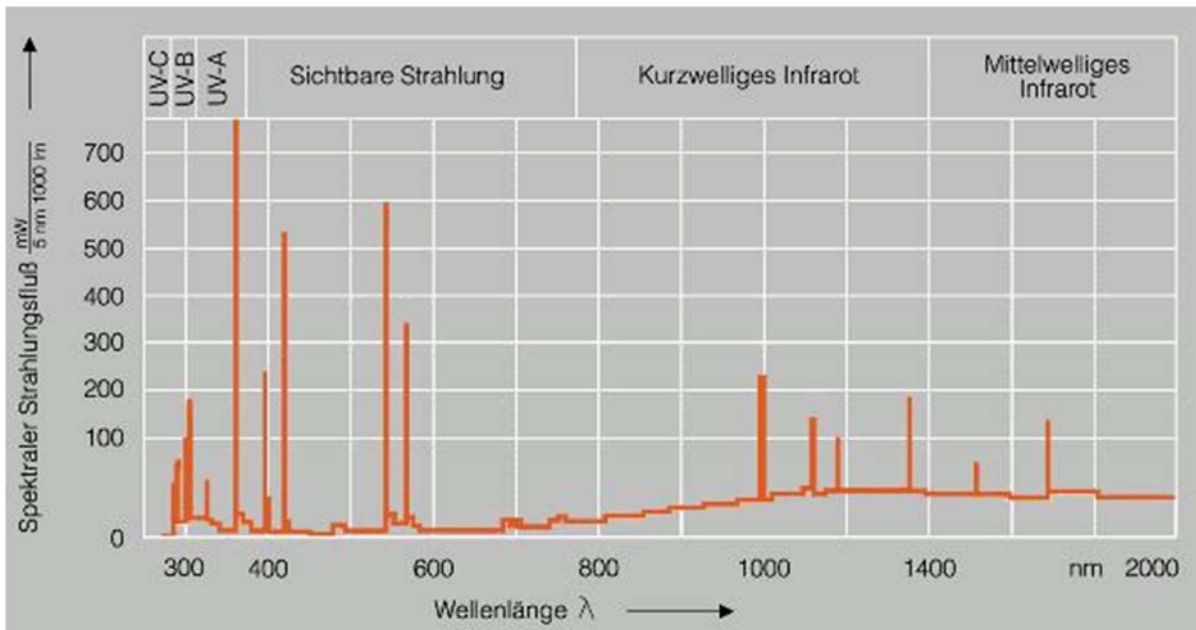


Figure C3 Emission spectra of Osram Ultra Vitalux 300W E27 lamp used for the photocatalytic water splitting.

Curriculum vitae

Simona Filice was born in September 28, 1986 in Cosenza. She attained her Master Degree in Chemistry (110/110) at the University of Calabria in 2012. After degree, she worked as intern for chemical and microbiological laboratories. She attended a second level master course in Prototyping services and Research for new technologies and new materials (SPRINT) at University of Calabria and she attained a qualification of technical expert in the use of complex instrumentation for the study and analysis of new technology and new materials with full marks (110/110 with honour). Within this period, she worked with a fellowship at the CNR-IMM institute of Catania since October 2013 to February 2014 and at PC-SM Mario Terenzi Laboratory, Department of Chemical and Chemical Technologies, University of Calabria, from June 2013 to November 2014. The research activity was mainly focused on the preparation and characterization of inorganic semiconductor nanomaterials, carbon nanomaterials and Nafion nanocomposites for fuel cell or photocatalytic applications. In November 2014, she started the PhD course in Materials Science and Nanotechnology at the University of Catania and CNR-IMM under the supervision of Dr. Silvia Scalese and Professor Giuseppe Compagnini. She spent part of her PhD course at Department of Process and Chemical Engineering – Warsaw University of Technology, with an Erasmus grant, under the supervision of Professor Leon Gradon. The main scientific interests are focused on laser irradiation processes for the modification of inorganic semiconductors or carbon nanomaterials for photocatalytic applications and water treatment and on the realization of polymer nanocomposites with photocatalytic or filtration properties for water purification. During the PhD course she presented the results of her research activity, giving both oral and poster contributions, at the following international conferences: IEEE NMDC 2014 (Aci Castello, Italy), E-MRS Spring Meeting 2015 (Lille, France), Graphita 2015 (Bologna, Italy), FisMat 2015 (Palermo, Italy), E-MRS Spring Meeting 2016 (Lille, France), ANGEL 2016 (Essen, Germany), NanoSEA 2016 (Giardini Naxos, Italy), Materials.it 2016 (Aci Castello, Italy), E-MRS Spring Meeting 2017 (Strasbourg, France). She won the Young Scientist Award at Symposium A of the E-MRS Spring Meeting 2016: “Hybrid materials: from the laboratory to the market”. She also won travel and participation grants as best PhD student curriculum and research project for ANGEL 2016 and the 8th EPF Summer School on Transport Phenomena in Polymers and Hybrid Materials. Simona Filice is author or co-author of several articles, published in international referred scientific journals. She is reviewer of several international scientific journals and assistant supervisor for bachelor and master degree students.

List of Publications

- D. D'Angelo, **S. Filice**, S. Libertino, V. Kosma, I. Nicotera, V. Privitera, S. Scalese, Photocatalytic properties of Nafion membranes containing graphene oxide/titania nanocomposites, 2014 IEEE 9th Nanotechnology Materials and Devices Conference, NMDC 2014.
- **S. Filice**, D. D'Angelo, S. Libertino, I. Nicotera, V. Kosma, V. Privitera, S. Scalese, Graphene oxide and titania hybrid Nafion membranes for efficient removal of methyl orange dye from water, *Carbon* 82 (2015) 489-499.
- **S. Filice**, D. D'Angelo, S.F. Spanò, G. Compagnini, M. Sinatra, L. D'Urso, E. Fazio, V. Privitera and S. Scalese, Modification of graphene oxide and graphene oxide-TiO₂ solutions by pulsed laser irradiation for dye removal from water, *Mater. Sci. Semic. Process.* (2015), 42, 50-53.
- S. Baldo, V. Scuderi, L. Tripodi, A. La Magna, S.G. Leonardi, N. Donato, G. Neri, **S. Filice** and S. Scalese, Defects and gas sensing properties of carbon nanotube-based devices, *J. SENS. SENS. SYST.* 4 (2015), 25–30.
- S. Scalese, I. Nicotera, D. D'Angelo, **S. Filice**, S. Libertino, C. Simari, K. Dimos, V. Privitera, Cationic and anionic azo-dye removal from water by sulfonated graphene oxide nanosheets in Nafion membranes, *New Journal of Chemistry*, 2016, **40**, 3654-3663
- Buccheri MA, D'Angelo D, Scalese S, Spanò SF, **Filice S**, Fazio E, Compagnini G, Zimbone M, Brundo MV, Pecoraro R, Alba A, Sinatra F, Rappazzo G, Privitera V. Modification of graphene oxide by laser irradiation: a new route to enhance antibacterial activity. *Nanotechnology*. 2016 Jun 17;27(24):245704.
- S. Filice, G. Compagnini, R. Fiorenza, S. Scirè, L. D'Urso, M. E. Fragalà, P. Russo, E. Fazio, S. Scalese, Laser processing of TiO₂ colloids for an enhanced photocatalytic water splitting activity, *Journal of Colloid and Interface Science*, (2017), 489, 181-187.

- Scalese S; Baldo S; D'Angelo D; **Filice S**; Bongiorno C; Reitano R; Fazio E; Conoci S; La Magna A, Electrical properties and oxygen functionalities in ethanol-treated and thermally modified graphene oxide, *Journal of Applied Physics*, (2017), 121 (15), 155105.
- G. Compagnini, C. La Rosa, L. D'Urso, S. Scirè, R. Fiorenza, **S. Filice**, S. Scalese, *Laser micro-nano-nanomanufacturing and 3D microprinting*, Springer, In Press.
- **S. Filice**, D. D'Angelo, A. Scarangella, D. Iannazzo, G. Compagnini and S. Scalese, Highly effective and reusable sulfonated pentablock copolymer nanocomposites for water purification applications. *RSC Advances*, (2017), 7(72):45521-45534.
- D. D'Angelo, **S. Filice**^{*}, A. Scarangella, D. Iannazzo, G. Compagnini, S. Scalese, Bi₂O₃ / Nexar® polymer nanocomposite membranes for visible photocatalytic applications, Submitted *Catalysis Today*.
- R. Pecoraro, D. D'Angelo, **S. Filice**, S. Scalese, F. Capparucci, F. Marino, C. Iaria, G. Guerriero, D. Tibullo, E. M. Scalisi, A. Salvaggio, I. Nicotera, M. V. Brundo, Toxicity evaluation of graphene oxide and titania loaded Nafion membranes in zebrafish, Submitted to *Frontiers in Physiology*.